

This item was submitted to Loughborough University as a PhD thesis by the author and is made available in the Institutional Repository (<https://dspace.lboro.ac.uk/>) under the following Creative Commons Licence conditions.



For the full text of this licence, please go to:
<http://creativecommons.org/licenses/by-nc-nd/2.5/>

BLL ID NO: D37572/81

LOUGHBOROUGH
UNIVERSITY OF TECHNOLOGY
LIBRARY

AUTHOR/FILING TITLE

VADHER, V

ACCESSION/COPY NO.

192019/02

VOL. NO.

CLASS MARK

~~1 JUL 1988~~

019 2019 02



3/

CH-2-

02

MATHEMATICAL MODELLING OF AIRCRAFT ELECTRICAL
POWER SYSTEMS

by

VINOD VASHRAM VADHER, B.Sc.(Hons), M.Phil, D.I.C., CEng.,
M.I.E.E.

A Doctoral Thesis

Submitted in partial fulfilment of the requirements

for the award of the degree of

Doctor of Philosophy

of the

Loughborough University of Technology

MARCH, 1981

Supervisor: Professor I R Smith
Head of Department of Electronic and Electrical
Engineering

C by VINOD VASHRAM VADHER, 1981

Loughborough University of Technology Library	
Recd	June 81
Class	
Rec. No.	192019/02

ACKNOWLEDGEMENTS

I would like to express my deepest gratitude to Professor I R Smith for his guidance throughout the period of research and for his help in many other aspects.

I am indebted to the Science Research Council and Loughborough University of Technology for the financial support during the course of my study. I am also grateful to the Electronic and Electrical Engineering department of the University and Mr B A Fanthome of the Royal Aircraft Establishment, Farnborough, for providing the test facility for the work described in this thesis.

I wish to thank Dr S Williams and other members of the staff for their help during the period of my study and my colleague, Mr G Kettleborough for the many stimulating and valuable discussions we had.

Finally, I would like to thank my wife for her patience and understanding during the period of study and Mrs J Smith for typing the thesis.

SYNOPSIS

The continuing developments in aircraft electrical power supply systems have been accompanied by a progressive narrowing of the transient and the steady-state voltage regulation limits within which the system must operate. The performance of a system is satisfactory only when it meets the conditions of the relevant performance specification, for example MIL-G-21480A (AS), as laid down by the aircraft manufacturer.

The most important of the specified requirements is the transient performance when the load change represents a significant percentage of the rating of the generator set. Most airborne electronic equipment is sensitive to the large voltage and (possibly) frequency changes which occur and which may result in damage to semiconductor devices, dropout of relays, introduction of spurious signals into computers and communication systems, etc. For these, and many other reasons, it is important to be able to predict accurately the maximum over and under voltages likely to be experienced by the supply system. Such a process requires an accurate model to be formulated for the system and for a technique to be developed for the efficient use of the model. The primary component of the power system is the generator unit, and this thesis is concerned with the modelling in state-variable form of the 3-stage generator unit found on board aircraft and the automatic voltage regulator with which it is invariably fitted. While the work described relates generally to a unit of about 40 KVA rating at 400 Hz, the methods of analysis described are quite general and can immediately be applied to other similar systems. Theoretical techniques for determining the ryb generator phase model parameters from the dqo and design parameters are given in the thesis, to enable the system transient response to be predicted before the system is actually built. By this means, the manufacturer is able to consider whether his designs need modifications to meet the relevant performance specifications before the system is actually built, which clearly represents a considerable saving in both finance and in time.

The modelling techniques presented in the thesis could, if desired, be extended to include the constant-speed drive of the generator^{or} unit, by again modelling this in a state-variable form to give differential equations that can be numerically integrated on a digital computer in the same way as are the equations of the electrical system.

The majority of loads applied to an aircraft generator are passive and can normally be represented by an equivalent series resistor and inductor. Many comparisons between the measured and theoretical voltage transients experienced by a typical aircraft generator for loads up to 1.5 p.u. are given in this thesis and it is established convincingly that the model developed provides an accurate prediction of the system performance.

An important active load frequently found on board an aircraft is the induction motor, and a complete induction motor/synchronous generator model was accordingly developed for the study of the switching transients experienced when the stationary motor is applied directly to the regulated generator. The generator model described includes the permanent magnet pilot exciter, with its rectified output being controlled and fed to the main exciter field and enables both the steady state and the transient performance of the overall system to be predicted for many of the operating conditions experienced by an actual aircraft system.

LIST OF PRINCIPAL SYMBOLS

A.V.R., a.v.r.	automatic voltage regulator
A_1	fundamental frequency component of current in phase with voltage (r.m.s)
B_1	fundamental frequency component of current in quadrature with voltage (r.m.s)
B_g	airgap flux density (T)
\hat{B}_g	peak value of airgap flux density (T)
C_1	ratio of the fundamental to the actual value of field form at pole centre
C_{ad}	normalised saturation polynomial obtained from open-circuit characteristic
C_{rr}, C_{ry} C_{rF}, C_{rD} C_{FF}, C_{DD} C_{FD}	normalised saturation polynomials for use in phase model analysis
C_{d1}	ratio of the amplitude of the fundamental airgap flux density produced by the d-axis armature current to that which would be produced with a uniform airgap equal to the effective airgap over the pole centre
C_{q1}	as for C_{d1} , but with the m.m.f. centred on the quadrature axis
C_p	the ratio of average to the maximum value of field form. (The field form is the wave of flux density due to field only).
E, E_a	phase voltage (r.m.s)
e_d	instantaneous d-axis voltage
E_{do}	open circuit d.c. output voltage of rectifier

E_d	d.c. output voltage of rectifier on load
ΔE_d	effective d.c. voltdrop due to commutation reactance X_c
E_f	field winding voltage
$E_{(N)}$	new value of E
$E_{(0)}$	old value of E
f	frequency
F_{ds}	m.m.f. due to armature current in the d-axis
F_{qs}	m.m.f. due to armature current in the q-axis
G_{vv}	$\frac{d(L_{vv})}{dt}$
G_{vu}	$\frac{d(L_{vu})}{dt}$
I_l	$\sqrt{A_l^2 + B_l^2}$
I_D	total direct axis current in the d-axis referred to the generator field current
I_N	neutral current
I_p	exciter phase current (r.m.s)
i_v, I_v	current in branch or winding v
K	ratio of the 3rd-harmonic to the fundamental component in the space distribution of armature m.m.f.
K_{aD}	coefficient of coupling between the armature phase with its axis lined in the d-axis and the d-axis damper windings
K_{aF}	coefficient of coupling between the armature phase with its axis lined in the d-axis and the field windings
K_{aQ}	coefficient of coupling between the armature phase with its axis lined in the q-axis and the q-axis damper windings

K_b	$\frac{\sin n_b \alpha_b}{n_b \sin \alpha_b}$
K_c	current gain of the rectifier equal to (d.c. output current/r.m.s. value of fundamental frequency component)
K_{eo}	open circuit gain of the exciter (E_{ae}/E_{fe})
K_f	field winding breadth factor, $= \frac{\pi C_1}{4 C_{d1}}$
K_{FD}	coefficient of coupling between the field and the d-axis damper windings
K_{go}	open circuit gain of the generator (E_{ag}/E_{fg})
K_v	the voltage gain of the rectifier equal to (d.c. output voltage/a.c. phase voltage (r.m.s))
K_w	armature phase winding factor
\uparrow	axial length of PMG magnet
L	axial length of generator rotor
L_{al}	leakage inductance of armature phase winding
L_D, L_Q	d- and q-axis armature phase self inductance coefficients of the generator respectively
L_S, L_R	the self inductance of induction motor stator and rotor phase windings respectively
L_{vL}	inductance of load connected to phase or winding v
L_{vv}	self inductance of winding v (secant value)
L'_{vv}	incremental self inductance of winding v
L_{vu}	mutual inductance between v and u windings (secant value)
L'_{vu}	incremental mutual inductance between v and u windings
m	no. of phases
M	stator to rotor phase mutual inductance coefficient of induction motor

M_D, M_Q	d- and q-axis armature phase to phase mutual inductance coefficients of the generator respectively
M_{DD}, M_{QQ}	armature phase to d- and q-axis damper winding mutual inductance coefficients respectively
M_F	d-axis armature phase to field winding mutual inductance coefficient
M_S	stator phase to phase mutual inductance of the induction motor
M_R	rotor phase to phase mutual inductance of the induction motor
N	no. of turns per phase
n_b	no. of damper bars
N_f	no. of turns per pole of field winding
P	no. of poles
p	$\frac{d}{dt}$
P.M.G.	permanent magnet generator
r	resistance of phase winding
r_{bed}, r_{beq}	equivalent single damper bar resistance including end ring effect in the d- and q-axis respectively
R_{Dd}, R_{Qq}	resistance of d- and q-axis damper windings referred to stator side
R_d	resistance of the load applied to the rectifier
RLF	reactance load factor ($\approx X_c/R_d$)
r_{fd}	field winding resistance referred to stator side
R_f	field winding resistance
R_S	stator phase winding resistance of induction motor
R_R	rotor phase winding resistance of induction motor
R_{vv}	resistance of winding v
R_{vL}	resistance of the load connected to winding v

s	Laplace operator
T_a	armature time constant
T'_{do}	open circuit transient time constant
T'_d	short circuit transient time constant
T_{DD}, T_{QQ}	d- and q-axis damper winding time constants respectively
T'_{dz}	transient time constant on load
T_{A1}, T_{F1}, T_{F2}	time constants of the a.v.r. feedback circuit
T_{R1}, T_{R2}	time constants of the a.v.r. voltage sensing circuit
T_1 to T_{12}	time constants of the a.v.r. (state variable model)
V_R	forward voltage drop across rectifier
V_v	voltage of branch or winding v
V_{vN}	phase (v) voltage
x_{ad}, x_{aq}	d- and q-axis armature reaction synchronous reactances respectively
x_c	commutation reactance
x_d, x_q	d- and q-axis synchronous reactances respectively
x'_d	d-axis transient reactance
x_{DD}, x_{DD}	d-axis self reactance of equivalent single circuit damper winding
$x_{D\ell}, x_{D\ell}$	d-axis leakage reactance of equivalent single circuit damper winding
x_{FF}, x_{FF}	self reactance of the field winding referred to stator side
$x_{F\ell}, x_{F\ell}$	leakage reactance of the field winding referred to stator side
x_ℓ	armature phase leakage reactance
$x_{Q\ell}, x_{Q\ell}$	q-axis leakage reactance of equivalent single circuit damper winding

x_{QQ}, X_{QQ}	q-axis self reactance of equivalent single circuit damper winding
Z_{vv}	impedance of branch or winding v
α	commutation angle
μ	delay angle
ϕ	power factor angle
ϕ_p	flux per pole
ϵ	small difference between two quantities ($< 10^{-2}$)
ψ_d, ψ_q	flux linkages in the d- and q-axis respectively
λ_a	specific permeance of the airgap
λ_{al}	armature phase leakage permeance
λ_F	specific permeance for field leakage due to pole body and tip
$\lambda_{LDd}, \lambda_{LQq}$	d- and q-axis equivalent single circuit damper winding's leakage permeance
$\lambda_{bed}, \lambda_{beq}$	d- and q-axis equivalent single bar leakage permeance including end ring effects
τ	pole pitch

S.I. units are used throughout the thesis except in Chapter 9, where formulae in imperial units are given. This is because the classical works by Kilgore ⁶⁸ and Talaat ⁵⁸, of which the derived formulae are an extension, are based on imperial units and also because the manufacturers in the U.K. and U.S.A. still work in imperial units.

Subscript notation for Tensors:

$[X_d]$	rectifier diode network tensor
$[X_e]$	exciter network tensor
$[X_m]$	tensor for a connected network with varying topology assuming all branches in conduction
$[X_n]$	tensor for a connected network with no change in topology or for a network with varying topology at a particular instance in time
$[X_p]$	primitive network tensor
$[X_{pm}]$	primitive induction motor tensor
$[X_{ps}]$	primitive a.c. supply tensor
$[]_t$	transpose of a tensor

Subscript notation for a branch or winding of network

e, E	exciter
g	generator

CONTENTS

	Page Nos
ACKNOWLEDGEMENTS	i
SYNOPSIS	ii
LIST OF PRINCIPAL SYMBOLS	iv
CONTENTS	xi
CHAPTER 1: INTRODUCTION	1
CHAPTER 2: PHASE MODEL OF A SYNCHRONOUS GENERATOR	4
2.1 Introduction	4
2.2 The Phase Model of a Synchronous Generator	5
2.3 Inductances Forming the [G] Tensor	8
2.3.1 Self Inductances	8
2.3.2 Mutual Inductances	8
2.3.3 Generator Inductance Coefficients	10
2.4 Effect of Magnetic Saturation on [L] and [G] Tensors	11
2.5 Determination of Phase Model Parameters of 2130 Generator	15
2.5.1 Measurement of Resistances	16
2.5.2 Measurement of Self Inductance of the Generator Phase Winding	16
2.5.3 Measurement of the Self Inductance of the Field Winding	17
2.5.4 Measurement of Phase to Phase Mutual Inductance	17
2.5.5 Measurement of Armature Phase to Field Mutual Inductance	18
2.5.6 A.C. Measurement of Generator Parameters	18
2.6 Design Parameters of 2130 3-stage Generator Unit	22
2.7 Predictions of Saturated Steady-State Inductances of 2130-Main Generator Using Finite-Element Field Solutions	22

	Page Nos
2.8 Conclusions	23
CHAPTER 3: MODELLING OF A BRUSHLESS EXCITATION SYSTEM ON A DIGITAL COMPUTER	39
3.1 Tensor Method of Analysis of Electrical Circuits	40
3.2 The Phase Model Analysis of a Brushless Exci- tation System for a Synchronous Generator	47
3.2.1 Exciter-Rectifier-Generator Model with 4-wire Load Connection	53
3.2.2 Exciter-Rectifier-Generator Model with 3-wire Load Connection	61
3.3 Differential Equations for Exciter-Rectifier- Generator Phase Model	62
3.3.1 Calculation of Diode Currents.....	67
3.3.2 Calculation of Diode Voltages.....	67
3.4 Comparison Between the Measured and Predicted Results	69
3.5 Conclusion	69
CHAPTER 4: MODELLING OF AN AUTOMATIC VOLTAGE REGULATOR	
4.1 Introduction	88
4.2 Description of Automatic Voltage Regulator	88
4.3 State Variable Analysis of Automatic Voltage Regulator	89
4.3.1 Voltage Sensing Circuit	89
4.3.2 Amplifier Circuit of A.V.R.	91
4.3.3 Feedback Circuit of A.V.R.	92
4.3.4 Computation of Transient Response of A.V.R. on a Digital Computer	94
4.4 Transfer Function Analysis of Automatic Voltage Regulator	95
4.4.1 Transfer Function Representation of Voltage Sensing Circuit	95

	Page Nos
4.4.2 Transfer Function Representation of A.V.R. Feedback Circuits	96
CHAPTER 5: MODELLING OF A REGULATED 3-STAGE GENERATOR UNIT	110
5.1 Synchronous Machine with a Rectifier Load	111
5.2 Modes of Operation of the Rectifier on Load	
5.2.1 Ideal Operation of the 3-phase Recti- fier	111
5.2.2 Actual Operation of the 3-phase Recti- fier	113
5.3 Steady State Operation of Exciter-Rectifier System	116
5.4 Transient Performance of Exciter on Load	116
5.4.1 Application of a Steady State Exciter Model to Generator Transient Condi- tions	117
5.5 Iterative Method of Calculating Exciter- Rectifier Transient Response	118
5.6 Comparison of the Measured and Predicted- Transients Following Application (and Rejection) of Generator Loads	120
5.6.1 Load Application Tests on 2130 Generator Unit Without A.V.R.	120
5.6.2 Load Application and Rejection Tests on 2130 Generator Including A.V.R.	120
5.7 Discussion and Conclusion	121
5.7.1 Exciter Field Current Transients	122
CHAPTER 6: THE TRANSFER FUNCTION OF A BRUSHLESS EXCITA- TION SYSTEM	152
6.1 Introduction	152
6.1.1 The Transfer Function of a Synchro- nous Generator	152

	Page Nos
6.1.2 Transfer Function of a Brushless Excitation System	158
6.2 The Effect of Changing the Reactance Load Factor and the Field Winding Resistance on the Performance of the Exciter-Rectifier	162
6.2.1 The Effect of Changing the Reactance Load Factor	162
6.2.2 The Effect of Changing the Generator Winding Resistance	162
6.3 Discussions and Comments	164
CHAPTER 7: INDUCTION MOTOR AS AN IMPACT LOAD APPLIED TO THE REGULATED GENERATOR UNIT	171
7.1 Modelling of the Induction Motor in Phase Quantities	171
7.2 Modelling of Induction Motor/Synchronous Generator Combination	180
7.3 Induction Motor as an Impact Load Applied to the Regulated 3-Stage Generator Unit	185
7.4 Conclusions and Discussions	186
CHAPTER 8: THE MATHEMATICAL MODEL OF PERMANENT MAGNET GENERATORS	205
8.1 Calculation of Open-Circuit Voltage of PMG from Tests at Standstill	205
8.2 Measurement of the PMG Inductances	206
8.3 Model of the PMG on Rectifier Load	207
8.4 Calculation of the PMG Phase Voltages	213
8.5 Comparison Between the Calculated and the Measured Performance of PMG on Rectifier Load	215
8.6 Conclusion	216
CHAPTER 9: CALCULATION OF PHASE MODEL PARAMETERS FROM $d_{\phi 0}$ AND DESIGN PARAMETERS	239
9.1 Relationship Between the $d_{\phi 0}$ Model and the ryb -Phase Model Equations	239

	Page Nos
9.2 Transformation of the Inductance Tensor [L_{ryb}] to [L_{dqo}]	242
9.3 Calculation of Inductance Coefficient of [L_{ryb}] from Design Parameters	248
9.4 Calculation of Armature Phase to Field Mutual Inductance (M_F) and Self Inductance (L_{FF}) of the Field Winding	249
9.4.1 Calculation of M_F and L_{FF} Using dqo Parameters	249
9.4.2 Calculation of M_F and L_{FF} Using Design Parameters	250
9.5 The Effective Constants of the Damper Windings	251
9.6 Calculation of the Constants of the Damper Windings from d- and q-Axis Reactances and Time Constants	253
9.6.1 The Coefficients of Coupling in the d-axis	253
9.6.2 The Coefficients of Coupling in the q-axis	255
9.6.3 The d-axis Damper Winding Time Con- stant	256
9.6.4 The q-axis Damper Winding Time Con- stant	256
9.7 Calculation of the Constants of the Damper Windings from Design Parameters	257
9.7.1 The Coefficient of Coupling in the d-axis	257
9.7.2 The Coefficient of Coupling in the q-axis	259
9.7.3 The d-axis Damper Winding Time Con- stant	260
9.7.4 The q-axis Damper Winding Time Con- stant	261

	Page Nos
9.8 Determination of the Saturation Characteristics for Use in Phase Model Analysis from the Open Circuit Characteristic	261
9.9 Conclusion	266
CHAPTER 10: AREAS OF FURTHER RESEARCH	274
CHAPTER 11: CONCLUSION	276
REFERENCES	278
APPENDIX A1: A1.1 Construction of 2130 3-Stage Generator Unit	287
A1.2 3-Stage Generator Unit Connected for Load Tests	287
A1.3 Main Generator Design Parameters	292
A1.4 Main Exciter Design Parameters	293
A1.5 Permanent Magnet Generator Parameters	294
APPENDIX A2: A2.1 Measurement of Self Inductance of a Coil	295
APPENDIX A3: Measurement of Mutual Inductances Between Two Coils	301
APPENDIX A4: Measurement of Mutual Inductances Between Two Coils Having a Common Resistive Path	305
APPENDIX A5: A5.1 Computation of Operational Impedance Tensor $[Z_m]$	309
A5.2 Computation of Independent Currents $[I_n]$ from Computed Values of $[I_m]$	311
A5.3 Computation of Diode Currents	311
A5.4 Computation of Voltages Across the Diodes $[V_D]$	312

APPENDIX A6:	Numerical Methods for the Solution of the Differential Equations on a Digital Computer	313
A6.1	Runge-Kutta Methods	313
APPENDIX A7:	A7.1 State Variable Model of A.V.R. Digital Computer Program	315
A7.2	Calculation of Non-Linear Gain of A.V.R. for Use in Transfer Function Model of A.V.R.	320
APPENDIX A8:	Transfer Function Analysis of A.V.R.	
A8.1	Voltage Sensing Circuit	327
A8.2	Negative Feedback Circuit	328
A8.3	Positive Feedback Circuit	331
APPENDIX A9 :	Saturation Characteristics of the Exciter	336
APPENDIX A10:	Relationship Between D.C. Power Output and Effective A.C. Power Supplied by the Exciter	340
APPENDIX A11:	A11.1 Induction Motor Design Data	341
A11.2	Calculation of Induction Motor Phase Model Parameters	341
APPENDIX A12:	A12.1 Electromagnetic Torque Equation of Induction Motor	343
A12.2	The Mechanical Load Torque Equation	343
APPENDIX 13:	Transformation of $[L_{ryb}]$ to $[L_{dq0}]$	344

CHAPTER 1

INTRODUCTION

The use of analogue computers for the solution of transient problems in a.c. power systems has been a subject of interest for many years.¹⁻³ The techniques developed have been found to be generally adequate when the equations for the system can be linearised, or where saturation in the generators can be represented approximately by the open-circuit characteristic of these machines. However, one significant limitation which often arises is the extent to which the various saturation and non-linear functions of the automatic voltage regulator and the exciter-rectifier system can be simulated.

This limitation has largely been overcome by the use of digital computing facilities, as this enables the solution of the overall equations to be obtained at each small step by computing the values of the non-linear functions. The digital computer enables very much more accurate predictions of the response of non-linear systems to be obtained than is possible by the use of analogue computers, as the latter relies heavily on the extent to which non-linear functions can be simulated using electronic hardware. The digital computer can therefore be used to predict the performance of a regulated generator by solving the differential equations using a numerical integration method and computing the values of non-linear functions at each time step.

Recent developments in the application of the coupled circuit approach to the solution of synchronous machine transient problems has evoked considerable interest in the use of numerical techniques for the solution of the differential equations involved. Although the basic form of these equations may be written down in terms of the inductances and resistances of the machine windings, their solution has constituted historically one of the major problems of machine analysis. Considerable attention was paid to the problem by Park⁴⁻⁶, who by using the work of Blondel⁷ and of Doherty and Nickle⁸ produced a transformation leading to the now familiar d-q statement of the machine equations. Although modelling in this form enables

algebraic solutions to be obtained in many transient studies, the comparatively recent development of high-power, digital computing facilities has brought about a revival of interest in the numerical solution of the basic or phase model form of the equations as opposed to the algebraic development leading to the d-q equations. As discussed in Chapter 2 of this thesis the use of the basic equations eliminates the various simplifying assumptions introduced by the d-q model and, for example, enables the inclusion of the higher-order spatial harmonics of the inductances inevitably present in a real machine. It also makes simpler the simulation of certain unbalanced fault and load conditions, which require considerable mathematical manipulation⁹⁻¹² in an algebraic solution developed from the d-q equations.

The effects of higher harmonics in the spatial variations on the airgap m.m.f. and the permeance on the machine inductances are included in the generator model, by the use of inductance variations measured on a typical aircraft generator. Nonlinearities in the inductances due to saturation in the iron structures of the machine are measured, using the ballistic techniques described by Jones¹³, Barton and Dunfield¹⁴ and Snider and Smith¹⁵. These methods enable the inductances of the armature and the field windings of the main generator to be readily measured, independently of any short-circuited damper windings and of eddy currents existing in various parts of the iron structure.

The overall model developed in this thesis for the 3-stage generator and its associated automatic voltage regulator is based on individual models for the various elements comprising the generator unit, with these being produced piecemeal before assembly into an overall package. The equations are framed in such a way as to facilitate consideration of the performance of the regulated generator in isolation, as is frequently found on board aircraft, and to deal with the impact conditions which arise when a stationary induction motor is switched directly to the generator.

In the thesis the tensor methods of Kron¹⁶⁻¹⁹ are used to obtain the overall differential equations for both a brushless exci-

tation system and a synchronous-generator/induction-motor combination. One reason for using Kron's technique is that it enables the equations for the inter-connected generator unit to be obtained easily from the individual equations for the elements which comprise it, and in particular it copes efficiently with the varying topology of the connected network as the pattern of diode conduction changes. The overall unit model also includes a permanent magnet generator, which is usually the first stage of the generating unit.

A linearised form of the transfer function of the exciter-rectifier-generator is developed in this thesis to show the effect of parameter variations on the operation of the brushless excitation system and the necessary conditions for optimising the power output of the exciter-rectifier.

Theoretical formulae are derived to enable the phase model parameters to be calculated from design data and the corresponding d-q parameters, so that the mathematical models derived can be used to investigate the performance of the system at a design stage. This would enable designs to be modified, if necessary, before the generator unit and/or the automatic voltage regulator are built. Areas of further research into the aircraft electrical power system, where the system models described in the thesis can be used are also discussed.

Throughout the thesis, the mathematical models developed for the power system are verified by considerable experimental work, and the good agreement obtained between computed and experimental results gives a high degree of confidence both in the methods of mathematical modelling described and in the models developed.

The details of the 2130 3-stage generator unit used for the work described in this thesis are given in Appendix (A1).

CHAPTER 2

PHASE MODEL OF A SYNCHRONOUS GENERATOR

2.1 Introduction

The standard 3-stage power generating unit for modern aircraft consists of the main generator, an exciter for supplying the field currents for the main generator via a rotating 3-phase rectifier bridge and a permanent magnet pilot exciter. This chapter deals with the modelling of the main generator, which has a 3-phase armature winding on the stator and the field winding, together with the damper windings, on the salient-pole rotor.

In order to determine both the transient and the steady state performance of the generator, a mathematical model is developed in the form of a set of simultaneous differential equations that fully describe the generator behaviour. The form these equations take depends on the choice of the reference frame in which they are written. The most commonly used is the dqo frame which has the important advantage over other frames that it contains only invariant coefficients. The use of this frame therefore results in a considerable reduction in computing time over the phase model during the numerical integration of the equations. However, there are a number of disadvantages with this model which limit its use. These are:

- 1) The simplifying assumptions that result in the time invariant coefficients assume a sinusoidal flux density distribution in the air-gap and neglect any harmonics produced by the non-sinusoidal distribution of the windings of the actual machine and the effects of the slots.
- 2) It is necessary to use a symmetrical component transformation, which increases considerably the computing time, when unbalanced load conditions are considered.
- 3) A major assumption in the development of this model, which is not true of the actual machine, is that the airgap permeance of the salient pole rotor machine is sinusoidal. This results

in the 2nd-harmonic coefficients of the armature phase self-inductance and the phase-to-phase mutual inductance being equal. While this assumption is reasonable at points under the pole faces, it is dubious at points in the interpolar space of the machine.

To overcome the inherent disadvantages of the dqo reference frame, the phase model is increasingly coming into use. The main disadvantage with this model is the need to assemble and to invert a time varying inductance tensor at each stage of the numerical solution of the machine differential equations, although this problem is now substantially overcome by the use of a modern high-speed digital computer. The phase model developed and described in this chapter was used for the subsequent transient analysis of a generator, following the application and rejection of load, as described in Chapter 5. It is readily possible with this model to include the effects of magnetic saturation on individual windings of the machine which results in a more accurate transient prediction than is possible with the dqo model, which generally assumes the effect of saturation on the direct axis armature reactance as given by the open circuit characteristic of the generator.

2.2 The Phase Model of a Synchronous Generator

The modelling of a synchronous generator in phase quantities has been studied by a number of authors²⁰⁻²³ with the effects of magnetic saturation in the generator and harmonics in the spatial variation of the inductances of the generator being included in the work of Snider²³.

(A 3-phase synchronous generator, with stationary armature windings and rotating field, d and q damper windings is represented by the model shown in Figure 2.1.) The neutral point of the armature phases is brought out to a terminal (N) as shown. If the load and the phase inductances and resistances of the individual phases are combined, the machine can be considered to be short-circuited and the corresponding differential equations in tensor form are given in Figure 2.2. In short form, these are:

$$[V] = [Z][I] = [L][pI] + [R][I] \quad 2.1$$

Since the inductances are time variant, the general form of equation 2.1 is

$$[V] = [L][pI] + [R + G][I] \quad 2.2$$

where

$$[G] = \frac{d}{dt} [L] = \frac{\partial}{\partial \theta} [L] \cdot \frac{d\theta}{dt} + \frac{\partial [L]}{\partial (I_d)} \cdot \frac{d(I_d)^*}{dt} \quad 2.3$$

If the generator is driven at constant speed, $\frac{d\theta}{dt} = \text{constant} = \omega$.
Therefore

$$[G] = \omega \frac{\partial [L]}{\partial \theta} + \frac{\partial [L]}{\partial (I_d)} \cdot \frac{d(I_d)}{dt} \quad 2.4$$

Equation 2.2 in state-variable form is

$$[pI] = [L]^{-1} [[V] - [R + G][I]] \quad 2.5$$

Equation 2.5 may be solved by a numerical integration method to give a new machine current vector $[I]$ at each time step.

The phase voltages are obtained from

$$\begin{aligned} V_{rN} &= - (R_{rL} i_r + L_{rL} p i_r) \\ V_{yN} &= - (R_{yL} i_y + L_{yL} p i_y) \\ V_{bN} &= - (R_{bL} i_b + L_{bL} p i_b) \end{aligned} \quad 2.6$$

* I_d is given by equation 2.21. $\theta = \theta_r$

The total neutral current is given by

$$i_N = i_r + i_y + i_b \quad 2.7$$

For a 3-wire load connection, the neutral point N is isolated, and

$$i_N = i_r + i_y + i_b = 0 \quad 2.8$$

This constraint can be included in the differential equations of Figure 2.2, by obtaining a current transformation tensor $[C]$ relating the 4-wire and 3-wire connections. Thus

$$[i_r \ i_y \ i_b \ i_F \ i_D \ i_Q]_t = [C][i_r \ i_y \ i_F \ i_D \ i_Q]_t \quad 2.9(a)$$

where

$$[C] = \begin{array}{|c|c|c|c|c|} \hline 1 & 0 & 0 & 0 & 0 \\ \hline 0 & 1 & 0 & 0 & 0 \\ \hline -1 & -1 & 0 & 0 & 0 \\ \hline 0 & 0 & 1 & 0 & 0 \\ \hline 0 & 0 & 0 & 1 & 0 \\ \hline 0 & 0 & 0 & 0 & 1 \\ \hline \end{array} \quad 2.9(b)$$

Using the impedance transformation ²³, the impedance for a 3-wire connection is

$$[Z] = [C]_t [Z] [C] \quad 2.10$$

This gives the operational differential equations in tensor form for the 3-wire connection, as illustrated in Figure 2.3.

2.3 Generator Inductance Coefficients

The inductance coefficients forming the [L] and [G] tensors in equations 2.2 and 2.3 are in general dependent on rotor position, and they have to be calculated at each step of the numerical integration of the equations. It is assumed in the development of the model that there is saturation in the direct axis, dependent on the total direct axis magnetisation m.m.f, and no saturation in the quadrature axis due to the large airgap or interpolar spaces. The inductances are therefore defined in terms of their direct and quadrature axis components, with the direct axis alone affected by the saturation.

2.3.1 Self Inductances

- a) The self inductance of the r phase of the generator armature, L_{rr} is

$$L_{rr} = L_D \left(\cos \theta_r + \frac{K}{3} \cos 3\theta_r \right)^2 + L_Q \left(\sin \theta_r - \frac{K}{3} \sin 3\theta_r \right)^2 \quad 2.11$$

and the self inductances of the y and b phases L_{yy} and L_{bb} are obtained by substituting $\theta_y (= \theta_r - \frac{2\pi}{3})$ and $\theta_b (= \theta_r - \frac{4\pi}{3})$ respectively in equation 2.11.

- b) The self inductance of the field winding L_{FF} is angle independent.
- c) The self inductances of the d and q axes damper windings L_{DD} and L_{QQ} respectively are angle independent.

2.3.2 Mutual Inductances

- a) The mutual inductance between the r and y phases of the armature is

$$L_{ry} = M_D \left(\cos \theta_r + \frac{K}{3} \cos 3\theta_r \right) \left(\cos \theta_y + \frac{K}{3} \cos 3\theta_y \right) + M_Q \left(\sin \theta_r - \frac{K}{3} \sin 3\theta_r \right) \left(\sin \theta_y - \frac{K}{3} \sin 3\theta_y \right) \quad 2.12$$

The mutual inductance between the r and b phases L_{rb} is obtained by substituting θ_b for θ_y in equation 2.12 and the mutual inductance between the y and b phases L_{yb} is obtained by substituting θ_y for θ_r and θ_b for θ_y in equation 2.12.

- b) The mutual inductance between the r phase of the armature and the field winding is

$$L_{rF} = M_F (\cos \theta_r + \frac{K}{3} \cos 3\theta_r) \quad 2.13$$

and the mutual inductances between the y and b phases and the field winding L_{yF} and L_{bF} are obtained by substituting θ_y and θ_b respectively for θ_r in equation 2.13.

- c) The mutual inductance between the r phase of the armature and the D-damper winding is

$$L_{rD} = M_{DD} (\cos \theta_r + \frac{K}{3} \cos 3\theta_r) \quad 2.14$$

and the mutual inductances between the y and b phases and the D-damper winding are obtained by substituting θ_y and θ_b respectively for θ_r in equation 2.14.

- d) The mutual inductance between the r phase of the armature and the Q-damper winding is

$$L_{rQ} = -M_{QQ} (\sin \theta_r - \frac{K}{3} \sin 3\theta_r) \quad 2.15$$

and the mutual inductances between the y and b phases and the Q-damper winding are obtained by substituting θ_y and θ_b respectively for θ_r in equation 2.15.

- e) The mutual inductance between the field and the D-damper windings L_{FD} is angle independent.

2.3.3 Inductances Forming the [G] Tensor

The rotational inductance tensor [G] is given by equation 2.4. It is found in practice that the term $\frac{\partial [L]}{\partial [I_d]} \cdot \frac{d(I_d)}{dt}$ is small compared with $\omega \cdot \frac{\partial [L]}{\partial \theta}$ and can be neglected. This results in a considerable saving in computing time as the [L] and [G] tensors are calculated at each time step during the numerical integration of the differential equations. The rotational inductance G_{rr} from L_{rr} is

$$\begin{aligned}
 G_{rr} &= \omega \cdot \frac{\partial L_{rr}}{\partial \theta_r} \\
 &= -\omega [2 L_D (\cos \theta_r + \frac{K}{3} \cos 3\theta_r)(\sin \theta_r + K \sin 3\theta_r) \\
 &\quad - 2 L_Q (\sin \theta_r - \frac{K}{3} \sin 3\theta_r)(\cos \theta_r - K \cos 3\theta_r)] \quad 2.16
 \end{aligned}$$

The rotational inductances G_{yy} and G_{bb} corresponding to L_{yy} and L_{bb} are obtained by substituting θ_y and θ_b respectively for θ_r in equation 2.16.

The rotational inductance G_{ry} from L_{ry} is

$$\begin{aligned}
 G_{ry} &= -\omega [M_D \{(\sin \theta_r + K \sin 3\theta_r)(\cos \theta_y + \frac{K}{3} \cos 3\theta_y) \\
 &\quad + (\cos \theta_r + \frac{K}{3} \cos 3\theta_r)(\sin \theta_y + K \sin 3\theta_y)\} \\
 &\quad - M_Q \{(\cos \theta_r - K \cos 3\theta_r)(\sin \theta_y - \frac{K}{3} \sin 3\theta_y) \\
 &\quad + (\sin \theta_r - \frac{K}{3} \sin 3\theta_r)(\cos \theta_y - K \cos 3\theta_y)\}] \quad 2.17
 \end{aligned}$$

The rotational inductance G_{rb} corresponding to L_{rb} is obtained by

substituting θ_b for θ_r in equation 2.17. The rotational inductance G_{yb} corresponding to L_{yb} is obtained by substituting θ_y for θ_r and θ_b for θ_y in equation 2.17 respectively.

The rotational inductance G_{rF} from L_{rF} is

$$G_{rF} = -\omega [M_F (\sin \theta_r + K \sin 3\theta_r)] \quad 2.18$$

and the rotational inductances G_{yF} and G_{bF} corresponding to L_{yF} and L_{bF} are obtained by substituting θ_y and θ_b respectively for θ_r in equation 2.18.

The rotational inductance G_{rD} from L_{rD} is

$$G_{rD} = -\omega [M_D (\sin \theta_r + K \sin 3\theta_r)] \quad 2.19$$

and the rotational inductances G_{yD} and G_{bD} corresponding to L_{yD} and L_{bD} are obtained by substituting θ_y and θ_b respectively for θ_r in equation 2.19.

The rotational inductance G_{rQ} from L_{rQ} is

$$G_{rQ} = -\omega [M_{QQ} (\cos \theta_r - K \cos 3\theta_r)] \quad 2.20$$

and the rotational inductances G_{yQ} and G_{bQ} corresponding to L_{yQ} and L_{bQ} are obtained by substituting θ_y and θ_b respectively for θ_r in equation 2.20.

2.4 Effect of Magnetic Saturation on [L] and [G] Tensors

As already stated, saturation effects in the direct axis only are considered, and saturation in the direct axis is regarded as due to the resultant m.m.f. along this axis. Since the saturation characteristic of a generator is usually given in terms of its excitation, the effective direct axis current is calculated

with reference to the field current as

$$I_d = i_F + \frac{N_D}{N_F} \cdot i_D + \frac{N_P}{N_F} \cdot (i_r \cos \theta_r + i_y \cos \theta_y + i_b \cos \theta_b) \quad 2.21$$

where $(\frac{N_D}{N_F})$ is the effective D-axis damper/field turns ratio and $(\frac{N_P}{N_F})$ is the effective armature phase/field turns ratio. The effective turns ratios are determined experimentally as discussed in reference 24.

The direct-axis inductances coefficient are

$$L_D = \frac{L_{rr}}{(1 + \frac{K}{3})^2} \quad \left| \quad \theta_r = 0 \right. \quad 2.22 \text{ from equation 2.11}$$

$$M_D = \frac{L_{ry}}{(-\frac{1}{2} + \frac{K}{3})(1 + \frac{K}{3})} \quad \left| \quad \theta_r = 0 \right. \quad 2.23 \text{ from equation 2.12}$$

$$M_F = \frac{L_{rF}}{(1 + \frac{K}{3})} \quad \left| \quad \theta_r = 0 \right. \quad 2.24 \text{ from equation 2.13}$$

$$M_{DD} = \frac{L_{rD}}{(1 + \frac{K}{3})} \quad \left| \quad \theta_r = 0 \right. \quad 2.25 \text{ from equation 2.14}$$

The quadrature axis inductance coefficients are

$$L_Q = \frac{L_{rr}}{(1 + \frac{K}{3})^2} \quad \left| \quad \theta_r = \pi/2 \right. \quad 2.26 \text{ from equation 2.11}$$

$$M_Q = \frac{L_{ry}}{\left(-\frac{1}{2} + \frac{K}{3}\right)\left(1 + \frac{K}{3}\right)} \quad \left| \quad \begin{array}{l} \text{2.27 from equation 2.11} \\ \theta_r = \pi/2 \end{array} \right.$$

$$M_{QQ} = - \frac{L_{rQ}}{\left(1 + \frac{K}{3}\right)} \quad \left| \quad \begin{array}{l} \text{2.28 from equation 2.15} \\ \theta_r = \pi/2 \end{array} \right.$$

where K is the ratio of the 3rd harmonic component to the fundamental component in the space distribution of armature mmf.

A Fourier Analysis of the spatial variation of the unsaturated values of r phase self inductance was used to obtain the numerical value of $\frac{K}{3}$. The variation of inductance expressed as a function of I_d for different level of saturation were obtained from measurements given in Figures 2.5 to 2.9. The direct axis inductance coefficients as a function of I_d are:

$$L_D = 3.90 \times 10^{-4} \cdot C_{rr} \text{ H.} \quad 2.29$$

$$\begin{aligned} \text{where } C_{rr} = & 1.0 + 0.03276 \times 10^{-2} I_d - 0.1793 \times 10^{-3} I_d^2 \\ & + 0.05591 \times 10^{-5} I_d^3 + 0.16575 \times 10^{-7} I_d^4 \\ & - 0.100198 \times 10^{-9} I_d^5 + \dots \end{aligned}$$

$$M_D = 3.76 \times 10^{-4} \cdot C_{ry} \text{ H.} \quad 2.30$$

$$\begin{aligned} \text{where } C_{ry} = & 1.0 - 0.3077 \times 10^{-3} I_d - 0.09366 \times 10^{-3} I_d^2 \\ & - 0.38951 \times 10^{-7} I_d^3 + 0.102251 \times 10^{-7} I_d^4 \\ & - 0.48634 \times 10^{-10} I_d^5 + \dots \end{aligned}$$

$$M_F = 2.07 \times 10^{-3} \cdot C_{rF} H. \quad 2.31$$

$$\begin{aligned} \text{where } C_{rF} = & 1.0 + 0.051726 \times 10^{-1} I_d - 0.44545 \times 10^{-3} I_d^2 \\ & + 0.056198 \times 10^{-4} I_d^3 - 0.26889 \times 10^{-7} I_d^4 \\ & + 0.401556 \times 10^{-10} I_d^5 + \dots \end{aligned}$$

$$L_{FF} = 11.5 \times 10^{-3} \cdot C_{FF} H. \quad 2.32$$

$$\begin{aligned} \text{where } C_{FF} = & 1.0 + 0.043011 \times 10^{-1} I_d - 0.040181 \times 10^{-2} I_d^2 \\ & + 0.045945 \times 10^{-4} I_d^3 - 0.016393 \times 10^{-6} I_d^4 \\ & + 0.01305 \times 10^{-10} I_d^5 \dots \end{aligned}$$

Due to the close proximity of the effective d-axis damper winding to the field winding, it is found in practice that the following approximations can be used.

$$C_{rD} = C_{rF}, \quad C_{DD} = C_{FF}, \quad C_{FD} = C_{FF} \quad 2.33$$

Therefore

$$M_{DD} = 1.41 \times 10^{-4} \cdot C_{rD} = 1.41 \times 10^{-4} \cdot C_{rF} H. \quad 2.34$$

$$L_{DD} = 1.07 \times 10^{-4} \cdot C_{DD} = 1.07 \times 10^{-4} \cdot C_{FF} H. \quad 2.35$$

$$L_{FD} = 1.710 \times 10^{-3} C_{FD} = 1.710 \times 10^{-3} \cdot C_{FF} H. \quad 2.36$$

To include the saturation characteristics in the computer program, polynomial equations which give a good fit to the measured results were obtained. It was found that a 5th order polynomial curve fit was within 2% error of the measured results and hence was regarded as describing the measured saturation characteristic.

The effect of saturation on the $[G]$ tensor is to introduce additional terms of the form $\frac{d(I_d)}{dt} \left(\frac{\partial(L)}{\partial(I_d)} \right)$. It was found by comparison of the predicted voltage transients for application and rejection of load that neglecting these additional terms does not significantly affect the results. The quadrature-axis coefficients of inductances were found to be

$$L_Q = 2.30 \times 10^{-4} \text{ H.} \quad 2.37$$

$$M_Q = 2.12 \times 10^{-4} \text{ H.} \quad 2.38$$

$$M_{QQ} = 2.45 \times 10^{-4} \text{ H.} \quad 2.39$$

$$L_{QQ} = 3.25 \times 10^{-4} \text{ H.} \quad 2.40$$

2.5 Determination of Phase Model Parameters of the 2130 Generator

Some of the parameters of the model can be directly determined from measurements at the terminals of the generator.

These are:

- a) The resistances of the armature phase and field windings.
- b) The self inductances of the armature phase and field windings.
- c) The phase to phase and phase to field mutual inductances.

The parameters that have to be measured by indirect methods such as an a.c. test are:

- a) The effective self inductances of the d- and q-axis damper windings.

- b) The effective mutual inductance between the phase winding and the d-axis damper winding (and the q-axis damper winding).
- c) The effective mutual inductance between the field and the d-axis damper winding.
- d) The effective resistances of the damper windings.

2.5.1 Measurement of Resistances

A Kelvin bridge was used to measure the armature phase resistances and the field winding. The ambient temperature during the measurements was 25°C.

The mean of the three phase resistances was measured as 0.0323Ω and the field resistance as 0.129Ω . Since the effect of 400 Hz currents is to increase the effective phase resistance to approximately twice the d.c. value²⁵, the armature phase resistance was assumed to be 0.0646Ω for calculation purposes.

2.5.2 Measurement of Self-Inductance of the Generator Phase Winding

- a) The angular variation of the self inductance of the armature phases were measured using the bridge circuit described in Appendix A2. For these measurements, no bias current was applied to the field winding, so that a measurement of the secant inductances was obtained. It is necessary in this test for the armature current to be such as to give an inductance value corresponding to the linear region of the B/H curve. If too high a value is used, the measured inductances will include the effects of saturation. The angular variation of the self inductance of phases r, y and b is shown in Figure 2.4.
- b) The incremental inductance of the r phase winding (L'_{rr}) when situated along and in the d axis was measured for different bias field

currents from 0 to 120A by reversing the armature phase current using the bridge circuit described in Appendix A2. The results obtained are shown in Figure 2.5. The secant value of the self inductance corresponding to a given field current was calculated from

$$L_{rr} = \frac{1}{I_f} \int_0^{I_f} L'_{rr} d I_f \quad 2.41$$

as discussed in Appendix A2. The variations in L_{rr} the secant inductance for the same range of the field current are also shown in Figure 2.5.

2.5.3 Measurement of the Self-Inductance of the Field Winding

The secant self-inductance of the field winding were measured for different values of field current from 0 to 120 A. to give the results shown in Figure 2.6. There was found to be no discernible effect due to variation in permeance caused by the armature slots as the angular position had no effect on the measured value of the inductance.

2.5.4 Measurement of Phase-to-Phase Mutual Inductance

- a) The angular variation of the r-phase to y-phase secant mutual inductance was measured using the bridge circuit of Appendix A4. The results obtained are shown in Figure 2.7.
- b) The incremental mutual inductance between the r and y phases was measured with the phase r along the d axis, for different bias field currents from 0 to 120 A. The results are as shown in Figure 2.8, together with the secant values of the inductance calculated from

$$L_{ry} = \frac{1}{I_f} \int_0^{I_f} L'_{ry} dI_f \quad 2.42$$

2.5.5 Measurement of Armature Phase to Field Mutual Inductance

- a) The angular variation of the field to armature y-phase mutual inductance was measured using the method described in Appendix A3 for different electrical angles θ_r . The procedure was repeated for y and b phases and the results obtained are shown in Figure 2.9.
- b) With the r-phase of the armature lying along the d-axis, the r-phase armature to the field mutual inductance was measured for reversal of the field current of up to 120 A. The results obtained are shown in Figure 2.10.

2.5.6 A.C. Measurement of Generator Parameters

Prescott and El-Kharashi have shown²⁶ that the effective damper parameters of a generator may be obtained indirectly by measuring the transient and subtransient inductances, L'_d and L''_d in the d-axis and L'_q and L''_q in the q-axis, using a ballistic or flux-meter method. This method does not however give the damper circuit time constants or the effective damper circuit resistances.

It is possible using the a.c. tests described by Snider and Smith²⁴ to obtain the full parameters for use in the phase model analysis. This method forms the basis of tests performed on the 2130 generator*. Figure 2.11 shows two coupled coils with resistances of R_1 , R_2 , self-inductances of L_{11} , L_{22} and a mutual inductance of M_{12} . If coil 2 is short-circuited and the effective resistance and inductance of the circuit are measured at the terminals of coil 1, the effective resistance R_e and inductance L_e of coil 2 are respectively:

$$R_e = \frac{\omega^2 M_{12}^2 R_2}{R_2^2 + \omega^2 L_{22}^2} \quad 2.43$$

* Details of the 2130 generator are given in Appendix A1.

and

$$L_e = \frac{-\omega^2 M_{12}^2 L_{22}}{R_2^2 + \omega^2 L_{22}^2} \quad 2.44$$

$$\text{giving } \left(\frac{L_{22}}{R_2}\right) = -\frac{L_e}{R_e} \quad 2.45$$

$$\text{and } M_{12} = \sqrt{\frac{R_e (R_2^2 + \omega^2 L_{22}^2)}{\omega^2 R_2}} \quad 2.46$$

If R_{1e} and L_{1e} are respectively the resistance and inductance measured at the input to coil 1 (with coil 2 short circuited) as shown in Figure 2.12

$$R_e = R_{1e} - R_1 \quad 2.47$$

$$L_e = L_{1e} - L_{11} \quad 2.48$$

a) Measurement of Armature Phase to D-Axis Damper Winding Parameters

An armature phase of the generator was aligned with the d-axis and excited from a variable-frequency voltage source as shown in Figure 2.13. The input voltage, current and power were measured for frequencies from 50 Hz to 600 Hz to determine the variation in the damper parameters with frequency. In terms of the armature phase winding and the d-axis damper circuit, equations 2.45 and 2.46 become respectively

$$\frac{L_{DD}}{R_{DD}} = -\frac{L_e}{R_e} \quad 2.49$$

$$M_{DD} = \sqrt{\frac{R_e (R_{DD}^2 + \omega^2 L_{DD}^2)}{\omega^2 R_{dd}}} \quad 2.50$$

which gives

$$\frac{M_{DD}^2}{R_{DD}} = \frac{R_e}{\omega^2} + R_e \left(\frac{L_{DD}}{R_{DD}} \right)^2 \quad 2.51$$

and

$$K_{aD} = \frac{M_{DD}}{\sqrt{L_a L_{DD}}} = \frac{1}{\sqrt{L_a}} \sqrt{\left(\frac{M_{DD}^2}{R_{DD}} \right) \cdot \left(\frac{R_{DD}}{L_{DD}} \right)} \quad 2.52$$

where L_a is the self-inductance of the armature phase in the d-axis. The variation of the d-axis damper time constant $\left(\frac{L_{DD}}{R_{DD}} \right)$ as a function of frequency is shown in Figure 2.14 together with the variations in $\left(\frac{M_{DD}^2}{R_{DD}} \right)$ and the coupling coefficient K_{aD} between the armature phase and the d-damper circuit. It is found from measurements of Figure 2.14 that $\left(\frac{M_{DD}^2}{R_{DD}} \right)$ decreases from 8×10^{-7} to 5.5×10^{-7} as the frequency rises from 50 Hz to 600 Hz. The results of Figure 2.14 also make clear the frequency dependence of the damper winding time constant $\left(\frac{L_{DD}}{R_{DD}} \right)$. The coefficient of coupling between the windings K_{aD} however remains constant. It is evident from the results that if the inductances are considered to be constant over this frequency range, the change in the damper winding time constant $\left(\frac{L_{DD}}{R_{DD}} \right)$ is due to the change in R_{DD} with frequency.

b) Measurement of Armature Phase to Q-Axis Damper Winding Parameters

An armature phase of the generator was aligned with the q-axis and the test repeated as for the d-axis damper windings. In terms of the armature phase winding and the q-axis damper circuit, equations 2.45 and 2.46 become.

$$\frac{L_{QQ}}{R_{QQ}} = - \frac{L_e}{R_e} \quad 2.53$$

$$\text{and } M_{QQ} = \frac{\sqrt{R_e (R_{QQ}^2 + \omega^2 L_{QQ}^2)}}{\omega^2 R_{QQ}} \quad 2.54$$

giving

$$\frac{M_{QQ}^2}{R_{QQ}} = \frac{R_e}{\omega^2} + R_e \left(\frac{L_{QQ}}{R_{QQ}} \right)^2 \quad 2.55$$

and

$$K_{aQ} = \frac{M_{QQ}}{\sqrt{L_a L_{QQ}}} = \frac{1}{\sqrt{L_a}} \sqrt{\left(\frac{M_{QQ}}{R_{QQ}} \right) \cdot \left(\frac{R_{QQ}}{L_{QQ}} \right)} \quad 2.56$$

where L_a is the self-inductance of the armature phase in the q-axis. It was not possible to measure the q-axis damper parameters accurately at frequencies less than 300 Hz due to the small excitation voltage (less than 1 V) required to circulate 10 A in the phase winding. The variation of $\left(\frac{M_{QQ}}{R_{QQ}} \right)$, K_{aQ} and $\left(\frac{L_{QQ}}{R_{QQ}} \right)$ as a function of frequency are shown in Figure 2.15. It is seen from the measurements that both $\left(\frac{M_{QQ}}{R_{QQ}} \right)$ and $\left(\frac{L_{QQ}}{R_{QQ}} \right)$ decrease as the frequency is increased from 300 Hz to 600 Hz, while the coefficient of coupling between the armature phase and the q-axis damper winding remains constant. If it is assumed that the inductance of the damper winding does not change with frequency, the results confirm the dependence of the damper winding resistance on frequency.

It is clear from consideration of Figures 2.14 and 2.15 that the coupling coefficient between the armature phase and the equivalent q-axis damper winding is *greater* than that between the armature and the equivalent d-axis damper winding. The q-axis damper winding time constant (at 400 Hz) is nearly three times that of d-axis damper winding time constant. The reasons for this are discussed in reference 27.

c) Measurement of Field Winding to D-Axis Damper Winding Parameters

The parameters of the field to d-axis damper winding were measured using the same basic arrangement as used for the armature phase to d-axis damper winding. However, for this test instead of varying the frequency, the field current was varied, to obtain the dependence of the results of a.c. measurement on the magnitude of the exciting current, as shown in Figure 2.16.

2.6 Design Parameters of 2130 3-Stage Generator Unit

The design parameters of 2130 generator unit, supplied by the manufacturers, are given in Appendix A1. Appendix A1 also includes photographs showing the construction of the 2130 generator unit and the unit when connected to the constant-speed drive for the transient load studies discussed in Chapter 5. The *dqo* design parameters can be used to calculate the phase model parameters as discussed in Chapter 9.

2.7 Predictions of Saturated Steady-State Inductances of 2130 Main Generator Using Finite-Element Field Solutions

As a part of collaborative programmes on the modelling of aircraft generating systems, G.E.C. (Stafford) have developed a finite element numerical method of predicting the saturated steady-state inductances of the main generator. The basic approach to the prediction of the inductances consists of first evaluating the flux distribution in the machine, taking into account the geometry and the magnetic saturation of the iron structure forming the rotor and stator of the generator. The inductances are then obtained from the flux linking the appropriate windings²⁸⁻³⁰. Comparison between the measured inductances L_{rr} , L_{FF} , L_{rF} and those predicted by the finite method are given in Figures 2.5, 2.6 and 2.10 respectively. The results show that the finite element predictions are close to the measured results, with the small differences being attributable to uncertainties over the airgap used for predictions and the actual airgap of the machine. The airgap used for predictions was 0.030 inches while the measured airgap was 0.035 inches.

2.8 Conclusion

The phase model of the synchronous generator has become widely used in recent years²⁰⁻²³ with the availability of fast digital computing facilities. Methods of measuring the phase model parameters are discussed in this chapter, with reference to the 2130 main generator. The measured parameters are used in Chapter 5 to predict the load switching transients experienced by the actual machine.

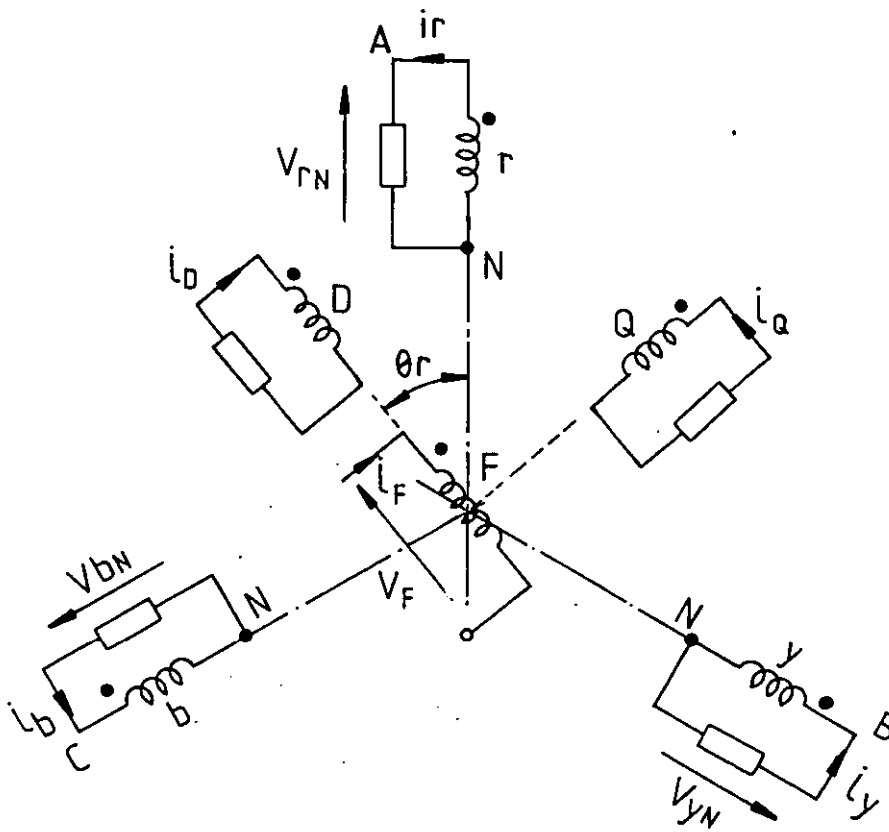


Figure 2.1 3-PHASE GENERATOR ON LOAD (4-WIRE CONNECTION)

0		$(R_r + pL_r)$	pL_{ry}	pL_{rb}	pL_{rF}	pL_{rD}	pL_{rQ}	i_r
0			$(R_y + pL_y)$	pL_{yb}	pL_{yF}	pL_{yD}	pL_{yQ}	i_y
0				$(R_b + pL_b)$	pL_{bF}	pL_{bD}	pL_{bQ}	i_b
V_F	=				$(R_{FF} + pL_{FF})$	pL_{FD}	0	i_F
0						$(R_{DD} + pL_{DD})$	0	i_D
0							$(R_{QQ} + pL_{QQ})$	i_Q

Symmetrical
about leading diagonal

where

$$\begin{aligned}
 L_r &= L_{rr} + L_{rL}, & R_r &= R_{rr} + R_{rL} \\
 L_y &= L_{yy} + L_{yL}, & R_y &= R_{yy} + R_{yL} \\
 L_b &= L_{bb} + L_{bL}, & R_b &= R_{bb} + R_{bL}
 \end{aligned}$$

FIGURE 2.2 Tensor Equations for 4-Wire Load Connection

0	$R_r + R_b + p(L_r + L_b - 2L_{rb})$	$R_b + pL$ $-p(L_{rb} + L_{yb} + L_{ry})$	$p(L_{rF} - L_{bF})$	$p(L_{rD} - L_{bD})$	$p(L_{rQ} - L_{bQ})$	i_r
0		$R_y + R_b$ $+p(L_y + L_b - 2L_{yb})$	$p(L_{yF} - L_{bF})$	$p(L_{yD} - L_{bD})$	$p(L_{yQ} - L_{bQ})$	i_y
V_F	Symmetrical about leading diagonal		$R_{FF} + pL_{FF}$	pL_{FD}	0	i_F
0				$R_{DD} + pL_{DD}$	0	i_D
0					$R_{QQ} + pL_{QQ}$	i_Q
0						

FIGURE 2.3 Tensor Equations for 3-Wire Load Connection

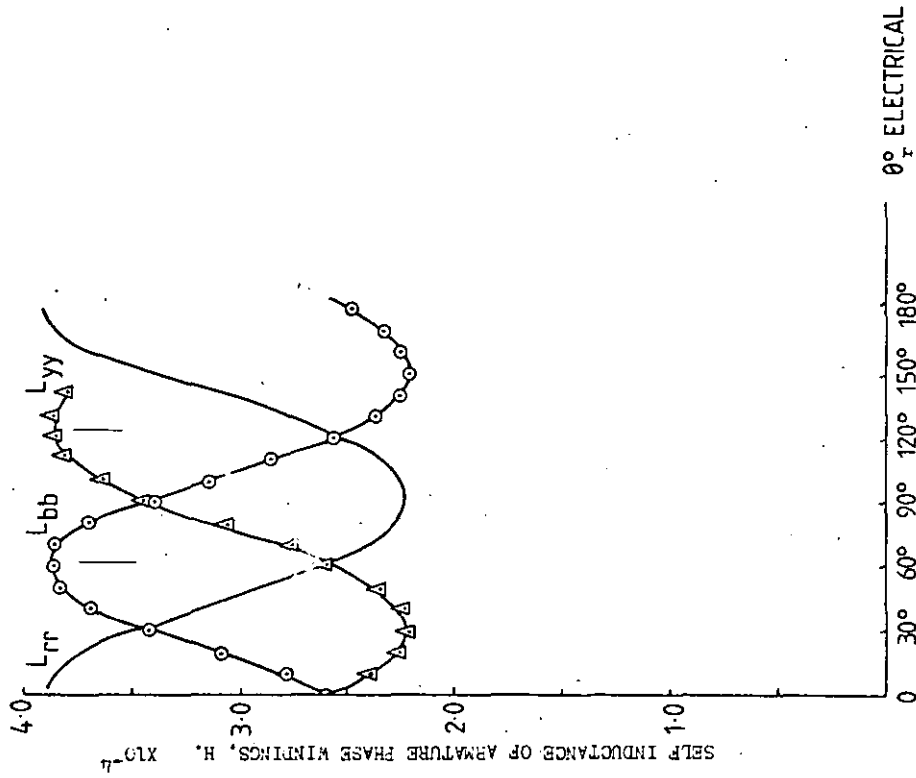


Figure 2.4 ANGULAR VARIATION OF ARMATURE PHASE SELF INDUCTANCE

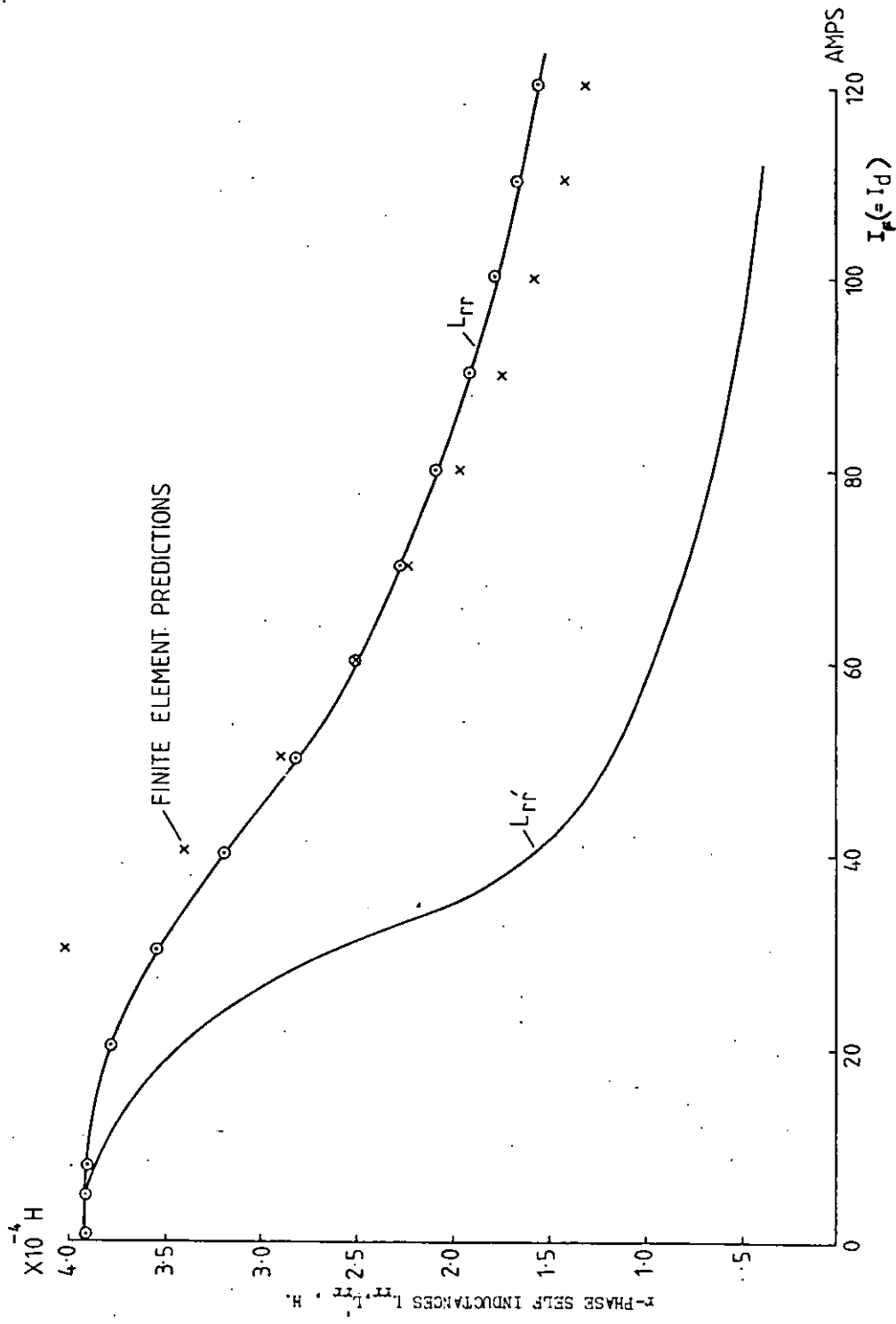


Figure 2.5 EFFECT OF SATURATION ON L_{rr} | $\theta_r = 0^\circ$

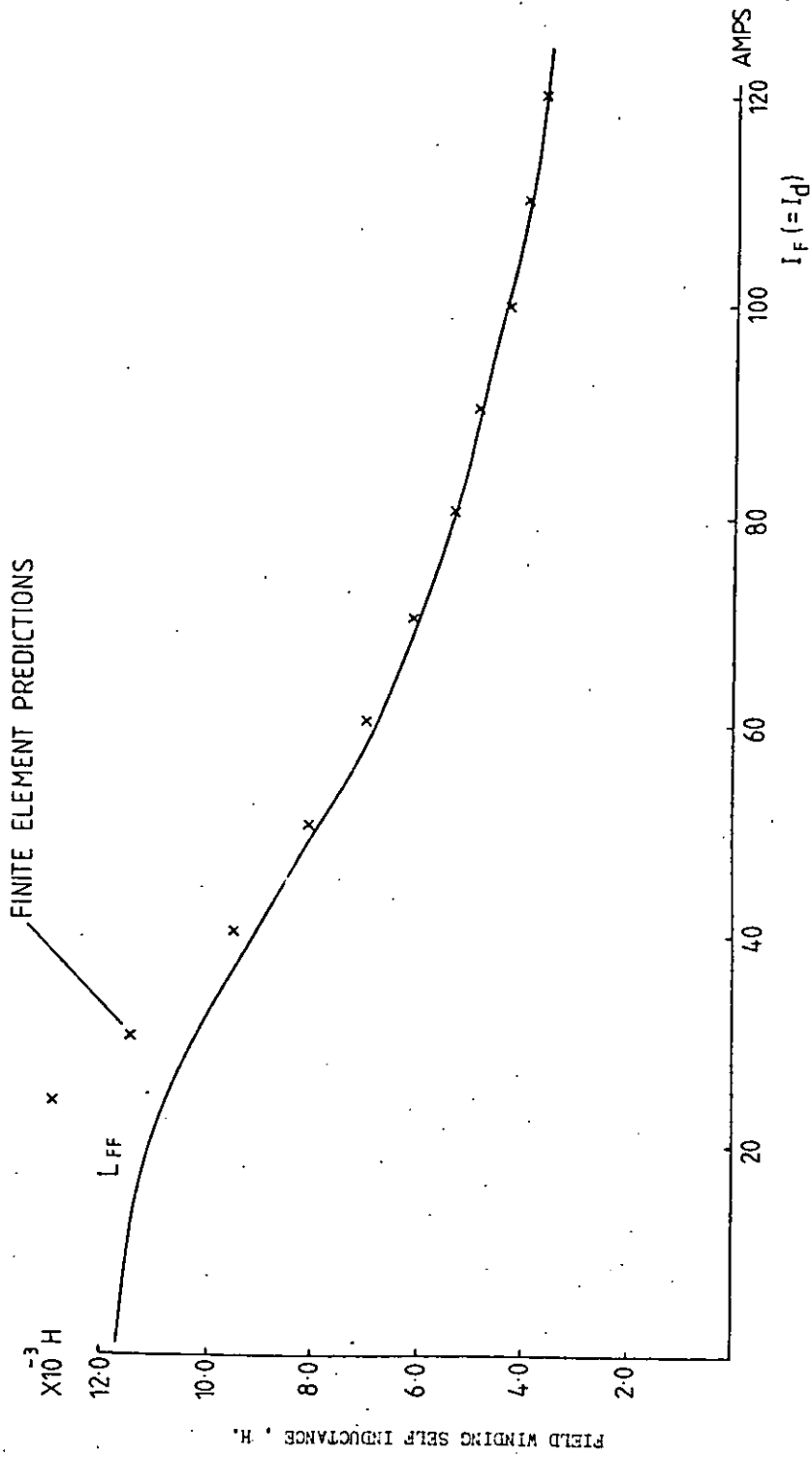


Figure 2.6 EFFECT OF SATURATION ON FIELD WINDING SELF INDUCTANCE L_{FF}

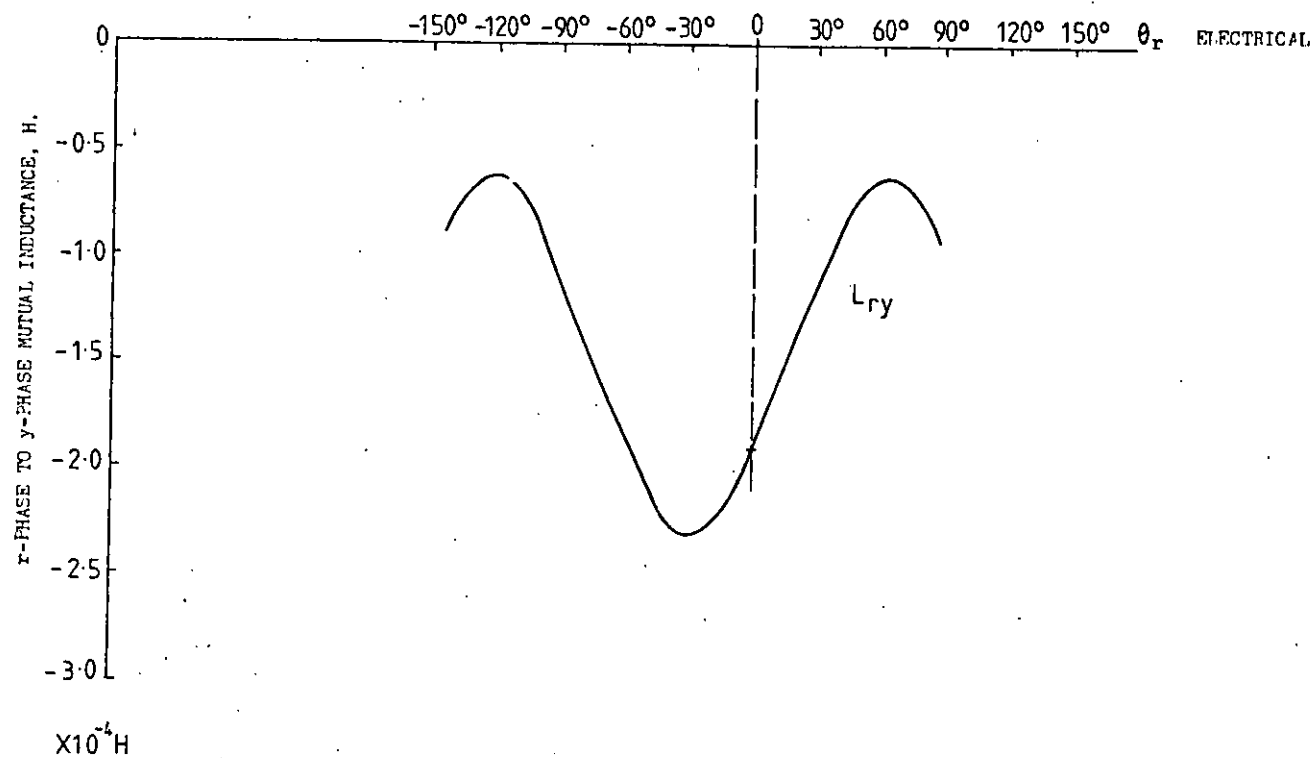


Figure 2.7 ANGULAR VARIATION OF r-PHASE TO y-PHASE MUTUAL INDUCTANCE

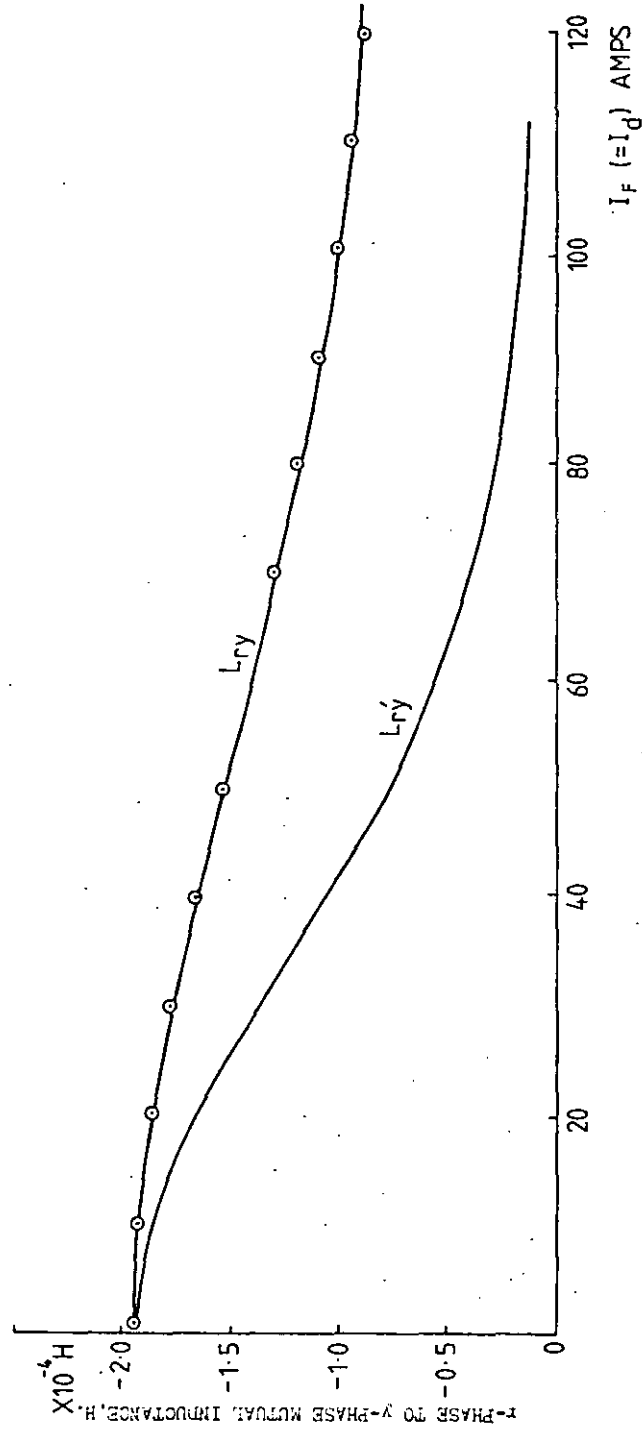


Figure 2.8 EFFECT OF D-AXIS SATURATION ON L_{ry} $\theta_r = 0^\circ$

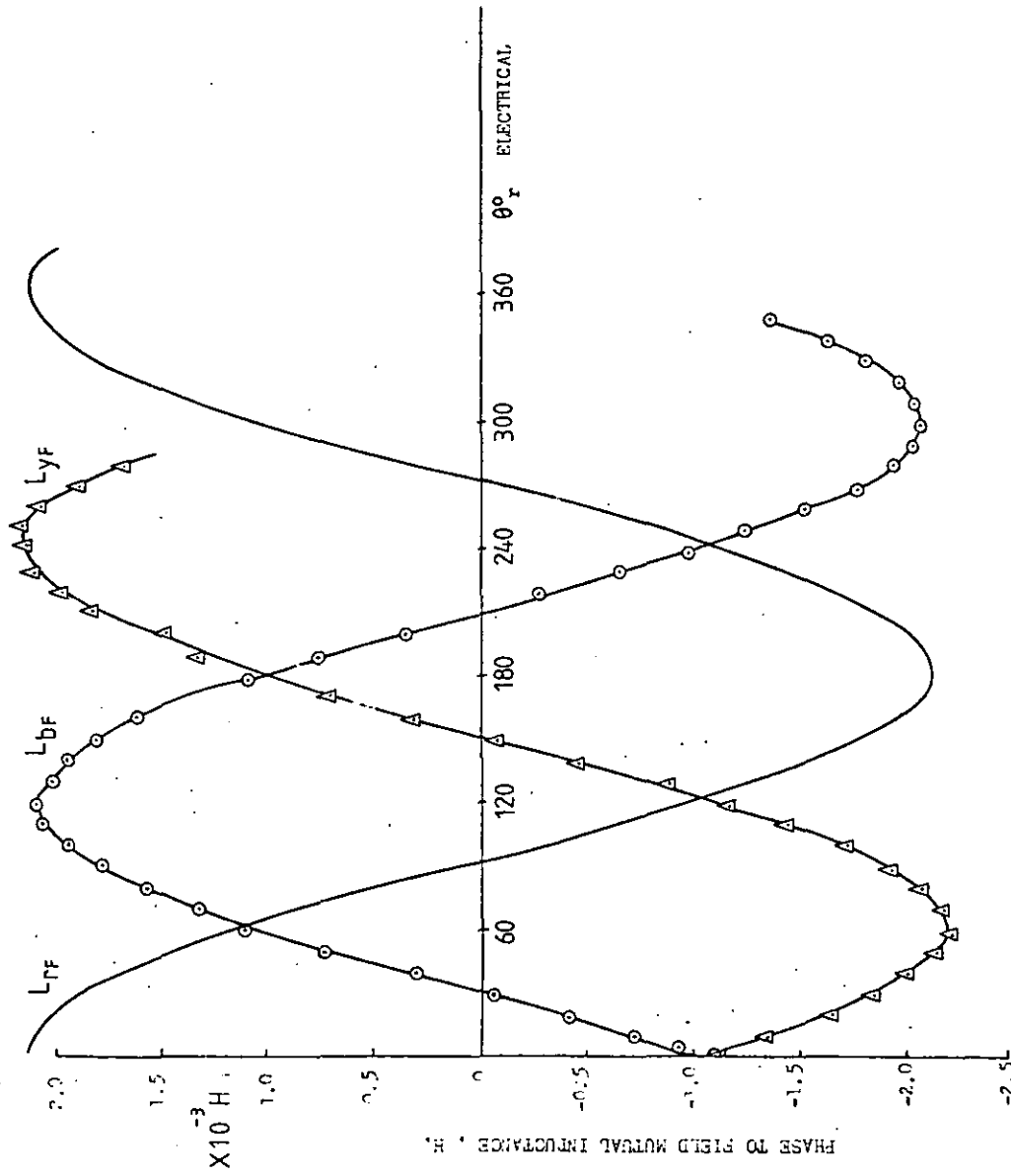


Figure 2.9 THE ANGULAR VARIATION OF PHASE TO FIELD MUTUAL INDUCTANCE

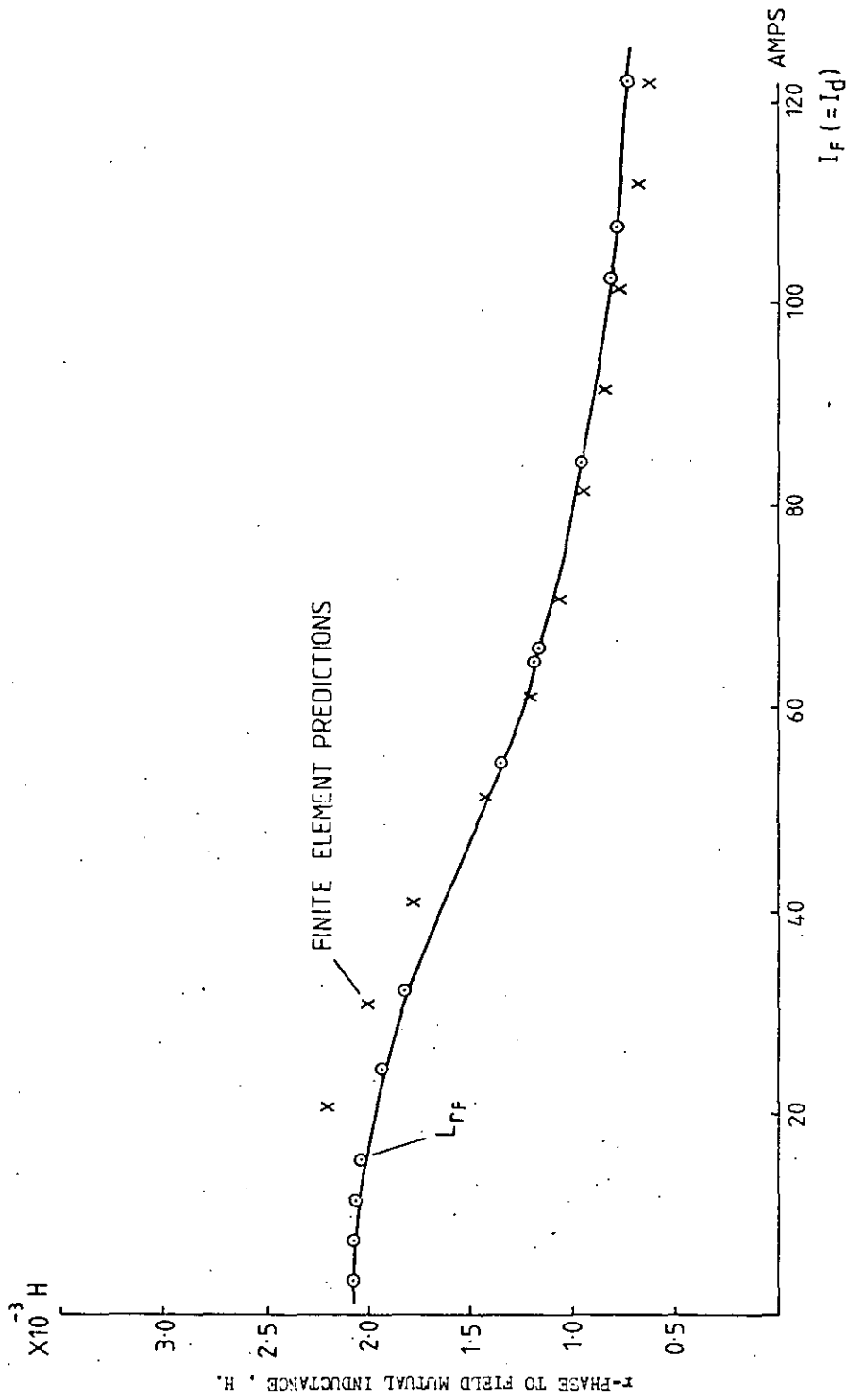


Figure 2.10 EFFECT OF SATURATION ON $L_{rF}/\theta_r = 0^\circ$

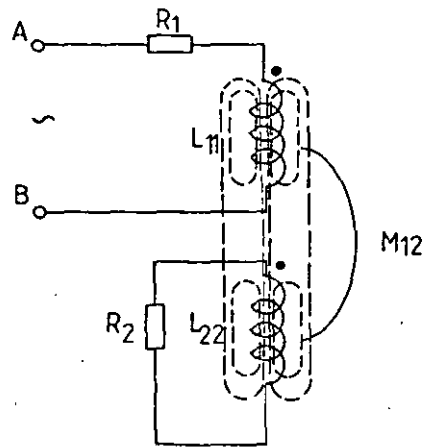


Figure 2.11 TWO MAGNETICALLY COUPLED CIRCUITS

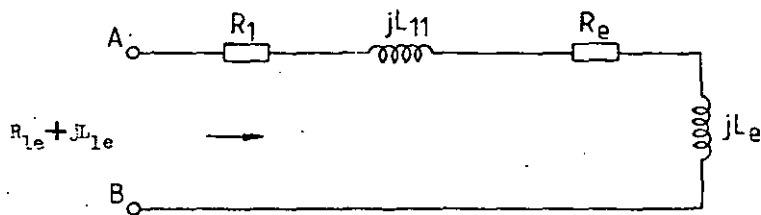


Figure 2.12 EQUIVALENT SERIES CIRCUIT OF FIGURE 2.11

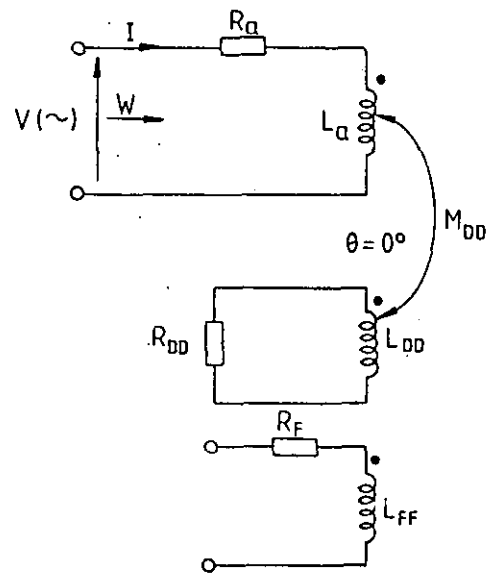


Figure 2.13 CIRCUIT FOR A.C. MEASUREMENT OF D-AXIS
DAMPER PARAMETERS

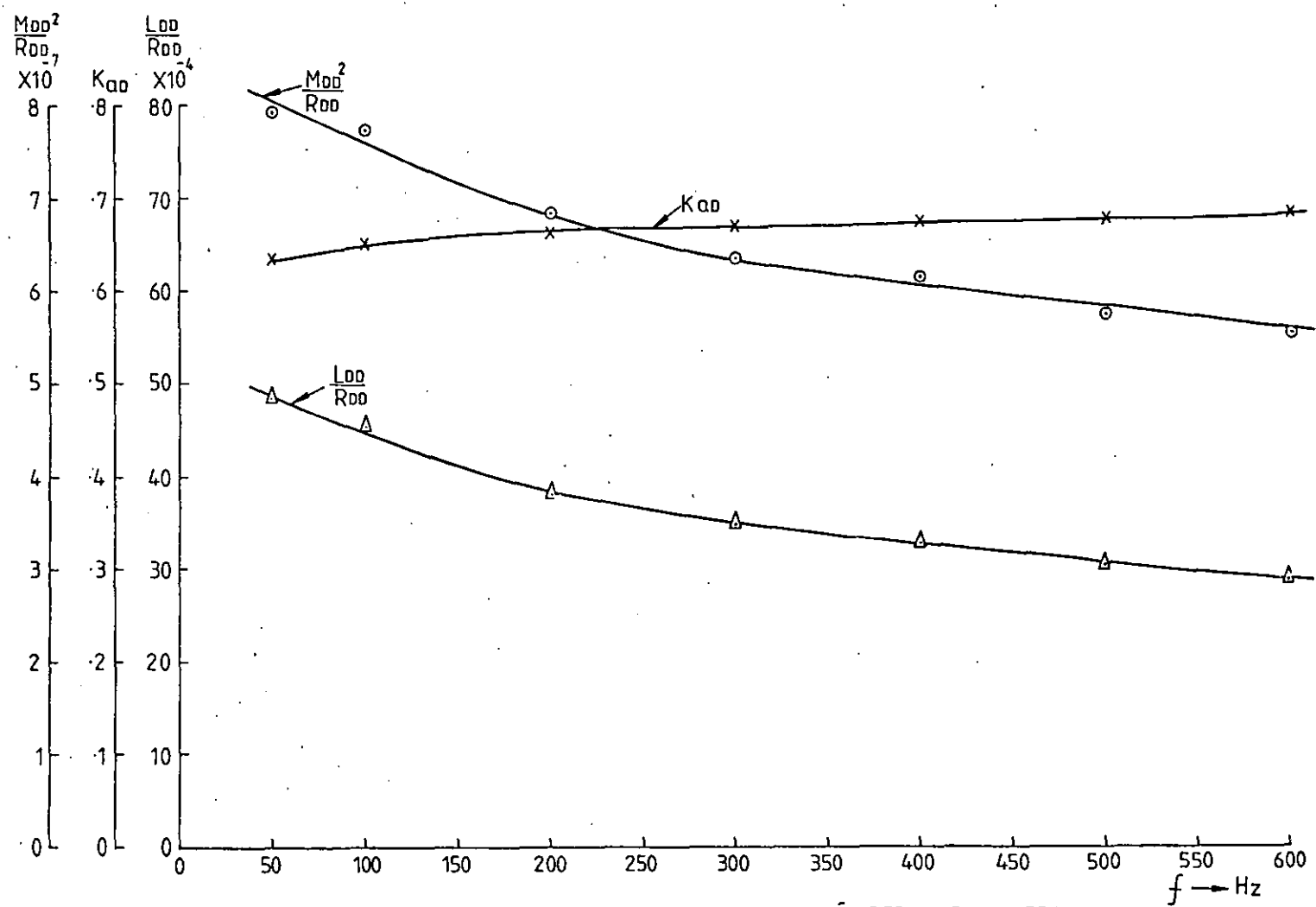


Figure 2.14 MEASUREMENT OF ARMATURE PHASE TO D-AXIS DAMPER PARAMETERS

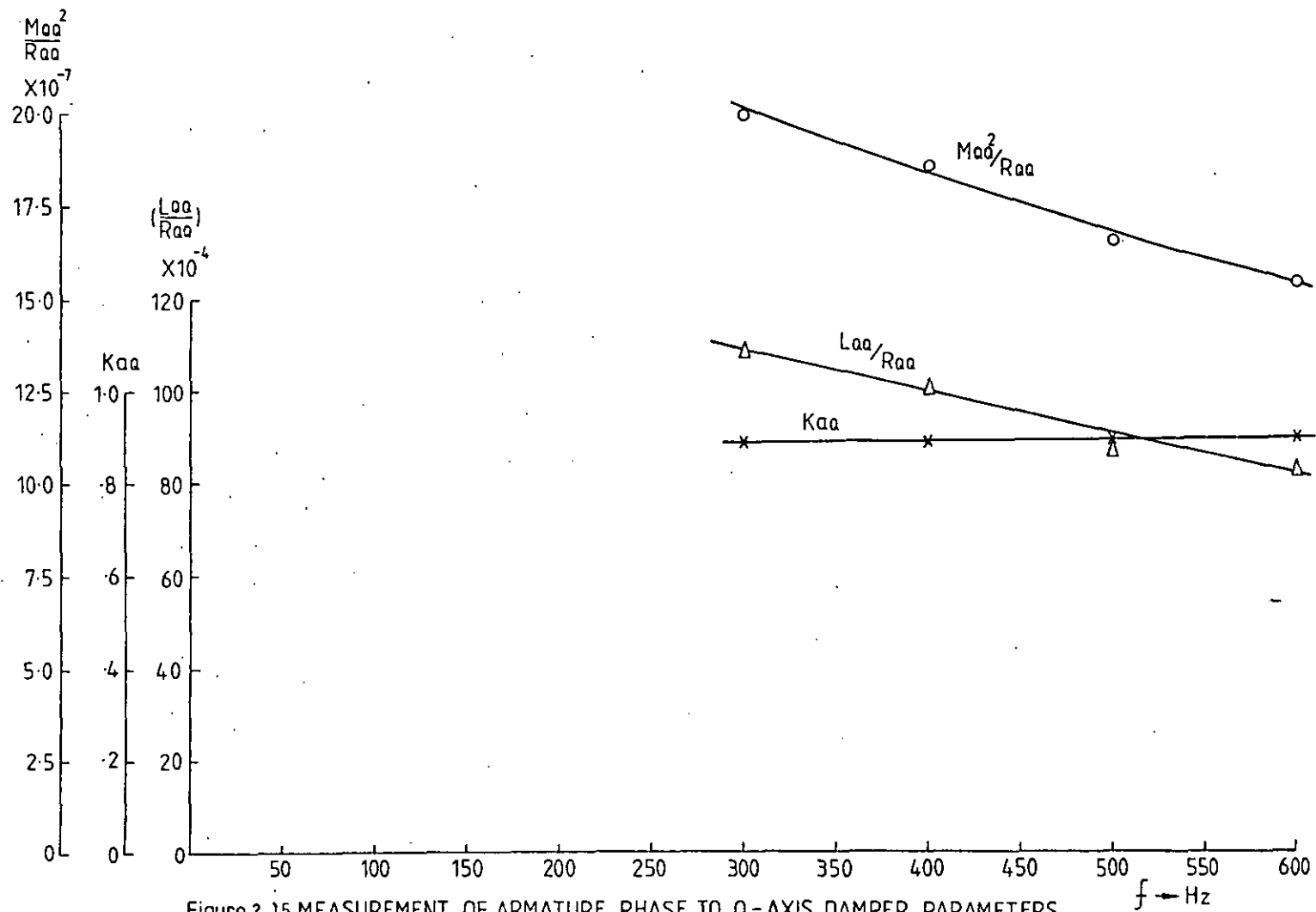


Figure 2.15 MEASUREMENT OF ARMATURE PHASE TO Q-AXIS DAMPER PARAMETERS

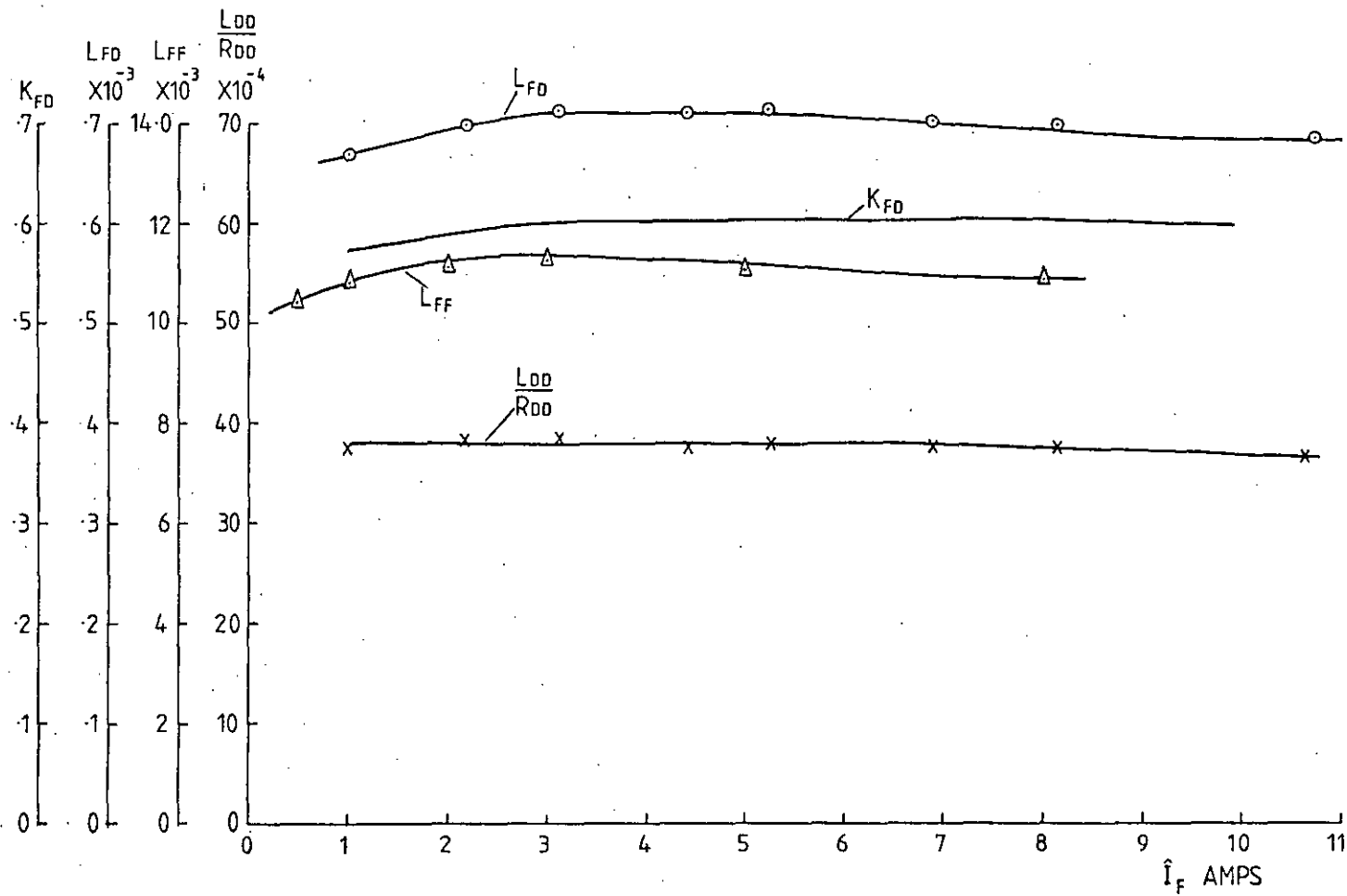


Figure 2.16 MEASUREMENT OF FIELD TO D-AXIS DAMPER PARAMETERS AT 50 Hz

CHAPTER 3

MODELLING OF A BRUSHLESS EXCITATION SYSTEM ON A DIGITAL COMPUTER

The term brushless excitation is applied to a synchronous machine excitation system in which the rectifier diodes rotating on the shaft replace the commutator of the classical d.c. excitation system. Since this system dispenses with brushes or rubbing contacts of any kind and results in practically maintenance free operation, it is universally adopted on the generator units on modern aircraft. The brushless excitation system has come into being since the sixties³¹⁻³⁴, with the development of simple, robust, efficient and highly reliable semiconductor rectifiers (diodes or thyristors). Since the semiconductor rectifier is the heart of the brushless excitation system, it is very important to be able to predict the diode current and reverse voltages, both during normal loading and under rectifier or generator fault conditions. The faults which have the most detrimental effects are a short circuit at the main generator terminals and asynchronous running off the infinite bus, which could be due to a fault in the rectifier system. When the generator is running asynchronously³⁴⁻³⁷ at slip frequency, a voltage is induced in the field winding and although the corresponding current can flow through the bridge diodes without hindrance during the positive half wave, the negative half wave is blocked and the induced voltage appears at the rectifier terminals.

During a short circuit at the terminals of the main generator the field current has superimposed on it a d.c. component, which decays with the transient time constant T'_d , and the generator frequency component which decays with the armature time constant T_a . For normal aircraft generators, $T'_d > T_a$, and the field current remains positive throughout the transient period. It is important

to consider the rectifier current during short circuit, to ensure proper selection of the rectifier current rating. The other feature of the rectifier duty is the voltage peaks which are superposed on the actual blocking voltage, and which occur at the end of each commutation period due to a sudden collapse of the current resulting from the decay of the charges in the silicon junction. The magnitude of the voltage peaks depend on the load, the characteristics of the rectifier, and the inductance of the circuit and they are effectively damped out by the use of capacitors³⁴ in any practical system. The model of the brushless excitation system described here is based on considering the rectifier as an ideal switch (discussed in Section 3.1). The capacitors which are normally connected across the rectifier diodes are neglected in the model so as to minimise the number of state variables, and hence reduce the computing time which would otherwise become excessive. The model of the brushless excitation system developed, using tensor methods, is shown to be able to predict all the characteristics of the system. This method of modelling the system on the digital computer has many advantages over the analytical methods described in recent papers by Franklin³⁸ where he considers the analysis of a generator with a bridge rectifier output. This type of analytical method results in very cumbersome expressions for the operation of the synchronous generator, since the rectifier load will have three separate modes of operation. Section 3.1 describes the tensor method for the analysis of electrical circuits which is extended to model the complete brushless excitation system in Sections 3.2 to 3.5.

3.1 Tensor Method of Analysis of Electrical Circuits

Kron's method of analysing electrical networks using a Matrix-Tensor approach are well known¹⁶⁻¹⁹. It is known³⁹ that the use of this approach reduces the time required for solving complicated

networks, as a digital computer can be easily programmed to assemble and to solve automatically the network equations. This feature is of particular importance when the network connections are changing (varying topology), for example when it includes thyristors or diodes. Under these situations, the classical method of solving the network by obtaining differential equations for each different state or topology may lead to a large number of differential equations⁴⁰⁻⁴¹ which would be cumbersome to handle with any errors in programming difficult to isolate. Kron's method provides a logical approach for solving such problems on a digital computer, and as it handles logically any changes in topology and produces the relevant differential equations at each stage of the solution, also readily handle abnormal load or fault conditions. The differential equations at each stage of the solution can be solved by the numerical integration techniques given in Appendix (A6).

The following steps are required for setting up the equations of an electrical network.

1. Establish the primitive mesh network and the parameters (i.e. I , Z , V), belonging to each branch.
 - a) If a branch consists of an impressed voltage only, it is represented as a branch with zero impedance.
 - b) If a branch consists of an impedance only, it is represented as a branch with zero voltage
 - c) The impedance tensor $[Z_p]$ of the primitive network is found. This contains a number of both rows and columns equal to the number of branches of the network, with the main diagonal elements being self-impedance terms and the off diagonal elements mutual impedance terms.
 - d) The impressed voltage tensor has as many elements as there are branches in the network.
 - e) The currents I_p flowing in the branches are the variables with the $[I_p]$ tensor having as many elements as there are branches in the network.

2. Form a transformation tensor $[C]$ relating the primitive network to the actual network.

a) Assume I_n independent currents for the actual network.
This number will be given by $(B+1) - N$,
where B is the number of branches and N the number of nodes of the network.

b) The transformation tensor $[C]$ is obtained by writing the branch currents I_p in terms of I_n

$$[I_p] = [C][I_n] \quad 3.1$$

3. The voltage tensor for the actual network is

$$[V_n] = [C]_t \cdot [V_p] \quad 3.2$$

where $[C]_t$ is the transpose of $[C]$.

4. The impedance tensor for the actual network is

$$[Z_n] = [C]_t \cdot [Z_p] \cdot [C] \quad 3.3$$

5. The voltage equation of the actual network is

$$[V_n] = [Z_n] \cdot [I_n] \quad 3.4$$

This gives $[I_n] = [Z_n]^{-1} \cdot [V_n]$ which is solved to obtain $[I_n]$
The branch current $[I_p]$ can be obtained by using equation 3.1.

The differential equations describing the transients in a linear electrical network are of the form

$$[V_n] = [L_n][pI_n] + [R_n][I_n] + [pL_n][I_n] \quad 3.5$$

A solution for the independent currents I_n as a function of time is obtained by denoting $[pI_n]$ by $[G_n]$ and arranging the equation 3.5 in the form

$$[pI_n] = [L_n]^{-1} \{ [V_n] - \{ [R_n] + [G_n] \} [I_n] \} \quad 3.6$$

Equation 3.6 is suitable for solution by a numerical integration method. The value of I_n is obtained at a succession of time steps $t, t + H, t + 2H$ etc. (where H is the time step length), with the corresponding branch currents being calculated using equation 3.1.

In electrical networks of changing topology, it is necessary to obtain the transformation tensor $[C]$ at each step in time. The steps describing the setting up of the $[Z_p], [I_p], [V_p]$ tensors are as above, except that instead of obtaining $[C]$ directly as described above, a transformation tensor $[C_1]$ is obtained relating the primitive network currents $[I_p]$ to $[I_n]$ where $[I_n]$ are the independent currents of the actual network when all the thyristors and or diodes are conducting. Depending on the state of the system (voltage across the diodes/thyristors, current through the diodes/thyristors, the presence or absence of thyristors trigger pulses), a transformation tensor $[C_2]$ is defined relating the independent currents $[I_n]$ to the actual currents that are permitted to flow in the network. If we denote the permissible currents by $[I_m]$

$$[I_n] = [C_2] \cdot [I_m] \quad 3.7$$

Therefore

$$[I_p] = [C_1] \cdot [I_n] = [C_1] \cdot [C_2] \cdot [I_m] = [C] \cdot [I_m] \quad 3.8$$

$$\text{where } [C] = [C_1] \cdot [C_2] \quad 3.9$$

$$[Z_m] = [C]_t \cdot [Z_p] \cdot [C] \quad 3.10$$

or

$$[Z_m] = [C_2]_t \cdot [Z_n] \cdot [C_2] \quad 3.11$$

$$[V_m] = [C]_t \cdot [V_p] \quad 3.12$$

or

$$[V_m] = [C_2]_t \cdot [V_n] \quad 3.13$$

and

$$[pI_m] = [L_m]^{-1} \{ [V_m] - \{ [R_m] + [G_m] \} \cdot [I_m] \} \quad 3.14$$

Equation 3.14 is solved by a numerical integration method to obtain $[I_m] \cdot [I_n]$ and hence $[I_p]$ are obtained using equations 3.7 and 3.8 respectively.

Instead of starting with branches forming a primitive network, it is possible to start with $[V_n]$, $[Z_n]$, $[I_n]$ as describing the primitive network for an electrical network with diodes and/or thyristors as branches. The following example illustrates the establishment of the equations of a network. Although a simple circuit is used, the approach is however of universal application. The advantages become apparent for medium and large networks, for example an exciter-rectifier-generator system.

If the network of Figure 3.1(a) is considered, the primitive mesh network is found by inspection as given in Figure 3.1(b). The primitive voltage, impedance and current tensors are:

$$[V_p] = \begin{bmatrix} V_1 \\ V_2 \\ -V_3 \\ 0 \end{bmatrix}, \quad 3.15(a)$$

$$[Z_p] = \begin{bmatrix} 0 & 0 & 0 & 0 \\ 0 & Z_2 & Z_{23} & 0 \\ 0 & Z_{32} & Z_3 & 0 \\ 0 & 0 & 0 & Z_4 \end{bmatrix} \quad 3.15(b)$$

$$[I_p] = \begin{bmatrix} I_1 \\ I_2 \\ I_3 \\ I_4 \end{bmatrix} \quad 3.15(c)$$

If the independent currents of the network are chosen as I_{n1} , I_{n2} , I_{n3} as shown in Figure 3.1(c), the transformation tensor $[C]$ is obtained, using equation 3.1, as

$$[C] = \begin{bmatrix} 1 & 1 & 1 \\ 1 & 0 & 0 \\ 0 & 1 & 0 \\ 0 & 0 & 1 \end{bmatrix} \quad 3.16$$

The voltage, current and impedance tensors are

$$[V_n] = [C]_t [V_p] = \begin{bmatrix} V_1 + V_2 \\ V_1 - V_3 \\ V_1 \end{bmatrix} \quad 3.17$$

$$[Z_n] = [C]_t [Z_p] [C] = \begin{bmatrix} Z_2 & Z_{23} & 0 \\ Z_{32} & Z_3 & 0 \\ 0 & 0 & Z_4 \end{bmatrix} \quad 3.18$$

and the independent currents I_n are found by solving equation 3.4.

The branch currents I_p are obtained by using equation 3.1. If the network is now considered with a switch (S) in branch 2 as shown in Figure 3.2(a), then, with S closed, the equations above still apply and $[C_1]$ is given by

$$[C_1] = \begin{bmatrix} 1 & 1 & 1 \\ 1 & 0 & 0 \\ 0 & 1 & 0 \\ 0 & 0 & 1 \end{bmatrix} \quad 3.19$$

With S open, the transformation matrix $[C_2]$ relating the currents I_n to the new independent currents I_m is

$$[I_n] = [C_2][I_m] \quad 3.20(a)$$

where $[C_2] = \begin{bmatrix} 0 & 0 \\ 1 & 0 \\ 0 & 1 \end{bmatrix} \quad 3.20(b)$

The voltage and impedance tensors for the new network given in Figure 3.2(a) are

$$[V_m] = [C_2]_t \cdot [V_n] = \begin{bmatrix} V_1 - V_3 \\ V_1 \end{bmatrix} \quad 3.21$$

$$[Z_m] = [C_2]_t \cdot [Z_n] \cdot [C_2] = \begin{bmatrix} Z_3 & 0 \\ 0 & Z_4 \end{bmatrix} \quad 3.22$$

If instead of S , a diode D is in branch 2, as shown in Figure 3.2(b), the operation of D can be considered as a switch which automatically opens or closes dependent on the state of the circuit. The diode switches ON (equivalent to S closed) if the voltage across it V_D exceeds the forward volt drop V_{FD} characteristic of the diode. The diode switches OFF as soon as the diode current drops to zero. (The reverse current which flows for a short time to redistribute the charges in the diode and brings it back to the blocking state is neglected in the analysis). The computer can be programmed to check the diode current or reverse voltage at each step of calculation and to determine the point of discontinuity. It can also be programmed to produce the transformation tensor for the next step of calculation. When the diode is OFF, the voltage across it can be computed by summing the voltages around the network given in Figure 3.1(c) in which all the diodes are conducting. William⁴² has shown that, by choosing the diode currents as the independent currents of the network, the voltages across the diode in the OFF state can be easily obtained from

$$[V] = [V_n] - [Z_n] \cdot [I_n] \quad 3.23$$

If the independent current (I_{n1} , I_{n2} etc) do not flow in the diode the corresponding voltage in $[V]$ is zero. If an independent current does flow in the diode, the corresponding voltage in $[V]$ is V_{FD} for the diode in the forward conduction or negative when the diode is not conducting.

3.2 The Phase Model Analysis of a Brushless Excitation System for a Synchronous Generator

The brushless excitation system used on the aircraft generator 2130 consists of a 3-phase exciter feeding the main generator field winding via a 3-phase full wave rectifier, as shown in Figure 3.3. The exciter output and hence the main generator output is controlled by the exciter field current. A phase model analysis for the exciter similar to that

used for the main generator can be used. However, since the exciter does not have damper circuits, it can adequately be represented by a 4×4 tensor instead of a 6×6 tensor required for the generator. The phase model can be further simplified by neglecting terms of the order 3 and higher in the Fourier expressions for the self and mutual inductances of the exciter windings. The resultant $[L_e]$ and $[G_e]$ tensors for the exciter are then as given by equations 3.28 and 3.29, respectively. The performance of the exciter is defined by:

$$[V_e] = [L_e] \cdot [pI_e] + [R_e] \cdot [I_e] + [G_e] \cdot [I_e] \quad 3.24$$

where

$$[V_e] = \begin{bmatrix} 0 \\ 0 \\ 0 \\ V_{FE} \end{bmatrix} \quad 3.25$$

$$[I_e] = \begin{bmatrix} I_a \\ I_b \\ I_c \\ I_{FE} \end{bmatrix} \quad 3.26$$

$$[R_e] = \begin{bmatrix} R_{aa} & 0 & 0 & 0 \\ 0 & R_{bb} & 0 & 0 \\ 0 & 0 & R_{cc} & 0 \\ 0 & 0 & 0 & R_{FFE} \end{bmatrix} \quad 3.27$$

The primitive voltage, current and impedance tensors for the exciter-rectifier-generator system of Figure 3.4 are given by equations 3.30, 3.31 and 3.33 respectively.

18

$[L_e] =$

$A_0 + A_2 \cos 2\theta$	$-B_0 + B_2 \cos (2\theta - 2\pi/3)$	$-B_0 + B_2 \cos (2\theta - 4\pi/3)$	$C_1 \cos (\theta)$
$-B_0 + B_2 \cos (2\theta - 2\pi/3)$	$A_0 + A_2 \cos (2\theta - 4\pi/3)$	$-B_0 + B_2 \cos (2\theta)$	$C_1 \cos (\theta - 2\pi/3)$
$-B_0 + B_2 \cos (2\theta - 4\pi/3)$	$-B_0 + B_2 \cos 2\theta$	$A_0 + A_2 \cos (2\theta - 2\pi/3)$	$C_1 \cos (\theta - 4\pi/3)$
$C_1 \cos (\theta)$	$C_1 \cos (\theta - 2\pi/3)$	$C_1 \cos (\theta - 4\pi/3)$	L_{FFE}

$[G_e] =$

$- 2 A_2 \sin (2\theta)$	$- 2 B_2 \sin (2\theta - 2\pi/3)$	$- 2 B_2 \sin (2\theta - 4\pi/3)$	$- C_1 \sin (\theta)$
$- 2 B_2 \sin (2\theta - 2\pi/3)$	$- 2 A_2 \sin (2\theta - 4\pi/3)$	$- 2 B_2 \sin (2\theta)$	$- C_1 \sin (\theta - 2\pi/3)$
$- 2 B_2 \sin (2\theta - 4\pi/3)$	$- 2 B_2 \sin (2\theta)$	$- 2 A_2 \sin (2\theta - 2\pi/3)$	$- C_1 \sin (\theta - 4\pi/3)$
$- C_1 \sin (\theta)$	$- C_1 \sin (\theta - 2\pi/3)$	$- C_1 \sin (\theta - 4\pi/3)$	0

3.29

$[V_p] =$

0
0
0
0
0
0
0
0
0
0
V_{FE}
0
0
0
0
0
0

3.30

$[I_p] =$

I_r
I_y
I_b
I_F
I_D
I_Q
I_a
I_b
I_c
I_{FE}
I_{D1}
I_{D2}
I_{D3}
I_{D4}
I_{D5}
I_{D6}

3.31

where

$[V_p] = [Z_p] \cdot [I_p]$

3.32

The number of independent currents depends on the type of connection of the load, with Figure 3.5 showing a 4-wire connection and Figure 3.6 a 3-wire connection with the independent currents being as shown.

$$[Z_p] =$$

Z_{rr}	Z_{ry}	Z_{rb}	Z_{rF}	Z_{rD}	Z_{rQ}										
Z_{yr}	Z_{yy}	Z_{yb}	Z_{yF}	Z_{yD}	Z_{yQ}										
Z_{br}	Z_{by}	Z_{bb}	Z_{bF}	Z_{bD}	Z_{bQ}										
Z_{Fr}	Z_{Fy}	Z_{Fb}	Z_{FF}	Z_{FD}	Z_{FQ}										
Z_{Dr}	Z_{Dy}	Z_{Db}	Z_{DF}	Z_{DD}	0										
Z_{Qr}	Z_{Qy}	Z_{Qb}	0	0	Z_{QQ}										
						Z_{aa}	Z_{ab}	Z_{ac}	Z_{aFE}						
						Z_{ba}	Z_{bb}	Z_{bc}	Z_{bFE}						
						Z_{ca}	Z_{cb}	Z_{cc}	Z_{cFE}						
						Z_{FEa}	Z_{FEb}	Z_{FEc}	Z_{FFE}						
										Z_{D1}					
											Z_{D2}				
												Z_{D3}			
													Z_{D4}		
														Z_{D5}	
															Z_{D6}

$[Z_g]$	0	0
0	$[Z_e]$	0
0	0	$[Z_d]$

=

3.33

3.2.1 Exciter-Rectifier-Generator Model with 4-wire Load Connection

The transformation tensor, $[C_1]$ for the 4-wire connection is obtained by inspection of Figures 3.3 and 3.5 as

ρ $[C_1] =$ $\begin{matrix} & \begin{matrix} 1 & 2 & 3 & 4 & 5 & 6 & 7 & 8 & 9 & 10 & 11 \end{matrix} \\ \begin{matrix} 1 \\ 2 \\ 3 \\ 4 \\ 5 \\ 6 \\ 7 \\ 8 \\ 9 \\ 10 \\ 11 \end{matrix} & \begin{bmatrix} 1 & 0 & 0 & 0 & 0 & 0 & 0 & 0 & 0 & 0 & 0 \\ 0 & 1 & 0 & 0 & 0 & 0 & 0 & 0 & 0 & 0 & 0 \\ 0 & 0 & 1 & 0 & 0 & 0 & 0 & 0 & 0 & 0 & 0 \\ 0 & 0 & 0 & 1 & 0 & 0 & 1 & 1 & 1 & 0 & 0 \\ 0 & 0 & 0 & 0 & 1 & 0 & 0 & 0 & 0 & 0 & 0 \\ 0 & 0 & 0 & 0 & 0 & 1 & 0 & 0 & 0 & 0 & 0 \\ 0 & 0 & 0 & 0 & 0 & 0 & -1 & 0 & 0 & -1 & 0 \\ 0 & 0 & 0 & 0 & 0 & 0 & 0 & -1 & 0 & 0 & -1 \\ 0 & 0 & 0 & 0 & 0 & 0 & 1 & 1 & 0 & 1 & 1 \\ 0 & 0 & 0 & 0 & 0 & 1 & 0 & 0 & 0 & 0 & 0 \\ 0 & 0 & 0 & 0 & 0 & 0 & 1 & 0 & 0 & 0 & 0 \\ 0 & 0 & 0 & 0 & 0 & 0 & 0 & 1 & 0 & 0 & 0 \\ 0 & 0 & 0 & 0 & 0 & 0 & 0 & 0 & 1 & 0 & 0 \\ 0 & 0 & 0 & 0 & 0 & 0 & 0 & 0 & 0 & 1 & 0 \\ 0 & 0 & 0 & 0 & 0 & 0 & -1 & -1 & -1 & -1 & -1 \end{bmatrix} \end{matrix}$

3.34

The current tensor $[I_n]$ for the 4-wire network is

$$[I_n] = [I_{1n} \ I_{2n} \ I_{3n} \ I_{4n} \ I_{5n} \ I_{6n} \ I_{7n} \ I_{8n} \ I_{9n} \ I_{10n} \ I_{11n}]_t \quad 3.35$$

and the voltage and impedance tensors $[V_n]$ and $[Z_n]$ are

$$[V_n] = [0 \ 0 \ 0 \ 0 \ 0 \ V_{FE} \ 0 \ 0 \ 0 \ 0 \ 0]_t \quad 3.36(a)$$

$$[Z_n] = [c]_t \cdot [Z_p] \cdot [c] \quad 3.36(b)$$

respectively.

To determine $[I_n]$ by numerical integration, it is first necessary to obtain

$[L_n]$, $[R_n]$, $[G_n]$ where $[G_n] = \frac{d}{dt} [L_n] = \frac{d\theta}{dt} \cdot \frac{d}{d\theta} [L_n]$. Thus

$$[L_n] = [C_1]_t \cdot [L_p] \cdot [C_1] \quad 3.37(a)$$

$$[R_n] = [C_1]_t \cdot [R_p] \cdot [C_1] \quad 3.37(b)$$

$$[G_n] = [C_1]_t \cdot [G_p] \cdot [C_1] \quad 3.37(c)$$

The individual $[L]$, $[R]$ and $[G]$ tensors for the loaded generator, exciter and rectifier system are:

$$[L_g] = \begin{array}{|c|c|c|c|c|c|} \hline L_r & L_{ry} & L_{rb} & L_{rF} & L_{rD} & L_{rQ} \\ \hline L_{yr} & L_y & L_{yb} & L_{yF} & L_{yD} & L_{yQ} \\ \hline L_{br} & L_{by} & L_b & L_{bF} & L_{bD} & L_{bQ} \\ \hline L_{Fr} & L_{Fy} & L_{Fb} & L_{FF} & L_{FD} & 0 \\ \hline L_{Dr} & L_{Dy} & L_{Db} & L_{DF} & L_{DD} & 0 \\ \hline L_{Qr} & L_{Qy} & L_{Qb} & 0 & 0 & L_{QQ} \\ \hline \end{array} \quad 3.38$$

where

$$L_r = L_{rr} + L_{rL}$$

$$L_y = L_{yy} + L_{yL}$$

$$L_b = L_{bb} + L_{bL}$$

$$[L_e] = \begin{array}{|c|c|c|c|} \hline L_{aa} & L_{ab} & L_{ac} & L_{aFE} \\ \hline L_{ba} & L_{bb} & L_{bc} & L_{bFE} \\ \hline L_{ca} & L_{cb} & L_{cc} & L_{cFE} \\ \hline L_{FEa} & L_{FEb} & L_{FEc} & L_{FFE} \\ \hline \end{array} \quad 3.39$$

$[L_d] = 0$, since diode inductances are zero.

3.40

$$[R_g] = \begin{bmatrix} R_r & 0 & 0 & 0 & 0 & 0 \\ 0 & R_y & 0 & 0 & 0 & 0 \\ 0 & 0 & R_b & 0 & 0 & 0 \\ 0 & 0 & 0 & R_{FF} & 0 & 0 \\ 0 & 0 & 0 & 0 & R_{DD} & 0 \\ 0 & 0 & 0 & 0 & 0 & R_{QQ} \end{bmatrix}$$

3.41

where

$$R_r = R_{rr} + R_{rL}$$

$$R_y = R_{yy} + R_{yL}$$

$$R_b = R_{bb} + R_{bL}$$

$$[R_e] = \begin{bmatrix} R_{aa} & 0 & 0 & 0 \\ 0 & R_{bb} & 0 & 0 \\ 0 & 0 & R_{cc} & 0 \\ 0 & 0 & 0 & R_{FFE} \end{bmatrix}$$

3.42

$[R_d] = 0$ (The primitive network assumes all diodes are conducting).

$$[G_g] = \begin{bmatrix} G_{rr} & G_{ry} & G_{rb} & G_{rF} & G_{rD} & G_{rQ} \\ G_{yr} & G_{yy} & G_{yb} & G_{yF} & G_{yD} & G_{yQ} \\ G_{br} & G_{by} & G_{bb} & G_{bF} & G_{bD} & G_{bQ} \\ G_{Fr} & G_{Fy} & G_{Fb} & 0 & 0 & 0 \\ G_{Dr} & G_{Dy} & G_{Db} & 0 & 0 & 0 \\ G_{Qr} & G_{Qy} & G_{Qb} & 0 & 0 & 0 \end{bmatrix}$$

3.43

$$[G_e] = \begin{bmatrix} G_{aa} & G_{ab} & G_{ac} & G_{aFE} \\ G_{ba} & G_{bb} & G_{bc} & G_{bFE} \\ G_{ca} & G_{cb} & G_{cc} & G_{cFE} \\ G_{FEa} & G_{FEb} & G_{FEc} & 0 \end{bmatrix} \quad 3.44$$

$$[G_d] = 0 \quad 3.45$$

Therefore $[L_n] = [C_1]_t$

$$\begin{bmatrix} [L_g] & 0 & 0 \\ 0 & [L_e] & 0 \\ 0 & 0 & 0 \end{bmatrix} [C_1] \quad 3.46$$

$$[R_n] = [C_1]_t \begin{bmatrix} [R_g] & 0 & 0 \\ 0 & [R_e] & 0 \\ 0 & 0 & 0 \end{bmatrix} [C_1] \quad 3.47$$

$$[G_n] = [C_1]_t \begin{bmatrix} [G_n] & 0 & 0 \\ 0 & [G_e] & 0 \\ 0 & 0 & 0 \end{bmatrix} [C_1] \quad 3.48$$

Even though the diode resistances and inductances are considered zero, the transformation tensor $[C_1]$ takes account of the conduction paths of the diodes. Since the primitive tensors $[Z_p]$, $[L_p]$, $[G_p]$ and $[R_p]$ contain many null off-diagonal elements, the impedance transformation can be simplified as given in Appendix A5. The network impedance matrices $[Z_n]$, $[L_n]$, $[G_n]$, $[R_n]$ for a 4-wire load connection are as given by equations 3.49, 3.50, 3.51 and 3.52, respectively.

$[Z_n] =$

Z_{rr}	Z_{ry}	Z_{rb}	Z_{rD}	Z_{rQ}	0	Z_{rF}	Z_{rF}	Z_{rF}	0	0
Z_{yr}	Z_{yy}	Z_{yb}	Z_{yD}	Z_{yQ}	0	Z_{yF}	Z_{yF}	Z_{yF}	0	0
Z_{br}	Z_{by}	Z_{bb}	Z_{bD}	Z_{bQ}	0	Z_{bF}	Z_{bF}	Z_{bF}	0	0
Z_{Dr}	Z_{Dy}	Z_{Db}	Z_{DD}	0	0	Z_{DF}	Z_{DF}	Z_{DF}	0	0
Z_{Qr}	Z_{Qy}	Z_{Qb}	0	Z_{QQ}	0	0	0	0	0	0
0	0	0	0	0	Z_{FFE}	$-Z_{aFE}$ $+Z_{cFE}$	$-Z_{bFE}$ $+Z_{cFE}$	0	$-Z_{aFE}$ $+Z_{cFE}$	$-Z_{bFE}$ $+Z_{cFE}$
Z_{Fr}	Z_{Fy}	Z_{Fb}	Z_{FD}	0	$-Z_{aFE}$ $+Z_{cFE}$	Z_{FF}^+ $+Z_{aa}-Z_{ac}$ $-Z_{ca}+Z_{cc}$	Z_{FF}^+ $+Z_{ab}-Z_{ac}$ $-Z_{cb}+Z_{cc}$	Z_{FF}	$Z_{aa}-Z_{ac}$ $-Z_{ca}+Z_{cc}$	$Z_{ab}-Z_{ac}$ $-Z_{cb}+Z_{cc}$
Z_{Fr}	Z_{Fy}	Z_{Fb}	Z_{FD}	0	$-Z_{bFE}$ $+Z_{cFE}$	Z_{FF}^+ $+Z_{ba}-Z_{bc}$ $-Z_{ca}+Z_{cc}$	Z_{FF}^+ $+Z_{bb}-Z_{bc}$ $-Z_{cb}+Z_{cc}$	Z_{FF}	$Z_{ba}-Z_{bc}$ $-Z_{ca}+Z_{cc}$	$Z_{bb}-Z_{bc}$ $-Z_{cb}+Z_{cc}$
Z_{Fr}	Z_{Fy}	Z_{Fb}	Z_{FD}	0	0	Z_{FF}	Z_{FF}	Z_{FF}	0	0
0	0	0	0	0	$-Z_{aFE}$ $+Z_{cFE}$	$Z_{aa}-Z_{ac}$ $-Z_{ca}+Z_{cc}$	$Z_{ab}-Z_{ac}$ $-Z_{cb}+Z_{cc}$	0	$Z_{aa}-Z_{ac}$ $-Z_{ca}+Z_{cc}$	$Z_{ab}-Z_{ac}$ $-Z_{cb}+Z_{cc}$
0	0	0	0	0	$-Z_{bFE}$ $+Z_{cFE}$	$Z_{ba}-Z_{bc}$ $-Z_{ca}+Z_{cc}$	$Z_{bb}-Z_{bc}$ $-Z_{cb}+Z_{cc}$	0	$Z_{ba}-Z_{bc}$ $-Z_{ca}+Z_{cc}$	$Z_{bb}-Z_{bc}$ $-Z_{cb}+Z_{cc}$

$[L_n] =$	L_r	L_{ry}	L_{rb}	L_{rD}	L_{rQ}	0	L_{rF}	L_{rF}	L_{rF}	0	0
	L_{yr}	L_y	L_{yb}	L_{yD}	L_{yQ}	0	L_{yF}	L_{yF}	L_{yF}	0	0
	L_{br}	L_{by}	L_b	L_{bD}	L_{bQ}	0	L_{bF}	L_{bF}	L_{bF}	0	0
	L_{Dr}	L_{Dy}	L_{Db}	L_{DD}	0	0	L_{DF}	L_{DF}	L_{DF}	0	0
	L_{Qr}	L_{Qy}	L_{Qb}	0	L_{QQ}	0	0	0	0	0	0
	0	0	0	0	0	L_{FFE}	$-L_{aFE}$ $+L_{cFE}$	$-L_{bFE}$ $+L_{cFE}$	0	$-L_{aFE}$ $+L_{cFE}$	$-L_{bFE}$ $+L_{cFE}$
	L_{Fr}	L_{Fy}	L_{Fb}	L_{FD}	0	$-L_{aFE}$ $-L_{cFE}$	L_{FF} $+L_{aa}-L_{ac}$ $-L_{ca}+L_{cc}$	L_{FF} $+L_{ab}-L_{ac}$ $-L_{cb}+L_{cc}$	L_{FF}	$L_{aa}-L_{ac}$ $-L_{ca}+L_{cc}$	$L_{ab}-L_{ac}$ $-L_{ca}+L_{cc}$
	L_{Fr}	L_{Fy}	L_{Fb}	L_{FD}	0	$-L_{bFE}$ $+L_{cFE}$	L_{FF} $+L_{ba}-L_{bc}$ $-L_{ca}+L_{cc}$	L_{FF} $+L_{bb}-L_{bc}$ $-L_{cb}+L_{cc}$	L_{FF}	$L_{ba}-L_{bc}$ $-L_{ca}+L_{cc}$	$L_{bb}-L_{bc}$ $-L_{cb}+L_{cc}$
	L_{Fr}	L_{Fy}	L_{Fb}	L_{FD}	0	0	L_{FF}	L_{FF}	L_{FF}	0	0
	0	0	0	0	0	$-L_{aFE}$ $+L_{cFE}$	$L_{aa}-L_{ac}$ $-L_{ca}+L_{cc}$	$L_{ab}-L_{ac}$ $-L_{cb}+L_{cc}$	0	$L_{aa}-L_{ac}$ $-L_{ca}+L_{cc}$	$L_{ab}-L_{ac}$ $-L_{cb}+L_{cc}$
	0	0	0	0	0	$-L_{bFE}$ $+L_{cFE}$	$L_{ba}-L_{bc}$ $-L_{ca}+L_{cc}$	$L_{bb}-L_{bc}$ $-L_{cb}+L_{cc}$	0	$L_{ba}-L_{bc}$ $-L_{ca}+L_{cc}$	$L_{bb}-L_{bc}$ $-L_{cb}+L_{cc}$

$[G_n] =$

G_{rr}	G_{ry}	G_{rb}	G_{rD}	G_{rQ}	0	G_{rF}	G_{rF}	G_{rF}	0	θ
G_{yr}	G_{yy}	G_{yb}	G_{yD}	G_{yQ}	0	G_{yF}	G_{yF}	G_{yF}	0	0
G_{br}	G_{by}	G_{bb}	G_{bD}	G_{bQ}	0	G_{bF}	G_{bF}	G_{bF}	0	0
G_{Dr}	G_{Dy}	G_{Db}	0	0	0	0	0	0	0	0
G_{Qr}	G_{Qy}	G_{Qb}	0	0	0	0	0	0	0	0
0	0	0	0	0	0	$-G_{aFE}$ $+G_{cFE}$	$-G_{bFE}$ $+G_{cFE}$	0	$-G_{aFE}$ $+G_{cFE}$	$-G_{bFE}$ $+G_{cFE}$
G_{Fr}	G_{Fy}	G_{Fb}	0	0	$-G_{aFE}$ $+G_{cFE}$	$G_{aa}-G_{ac}$ $-G_{ca}+G_{cc}$	$G_{ab}-G_{ac}$ $-G_{cb}+G_{cc}$	0	$G_{aa}-G_{ac}$ $-G_{ca}+G_{cc}$	$G_{ab}-G_{ac}$ $-G_{cb}+G_{cc}$
G_{Fr}	G_{Fy}	G_{Fb}	0	0	$-G_{bFE}$ $+G_{cFE}$	$G_{ba}-G_{bc}$ $-G_{ca}+G_{cc}$	$G_{bb}-G_{bc}$ $-G_{cb}+G_{cc}$	0	$G_{ba}-G_{bc}$ $-G_{ca}+G_{cc}$	$G_{bb}-G_{bc}$ $-G_{cb}+G_{cc}$
G_{Fr}	G_{Fy}	G_{Fb}	0	0	0	0	0	0	0	0
0	0	0	0	0	$-G_{aFE}$ $+G_{cFE}$	$G_{aa}-G_{ac}$ $-G_{ca}+G_{cc}$	$G_{ab}-G_{ac}$ $-G_{cb}+G_{cc}$	0	$G_{aa}-G_{ac}$ $-G_{ca}+G_{cc}$	$G_{ab}-G_{ac}$ $-G_{cb}+G_{cc}$
0	0	0	0	0	$-G_{bFE}$ $+G_{cFE}$	$G_{ba}-G_{bc}$ $-G_{ca}+G_{cc}$	$G_{bb}-G_{bc}$ $-G_{cb}+G_{cc}$	0	$G_{ba}-G_{bc}$ $-G_{ca}+G_{cc}$	$G_{bb}-G_{bc}$ $-G_{cb}+G_{cc}$

$[R_n] =$

R_r										
	R_y									
		R_b								
			R_{DD}							
				R_{QQ}						
					R_{FFE}					
						R_{FF} $+R_{aa}+R_{cc}$	R_{FF} $+R_{cc}$	R_{FF}	$R_{aa}+$ R_{cc}	R_{cc}
						R_{FF} $+R_{cc}$	R_{FF} $+R_{bb}$ $+R_{cc}$	R_{FF}	R_{cc}	$R_{bb}+$ R_{cc}
						R_{FF}	R_{FF}	R_{FF}	0	0
						$R_{aa}+$ R_{cc}	R_{cc}	0	$R_{aa}+$ R_{cc}	R_{cc}
						R_{cc}	$R_{bb}+$ R_{cc}	0	R_{cc}	$R_{bb}+$ R_{cc}

3.2.2 Exciter-Rectifier-Generator Model with 3-wire Load Connection

Since there is now no neutral current in the generator, there are only two independent armature currents instead of three. The impedance connected to each armature phase is the impedance between the line and the star point of the load. The primitive voltage, current and impedance tensors are as for the 4-wire connection, as the primitive tensors are independent of the connection of the system branches.

The transformation tensor $[C_1]$ is obtained by writing the branch currents I_p of Figure 3.3 in terms of the independent currents I_n for the 3-wire load connection shown in Figure 3.6 as

$$[C_1] =$$

1									
	1								
-1	-1								
					1	1	1		
		1							
			1						
					-1			-1	
						-1			-1
					1	1		1	1
				1					
					1				
						1			
							1		
								1	
									1
					-1	-1	-1	-1	-1

3.53

The voltage matrix $[V_n]$ and $[Z_n]$ for the 3-wire load connection are

$$[V_n] = [0 \ 0 \ 0 \ 0 \ V_{FE} \ 0 \ 0 \ 0 \ 0 \ 0]_t \quad 3.54$$

and

with $[Z_n]$ as given by equation 3.55 the corresponding matrices $[L_n]$, $[G_n]$ and $[R_n]$ are given by equations 3.56, 3.57 and 3.58 respectively.

3.3 Differential Equations for Exciter-Rectifier-Generator Phase Model

Having obtained the current, voltage and impedance tensors for both the 4-wire and 3-wire load connections, it is now necessary to obtain the operational current, voltage and impedance matrices depending on the diodes that are conducting at a particular instant in time.

Consider the 4-wire connection of Figure 3.5 showing the independent currents I_n . If diodes 1, 2 and 6 are conducting, the operational currents I_m are as shown in Figure 3.7. The transformation tensor $[C_2]$ relating I_n to I_m is

$$[C_2] = \begin{bmatrix} 1 & & & & & & & \\ & 1 & & & & & & \\ & & 1 & & & & & \\ & & & 1 & & & & \\ & & & & 1 & & & \\ & & & & & 1 & & \\ & & & & & & 1 & \\ & & & & & & & 1 \\ & & & & & & & \\ & & & & & & & \\ & & & & & & & \\ & & & & & & & \end{bmatrix} = \begin{bmatrix} [C_{21}] & [C_{22}] \\ [C_{23}] & [C_{24}] \end{bmatrix} \quad 3.59$$

The operational voltage and impedance tensors corresponding to diodes 1, 2 and 6 conducting are found using equations 3.13 and 3.11 respectively using the transformation tensor $[C_2]$ given by equation (3.59).

$[Z_n] =$

$Z_r - Z_{rb}$ $-Z_{br} + Z_b$	$Z_{ry} - Z_{rb}$ $-Z_{by} + Z_b$	Z_{rD} $-Z_{bD}$	Z_{rQ} $-Z_{bQ}$	0	Z_{rF} $-Z_{bF}$	Z_{rF} $-Z_{bF}$	Z_{rF} $-Z_{bF}$	0	0
$Z_{yr} - Z_{yb}$ $-Z_{br} + Z_b$	$Z_y - Z_{yb}$ $-Z_{by} + Z_b$	Z_{yD} $-Z_{bD}$	Z_{yQ} $-Z_{bQ}$	0	Z_{yF} $-Z_{bF}$	Z_{yF} $-Z_{bF}$	Z_{yF} $-Z_{bF}$	0	0
Z_{Dr} $-Z_{Db}$	Z_{Dy} $-Z_{Db}$	Z_{DD}	0	0	Z_{DF}	Z_{DF}	Z_{DF}	0	0
Z_{Qr} $-Z_{Qb}$	Z_{Qy} $-Z_{Qb}$	0	Z_{QQ}	0	0	0	0	0	0
0	0	0	0	Z_{FFE}	$-Z_{aFE}$ $+Z_{cFE}$	$-Z_{bFE}$ $+Z_{cFE}$	0	$-Z_{aFE}$ $+Z_{cFE}$	$-Z_{bFE}$ $+Z_{cFE}$
Z_{Fr} $-Z_{Fb}$	Z_{Fy} $-Z_{Fb}$	Z_{FD}	0	$-Z_{aFE}$ $+Z_{cFE}$	Z_{FF} $+Z_{aa} - Z_{ac}$ $-Z_{ca} + Z_{cc}$	Z_{FF} $+Z_{ab} - Z_{ac}$ $-Z_{cb} + Z_{cc}$	Z_{FF}	$Z_{aa} - Z_{ac}$ $-Z_{ca} + Z_{cc}$	$Z_{ab} - Z_{ac}$ $-Z_{cb} + Z_{cc}$
Z_{Fr} $-Z_{Fb}$	Z_{Fy} $-Z_{Fb}$	Z_{FD}	0	$-Z_{bFE}$ $+Z_{cFE}$	Z_{FF} $+Z_{ba} - Z_{bc}$ $-Z_{ca} + Z_{cc}$	Z_{FF}^+ $Z_{bb} - Z_{bc}$ $-Z_{cb} + Z_{cc}$	Z_{FF}	$Z_{ba} - Z_{bc}$ $-Z_{ca} + Z_{cc}$	$Z_{bb} - Z_{bc}$ $-Z_{cb} + Z_{cc}$
Z_{Fr} $-Z_{Fb}$	Z_{Fy} $-Z_{Fb}$	Z_{FD}	0	0	Z_{FF}	Z_{FF}	Z_{FF}	0	0
0	0	0	0	$-Z_{aFE}$ $+Z_{cFE}$	$Z_{aa} - Z_{ac}$ $-Z_{ca} + Z_{cc}$	$Z_{ab} - Z_{ac}$ $-Z_{cb} + Z_{cc}$	0	$Z_{aa} - Z_{ac}$ $-Z_{ca} + Z_{cc}$	$Z_{ab} - Z_{ac}$ $-Z_{cb} + Z_{cc}$
0	0	0	0	$-Z_{bFE}$ $+Z_{cFE}$	$Z_{ba} - Z_{bc}$ $-Z_{ca} + Z_{cc}$	$Z_{bb} - Z_{bc}$ $-Z_{cb} + Z_{cc}$	0	$Z_{ba} - Z_{bc}$ $-Z_{ca} + Z_{cc}$	$Z_{bb} - Z_{bc}$ $-Z_{cb} + Z_{cc}$

$$[L_n] =$$

$L_r - L_{rb}$ $-L_{br} + L_b$	$L_{ry} - L_{rb}$ $-L_{by} + L_b$	L_{rD} $-L_{rD}$	L_{rQ} $-L_{bQ}$	0	L_{rF} $-L_{bF}$	L_{rF} $-L_{bF}$	L_{rF} $-L_{bF}$	0	0
$L_{yr} - L_{yb}$ $-L_{br} + L_b$	$L_y - L_{yb}$ $-L_{by} + L_b$	L_{yD} $-L_{bD}$	L_{yQ} $-L_{bQ}$	0	L_{yF} $-L_{bF}$	L_{yF} $-L_{bF}$	L_{yF} $-L_{bF}$	0	0
L_{Dr} $-L_{Db}$	L_{Dy} $-L_{Db}$	L_{DD}	0	0	L_{DF}	L_{DF}	L_{DF}	0	0
L_{Qr} $-L_{Qb}$	L_{Qy} $-L_{Qb}$	0	L_{QQ}	0	0	0	0	0	0
0	0	0		L_{FFE}	$-L_{aFE}$ $+L_{cFE}$	$-L_{bFE}$ $+L_{cFE}$	0	$-L_{aFE}$ $+L_{cFE}$	$-L_{bFE}$ $+L_{cFE}$
L_{Fr} $-L_{Fb}$	L_{yF} $-L_{bF}$	L_{DF}	0	$-L_{aFE}$ $+L_{cFE}$	L_{FF}^+ $L_{aa} - L_{ac}$ $-L_{ca} + L_{cc}$	L_{FF}^+ $L_{ab} - L_{ac}$ $-L_{cb} + L_{cc}$	L_{FF}	$L_{aa} - L_{ac}$ $-L_{ca} + L_{cc}$	$L_{ab} - L_{ac}$ $-L_{cb} + L_{cc}$
L_{Fr} $-L_{Fb}$	L_{yF} $-L_{bF}$	L_{DF}	0	$-L_{bFE}$ $+L_{cFE}$	L_{FF}^+ $L_{ba} - L_{bc}$ $-L_{ca} + L_{cc}$	L_{FF}^+ $L_{bb} - L_{bc}$ $-L_{cb} + L_{cc}$	L_{FF}	$L_{ba} - L_{bc}$ $-L_{ca} + L_{cc}$	$L_{bb} - L_{bc}$ $-L_{cb} + L_{cc}$
L_{Fr} $-L_{Fb}$	L_{yF} $-L_{bF}$	L_{DF}	0	0	L_{FE}	L_{FF}	L_{FF}	0	0
0	0	0	0	$-L_{aFE}$ $+L_{cFE}$	$L_{aa} - L_{ac}$ $-L_{ca} + L_{cc}$	$L_{ab} - L_{ac}$ $-L_{cb} + L_{cc}$	0	$L_{aa} - L_{ac}$ $-L_{ca} + L_{cc}$	$L_{ab} - L_{ac}$ $-L_{cb} + L_{cc}$
0	0	0	0	$-L_{bFE}$ $+L_{cFE}$	$L_{ba} - L_{bc}$ $-L_{ca} + L_{cc}$	$L_{bb} - L_{bc}$ $-L_{cb} + L_{cc}$	0	$L_{ba} - L_{bc}$ $-L_{ca} + L_{cc}$	$L_{bb} - L_{bc}$ $-L_{cb} + L_{cc}$

n] =

$G_{rr}-G_{rb}$ $-G_{br}+G_{bb}$	$G_{ry}-G_{rb}$ $-G_{by}+G_{bb}$	G_{rD} $-G_{bD}$	G_{rQ} $-G_{bQ}$	0	G_{rF} $-G_{bF}$	G_{rF} $-G_{bF}$	G_{rF} $-G_{bF}$	0	0
$G_{yr}-G_{yb}$ $-G_{br}+G_{bb}$	$G_{yy}-G_{yb}$ $-G_{by}+G_{bb}$	G_{yD} $-G_{bD}$	G_{yQ} $-G_{bQ}$	0	G_{yF} $-G_{bF}$	G_{yF} $-G_{bF}$	G_{yF} $-G_{bF}$	0	0
G_{Dr} $-G_{Db}$	G_{Dy} $-G_{Db}$	0	0	0	0	0	0	0	0
G_{Qr} $-G_{Qb}$	G_{Qy} $-G_{Qb}$	0	0	0	0	0	0	0	0
0	0	0	0	0	$-G_{aFE}$ $+G_{cFE}$	$-G_{bFE}$ $+G_{cFE}$	0	$-G_{aFE}$ $+G_{cFE}$	$-G_{bFE}$ $+G_{cFE}$
G_{Fr} $-G_{Fb}$	G_{Fy} $-G_{Fb}$	0	0	$-G_{aFE}$ $+G_{cFE}$	$G_{aa}-G_{ac}$ $-G_{ca}+G_{cc}$	$G_{ab}-G_{ac}$ $-G_{cb}+G_{cc}$	0	$G_{aa}-G_{ac}$ $-G_{ca}+G_{cc}$	$G_{ab}-G_{ac}$ $-G_{cb}+G_{cc}$
G_{Fr} $-G_{Fb}$	G_{Fy} $-G_{Fb}$	0	0	$-G_{bFE}$ $+G_{cFE}$	$G_{ba}-G_{bc}$ $-G_{ca}+G_{cc}$	$G_{bb}-G_{bc}$ $-G_{cb}+G_{cc}$	0	$G_{ba}-G_{bc}$ $-G_{ca}+G_{cc}$	$G_{bb}-G_{bc}$ $-G_{cb}+G_{cc}$
G_{Fr} $-G_{Fb}$	G_{Fy} $-G_{Fb}$	0	0	0	0	0	0	0	0
0	0	0	0	$-G_{aFE}$ $+G_{cFE}$	$G_{aa}-G_{ac}$ $-G_{ca}+G_{cc}$	$G_{ab}-G_{ac}$ $-G_{cb}+G_{cc}$	0	$G_{aa}-G_{ac}$ $-G_{ca}+G_{cc}$	$G_{ab}-G_{ac}$ $-G_{cb}+G_{cc}$
0	0	0	0	$-G_{bFE}$ $+G_{cFE}$	$G_{ba}-G_{bc}$ $-G_{ca}+G_{cc}$	$G_{bb}-G_{bc}$ $-G_{cb}+G_{cc}$	0	$G_{ba}-G_{bc}$ $-G_{ca}+G_{cc}$	$G_{bb}-G_{bc}$ $-G_{cb}+G_{cc}$

$[R_n] =$

$R_x + R_b$	R_b								
R_b	$R_y + R_b$								
		R_{DD}							
			R_{QQ}						
				R_{FFE}					
					$R_{FF}^+ + R_{aa} + R_{cc}$	$R_{FF} + R_{cc}$	R_{FF}	$R_{aa} + R_{cc}$	R_{cc}
					$R_{FF} + R_{cc}$	$R_{FF}^+ + R_{bb} + R_{cc}$	R_{FF}	R_{cc}	$R_{bb} + R_{cc}$
					R_{FF}	R_{FF}	R_{FF}	0	0
					$R_{aa} + R_{cc}$	R_{cc}	0	$R_{aa} + R_{cc}$	R_{cc}
					R_{cc}	$R_{bb} + R_{cc}$	0	R_{cc}	$R_{bb} + R_{cc}$

The operational currents $[I_m]$ are obtained by numerical integration of equation 3.14.

3.3.1 Calculation of Diode Currents

Having obtained $[I_m]$ and $[pI_m]$ at a particular instant in time using equation 3.14, the diode currents and voltages are calculated as follows:

$$[I_n] = [C_2][I_m] \quad 3.60(a), \quad [pI_n] = [C_2][pI_m] \quad 3.60(b)$$

The diode currents are

$$I_{D1} = I_{7n}$$

$$I_{D2} = I_{8n}$$

$$I_{D3} = I_{9n}$$

$$I_{D4} = I_{10n}$$

$$I_{D5} = I_{11n}$$

$$I_{D6} = -(I_{7n} + I_{8n} + I_{9n} + I_{10n} + I_{11n})$$

3.3.2 Calculation of Diode Voltages

The diode voltages are found by computing the mesh-sum voltages, $[V]$, for the independent current network by the application of Kirchhoff's Laws. Thus

$$0 = [Z_n][I_n] - [V_n] + [V]$$

or

$$[V] = [V_n] - [L_n][pI_n] - \{[R_n] + [G_n]\}[I_n] \quad 3.62$$

and, as diode D6 appears in the last five meshes, the voltage across D6, also appears in these meshes. Hence the form of $[V]$ is

$$[V] = \begin{bmatrix} V_1 \\ V_2 \\ V_3 \\ V_4 \\ V_5 \\ V_6 \\ V_7 \\ V_8 \\ V_9 \\ V_{10} \\ V_{11} \end{bmatrix} = \begin{bmatrix} 0 \\ 0 \\ 0 \\ 0 \\ 0 \\ 0 \\ V_{D1} - V_{D6} \\ V_{D2} - V_{D6} \\ V_{D3} - V_{D6} \\ V_{D4} - V_{D6} \\ V_{D5} - V_{D6} \end{bmatrix} \quad 3.63$$

As diodes D1, D2 and D6 are assumed to be in forward conduction, V_{D1} , V_{D2} and V_{D6} are equal to the forward volt drop V_{FD} characteristic of the diode (which is assumed to be negligible compared with other voltages in the system). Therefore the diode voltages are obtained from equation 3.63 as:

$$V_{D1} = V_7 = 0$$

$$V_{D2} = V_8 = 0$$

$$V_{D3} = V_9 \quad 3.64$$

$$V_{D4} = V_{10}$$

$$V_{D5} = V_{11}$$

However, the way in which the currents and voltages in the lower limbs of the diode bridge have been defined as shown in Figure 3.3, are in fact in opposite direction to that necessary for testing for turning on or turning off. Hence V_{D4} , V_{D5} , V_{D6} and I_{D4} , I_{D5} , I_{D6} are reversed in direction for this purpose.

3.4 Comparison Between the Measured and Predicted Results

A computer program was prepared to assemble and solve the differential equations of the brushless excitation system described in Sections 3.2 and 3.3. The computer program flow chart is shown in Figure 3.8. The differential equations were numerically integrated on the digital computer using the Runge-Kutta 4th-order method described in Appendix A6 . It was not possible to measure the exciter phase current, the diode reverse voltages, the diode forward currents of the rectifier bridge and the generator field current as the exciter armature windings, the bridge rectifier and the generator field windings are mounted on the rotor shaft which is rotating at 12000 rpm. To be able to measure these parameters, it would be necessary to bring out the exciter armature winding output terminals and the generator field winding terminals to an external bridge rectifier via slip rings. Due to the very compact assembly of the generator unit, as shown by photographs of the unit in Appendix (A1), it was not possible to do this. Therefore, the predicted exciter phase current, diode forward current and reverse voltage waveforms are compared with the measured waveforms of a similar aircraft generator unit reported in reference 43 . These waveforms are reproduced here to show that the predicted waveforms are very similar to the measured waveforms. The predicted waveforms under steady state conditions using the computer program, for a 1 p.u. 0.75 p.f., 3-phase star connected balanced load, applied to the generator terminals with a constant 10V exciter field voltage are given in Figures 3.9 to 3.15.

Figures 3.9(a) and 3.9(b) provide a comparison between the predicted and measured exciter field current waveforms. Similarly Figures 3.10(a) and 3.10(b) provide a comparison between the predicted and measured exciter phase currents. Figures 3.11 and 3.12(a) show the predicted reverse voltage across the diode and the forward conduction current respectively for the diode D_1 of the bridge rectifier. Figure 3.12(b) shows the measured reverse voltage and forward current waveforms. It can be seen that the predicted and measured forward current waveforms of the diode are identical.

The measured reverse voltage across the diode is displayed as a positive voltage while the predicted reverse voltage is considered to be negative. It can be seen that when either one of the reverse voltage waveforms is inverted, the predicted and measured reverse voltage across the diode are identical.

Figures 3.13(a) and 3.13(b) provide a comparison between the predicted and the measured generator field voltage waveforms. It can be seen from the comparison of waveforms of the generator field voltage, that they are identical except for small spikes in the measured voltage waveform, which can also be seen on the measured reverse voltage across the diode in Figure 3.12(b). These spikes are due to non-ideal behaviour of the diodes of the bridge rectifier. The diodes allow a reverse current flow to redistribute the charges in the p-n junction of the diode before it assumes the blocking state. The sudden collapse of this reverse current results in voltages being induced in the windings of the machine due to the inductances of the circuit and hence appearing as spikes in the reverse voltage across the non-conducting diodes of the bridge and in the voltage applied to the generator field winding. Figures 3.14 and 3.15 show the predicted generator field current and the load phase current. The exciter field current and the load phase current were measured to be 1.23A and 94.2A (rms) respectively. The predicted exciter field current and the load phase current are 1.3A and 95.5A (rms) respectively. It can be seen that the input output currents, which are the measurable quantities, are accurately predicted.

The computer program is also able to predict the transient behaviour as it determines the state of the circuit and the relevant differential equations at each step during the numerical integration on the digital computer. For example, the predicted transients following a step change from 10V to 25V in exciter field voltage are given in Figures 3.16 to 3.22. It can be seen from the exciter field current and the generator field voltage transients of Figures 3.16 and 3.20 respectively that the response of the exciter is fast due to the changes in the exciter field voltage. The genera-

tor field current build up as shown in Figure 3.21, is much slower, with 1 p.u. 0.75 p.f. load connected to the generator, compared to the exciter field current. Since the exciter phase current and the diode forward conduction current depend on the generator field current, it can be seen from Figures 3.17 and 3.19 respectively that the build up of these currents are directly dependent on the build up of generator field current. The consequence of the fast rise in the exciter field current is also to increase the reverse voltages across the diodes of the rectifier bridge as shown in Figure 3.18.

3.5 Conclusion

This chapter has described the application of Kron's tensor methods for the analysis of electrical networks with varying topology. The methods were applied to the digital computer analysis of a brushless excitation system. Close agreement between the predicted and measured results on a similar system was obtained as discussed in Section 3.4, showing that the model developed using the tensor methods can be used for both design and system study purposes in predicting the steady state and transient characteristics of the brushless excitation system.

Since the model of the brushless excitation system predicts the voltage spikes across the diodes of the rectifier bridge accurately both during the steady state operation and during transients, (as shown in Figures 3.11 and 3.18 respectively), the model enables the diodes of correct reverse voltage rating to be selected.

For radio interference studies etc. a more detailed characteristic of the diode to account for the nonlinear behaviour of the diode in forward conduction and the reverse current flow until the diode assumes the blocking state can be programmed, but for general purpose system models, the diodes can be assumed to be ideal without any loss of accuracy in predicting the behaviour of the system.

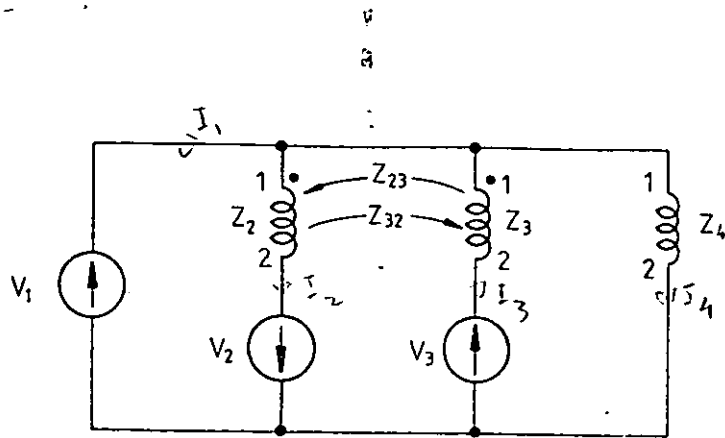


Figure 3.1(a) EXAMPLE NETWORK

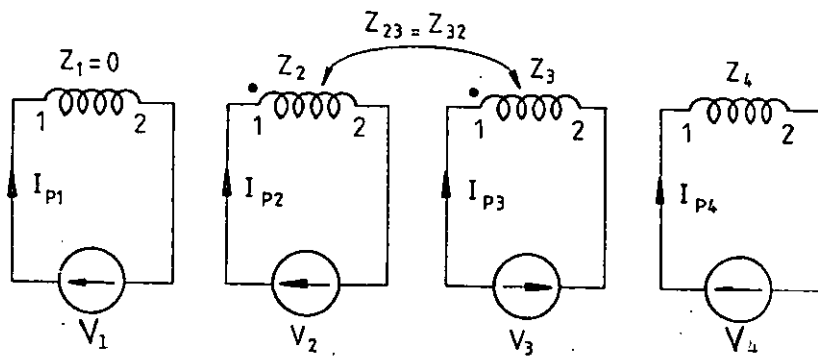


Figure 3.1(b) PRIMITIVE NETWORKS REPRESENTING NETWORK OF FIGURE 3.1(a)

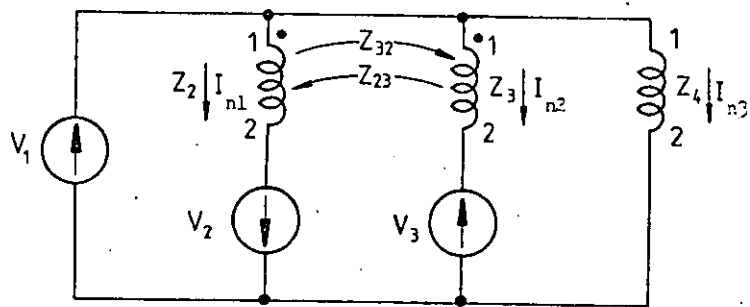


Figure 3.1(c) INDEPENDENT CURRENTS OF NETWORK OF FIGURE 3.1(a)

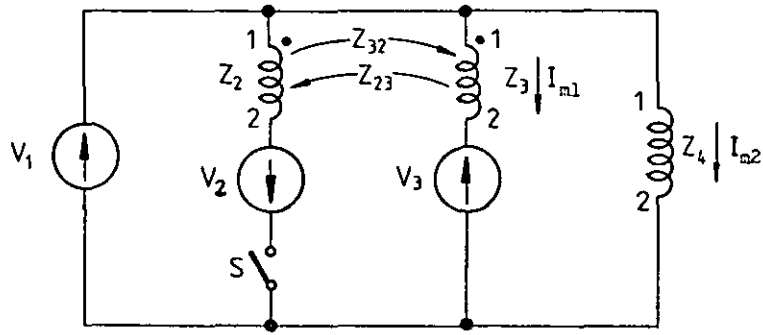


Figure 3.2(a) NETWORK OF FIGURE 3.1(a) WITH SWITCH S

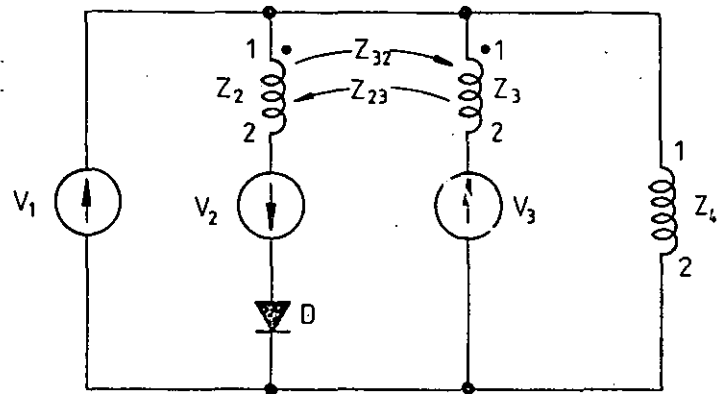
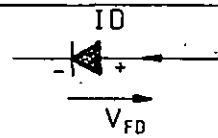


Figure 3.2(b) NETWORK OF FIGURE 3.1(a) WITH DIODE D



DIODE REPRESENTATION

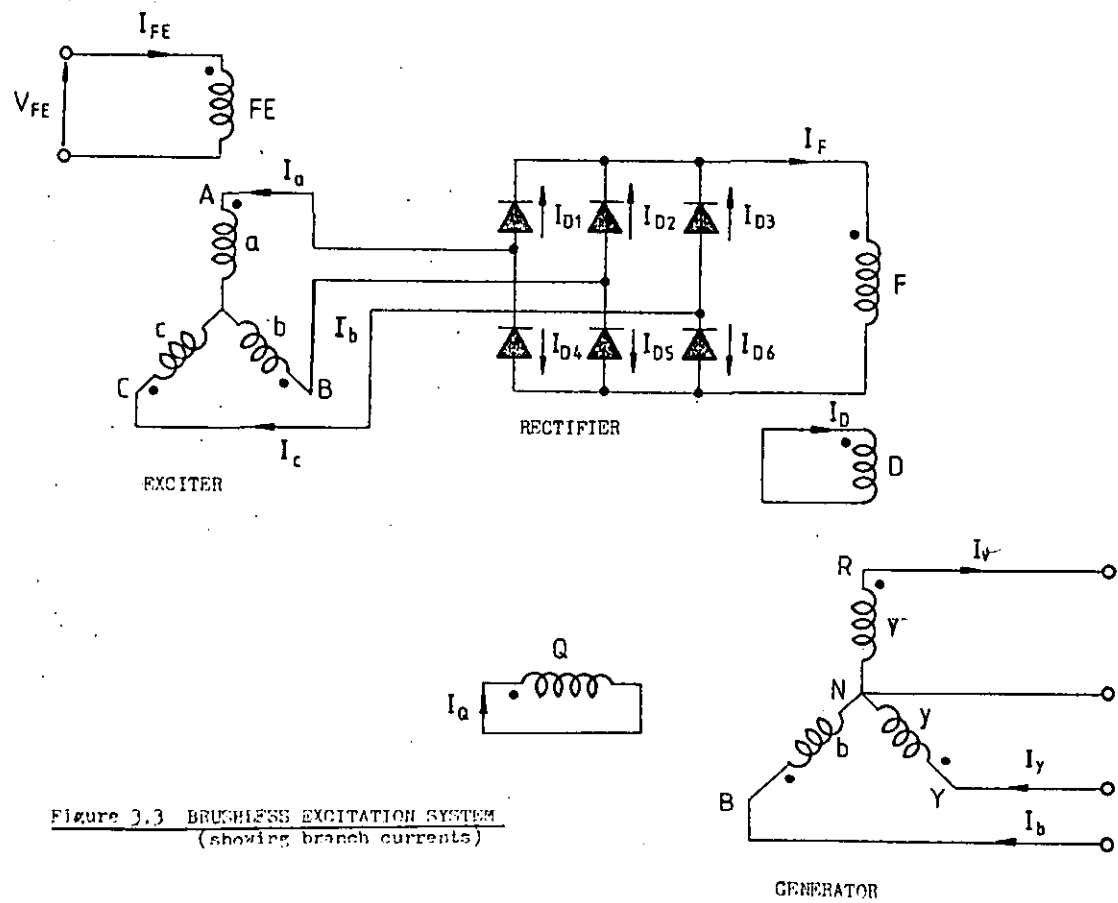


Figure 2.3 BRUSHLESS EXCITATION SYSTEM
(showing branch currents)

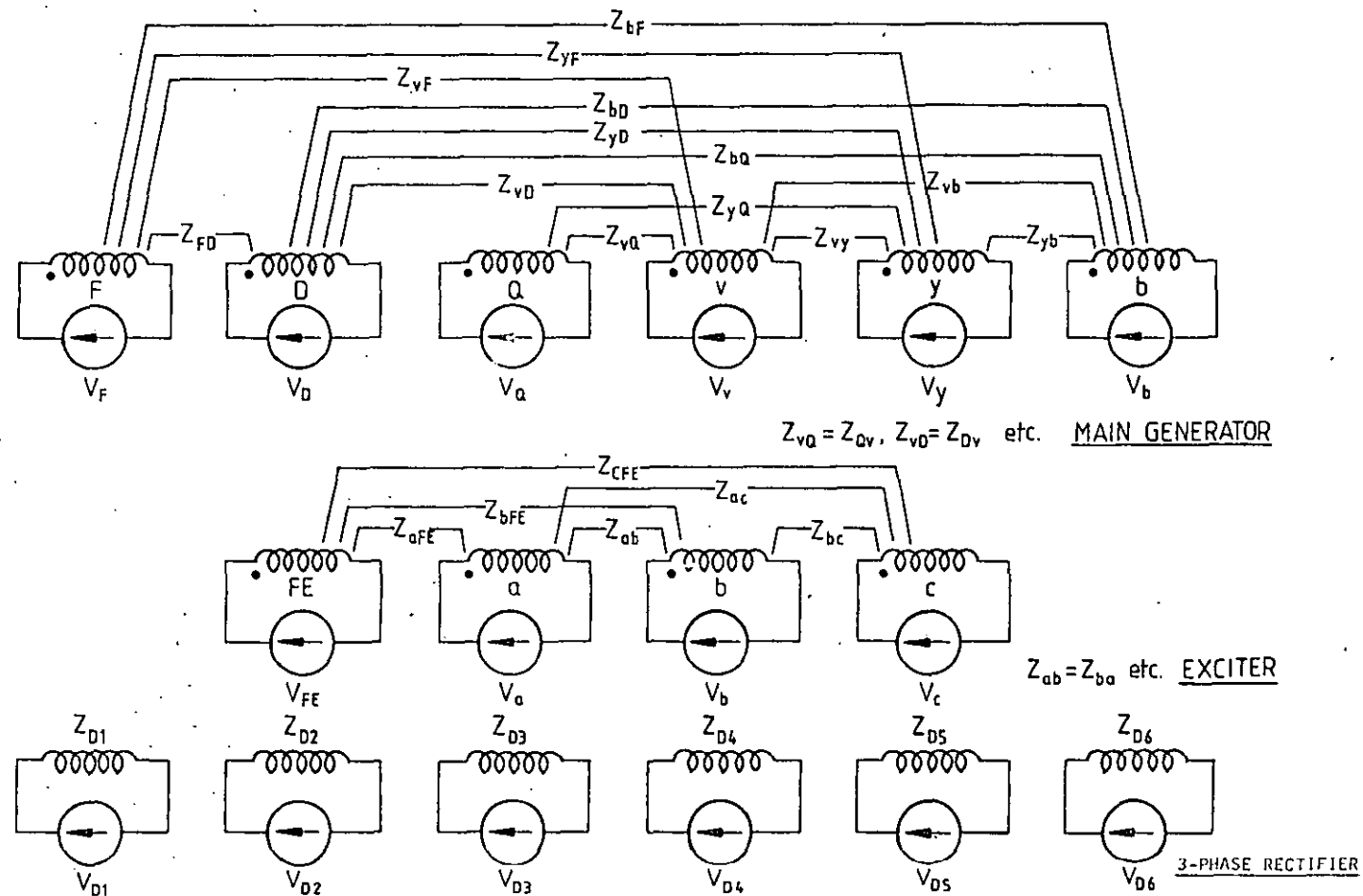


Figure 3.4

PRIMITIVE NETWORKS REPRESENTING EXCITER-RECTIFIER-GENERATOR SYSTEM

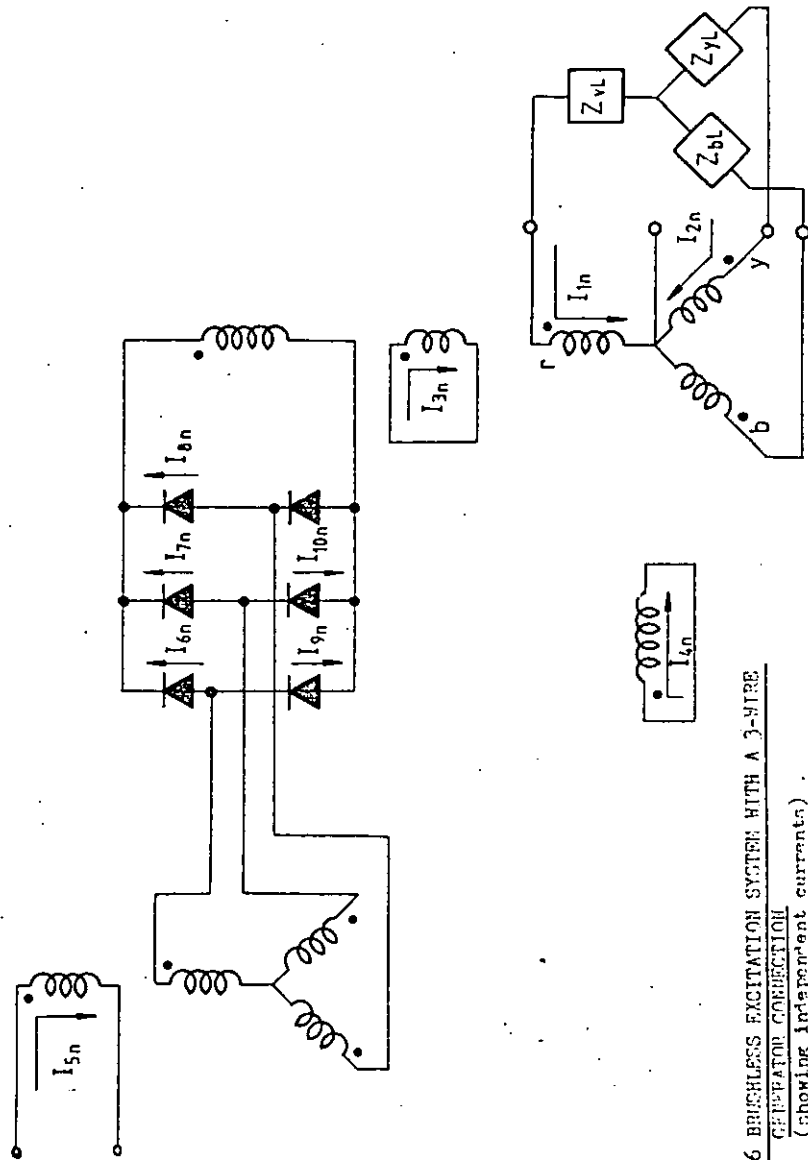


FIGURE 2.6 BRUSHLESS EXCITATION SYSTEM WITH A 3-WIRE
GENERATOR CORRECTION
(showing independent currents)

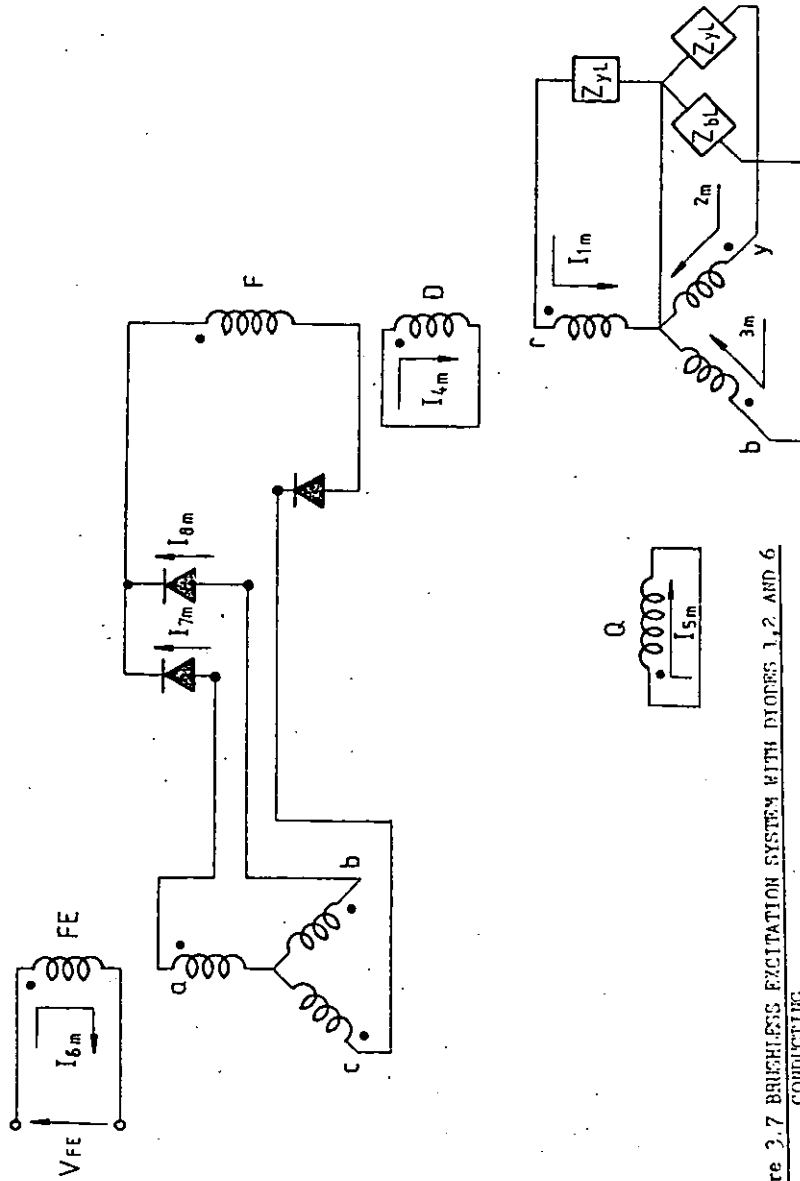


Figure 2.7 BRUSHLESS EXCITATION SYSTEM WITH DIODES 1, 2, AND 6 CONDUCTING

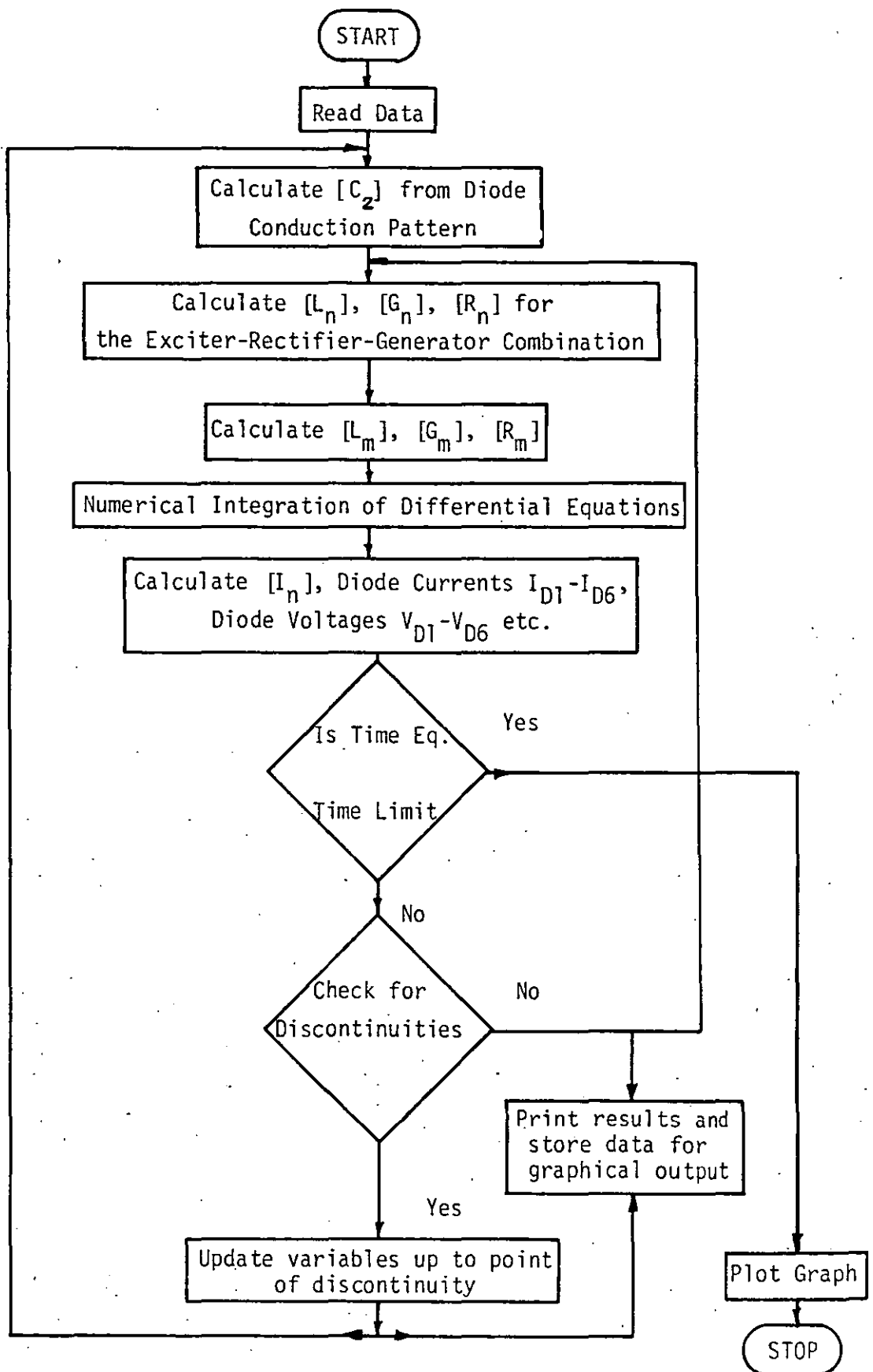
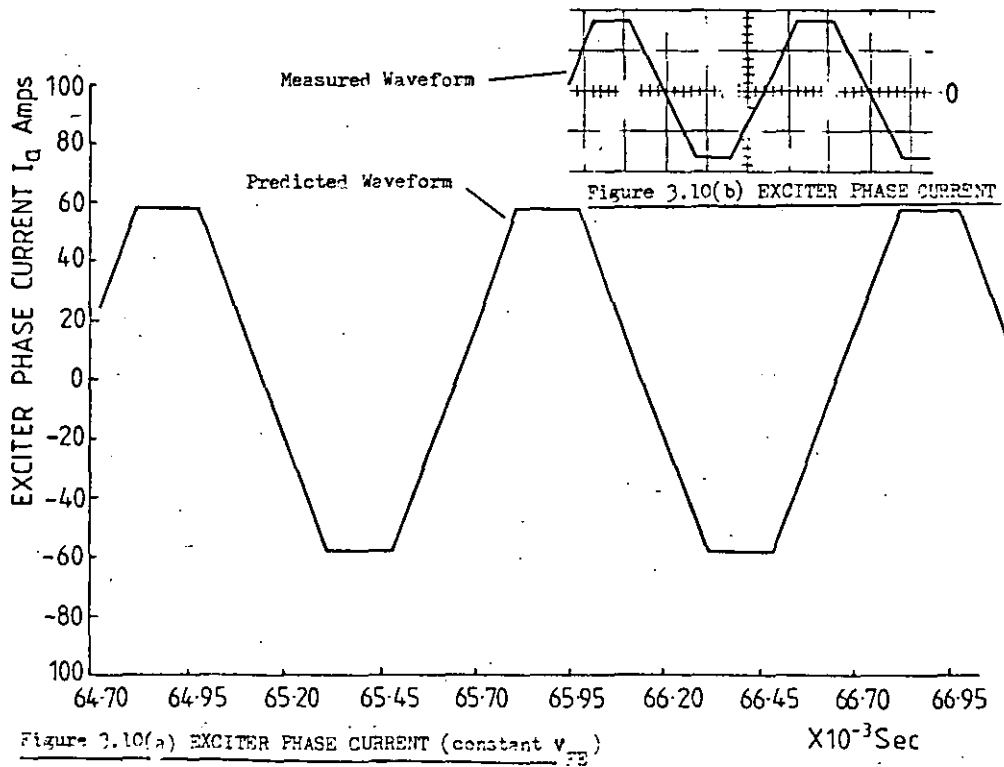
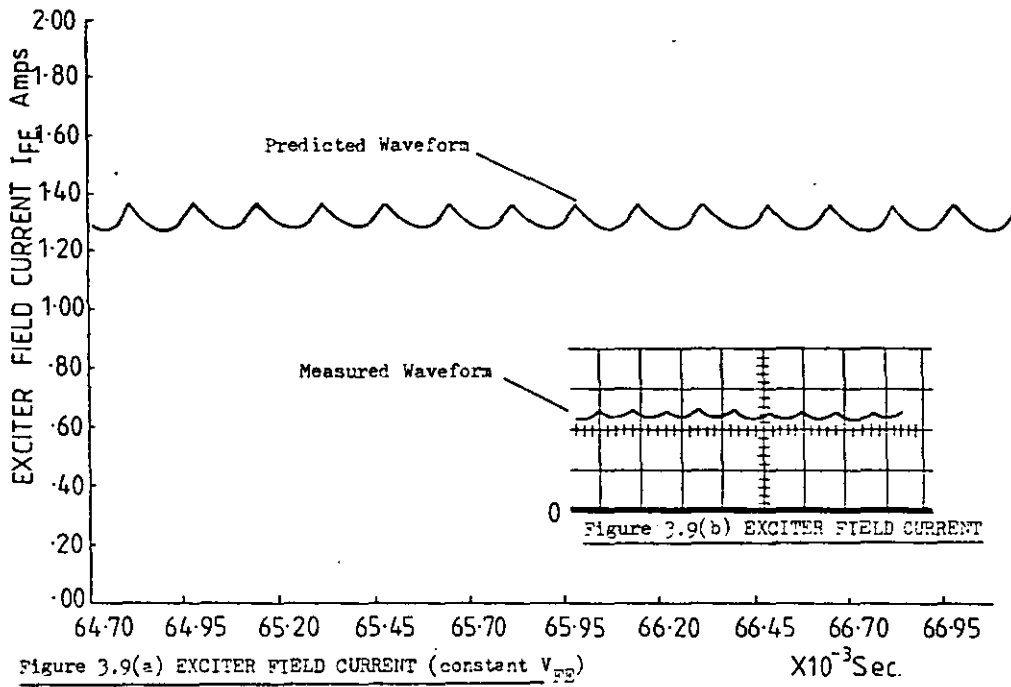
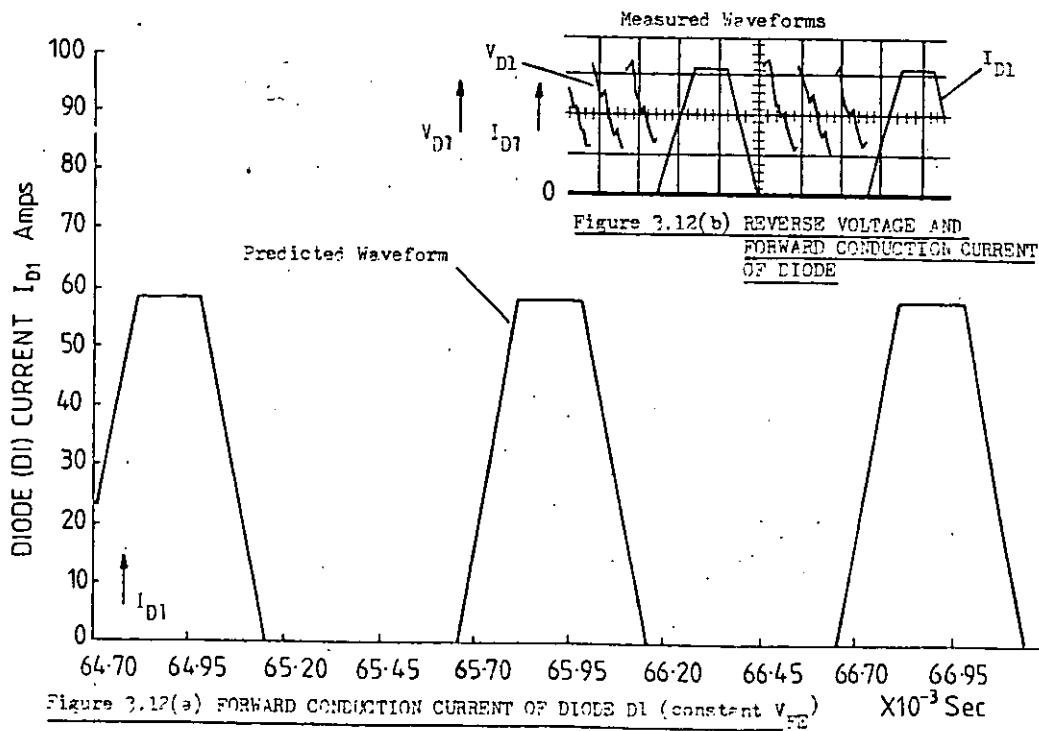
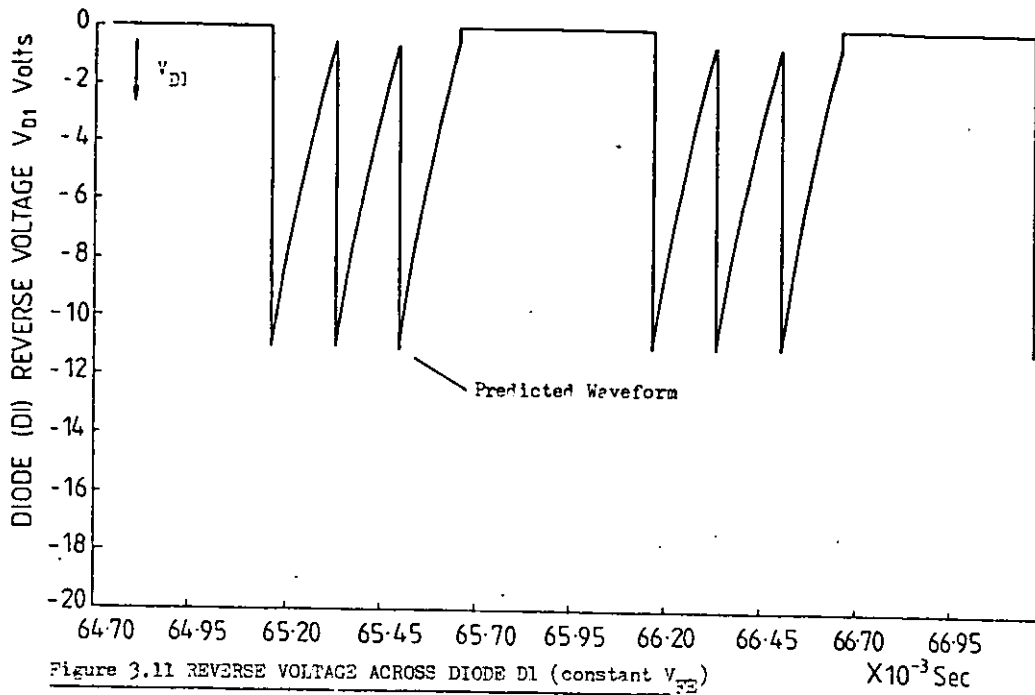
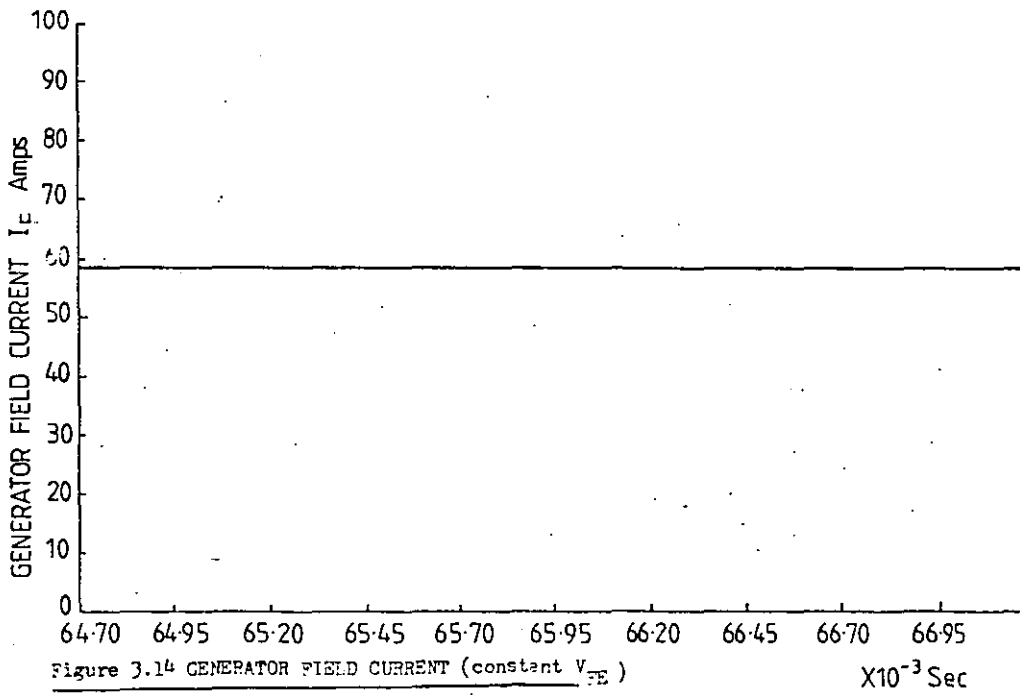
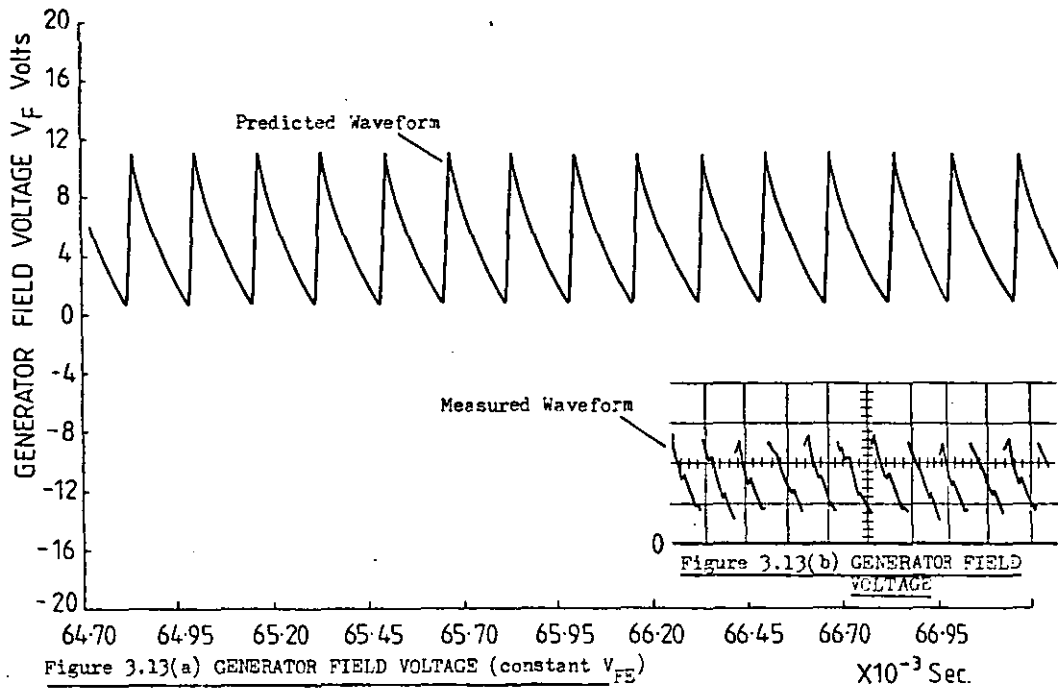


FIGURE 3.8 Exciter-Rectifier-Generator Computer Program Flow Diagram.







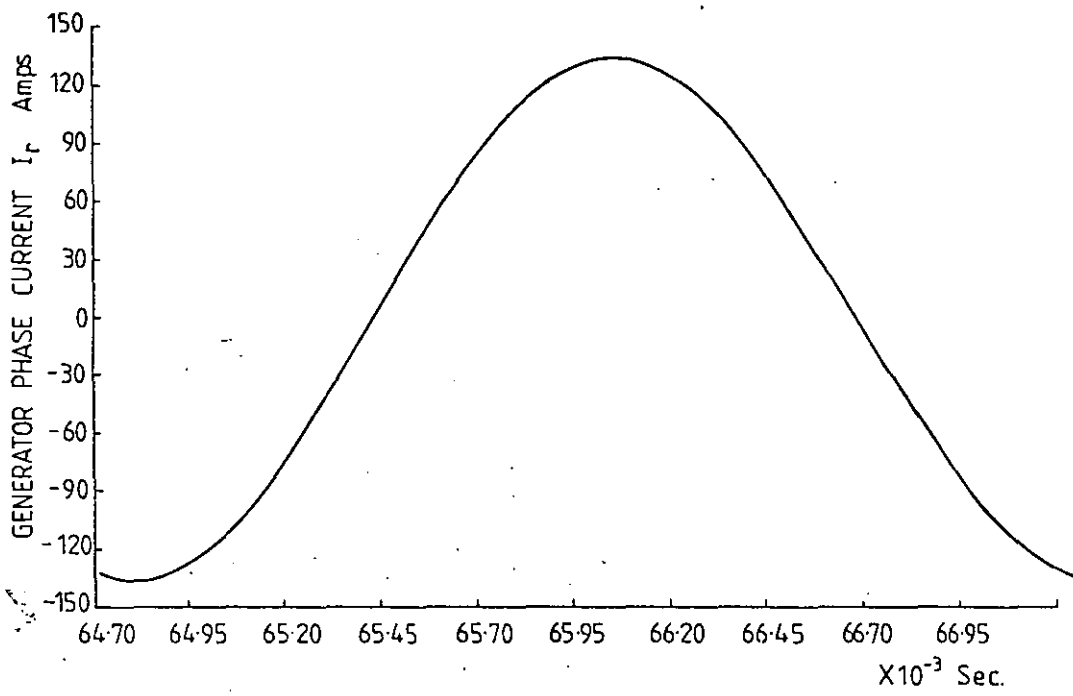


Figure 3.15 GENERATOR r-PHASE CURRENT (constant V_{FS})

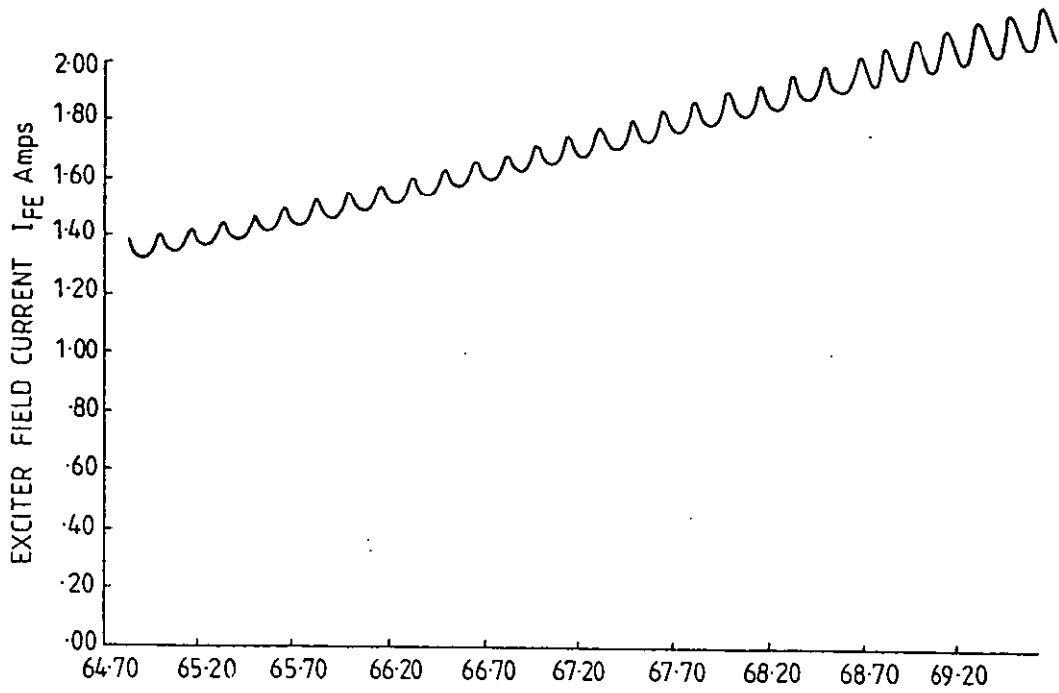


Figure 3.16 EXCITER FIELD CURRENT TRANSIENT PREDICTION FOR A
STEP INCREASE IN V_{FE} $\times 10^{-3}$ Sec.

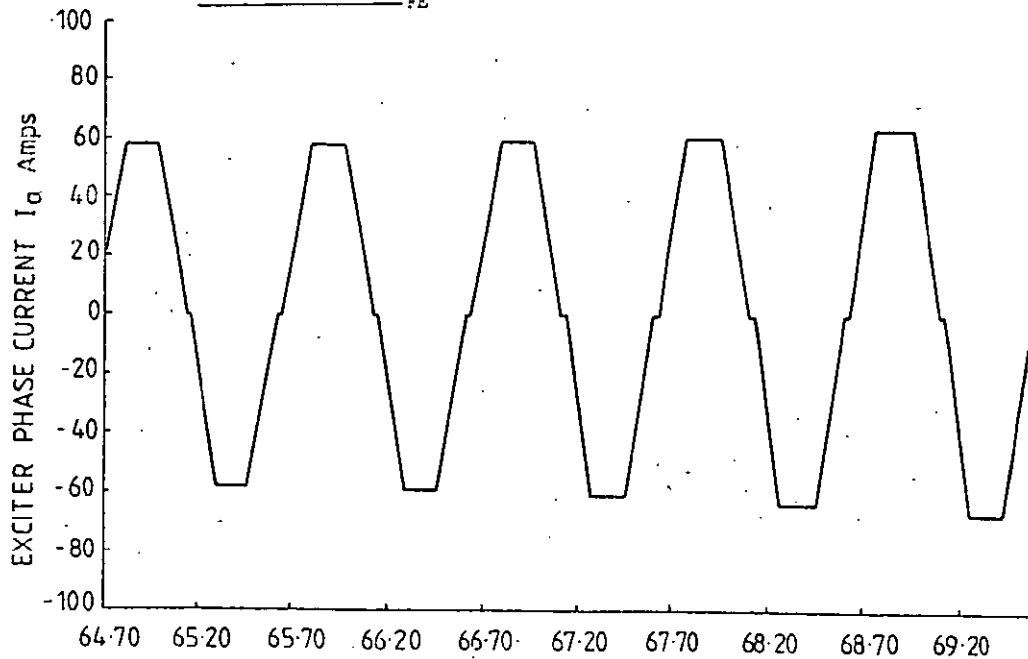


Figure 3.17 EXCITER PHASE CURRENT TRANSIENT PREDICTION FOR A
STEP INCREASE IN V_{FE} $\times 10^{-3}$ Sec.

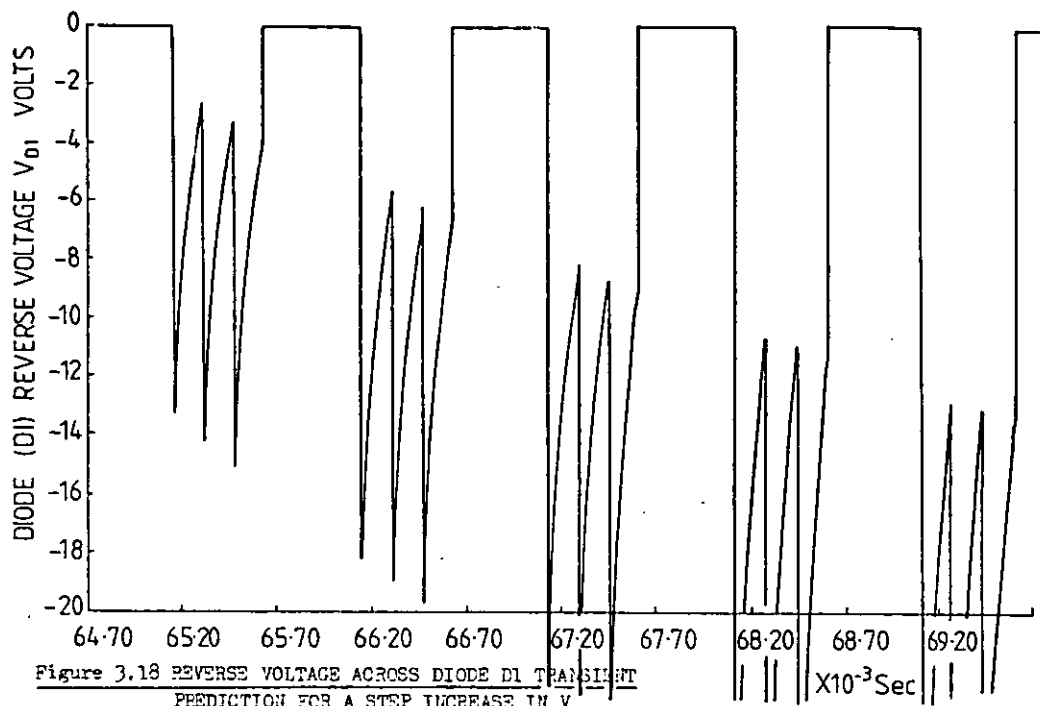


Figure 3.18 REVERSE VOLTAGE ACROSS DIODE D1 TRANSIENT
PREDICTION FOR A STEP INCREASE IN V_{FE}

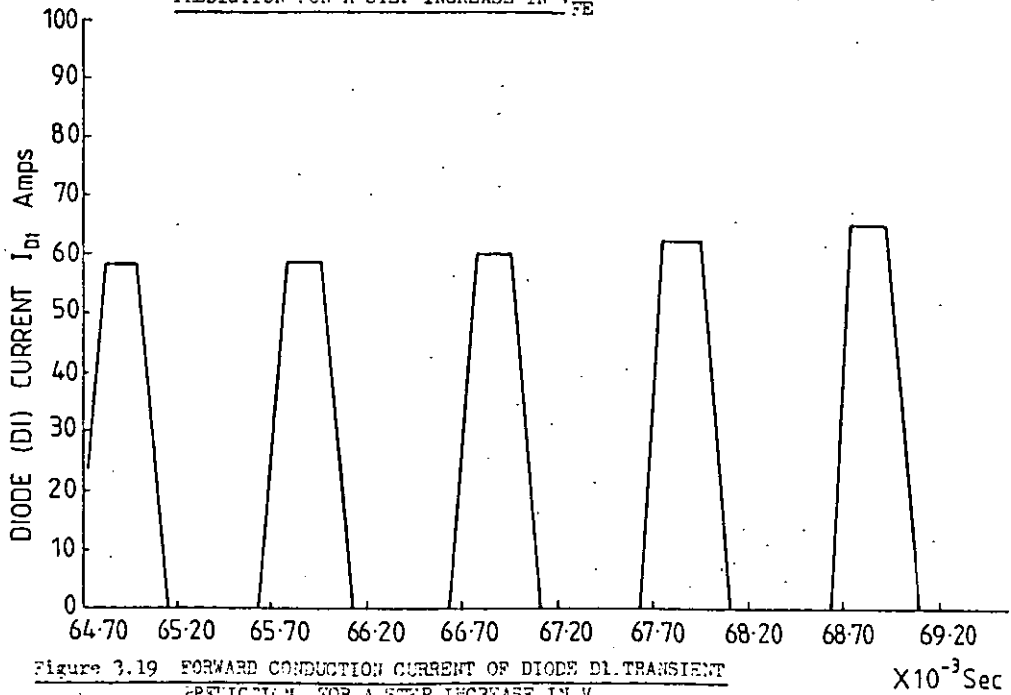


Figure 3.19 FORWARD CONDUCTION CURRENT OF DIODE D1 TRANSIENT
PREDICTION FOR A STEP INCREASE IN V_{FE}

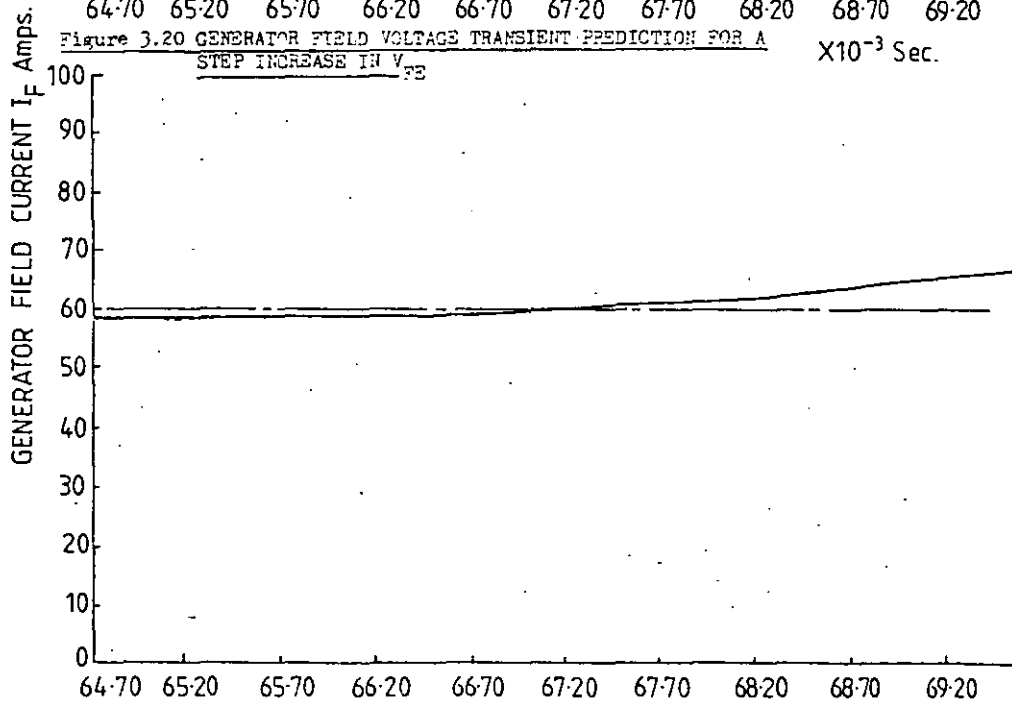
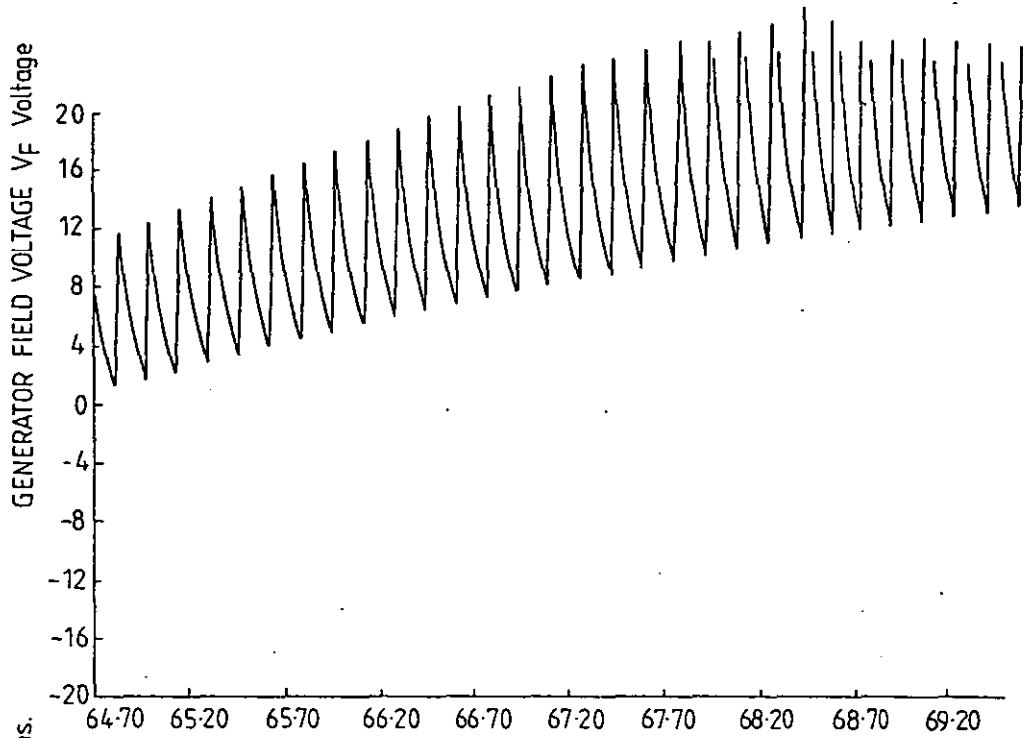


Figure 3.21 GENERATOR FIELD CURRENT TRANSIENT PREDICTION FOR A
STEP INCREASE IN V_{FE} $\times 10^{-3}$ Sec

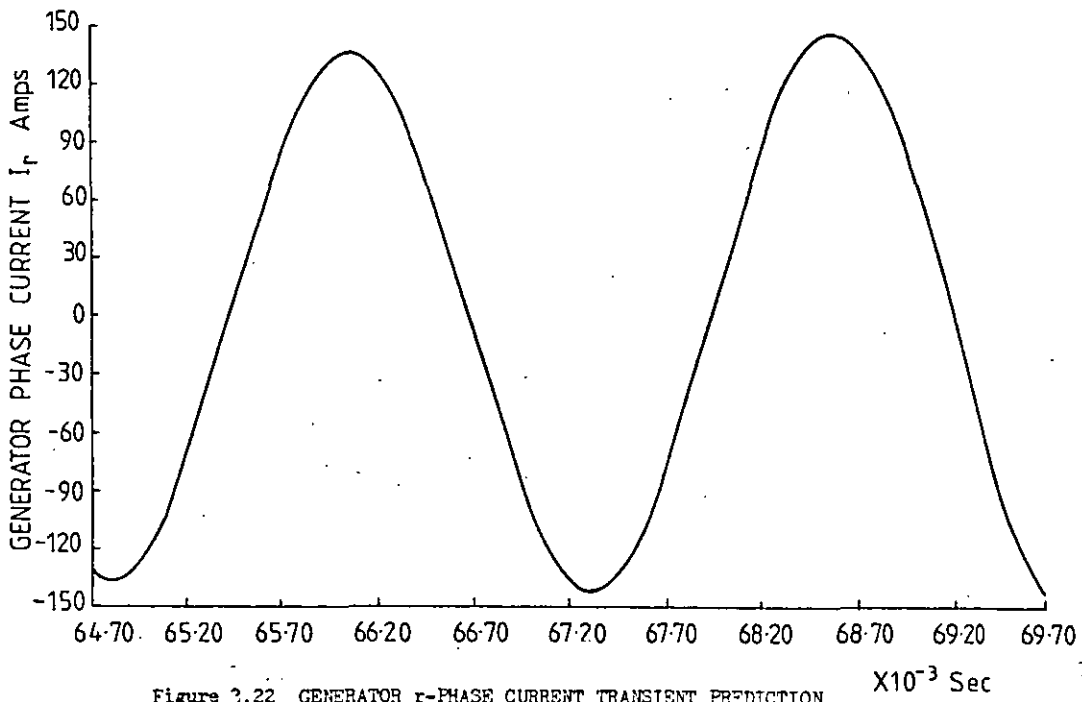


Figure 3.22 GENERATOR r-PHASE CURRENT TRANSIENT PREDICTION
FOR A STEP INCREASE IN V_{FE}

CHAPTER 4

MODELLING OF AN AUTOMATIC VOLTAGE REGULATOR

4.1 Introduction

An automatic voltage regulator (a.v.r) forms an important part of any electrical generating system and it is necessary that its performance can be accurately predicted when a model of the electrical system is obtained for system studies. This chapter describes two methods of modelling the a.v.r. used on aircraft power systems. The first of these is the state variable method based on the actual components used in the a.v.r, with the state variables being the voltages across any capacitors present in the circuit and the current through any inductors which may be present. The second method is a transfer function analysis, based on obtaining the transfer functions of the individual networks which form the a.v.r. and then representing the voltage regulator in block form⁴⁴ for subsequent analytical purposes.

Both models result in differential equations that can be solved on a digital computer using any suitable numerical integration method. Both the models were used for the transient analysis of the regulated generator unit described in Chapter 5.

4.2 Description of Automatic Voltage Regulator

The automatic voltage regulator designed for use with the 2130 generator unit is shown in Figure 4.1 in block diagram form, with the circuit diagram of the actual components being given in Figures 4.2 and 4.3. The exciter field voltage supply is obtained from the 3-phase full-wave rectified output of the permanent-magnet-generator pilot exciter.

The effective voltage applied to the exciter field winding is controlled by the power transistor Q1, which has a zener

diode ZDI across its terminals to prevent transient peak voltages from damaging the transistor as it switches from ON to OFF. The switching frequency and the ON to OFF time ratio of QI is controlled in turn by the automatic voltage regulator. The free-wheel diode D13 enables the exciter field current to continue to flow when transistor QI switches OFF. Capacitor C_6 is for smoothing purposes and inductor L_6 is to prevent the QI from effectively shortcircuiting the d.c. supply when it switches ON, as the diode D_{13} is not in its blocking state when QI is OFF.

Resistor R_1 in parallel with L_6 forms a path for the current in the inductor when QI switches OFF. Inductors L_4 and L_5 are for smoothing the effective voltage applied to the exciter field winding.

4.3 State Variable Analysis of Automatic Voltage Regulator

4.3.1 Voltage Sensing Circuit

The high-phase take-over circuit forming part of the voltage sensing circuit and shown in Figure 4.4(a), limits the maximum generator voltage to 125 V r.m.s. (line to neutral) under line-to-line or line-to-neutral or line-to-earth faults. For normal load conditions, the voltage sensing circuit shown in Figure 4.4(a) consisting of components R_{10} , R_{11} , R_{12} , C_{13} , C_{14} is operational, and the voltage V applied to this network at any instant is equal to the maximum (positive) voltage of the phases, depending on the values of V_A , V_B , V_C at that instant and assuming the diode volt drop to be negligible. Hence if $V_A > V_B$, $V_A > V_C$, the voltage applied to the voltage sensing circuit V equals V_A . (Diode D_1 is in forward conduction and diodes D_2 and D_3 are reverse biased). The voltage sensing circuit can be represented as in Figure 4.4(b) for which

$$-R_{10} I_{10} - V_{13} + V = 0 \quad 4.1 \text{ a}$$

$$-C_{13} \dot{V}_{13} - I_{11} + I_{10} = 0 \quad 4.1 \text{ b}$$

where $\dot{V}_{13} = \frac{d}{dt} (V_{13})$

$$- I_{11} R_{11} - I_{12} R_{12} + V_{13} = 0 \text{ (i.e. } - I_{11} R_{11} - V_{14} + V_{13} = 0) \quad 4.1c$$

$$- C_{14} \dot{V}_{14} - I_{12} + I_{11} = 0 \quad 4.1d$$

$$- V_{14} + R_{12} I_{12} = 0 \quad 4.1e$$

On this basis, the circuit can be represented by the flow diagram of Figure 4.4(c), which is particularly useful when analysing the circuit with the aid of an analogue computer. The differential equations describing the behaviour of the circuit are, by inspection

$$\begin{bmatrix} \dot{V}_{13} \\ \dot{V}_{14} \end{bmatrix} = \begin{bmatrix} -(T_8 + T_9) & + T_9 \\ T_{10} & - T_{11} \end{bmatrix} \begin{bmatrix} V_{13} \\ V_{14} \end{bmatrix} + \begin{bmatrix} T_{12} \\ 0 \end{bmatrix} [V] \quad 4.2$$

where:

$$T_8 = \frac{1}{R_{10} C_{13}} \quad 4.3$$

$$T_9 = \frac{1}{R_{11} C_{13}} \quad 4.4$$

$$T_{10} = \frac{1}{R_{11} C_{14}} \quad 4.5$$

$$T_{11} = \frac{1}{R_{12} C_{14}} + T_{10} \quad 4.6$$

$$T_{12} = \frac{1}{R_{10} C_{13}} \quad 4.7$$

4.3.2 Amplifier Circuit of A.V.R.

The performance of the a.v.r. amplifier stages can be determined by considering Figure 4.5(a), where only the power stages, the output voltage of the voltage sensing circuit and the reference voltage are considered. The operational amplifier A₁ is of the inverting type, so that when $V_X < V_Y$, $V_A = +5V$, and when $V_X > V_Y$, $V_A = 0V$. The operating sequence is as follows:

When $V_X < V_Y$, $V_A = +5V$, Q₁ switches ON which switches ON Q₂, Q₃ and hence Q_I, the power transistor. When $V_X > V_Y$, $V_A = 0V$, Q₁ switches OFF, which in turn switches OFF Q₂ and Q₃. Q₄ switches ON and hence Q_I is switched OFF. The switching frequency and the ON/OFF time ratio of transistor Q_I both depend on the voltages V_X and V_Y .

The output voltage V_{14} , of the voltage sensing circuit is connected to the (-) input terminal of the operational amplifier A₁ as shown in Figure 4.5(a) via an emitter follower circuit and resistor R_A. Similarly the reference voltage V_R, which is the voltage across zener diode Z_R is connected to the (-) input terminal of the operational amplifier A₁ as shown in Figure 4.5(a) via an emitter follower circuit and resistor R_B. The advantages of the emitter follower circuits are high input impedance, near unity gain, low output impedance and no phase shift, which eliminates any interactive effect of connecting the voltage sensing circuit output voltage V_{14} , the reference voltage output V_R and the negative feedback voltage to the (-) summing terminal of the operational amplifier on the voltage sensing circuit or the reference voltage circuit. The output voltage V_{14} of the voltage sensing circuit and the reference voltage V_R can be represented as a voltage source V_{E1}, with the resistor R₁ in series as shown in Figure 4.5(b)

With $R_A = R_B = 10 \text{ K}\Omega$

$$\text{then } V_{E1} = \frac{V_{14} + V_R}{2}$$

and $R_1 = 5 \text{ K}\Omega$.

The reverse voltage drop across the zener diode Z_R is 6.2 V. Therefore the reference voltage V_R is -6.2 V. The output from the voltage sensing circuit (V_{14}) can be approximate to a d.c. voltage plus a 3rd-harmonic of the generator frequency introduced by the half-wave rectifier. Thus $V_{14} = V_1 + V_2 \sin(3\omega t)$. V_{14} is adjusted by the resistance potentiometer SIT 1 shown in Figure 4.4(a), depending on the required output voltage of the generator. The approximate values of V_1 and V_2 obtained from the analysis of the voltage sensing circuit of Figure 4.4(b) with the rated generator voltage are:

$$V_1 = 6.3 \text{ V}$$

and

$$V_2 = 0.20 \text{ V}$$

Therefore

$$\begin{aligned} V_{E1} &= \frac{-6.2 + 6.3 + 0.20 \sin(3\omega t)}{2} \\ &= 0.05 + 0.10 \sin(3\omega t) \end{aligned} \quad 4.8$$

During transients, on application or rejection of load, the feedback circuits shown in Figure 4.3 affect the voltage V_{E1} and therefore equation 4.8 for V_{E1} does not apply. For transient analysis, it is necessary to solve the differential equations derived for the system given in Sections 4.3.1, 4.3.3 and 4.4.2. Under steady state conditions, equation 4.8 for V_{E1} apply and the voltage applied to the exciter field winding is shown in Figure 4.5(c). The time delay between the operational amplifier A1 and the a.v.r output V_{FE} is negligibly small when compared with the time constants of the feedback circuits and also those of the exciter and the generator. The operational amplifier A1 and the gain stages of the a.v.r. formed by transistors Q_1 , Q_2 , Q_3 , Q_4 and QI can be represented by one amplifier (A), shown in Figure 4.6(a), whose output depends on V_X and V_Y .

4.3.3 Feedback Circuit of A.V.R.

The feedback circuit of the a.v.r. consists of a 'Totem Pole Pair' Q_5 and Q_6 transistor circuit feeding an RC network, as shown in Figure 4.3. The voltage applied to the RC network depends on the

switching frequency and the ON/OFF time ratio of the power transistor Q1. When Q1 is ON, Q6 switches ON and the RC network is effectively connected to the d.c. supply (minus the volt drop in the zener diode ZD2 and the volt drop across Q6). When Q1 switches OFF, Q6 switches OFF and Q5 switches ON, and the voltage applied to the RC network is effectively zero. Since the switching of the power transistor determines the voltage applied to the exciter field winding, the voltage applied to the RC-feedback network is also approximately of the same magnitude, as the forward volt drop in the zener diode ZD1 is only some 5% of the d.c. voltage. The performance of the feedback circuit can be determined by considering the simplified circuit shown in Figure 4.6(a), where the amplifier A represents the switching action of the operational amplifier A_1 and its switching power amplifier stages. If the d.c. supply voltage is V_{DC} , the performance of the amplifier A can be represented by

$$V_X < V_Y, \quad V_O = V_{DC} \quad 4.9(a)$$

$$V_X > V_Y, \quad V_O = 0 \quad 4.9(b)$$

Figure 4.6(a) can be further simplified for analytical purposes to that given in Figure 4.6(b). The equations for the feedback circuit given in Figure 4.6(b) are

$$-R_8 I_8 - V_2 - V_7 + V_{E1} = 0 \quad 4.10(a)$$

$$-C_2 \dot{V}_2 + I_8 = 0 \quad 4.10(b)$$

$$-C_6 \dot{V}_7 - \left(\frac{1}{R_9}\right) V_7 - I_4 + I_8 = 0 \quad 4.10(c)$$

$$-R_4 I_4 - V_O + V_7 = 0 \quad 4.10(d)$$

The feedback network and the amplifier switching actions can be represented by the flow diagram of Figure 4.6(c), from which the differential equations for the feedback circuit follow by inspection as

$$\begin{array}{|c|} \hline \dot{V}_2 \\ \hline \dot{V}_7 \\ \hline \end{array} = \begin{array}{|c|c|} \hline -T_1 & -T_2 \\ \hline -T_3 & -T_4 \\ \hline \end{array} \begin{array}{|c|} \hline V_2 \\ \hline V_7 \\ \hline \end{array} + \begin{array}{|c|c|} \hline T_5 & 0 \\ \hline T_6 & T_7 \\ \hline \end{array} \begin{array}{|c|} \hline V_{E1} \\ \hline V_0 \\ \hline \end{array} \quad 4.11$$

$$\text{where } T_1 = T_2 = T_5 = \frac{1}{C_2 R_8} \quad 4.12$$

$$T_3 = T_6 = \frac{1}{C_7 R_8} \quad 4.13$$

$$T_4 = \frac{1}{C_7} \left(\frac{1}{R_4} + \frac{1}{R_9} + \frac{1}{R_8} \right) \quad 4.14$$

$$T_7 = \frac{1}{C_7 R_4} \quad 4.15$$

The above differential equations can be solved by a numerical integration method, with the voltage V_0 being obtained at each step of integration by calculating V_X , V_Y and $V_Z = V_X - V_Y$.

$$\text{If } V_Z < 0, \quad V_0 = V_{DC} \quad 4.16a$$

$$\text{If } V_Z > 0, \quad V_0 = 0 \quad 4.16b$$

4.3.4 Computation of Transient Response of A.V.R. on a Digital Computer

A computer program for obtaining the transient response of the a.v.r. is given in Appendix A7. As the output voltage (V_{FE}) of the a.v.r. depends on the absolute value of $(V_X - V_Y)$ it is necessary to use a small steplength to ensure an accurate response characteristic.

4.4 Transfer Function Analysis of Automatic Voltage Regulator

The I.E.E.E. Committee Report "Computer Representation of Excitation Systems"⁴⁵ lists a number of different types of excitation systems in use today. The recommended computer representation of a rotating rectifier system (brushless) is given in Figure 4.7. The most difficult part in this representation is the determination of the effective gain of the a.v.r., as this is a nonlinear function of the error signal ($V_X - V_Y$) input to the power amplifier stage. Having determined the effective gain of the power amplifier stages either by measurement or by the state variable analysis discussed in Appendix A7, it is possible to represent the a.v.r. in terms of transfer functions for each of its constituent 'blocks'.

4.4.1 Transfer Function Representation of Voltage Sensing Circuit

It is shown in Appendix A8 that for the voltage sensing circuit shown in Figure 4.4(a)

$$\frac{V_S}{V_T} = \frac{K_R}{(1 + sT_{R1})(1 + sT_{R2})} \quad 4.17$$

where:

$$K_R = 4.0475 \times 10^{-2}$$

$$T_{R1} T_{R2} = 0.64754 \times 10^{-6} \text{ s}^2$$

$$T_{R1} + T_{R2} = 1.76631 \times 10^{-3} \text{ s}$$

$$\frac{1}{T_{R1} T_{R2}} = 1.544306 \times 10^6 \text{ s}^{-2}$$

$$\frac{T_{R1} + T_{R2}}{T_{R1} T_{R2}} = 2.72772 \times 10^3 \text{ s}^{-1}$$

in which

V_s is the *mean* value of the output voltage of the voltage sensing circuit.

V_T is the *peak* line to neutral voltage of the generator under balanced load conditions.

4.4.2 Transfer Function Representation of A.V.R. Feedback Circuits

It is shown in Appendix A8 that the transfer function for the negative feedback path is

$$\frac{V_{F1}}{V_{FE}} = \frac{s K_F}{(1 + sT_{F1})(1 + sT_{F2})} \quad 4.18$$

where:

$$K_F = 0.5 \times 10^{-3}$$

$$T_{F1} + T_{F2} = 26.9 \times 10^{-3} \quad s$$

$$T_{F1} T_{F2} = 145.7 \times 10^{-6} \quad s^2$$

$$\frac{1}{T_{F1} T_{F2}} = 6.86 \times 10^{-3} \quad s^{-2}$$

$$\frac{T_{F1} + T_{F2}}{T_{F1} T_{F2}} = 184.63 \times 10^{-6} \quad s^{-1}$$

It is shown in Appendix A8 that the transfer function for the positive feedback path is

$$\frac{V_{F2}}{V_{FE}} = \frac{K_1 (1 + sT_{A1})}{(1 + sT_{F1})(1 + sT_{F2})} \quad 4.19$$

\dot{V}_S
\dot{V}_S
\dot{V}_{F1}
\dot{V}_{F1}
\dot{V}_{F2}
\dot{V}_{F2}

=

0	1	0	0	0	0
$-\frac{1}{T_{R1}T_{R2}}$	$-\frac{(T_{R1}+T_{R2})}{T_{R1}T_{R2}}$	0	0	0	0
0	0	0	1	0	0
0	0	$-\frac{1}{T_{F1}T_{F2}}$	$-\frac{(T_{F1}+T_{F2})}{T_{F1}T_{F2}}$	0	0
0	0	0	0	0	1
0	0	0	0	$-\frac{1}{T_{F1}T_{F2}}$	$-\frac{(T_{F1}+T_{F2})}{T_{F1}T_{F2}}$

V_S
V_S
V_{F1}
V_{F1}
V_{F2}
V_{F2}

+

0	0	0
0	0	$\frac{K_R}{T_{R1}T_{R2}}$
0	0	0
0	$\frac{K_F}{T_{F1}T_{F2}}$	0
0	0	0
$\frac{K_1}{T_{F1}T_{F2}}$	$\frac{K_1 T_{A1}}{T_{F1}T_{F2}}$	0

V_{FE}
V_{FE}
V_T

97

i.e. $[pX] = [A][X] + [B][Y]$

where:

$$K_1 = 1.08393 \times 10^{-3}$$

$$T_{A1} = 15.0 \times 10^{-3} \quad s$$

$$\frac{K_1}{T_{F1} T_{F2}} = 7.4395 \quad s^{-2}$$

$$\frac{K_1 T_{A1}}{T_{F1} T_{F2}} = 111.592 \times 10^{-3} \quad s^{-1}$$

The computer representation of the a.v.r. used with the 2130 generator is shown in Figure 4.1. A fall in the generator terminal voltage results in the error signal V_{E1} becoming more negative and hence in an increase in the output voltage of the amplifier applied to the exciter field winding. Having obtained all the required transfer functions describing the behaviour of the a.v.r., the differential equations for solution by use of a digital computer are obtained as in equation 4.20.

Additional equations which are required to be solved together with the differential equations 4.20 are

$$V_{E2} = \frac{V_s + V_{REF}(-)}{2} + V_{F1} - V_{F2} \quad 4.21$$

$$\dot{V}_{E2} = \frac{\dot{V}_s}{2} + \dot{V}_{F1} - \dot{V}_{F2} \quad 4.22$$

$$V_{FE} = \frac{V_{DC}}{\pi} \left[\frac{\pi}{2} - \text{Atan} \left(\frac{V_{E2}}{A} \right) \right] \quad 4.23$$

$$\dot{V}_{FE} = \frac{V_{DC}}{\pi} \cdot A \cdot \dot{V}_{E2} \cdot \left[\frac{1}{A^2 + V_{E2}^2} \right] \quad 4.24$$

Equations 4.21 to 4.24 are derived in Appendix A7

Equation 4.21 gives the error signal V_{E2} , which is input to the nonlinear power amplifier, as shown in Figure 4.1. The output voltage V_{FE} of the nonlinear power amplifier as a function of V_{E2} is given by equation 4.23.

It was found from the solution of the state variable model differential equations that the size of the time step required to maintain the accuracy in the output voltage V_0 , due to switching action of amplifier A, was of the order of 2×10^{-5} sec. This is approximately 40 steps per cycle of the 3rd-harmonic of generator frequency. The time step required for the same accuracy in prediction of V_0 using the transfer function model differential equations is of the order of 1×10^{-4} sec, which is 25 steps per cycle of generator frequency. This difference in time steps required is because the state variable model calculates absolute values of ON and OFF time of the a.v.r. output, while the transfer function model calculates mean voltage output of the a.v.r. as given by equation 4.23.

The advantage of using a transfer function computer representation of the a.v.r. over the state variable method is that the time step required for numerical integration is increased from about 2.0×10^{-5} s to 1×10^{-4} s, resulting in a reduction of computing time by a factor of 5. This is important when the a.v.r. exciter and the generator differential equations are solved together, to obtain the transient response following the application or rejection of load. To study unbalanced load conditions, it is necessary to use a state variable representation of the a.v.r., as this takes into account variations of all the generator terminal voltages at every instant of time. The state variable and transfer function models of the a.v.r. were used for the transient analysis of the regulated generator unit described in Chapter 5.

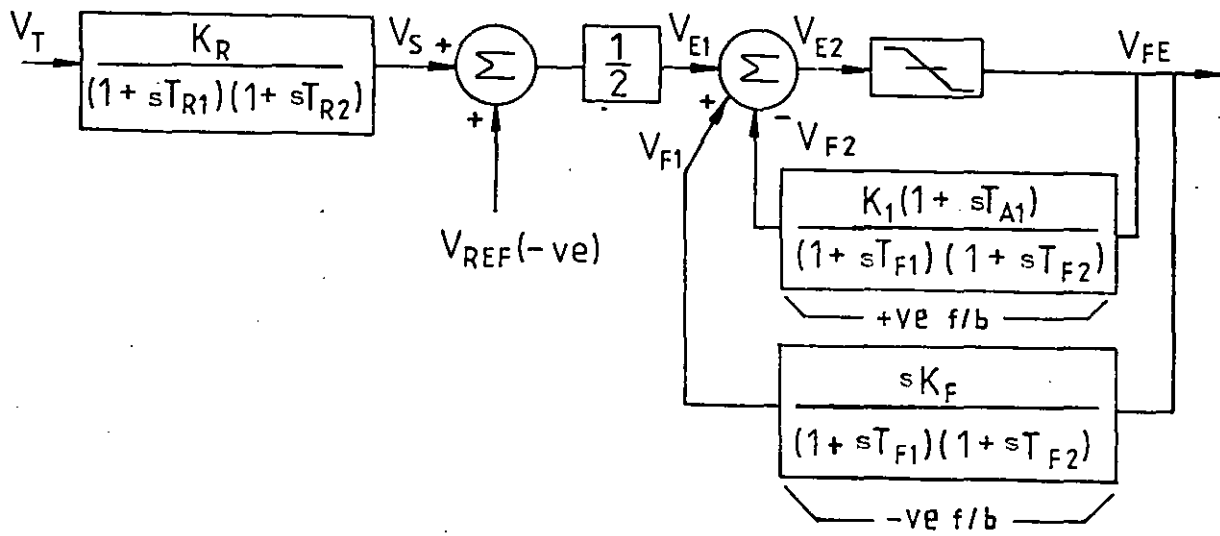


Figure 4.1 BLOCK DIAGRAM REPRESENTATION OF AUTOMATIC VOLTAGE REGULATOR USED WITH 2130 GENERATOR UNIT

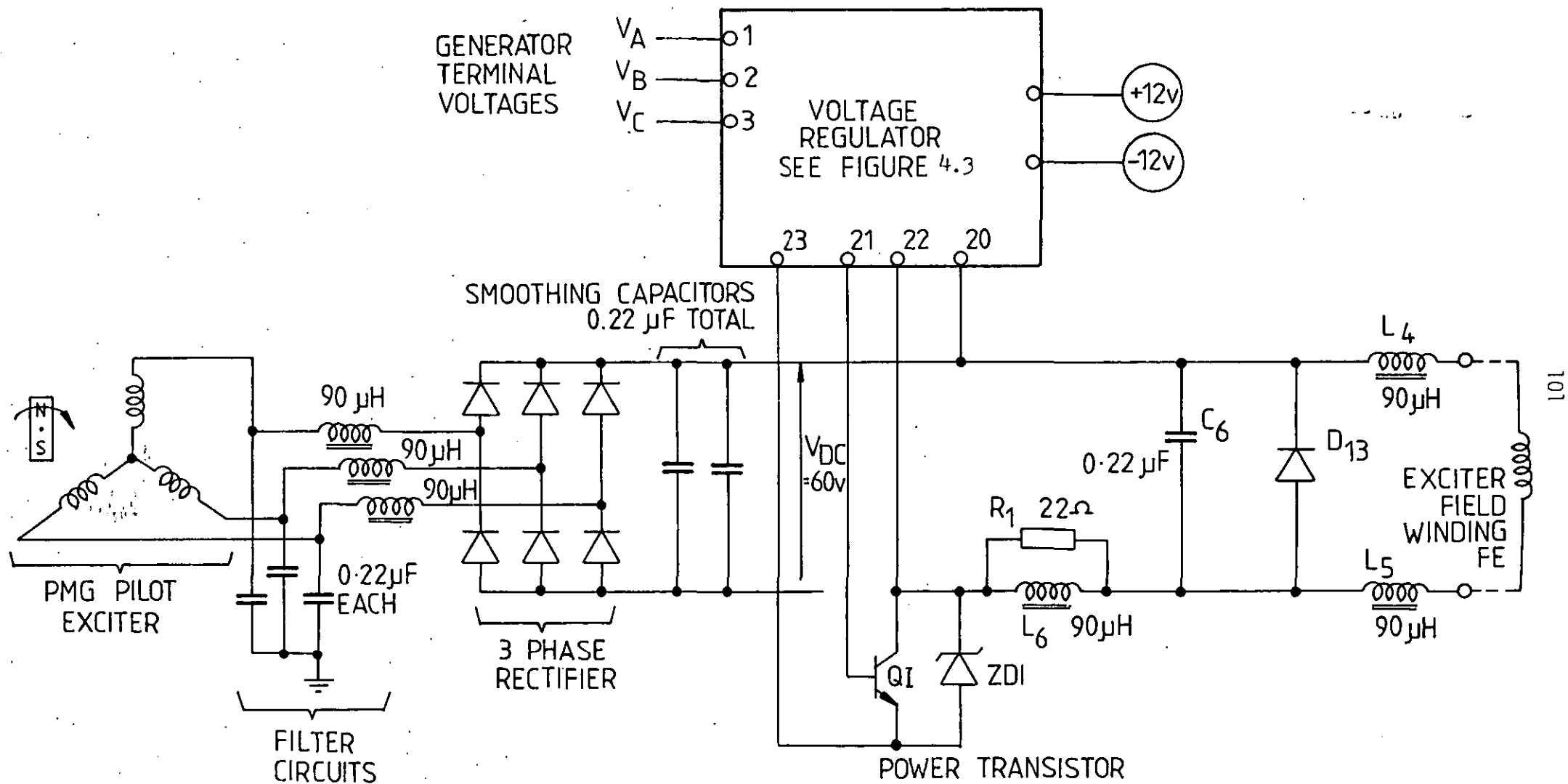


Figure 4.2 CIRCUIT DIAGRAM OF THE AUTOMATIC VOLTAGE REGULATOR, PERMANENT MAGNET GENERATOR AND EXCITER FIELD WINDING CONNECTION

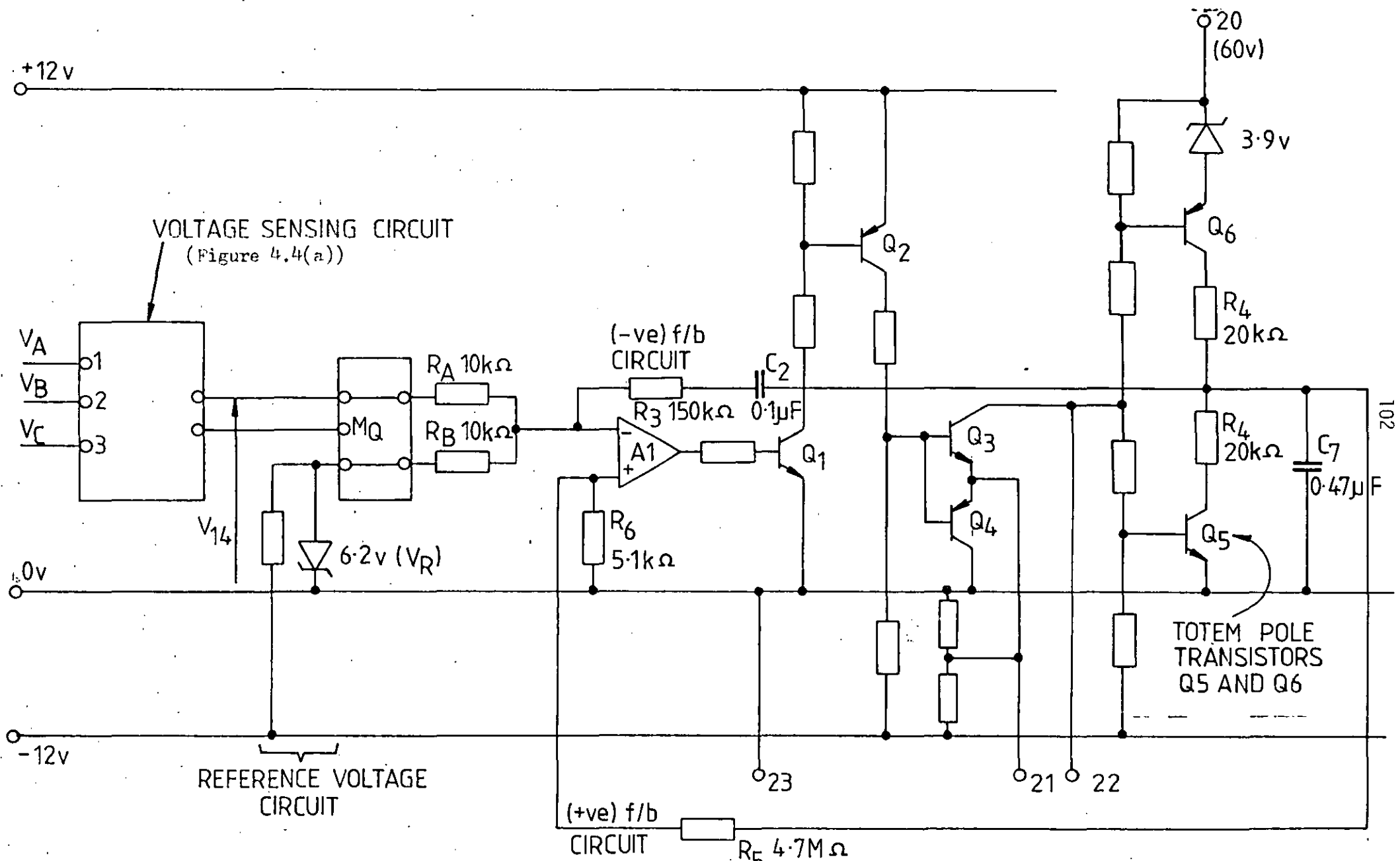


Figure 4.3 CIRCUIT DIAGRAM OF THE AUTOMATIC VOLTAGE REGULATOR (connection to the power stage shown in figure 4.2)

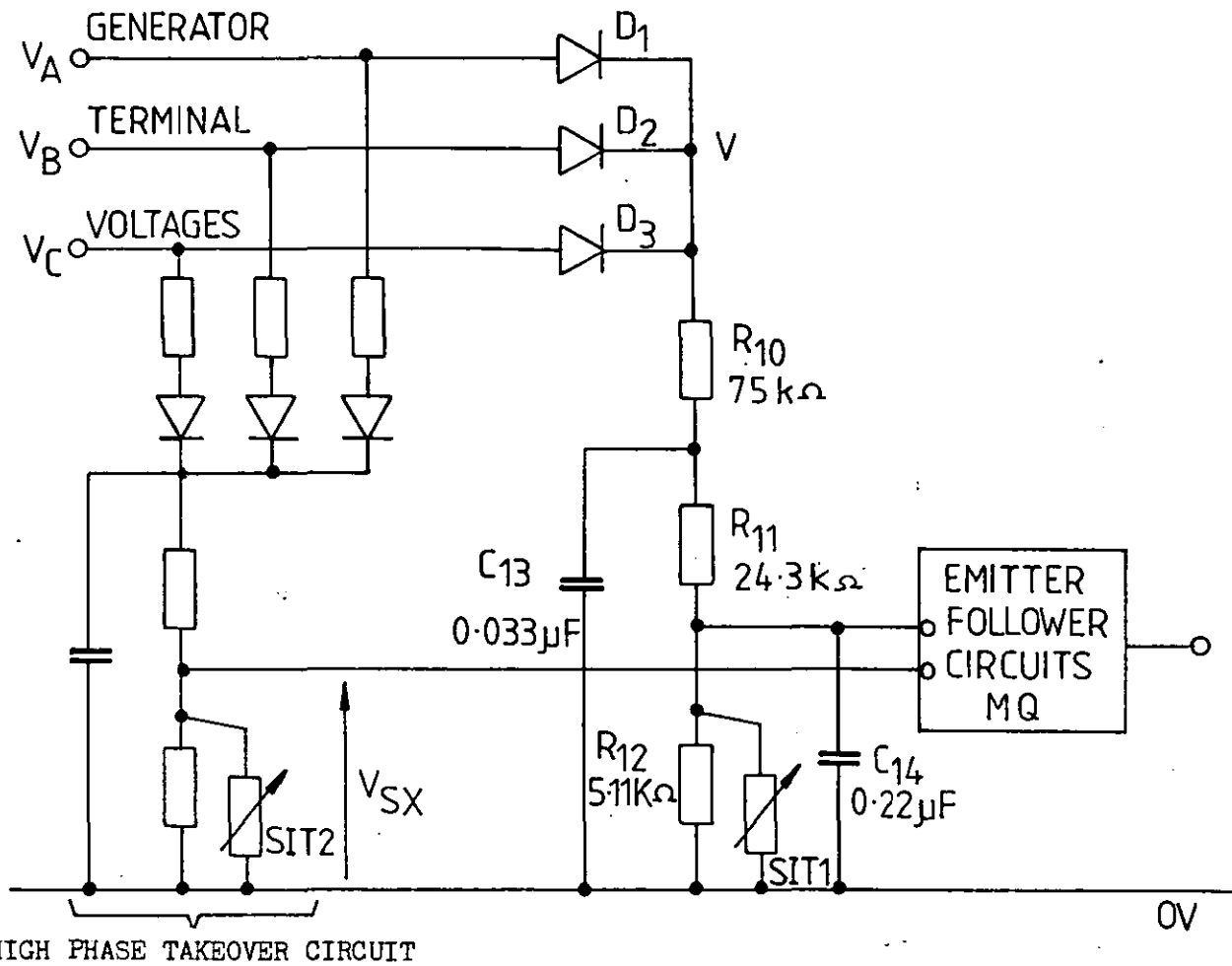


Figure 4.4(a) VOLTAGE SENSING CIRCUIT OF AUTOMATIC VOLTAGE REGULATOR

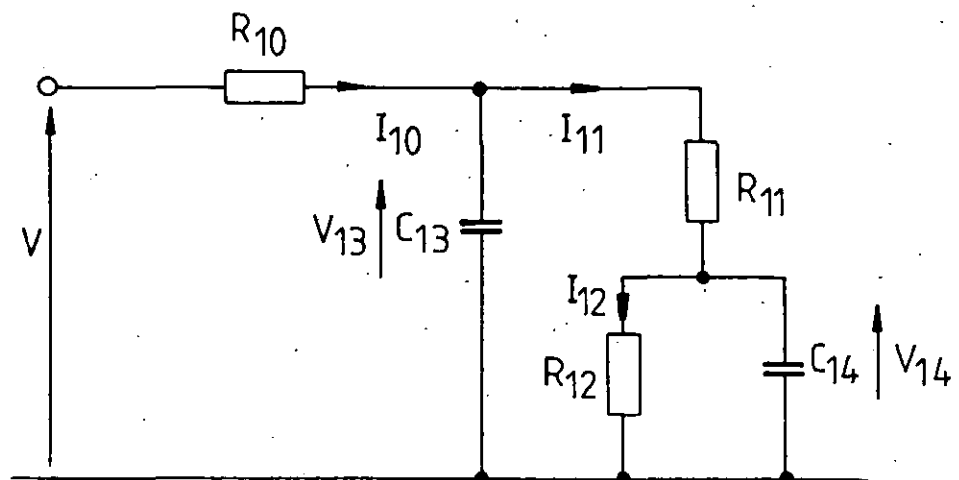


Figure 4.4(b) THE VOLTAGE SENSING CIRCUIT SHOWING INDEPENDENT CURRENTS AND STATE VARIABLES

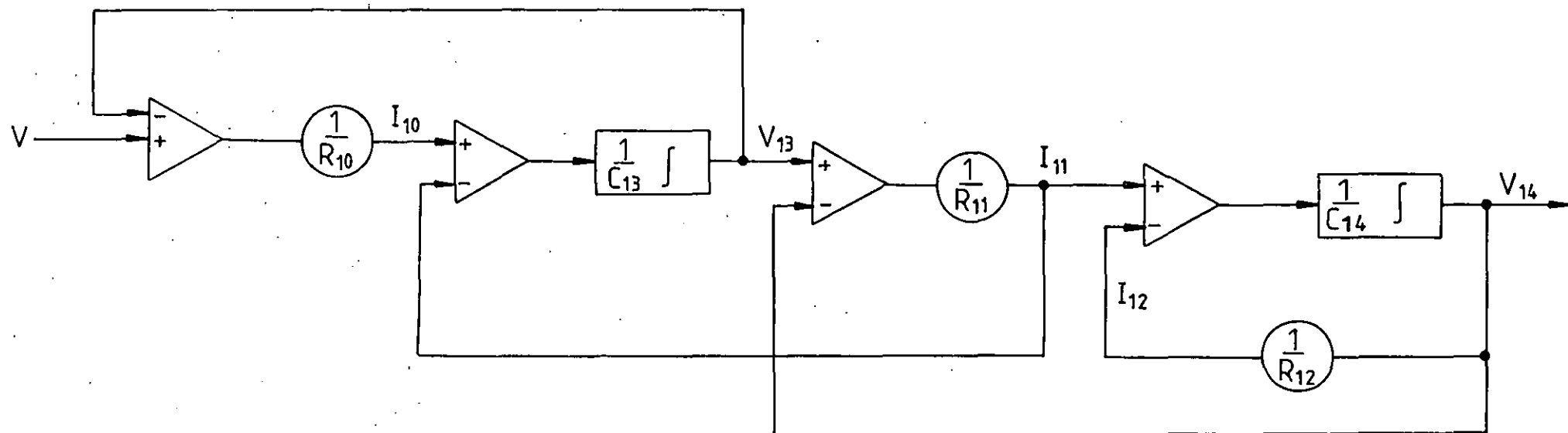


Figure 4.4(c) VOLTAGE SENSING CIRCUIT FLOW DIAGRAM

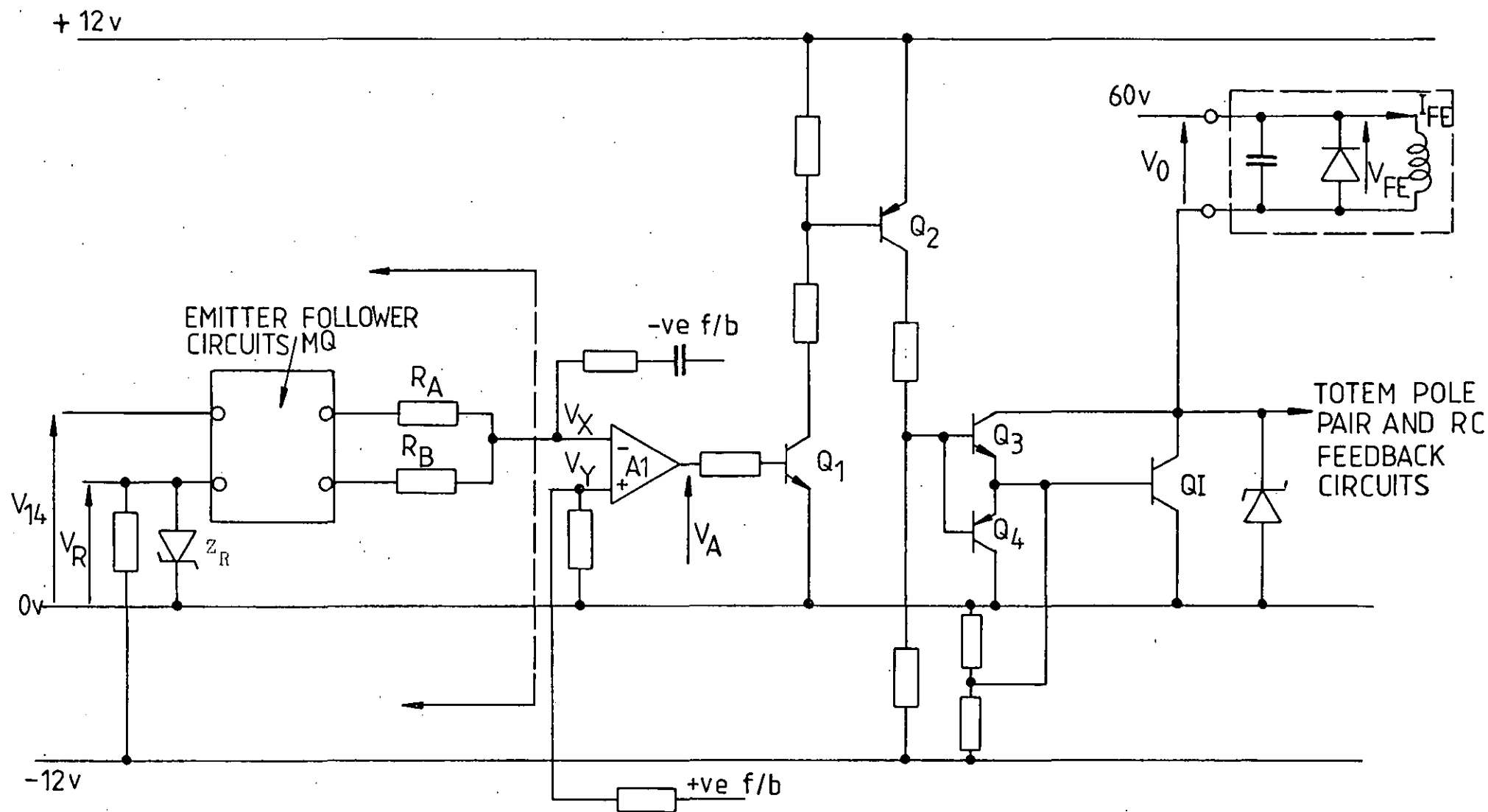


Figure 4.5(a) CIRCUIT DIAGRAM OF THE POWER STAGES OF THE AUTOMATIC VOLTAGE REGULATOR
(details of feedback circuits not shown)

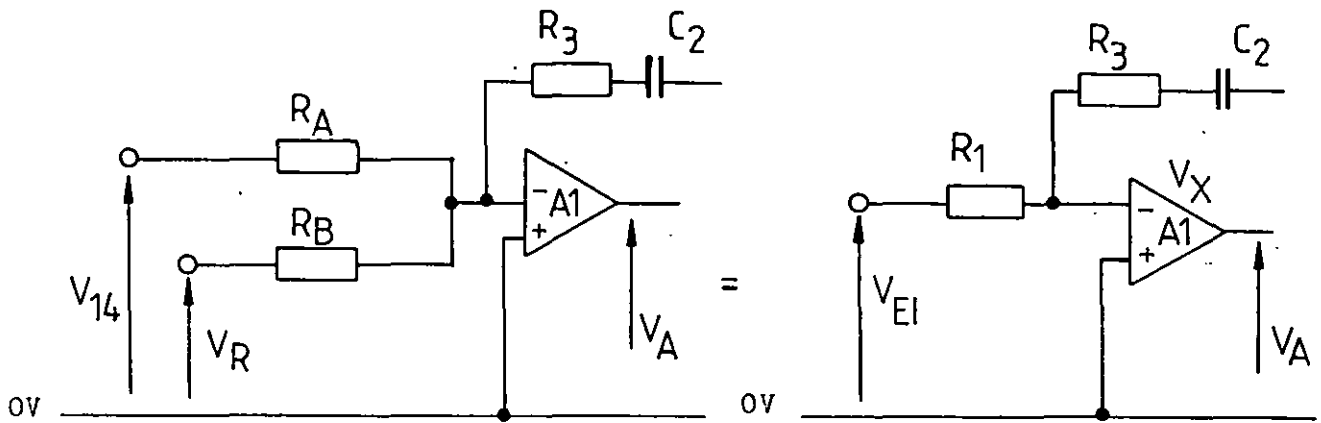


Figure 4.5(b) SIMPLIFICATION OF VOLTAGES INPUT TO AMPLIFIER A1

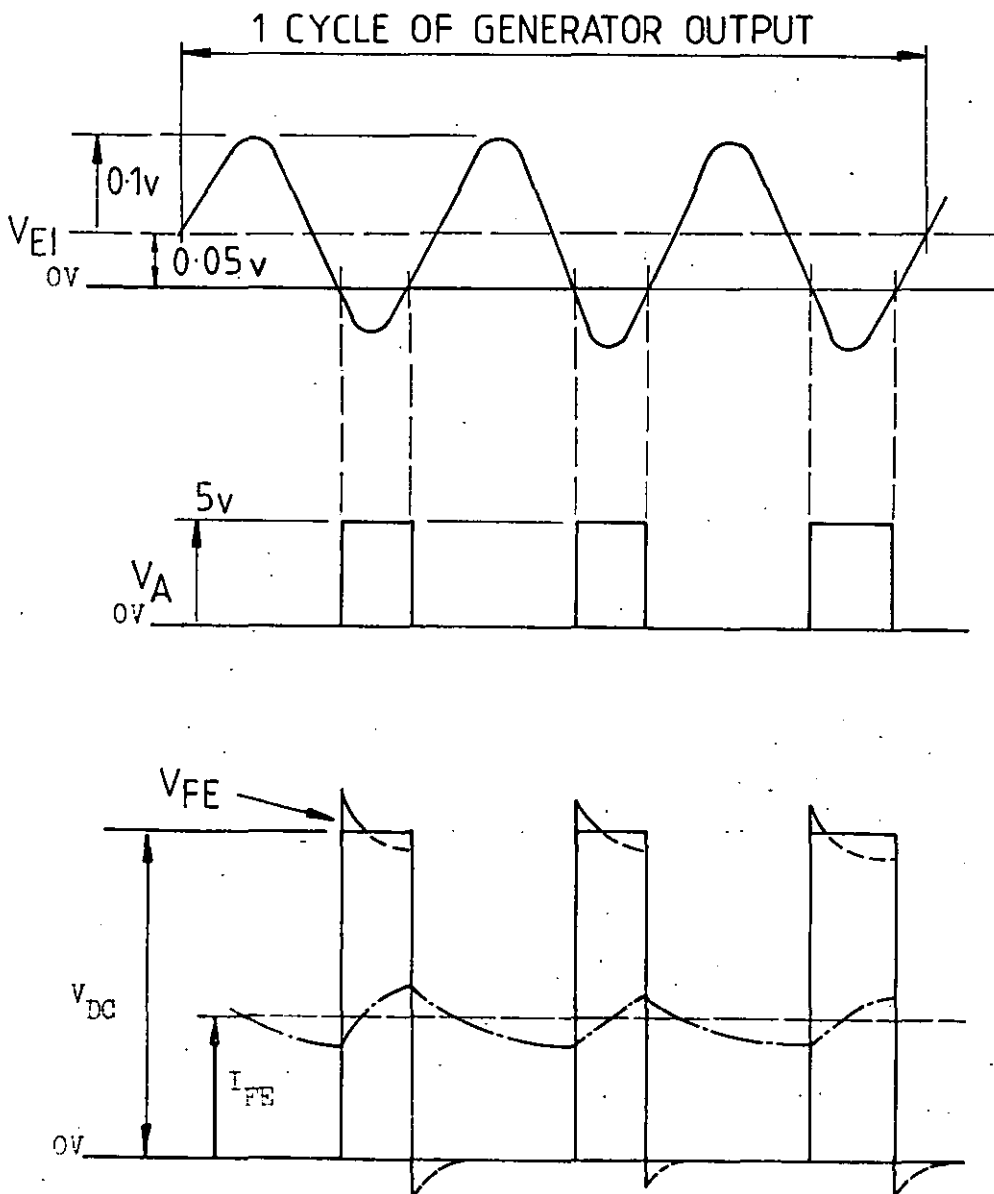


Figure 4.5(c) EFFECTIVE VOLTAGE APPLIED TO EXCITER FIELD WINDING

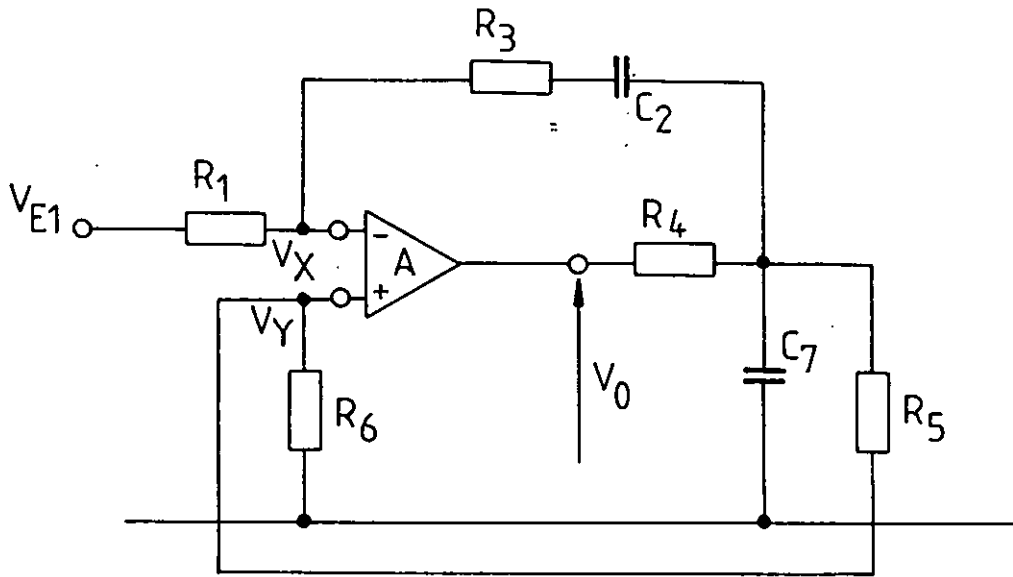


Figure 4.6(a) SIMPLIFIED CIRCUIT OF AMPLIFIER AND FEEDBACK CIRCUITS OF A.V.R.

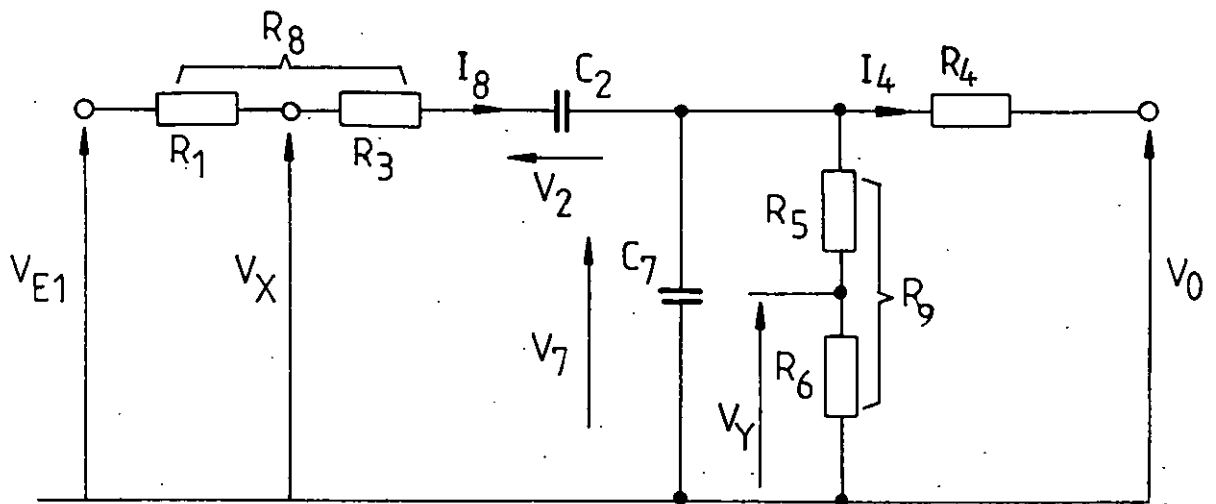


Figure 4.6(b) INDEPENDENT CURRENTS AND STATE VARIABLES OF AMPLIFIER AND FEEDBACK CIRCUITS OF A.V.R.

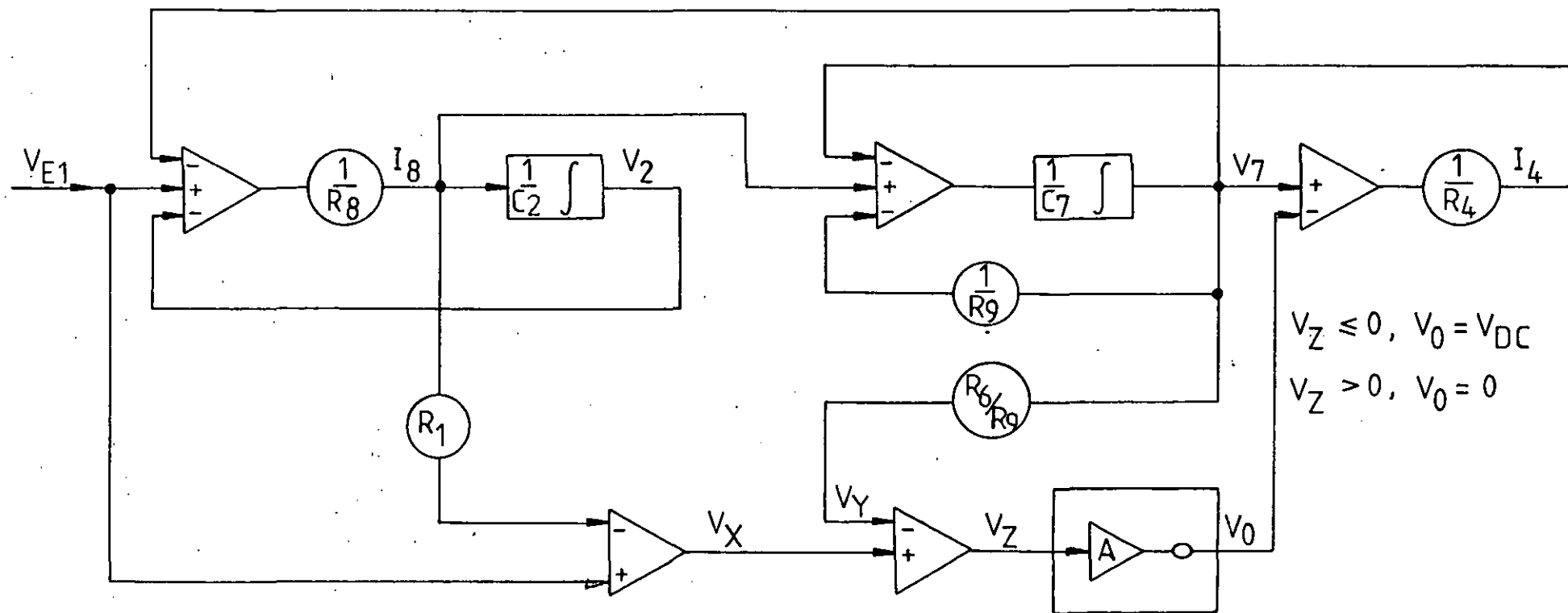


Figure 4.6(c) FLOW DIAGRAM OF AMPLIFIER AND FEEDBACK CIRCUITS OF A.V.R.

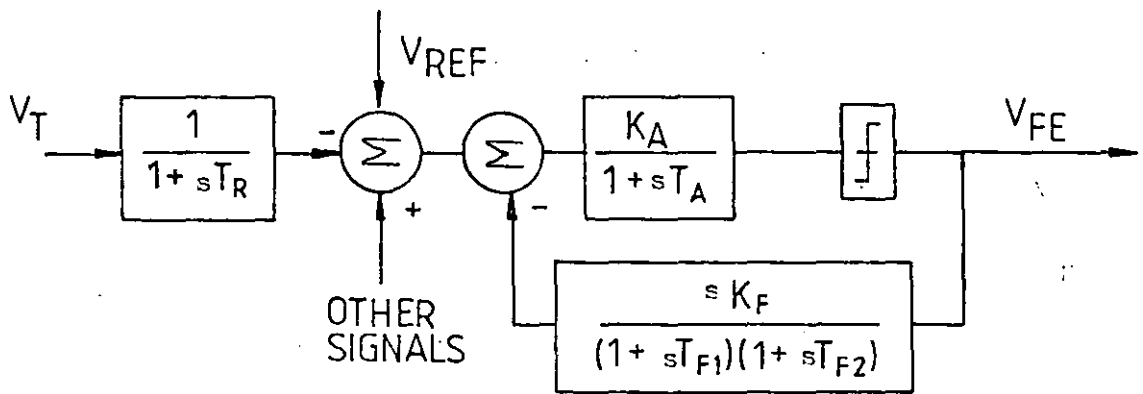


Figure 4.7 TYPE 2 EXCITATION SYSTEM REPRESENTATION,
ROTATING RECTIFIER SYSTEM.

CHAPTER 5

MODELLING OF A REGULATED 3-STAGE GENERATOR UNIT

The a.c. exciter and rectifier supplying field current to the main machine of a 3-stage generator play an important part in determining the overall generator response, in conjunction of course with the automatic voltage regulator. This makes it clearly important to use a model of the exciter and rectifier system which exhibits all the characteristics of the actual system units during both steady state and transient conditions.

A phase model of the exciter, similar to that of the main generator described in Chapter 3, would provide a very accurate model of the system. However, due to the complexity of this model, a large amount of computer memory and computing time would be required for its numerical solution, and it is therefore clearly impracticable to investigate on this basis the transient analysis of a regulated generator over a large number of cycles unless a large digital computer is available. In this Chapter, a simplified model of an exciter rectifier is presented, which includes most of the characteristics of the practical exciter-rectifier system and which is adequate for the overall transient analysis of a 3-stage generator. The results obtained when this simplified model is used with the phase model of the generator (discussed in Chapter 2) and the a.v.r. (discussed in Chapter 4) in predicting the transient performance of the 2130 regulated generator system are given in Section 5.6 of this chapter.

The operation of the rectifier circuits and the effect of line reactance on its modes of operation are well known⁴⁶. Some early attempts at expressing the effect of the rectifier load in terms of the effective a.c. impedance and its power factor are given in references 47-49. Gayek⁴³ described a method of calculating the steady-state operating point of the exciter-rectifier, which is now the standard method used by manufacturers. It is shown in this Chapter how the steady-state operational equations of the rectifier can be extended to predict the transient performance of the regulated system.

5.1 Synchronous Machine with a Rectifier Load

The rectifier presents a very unfavourable load to the exciter as the resulting armature currents are of rectangular or trapezoidal waveform⁵⁰. This results in undesirable harmonic m.m.f.'s being produced in the airgap of the exciter, with corresponding e.m.f.'s generated in the field and damper windings and in the iron core of the field windings. The additional losses produced reduce the power output available from a given frame size of the exciter, and for this reason there are generally no damper windings on the exciter⁵¹.

If idealised diode operation is considered, the current transfer from one phase to the next occurs as soon as the voltage generated in the second phase exceeds that in the first. Figure 5.1(a) shows an idealised circuit model of an exciter and Figures 5.1(b) and 5.1(c) show respectively the phase voltages and the corresponding armature currents with a 3-phase rectifier load and a completely smoothed load current. When the d-axis is positioned between $\theta = 30^\circ$ and $\theta = 90^\circ$, phases a and b are conducting and the resultant m.m.f. is shown in Figure 5.2(b): When $\theta = 90^\circ$, diode commutation takes place, with phase c taking over from phase b between $\theta = 90^\circ$ and $\theta = 150^\circ$. Phases a and c are now conducting and the resultant fixed m.m.f. is shown in Figure 5.2(c). The axis of the armature m.m.f. thus jumps 60° each time diode commutation occurs and lags the d-axis by 60° to 120° . The jumps in the armature m.m.f. induces e.m.f.'s in the field winding (and damper windings if present). The 6th-harmonic ripple current seen in the field current of an exciter is due to this phenomenon.

5.2 Modes of Operation of the Rectifier on Load

5.2.1 Ideal Operation of the 3-Phase Rectifier

If the a.c. source reactance X_c is zero and the load resistance R_d is in series with a large smoothing inductance L , as shown in Figure 5.3, the rectifier waveforms are as shown in Figure 5.4.

If the volt drop in the rectifiers is neglected, the mean d.c. output voltage is

$$E_{do} = \frac{3}{\pi} \sqrt{6} E = 2.34 E \quad 5.1$$

where E is the r.m.s. phase voltage.

The mean diode current is

$$I_R = \frac{1}{3} I \quad 5.2$$

and the r.m.s. armature phase current is

$$I_p = \sqrt{\frac{2}{3}} I = 0.818 I \quad 5.3$$

The r.m.s. values of the in phase and quadrature components of the harmonic currents in the phase windings of the exciter are by Fourier Analysis

$$A_n = \frac{2\sqrt{2}}{\pi} \cdot I \cdot \cos\left(\frac{n\pi}{6}\right) \quad 5.4(a)$$

$$B_n = 0 \quad 5.4(b)$$

so that the fundamental frequency r.m.s. current in the phase winding is

$$A_1 = \frac{\sqrt{6}}{\pi} I = 0.78 I \quad 5.5$$

5.2.2 Actual Operation of the 3-Phase Rectifier

The idealising assumption of no source reactance is of course far from realized in a brushless generator situation, when the presence of a source reactance X_c prevents the instantaneous transfer of current from one rectifier to another.

During commutation both rectifiers in one side of the bridge are conducting, and with the resultant circuit conditions as shown in Figures 5.5(a) and 5.5(b) the source sees effectively a line to line short circuit.

The voltage of a pair of short circuited rectifier terminals is the mean of the corresponding two phase voltages and the commutation is dependent on a reactance load factor RLF defined as

$$RLF = \frac{I X_c}{E_d} \quad 5.6$$

$$= \frac{X_c}{R_d} \quad \text{where } R_d \text{ is the load resistance} \quad 5.7$$

The rectifier operates in three distinct modes ⁵² depending on the value of RLF. The commutation angle (α) and the delay angle (μ), which are both dependent on value of RLF, determine the mode of operation of the rectifier. The effect of α and μ is to reduce the output voltage by an amount ΔE_d from its ideal value, E_{do} , where

$$E_d = E_{do} - \Delta E_d \quad 5.8$$

The three modes of operation of the rectifier and the corresponding relationships between the commutation angle α , delay angle μ , E , E_d , ΔE_d etc. are summarised in Table 5.1. The waveforms of the rectifier for operation in modes I, II and III are shown in Figures 5.6(a), 5.6(b) and 5.6(c) respectively.

The relationship between the a.c. phase current I_p (r.m.s) and the d.c. load current I in terms of α and μ is ⁵³

$$I_p = \sqrt{\left(\frac{2}{3}\right)} I \sqrt{1 - 3f(\alpha, \mu)} \quad 5.9(a)$$

where:

$$f(\alpha, \mu) = \frac{1}{2\pi} \left[\frac{\sin \mu \cdot [2 + \cos(\mu + 2\alpha)] - \mu [1 + 2 \cos \alpha \cos (\mu + \alpha)]}{[\cos \alpha - \cos (\mu + \alpha)]^2} \right] \quad 5.9(b)$$

Fourier Analysis of the exciter phase currents gives the fundamental frequency components as

$$A_1 = I \cdot h_1(\alpha, \mu) \quad 5.10(a)$$

$$B_1 = I \cdot h_2(\alpha, \mu) \quad 5.10(b)$$

where:

$$h_1 = \frac{1}{\pi} \sqrt{\left(\frac{3}{2}\right)} [\cos \alpha + \cos (\mu + \alpha)] \quad 5.10(c)$$

and

$$h_2 = \frac{1}{\pi} \sqrt{\left(\frac{3}{2}\right)} \left[\frac{\sin 2(\mu + \alpha) - \sin(\alpha) - 2\mu}{2[\cos \alpha - \cos (\mu + \alpha)]} \right] \quad 5.10(d)$$

where I_1 , the r.m.s. of the fundamental frequency current, is

$$I_1 = \sqrt{A_1^2 + B_1^2} \quad 5.11$$

The effective a.c. load power factor angle ϕ is

$$\phi = \tan^{-1} \left(\frac{B_1}{A_1} \right) \quad 5.12$$

The effective per phase a.c. voltage E (r.m.s) in terms of the d.c. voltage E_d is

$$E = E_d \cdot h_3 (\alpha, \mu) \quad 5.13(a)$$

$$\text{where: } h_3 = \frac{\pi}{3\sqrt{6}} \left[\frac{2}{1 + \cos \mu} \right] \quad \text{Mode I} \quad 5.13(b)$$

$$h_3 = \frac{\sqrt{2} \pi}{9 [\cos (\alpha + 30^\circ)]} \quad \text{Mode II} \quad 5.13(c)$$

$$h_3 = \frac{\sqrt{2} \pi}{9 [1 - \sin (\mu - 30^\circ)]} \quad \text{Mode III} \quad 5.13(d)$$

The equivalent a.c. load impedance per phase as seen by the exciter is

$$Z = \frac{E}{I_1} \quad 5.14$$

If Z is represented as an equivalent series-connected resistance R and reactance X then

$$R = Z \cos \phi \quad 5.15(a)$$

$$X = Z \sin \phi \quad 5.15(b)$$

5.3 Steady State Operation of Exciter-Rectifier System

If the exciter is represented as a voltage behind the commutation reactance X_c , as shown in Figure 5.3, the steady-state performance of the exciter/rectifier can be obtained using the performance equations of Table 5.1. The characteristics of the exciter-rectifier system are given in Figures 5.7 and 5.8 as follows:

Figure 5.7(a) shows the variation of α and μ with RLF.

Figure 5.7(b) shows the $f(\alpha, \mu)$ variation with RLF.

Figure 5.7(c) shows how the components of the fundamental frequency armature currents A_1 , B_1 , vary with RLF.

Figure 5.8(a) shows the effect of RLF on the d.c. output voltage E_d

Figure 5.8(b) shows the regulation characteristic of the rectifier operating in modes I, II and III, by considering Z_Δ to represent the volt drop from the ideal d.c. output voltage E_{do} . Z_Δ represents the loss of voltage due to commutation.

5.4 Transient Performance of Exciter on Load

As the frequency of operation of the exciter is $2\frac{1}{2}$ x the fundamental frequency of the generator*, the exciter response is much faster than the generator response and changes in the exciter field current are much more rapid than in the corresponding generator field current. This enables the exciter phasor diagram shown in Figure 5.9 to be used as the basis of a transient analysis.

* The frequency of operation of the generator is 400 Hz and that of the exciter is 1000 Hz.

5.4.1 Application of a Steady State Exciter Model to Generator Transient Conditions

Any sudden change in the generator load forces a sudden change in the generator field current. The magnitude of the change is a function of the load impedance and its power factor, together with the generator reactances.

When the generator field current increases on the application of load, the exciter armature current increases accordingly. If the generator field current increases sufficiently, it may present an effectively short-circuited load to the exciter, and force the rectifier to operate in Mode III. If the exciter is unable to meet the field current demanded by the generator, the rectifier acts as a short-circuit path to both the generator field current and the exciter armature current so that these currents become mutually independent⁵⁴. The increase in the exciter armature current is reflected in an increase in its field current in the same way as in the generator. This increase is seen by the exciter-rectifier as an effective reduction in its load resistance R_d . This increases RLF and hence, depending on the value of RLF, forces the exciter-rectifier system to operate in either mode II or mode III. When load is removed from the generator, the decrease in field current is seen as an effective increase in R_d . This results in a shift of operation of the exciter rectifier to mode I as RLF is effectively reduced.

A steady-state model of the exciter-rectifier system can be used to analyse the rectifier-exciter-generator system during a transient process, if the exciter field transient time constant and the changes in the rectifier mode of operation are calculated during the step-by-step solution of the generator differential equations. The exciter transient time constant takes into account the a.c. load impedance as seen by the exciter, and the changes in the mode of operation of the rectifier takes into account the response of the exciter-rectifier system to changes in field current. The step-by-step changes in the exciter vector diagram are calculated iteratively at each step of the solution of the generator differential equations on the digital computer. Since the phasor diagram is based on steady-state conditions, the

changes in the exciter armature current are not reflected into the exciter field winding.

The exciter transient time constant on load is given by

$$T'_{dz} = T'_{do} \frac{[R_L^2 + (x'_{de} + X)(x_{qe} + X)]}{[R_L^2 + (x_{de} + X)(x_{qe} + X)]} \quad 5.16$$

where: $T'_{do} = \frac{L_{FFE}}{R_{FE}}$, $R_L = R_p + R$

L_{FFE} : Self inductance of the exciter field winding

R_{FE} : Resistance of the exciter field winding

x'_{de} : Exciter direct-axis transient reactance

x_{de} : Exciter direct-axis synchronous reactance

x_{qe} : Exciter quadrature-axis synchronous reactance

X : is the exciter load reactance per phase

R : is the exciter load resistance per phase

R_p : is the exciter phase winding resistance

5.5 Iterative Method of Calculating Exciter-Rectifier Transient Response

The iterative method used to calculate the exciter-rectifier response is shown by the flow diagram of Figure 5.10. The self-inductance of the exciter field winding is dependent on the saturation of the field flux path, which is in turn determined by the total

d-axis current ($I_{FFE} - I_{dl}$), where I_{FFE} is the exciter field current and I_{dl} is the d-axis component of the exciter armature currents. Similarly the gain K_E defined as the per-phase open-circuit voltage of the exciter per-unit exciter field current is dependent on the d-axis saturation level, so that

$$L_{FFE} = f_1 (I_{FFE} - I_{dl}) \quad 5.17$$

$$K_E = f_2 (I_{FFE} - I_{dl}) \quad 5.18$$

The function f_1 was obtained by measuring the secant inductance of the exciter field winding for different values of field current. Similarly, the function f_2 was obtained by measuring the secant value of the mutual inductance between the armature phase in the d-axis and the field winding for different values of field current. Functions f_1 and f_2 are given in Appendix A9.

Referring to Figure 5.10, the output phase voltages of the generator are used to determine the exciter field voltage V_{FFE} , using either of the two models of the automatic voltage regulator (a.v.r) described in Chapter 4. Subscripts (0) refers to the values of the parameters at time T and (N) to their values at time $T = T+H$, where H is the time step used for successive numerical integration of the generator equations.

$I_{FFE(N)}$ is obtained by numerical integration of

$$p(I_{FFE}) = \frac{V_{FFE} - R_{FFE} \cdot I_{FFE}}{L_{FFE} \cdot ELF} \quad 5.19$$

where

$$ELF = \frac{R_L^2 + (x_{de}' + X)(x_{qe} + X)}{R_L^2 + (x_{de} + X)(x_{qe} + X)} \quad 5.20$$

Since the rectifiers are in practice far from ideal, there is always a voltdrop during forward conduction. This is accounted for by subtracting V_R , the rectifier voltdrop, from the effective d.c. output voltage E_d to obtain the generator field voltage V_{Fg} .

5.6 Comparison of the Measured and Predicted Transients Following Application (and Rejection) of Generator Loads

5.6.1 Load Application Tests on 2130 Generator Unit Without a.v.r.

In order to test the exciter-rectifier-generator model, the field of the main exciter was supplied from a 12 V battery in place of the a.v.r. The exciter field current was adjusted to give rated open-circuit voltage of the generator of 115 V r.m.s. (162 V peak). Figure 5.11 shows a comparison between the measured phase voltage peaks and the predicted values, following the application of a 40 kVA zero p.f. lagging load. Similarly Figure 5.12 shows a comparison of the measured and predicted phase voltage peaks on application of a 60 kVA 0.75 p.f. lagging load. The close agreement evident in both figures between measured and predicted results shows that the exciter-rectifier-generator model can with confidence be used as the basis for further investigations.

5.6.2 Load Application and Rejection Tests on 2130 Generator Including a.v.r.

The load application and rejection transients were predicted using the two models of the a.v.r. described in Chapter 4. The transients predicted by using the transfer function model of a.v.r. are called Model 1 and those predicted using the state variable model are called Model 2. The phase model of the generator (described in Chapter 2) and the exciter-rectifier model described in this chapter were used for both Model 1 and Model 2 predictions.

Figures 5.13 and 5.14 show respectively comparisons between both the measured and predicted phase voltages and the exciter field current transients following the application of a 40 kVA unity p.f. load. Figures 5.15 and 5.16 show comparisons between both the measured and predicted phase voltages and the exciter field current transients following rejection of the same load. Similarly, Figures 5.17 to 5.20 show comparisons between both the measured and predicted phase voltages and the exciter field current transients on application and rejection of a 40 kVA zero p.f. lagging load.

Figures 5.21 to 5.24 show comparisons between the measured and predicted phase voltages and exciter field current transients on application and rejection of a 60 kVA unity p.f. load. Similarly Figures 5.25 to 5.28 show comparisons between both the measured and predicted phase voltages and the exciter field current transients on application and rejection of a 60 kVA 0.75 p.f. lagging load.

5.7 Discussion and Conclusion

The results of the tests performed show that the exciter-generator model developed predicts the voltage transient accurately following the application of different loads, as confirmed by tests using a 12 V battery to supply the exciter field current. The results of Figures 5.13 to 5.28 show that it is possible, using the models of a.v.r. described in Chapter 4 and the exciter-rectifier-model described in this Chapter (and the generator model described in Chapter 2) to predict accurately the transient voltage output of the generator following the application or rejection of a balanced 3-phase load. Unbalanced load conditions were not considered in the present investigation, but the phase model of the generator, together with the state-variable model of the a.v.r., would be expected to provide results of the same accuracy as those presented for balanced loads as the a.v.r. responds to actual phase voltages in the state-variable model, while the transfer function model calcu-

lates the effective phase voltage on the assumption that a balanced 3-phase load is applied to the generator.

5.7.1 Exciter Field Current Transient

It is found that transient currents are induced in the exciter field winding following the application and rejection of a load at the generator terminals. The model described in this chapter shows the exciter field current response due to the action of the a.v.r. and hence for accurate prediction of the exciter field current *transient*, the transient current induced due to the load changes at the generator terminals would have to be added to the transient current due to the action of a.v.r. There is a 6th-harmonic ripple current on the d.c. level of the exciter field current, as discussed in Chapter 3. The measured results of the exciter field current transients show bands marked I signifying the magnitude of this ripple current.

Having discussed some of the relevant points which may limit the accuracy of prediction of the exciter field current transient, it is nevertheless clear from the results obtained by test that these do not significantly affect the generator voltage transients. The steady state exciter field current, the voltage dip (or rise) and settling time following both the application and rejection of a load are accurately predicted.

TABLE 5.1 SUMMARY OF PERFORMANCE EQUATIONS FOR 3-PHASE FULL WAVE BRIDGE RECTIFIER

Quantity	Mode I	Mode II	Mode III
μ	0 to 60°	60°	60 to 120°
α	0	0 to 30°	30°
$\frac{I_d X_c}{E}$	0 to $\frac{\sqrt{6}}{4}$	$\frac{\sqrt{6}}{4}$ to $\frac{3\sqrt{2}}{4}$	$\frac{3\sqrt{2}}{4}$ to $\sqrt{2}$
$\frac{I_d X_c}{E_d}$	0 to $\frac{\pi}{9}$	$\frac{\pi}{9}$ to $\frac{\pi}{3}$	$\frac{\pi}{3}$ to ∞
E	$\frac{\pi}{3\sqrt{6}} [1 + \frac{3}{\pi} \frac{I_d X_c}{E_d}] E_d$	$\frac{\sqrt{2} \pi}{9 \cos(\alpha + 30^\circ)} E_d$	$\frac{\sqrt{2} \pi}{9 [1 - \sin(\mu - 30^\circ)]} E_d$
E_{do}	$[1 + \frac{3}{\pi} \frac{I_d X_c}{E_d}] E_d$	$\frac{2\sqrt{3}}{3 \cos(\alpha + 30^\circ)} E_d$	$\frac{2\sqrt{3}}{3 [1 - \sin(\mu - 30^\circ)]} E_d$
ΔE_d	$\frac{3}{\pi} I_d X_c$	$[\frac{2\sqrt{3}}{3 \cos(\alpha + 30^\circ)} - 1] E_d$	$[\frac{2\sqrt{3}}{3 [1 - \sin(\mu - 30^\circ)]} - 1] E_d$
$\cos \mu$	$\frac{1 - \frac{3}{\pi} \frac{I_d X_c}{E_d}}{1 - \frac{3}{\pi} \frac{I_d X_c}{E_d}}$	-	-
$\tan(\alpha + 30^\circ)$	-	$\frac{1}{\sqrt{3}} \frac{9}{\pi} \frac{I_d X_c}{E_d}$	-
$\sin(\mu - 30^\circ)$	-	-	$\frac{\frac{9}{\pi} \frac{I_d X_c}{E_d} - 1}{\frac{9}{\pi} \frac{I_d X_c}{E_d} + 1}$

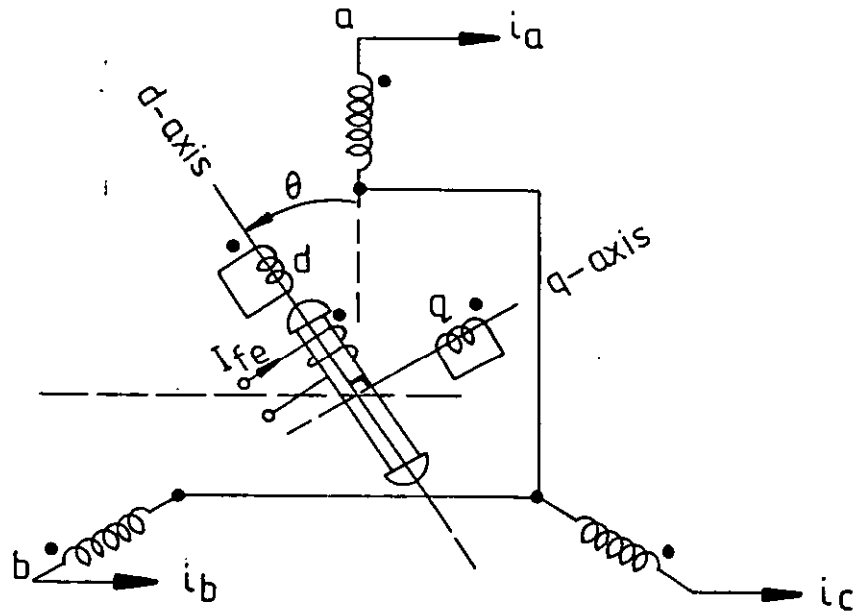


Figure 5.1(a) THE 3-PHASE EXCITER WINDING CONNECTIONS

Figure 5.1(b)
EXCITER PHASE VOLTAGES

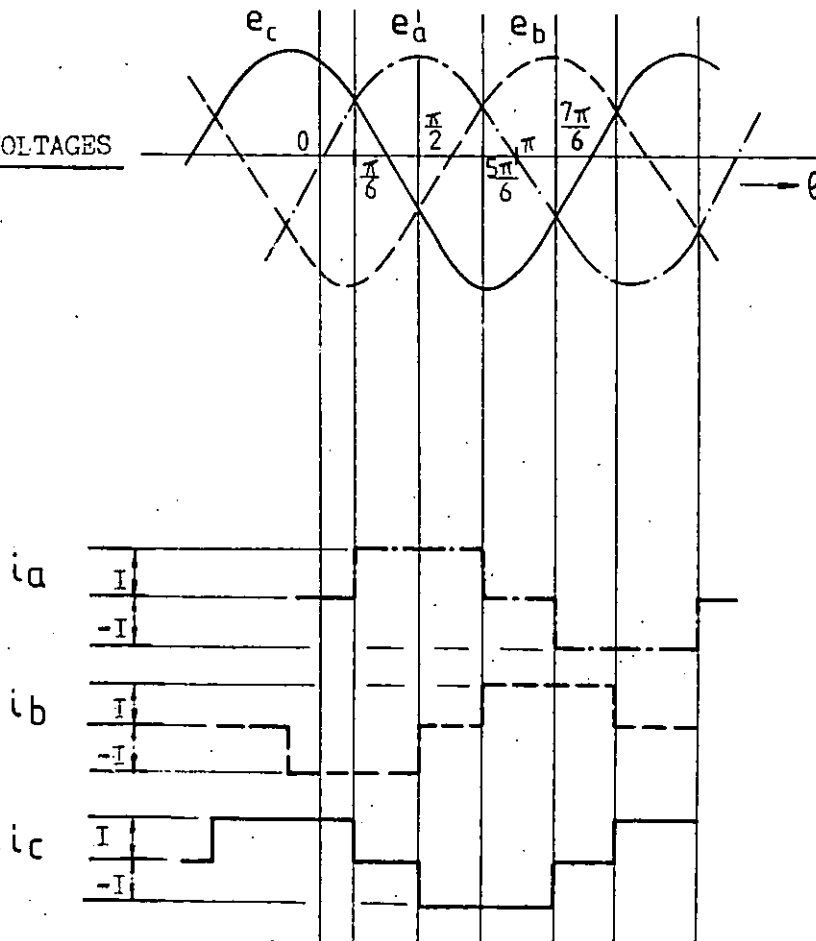


Figure 5.1(c) EXCITER PHASE CURRENTS (assuming zero commutation reactance)

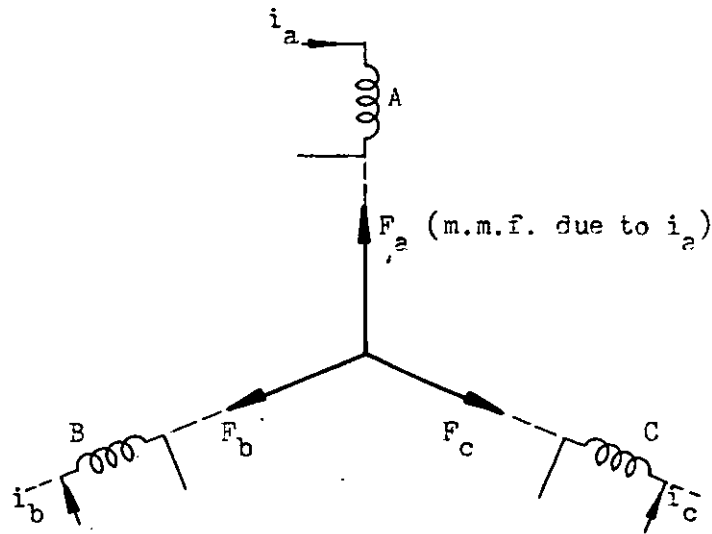


Figure 5.2(a) DIRECTION OF M.M.F. DUE TO EXCITER PHASE CURRENTS

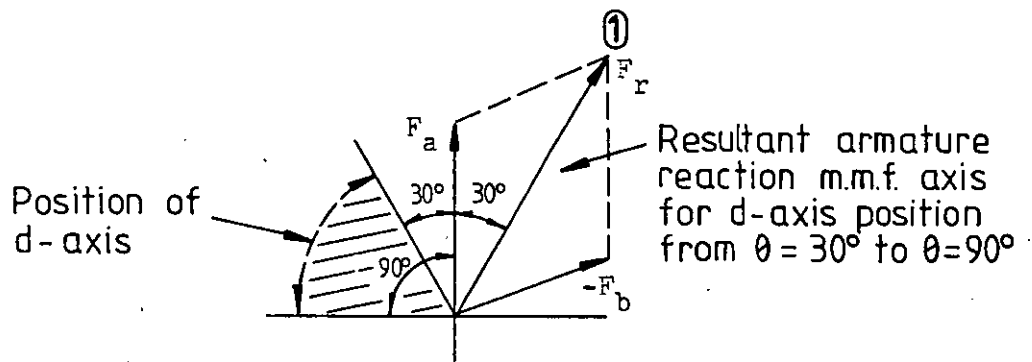


Figure 5.2(b) POSITION OF RESULTANT M.M.F. WITH RESPECT TO d-AXIS
(phases A and B conducting)

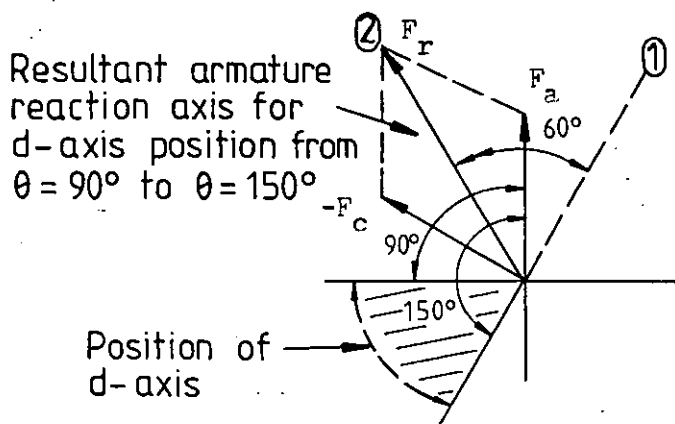


Figure 5.2(c) SHIFT IN POSITION OF RESULTANT M.M.F. FROM (1) TO (2)
DUE TO COMMUTATION OF RECTIFIER DIODES
(current transfer from phase B to phase C)

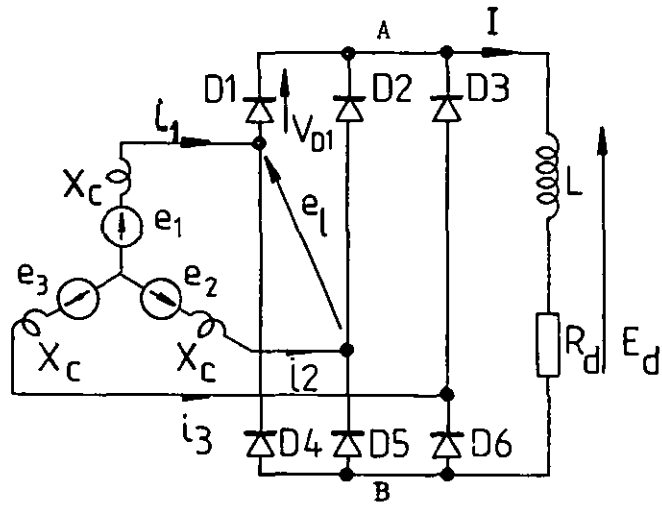


Figure 5.3 3-PHASE SUPPLY WITH A FULL WAVE RECTIFIER BRIDGE AND A HIGHLY INDUCTIVE LOAD

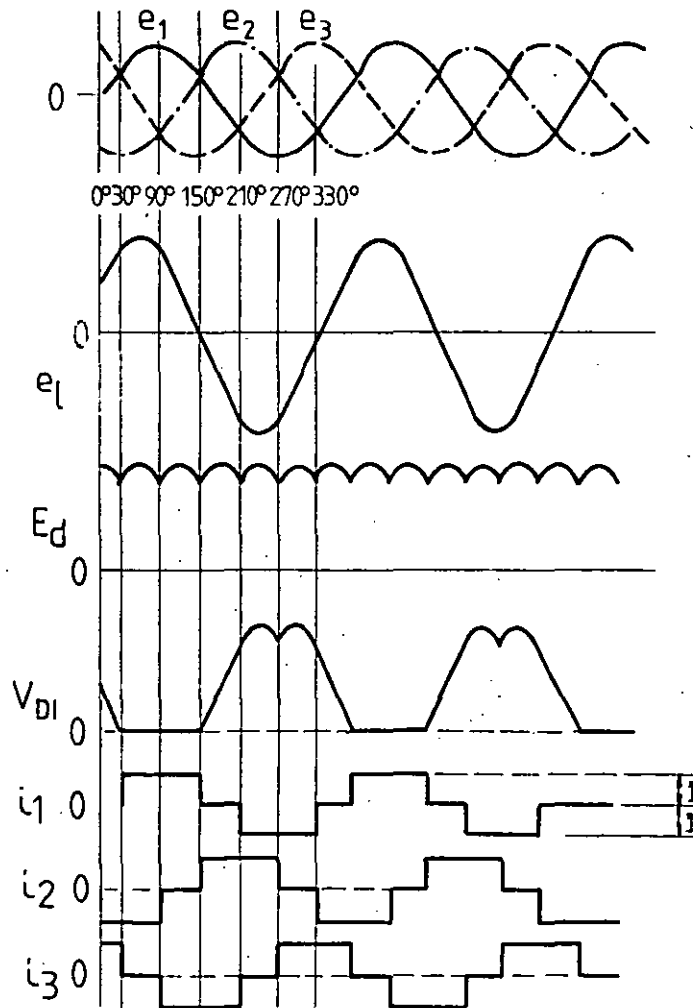


Figure 5.4 THE CHARACTERISTICS OF CIRCUIT OF Figure 5.3 UNDER IDEAL CONDITION. (X_c , the commutation reactance equal to zero)

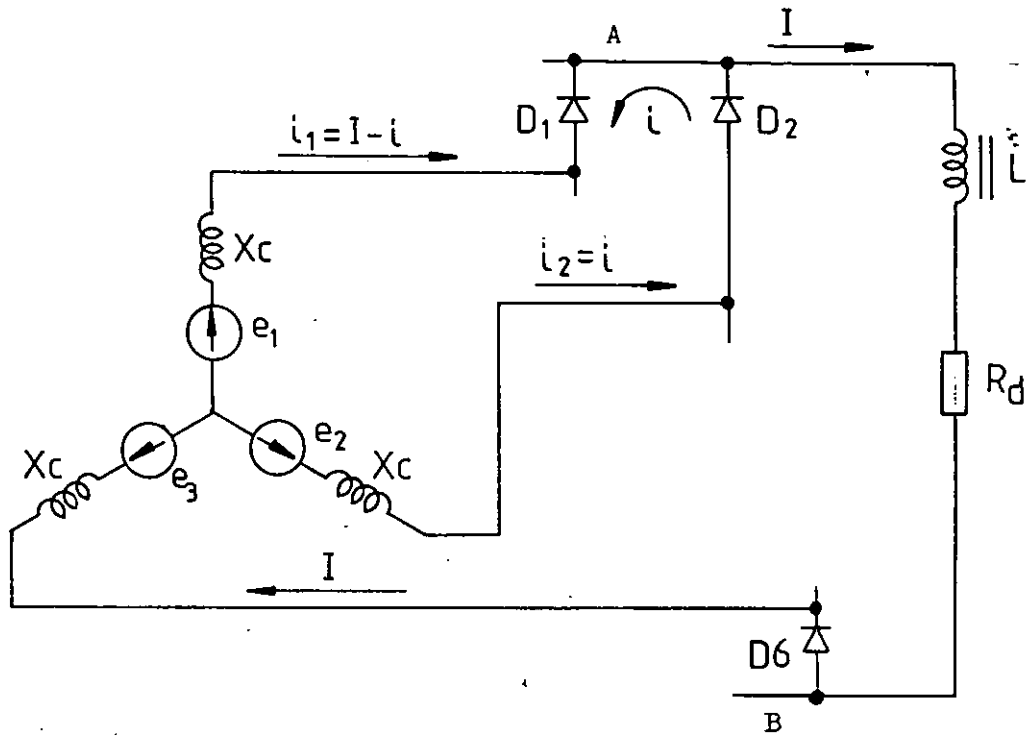


Figure 5.5(a) LINE-TO-LINE SHORT CIRCUIT CONDITION DURING COMMUTATION DUE TO COMMUTATION REACTANCE X_c

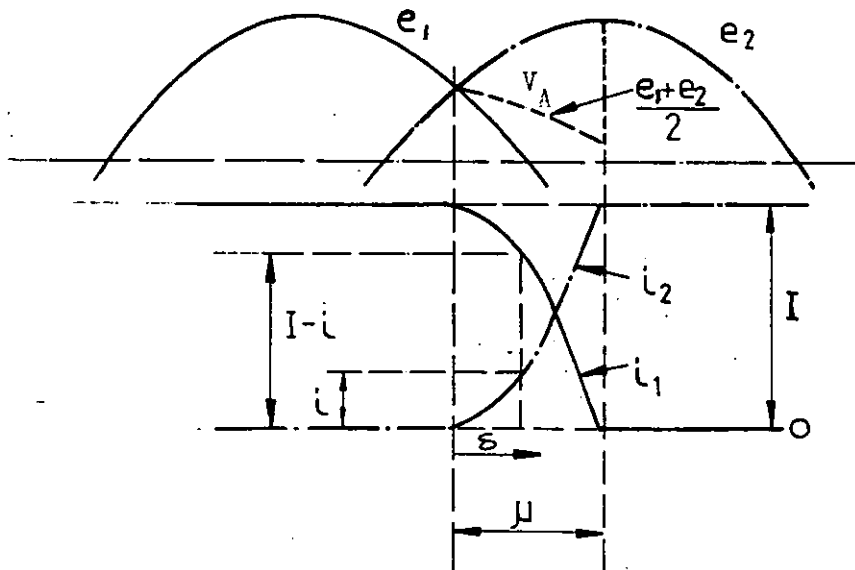


Figure 5.5(b) THE EFFECT OF COMMUTATION REACTANCE X_c ON OUTPUT VOLTAGE (Point A) AND THE SUPPLY CURRENTS i_1, i_2

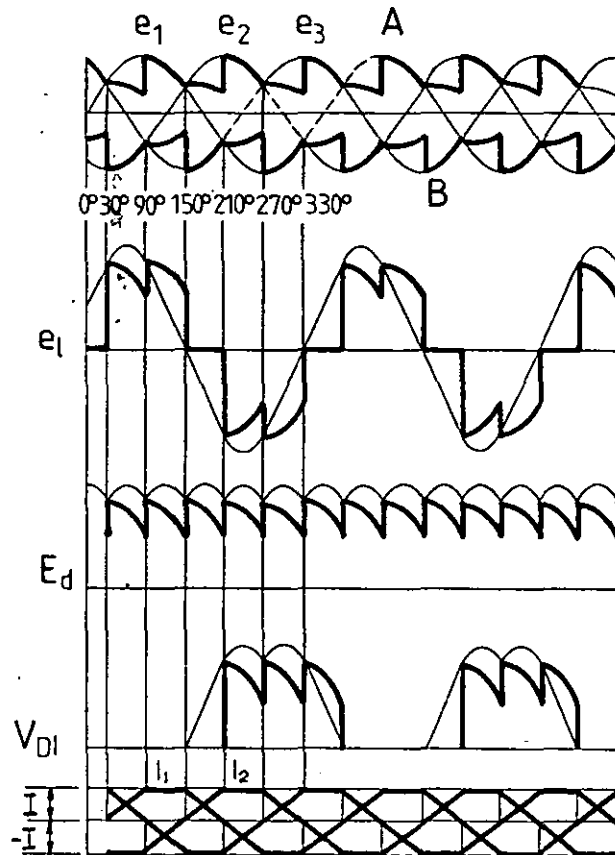


Figure 5.6(a) THE CHARACTERISTICS OF CIRCUIT OF Figure 5.3 UNDER MODE I OPERATION

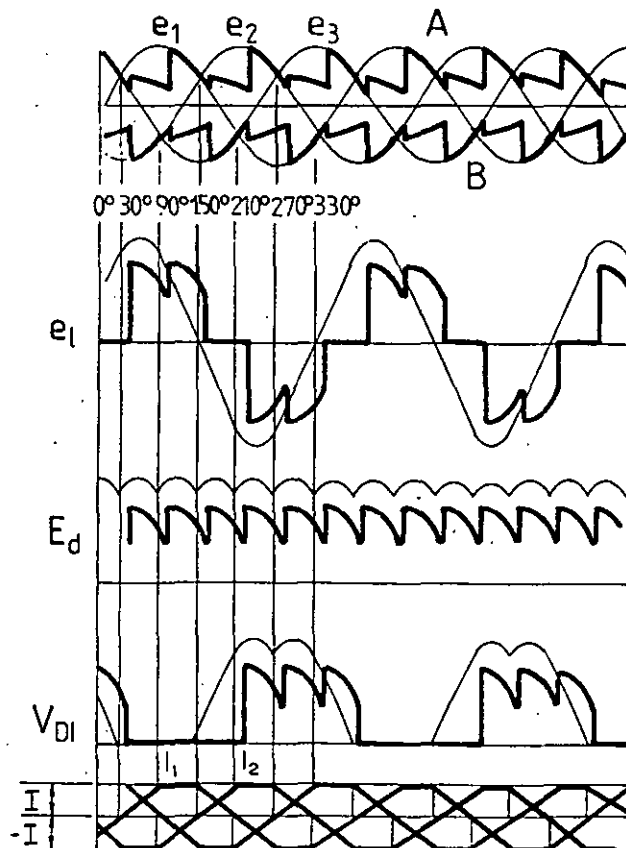


Figure 5.6(b) THE CHARACTERISTICS OF CIRCUIT OF Figure 5.3 UNDER MODE II OPERATION

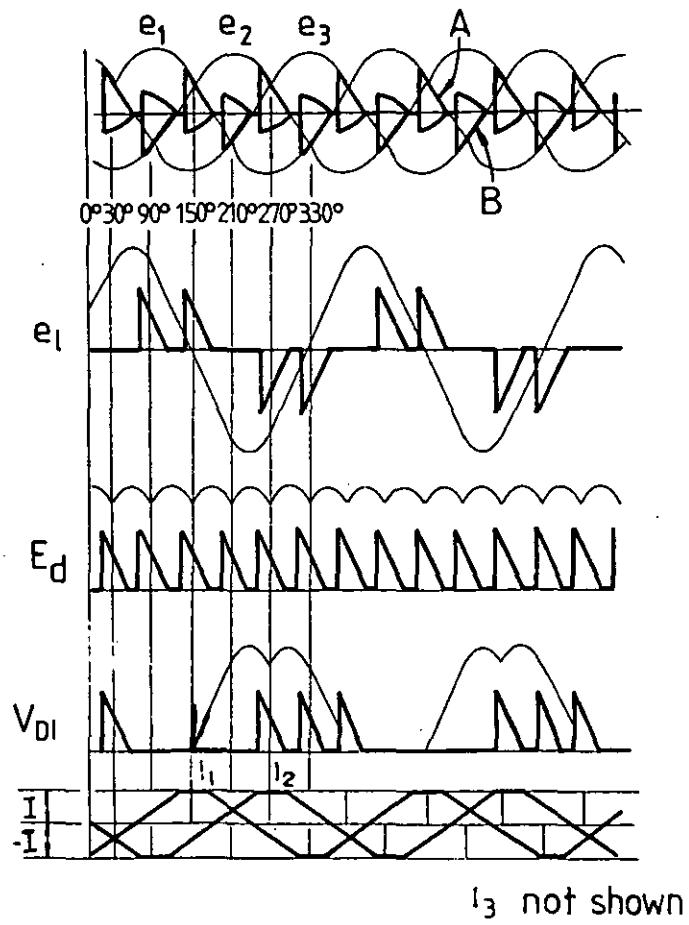


Figure 5.6(c) THE CHARACTERISTICS OF CIRCUIT OF Figure 5.3 UNDER MODE III OPERATION

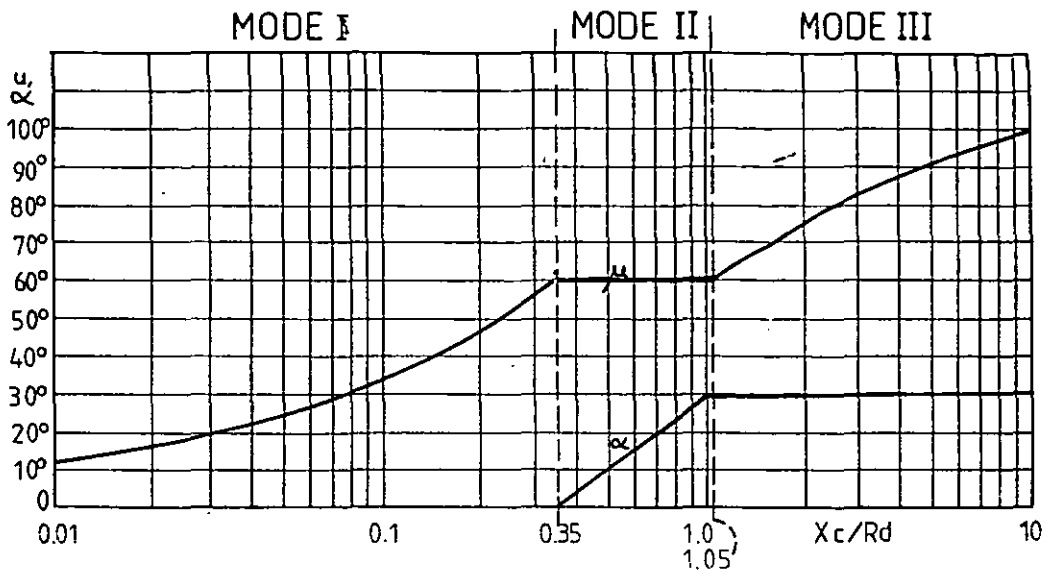


Figure 5.7(a) OVERLAP ANGLE (μ) AND RETARD ANGLE (α) AS FUNCTIONS OF RLF (X_c/R_d)

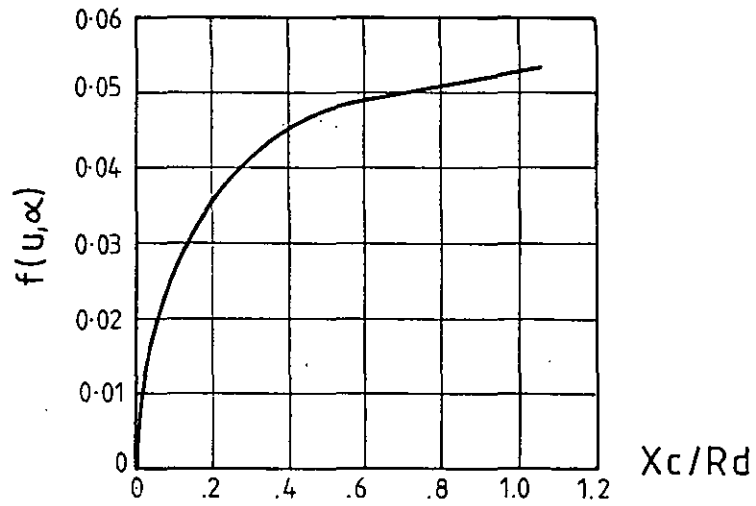


Figure 5.7(b) $f(\mu, \alpha)$ AS A FUNCTION OF RLF (X_c/R_d)

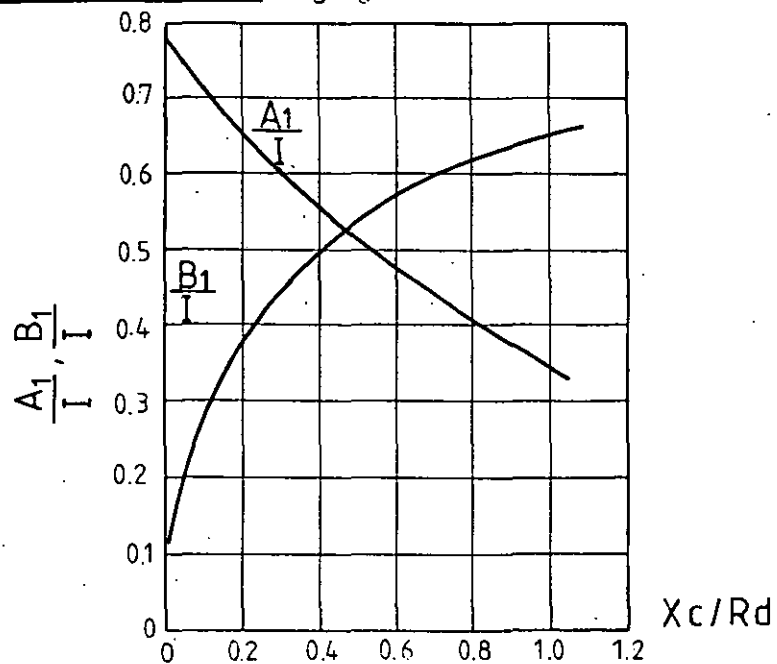


Figure 5.7(c) THE REAL AND REACTIVE COMPONENTS OF A.C. LINE CURRENT PER UNIT OF D.C. CURRENT AS FUNCTIONS OF RLF (X_c/R_d)

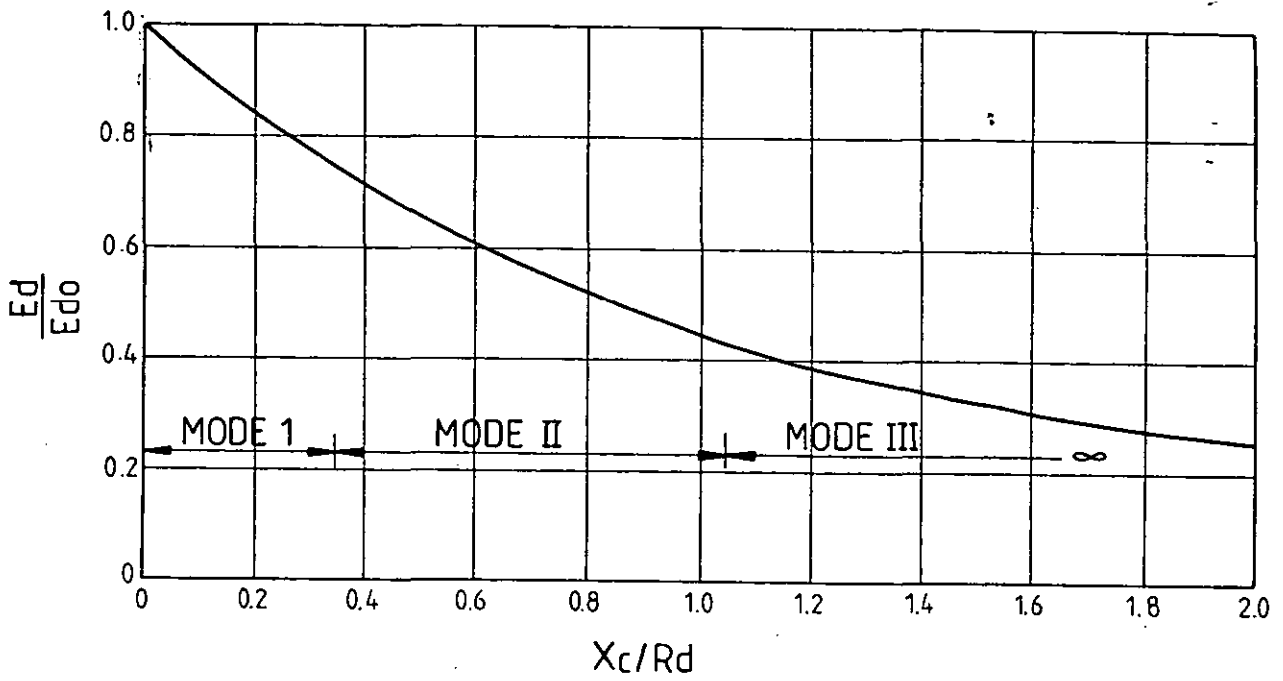


Figure 5.8(a) PER-UNIT RECTIFIER SYSTEM OUTPUT AS A FUNCTION OF RLF (X_c/R_d)

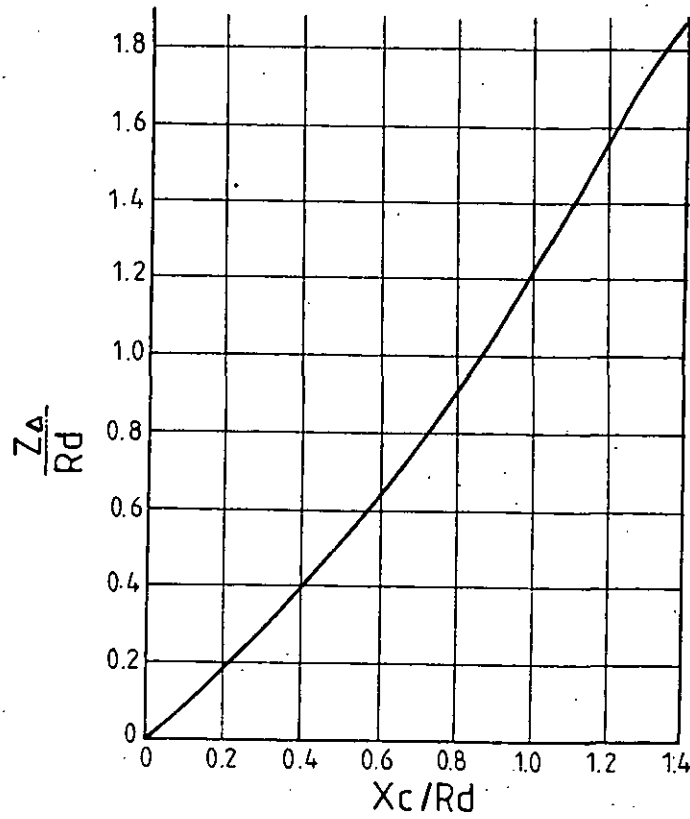


Figure 5.8(b) EQUIVALENT IMPEDANCE OF RECTIFIER SYSTEM AS A FUNCTION OF RLF (X_c/R_d)

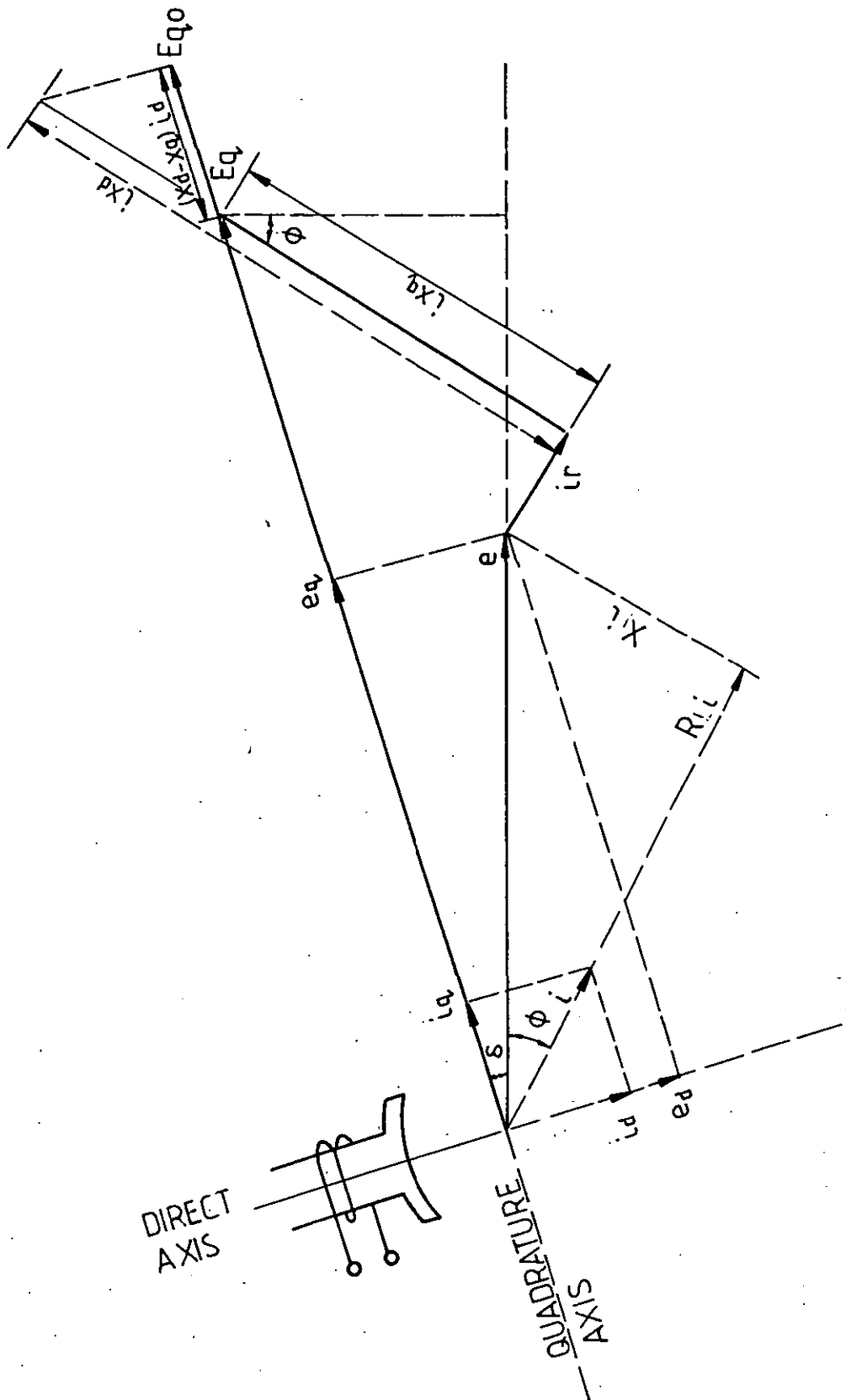


Figure 5.9 PHASOR DIAGRAM REPRESENTING THE OPERATION OF A.C. EXCITER

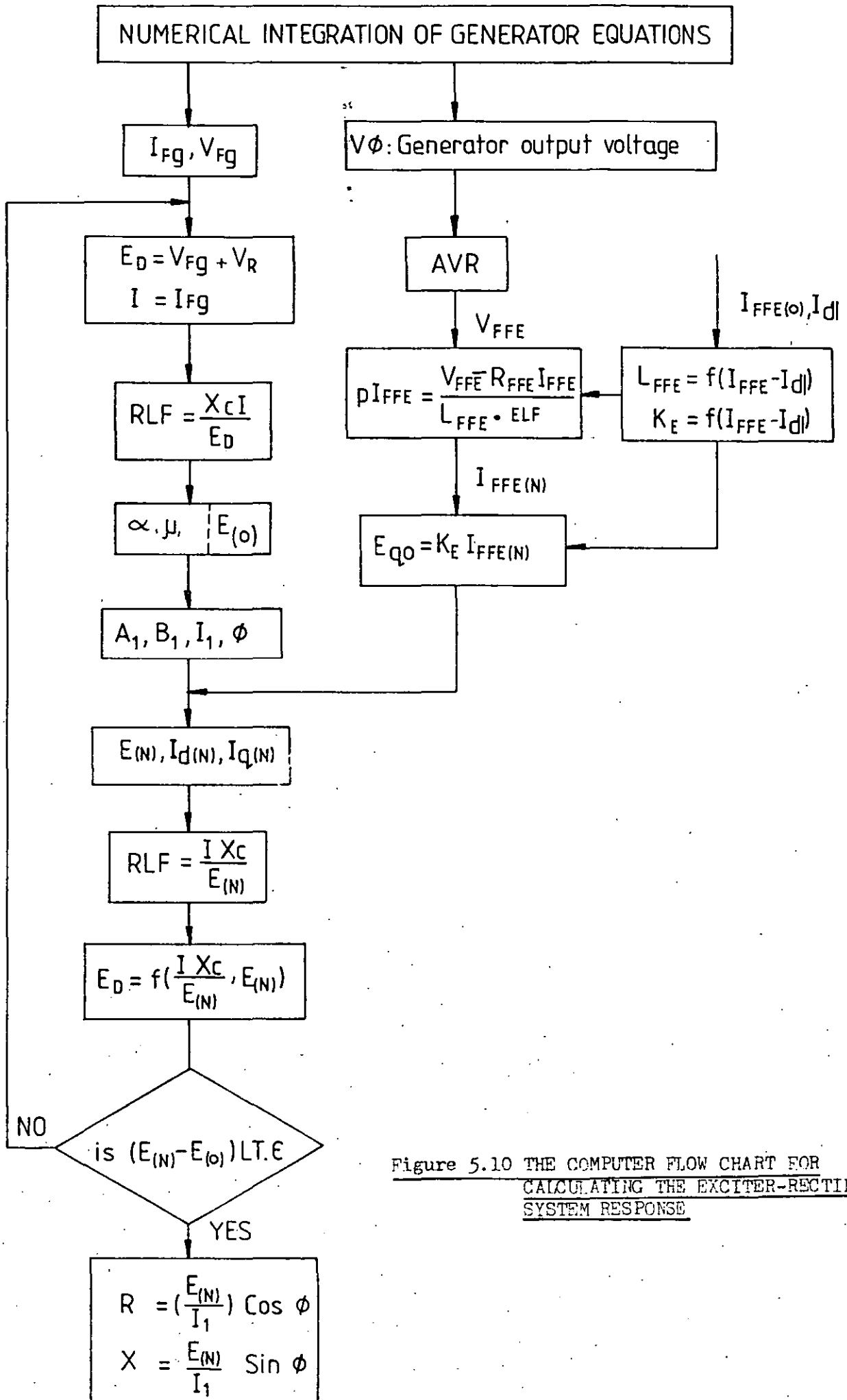


Figure 5.10 THE COMPUTER FLOW CHART FOR
CALCULATING THE EXCITER-RECTIFIER
SYSTEM RESPONSE

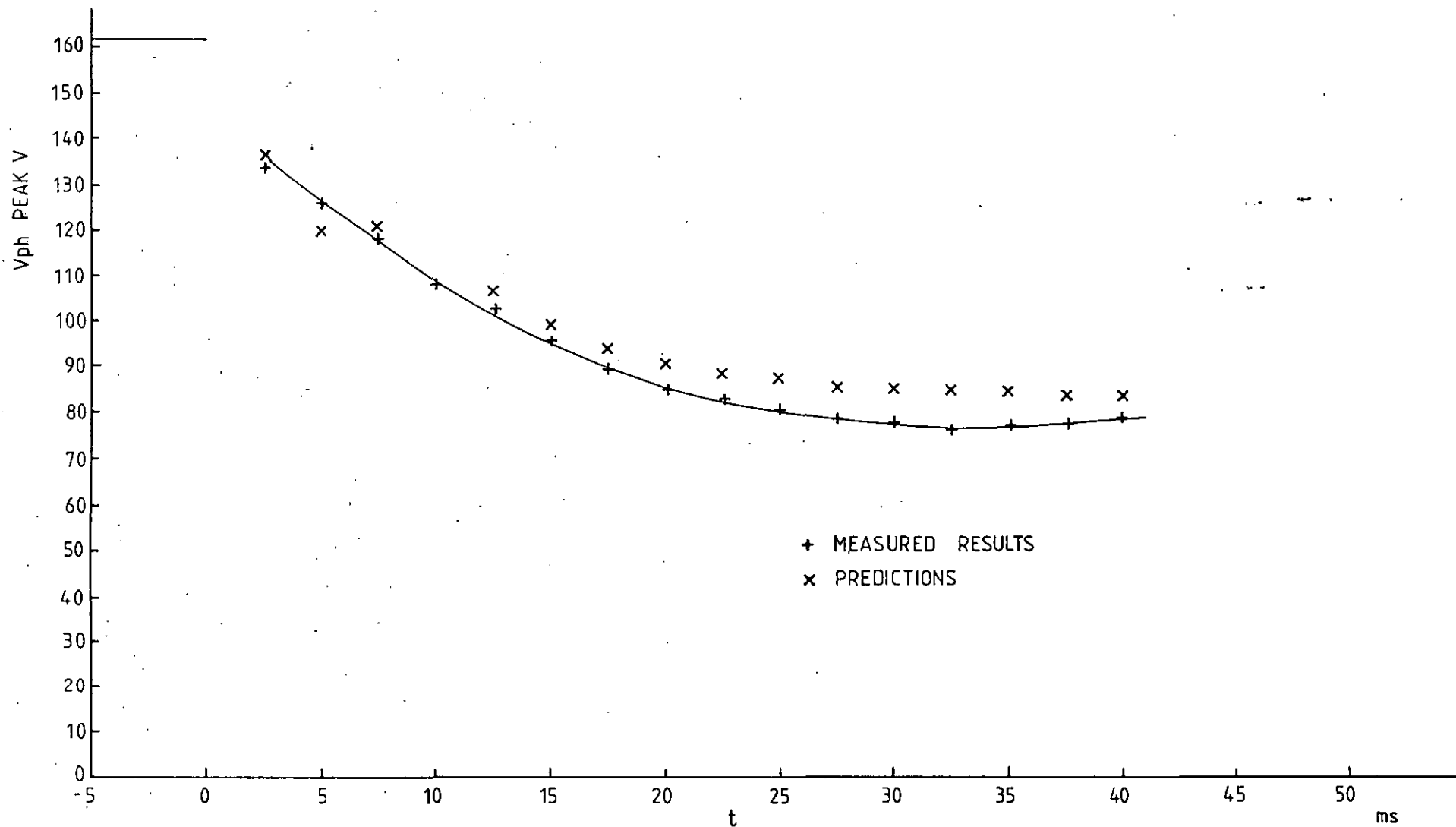


Figure 5.11 APPLICATION OF 40 kVA 0 P.F. LOAD

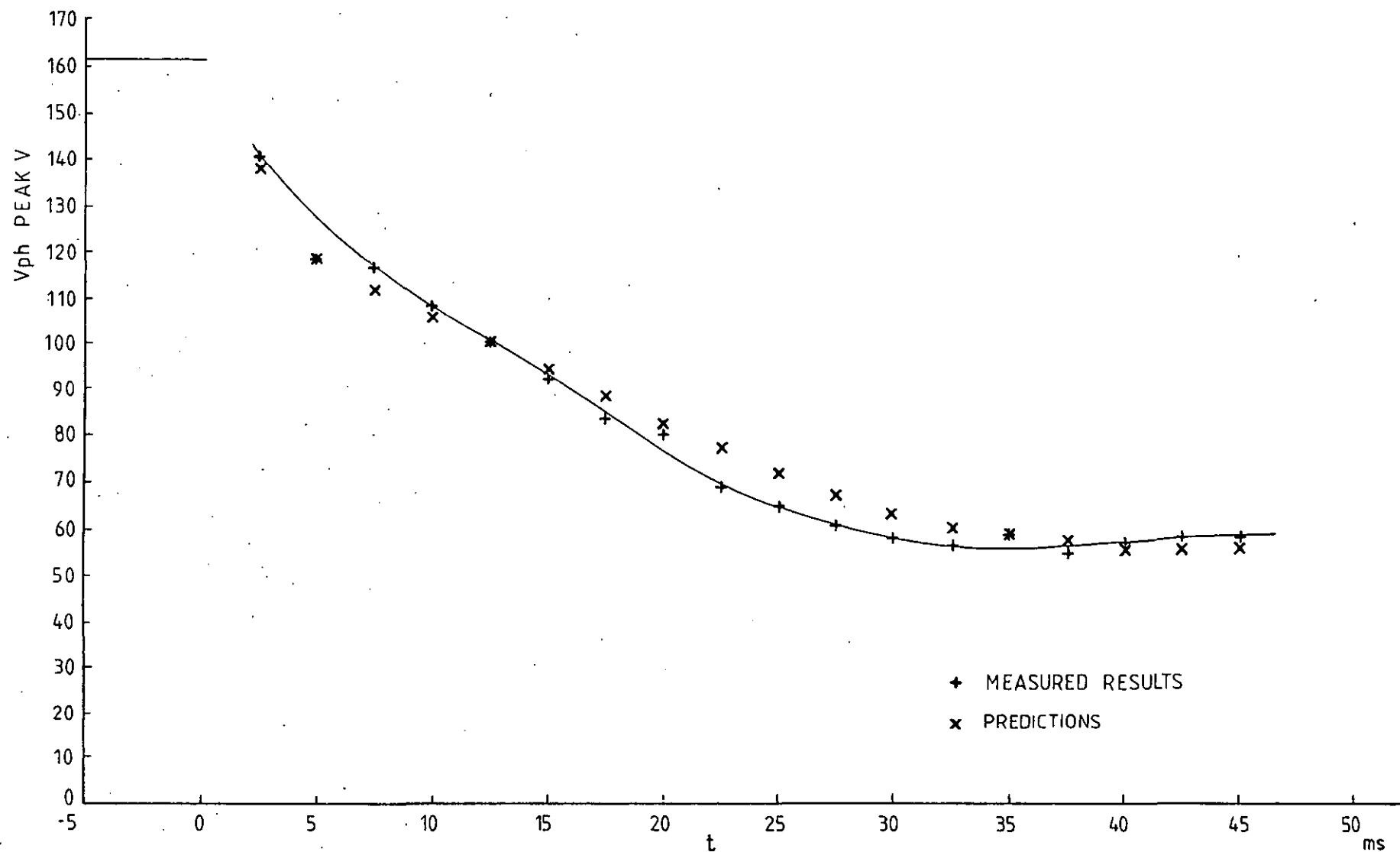


Figure 5.12 APPLICATION OF 60 kVA 0.75 P.F. LOAD

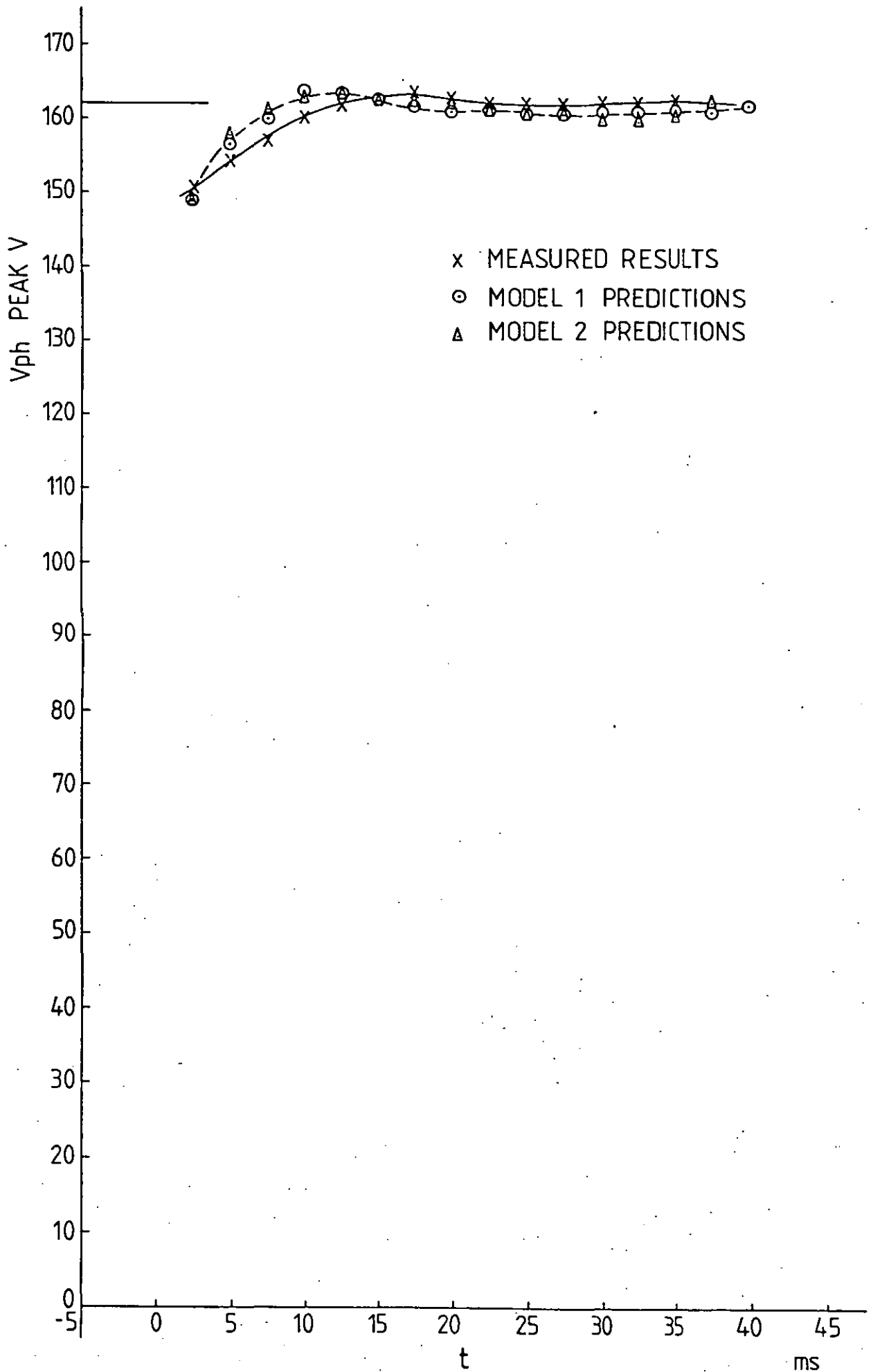


Figure 5.13 40 kVA 1 P.F. LOAD APPLICATION TRANSIENT

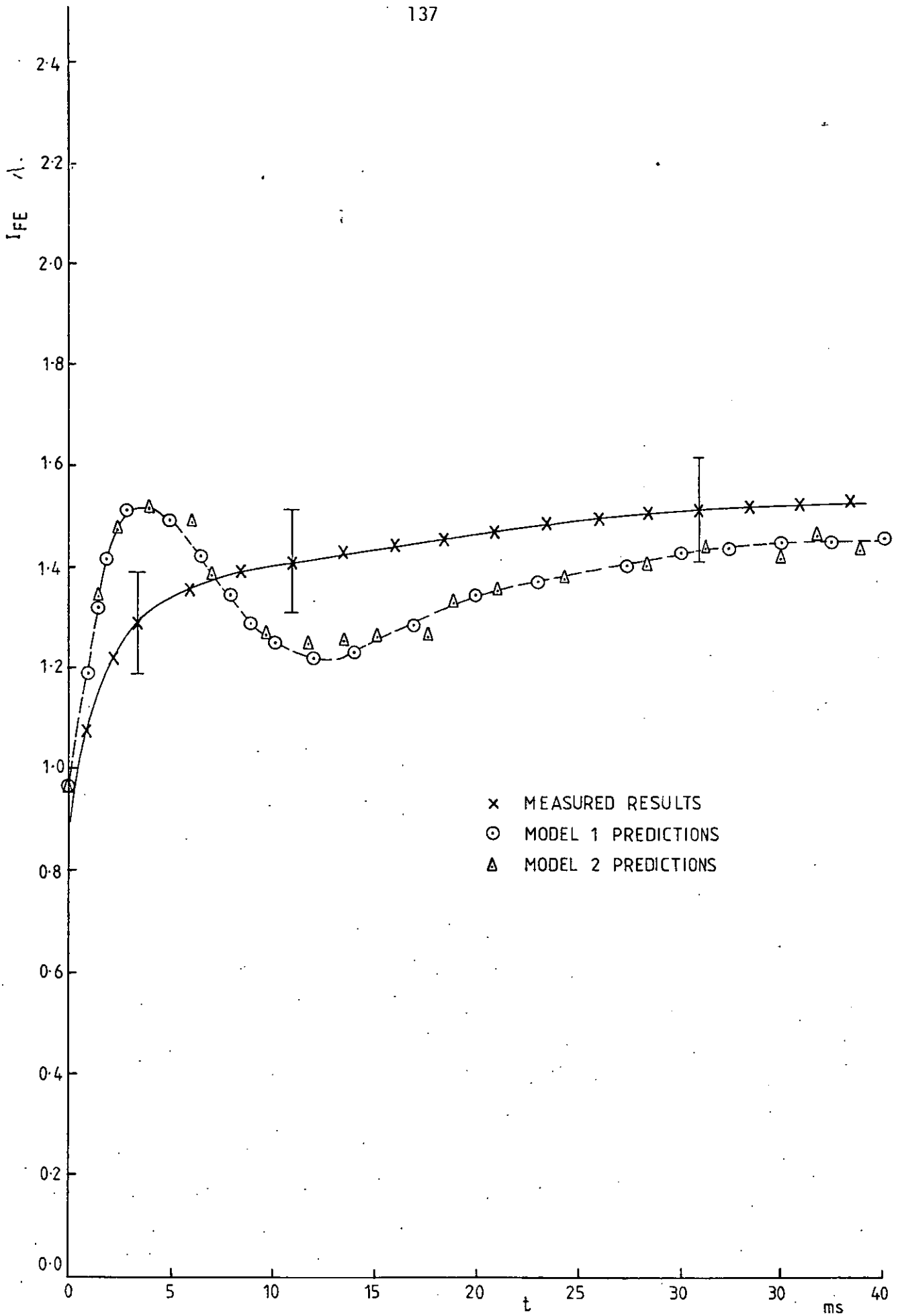


Figure 5.14 40 kVA 1 P.F. LOAD APPLICATION TRANSIENT

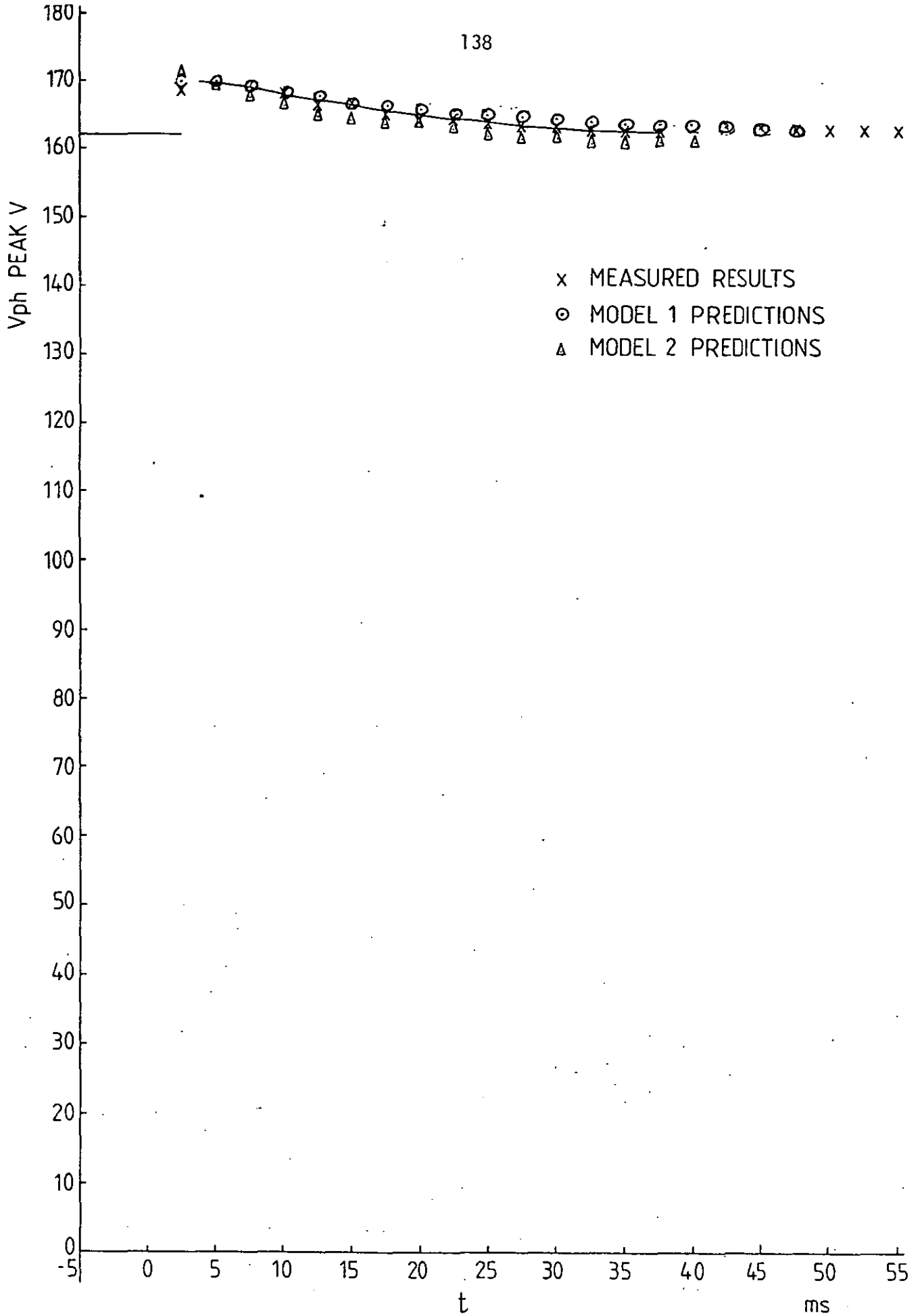


Figure 5.15 40 kVA 1 P.F. LOAD REJECTION TRANSIENT

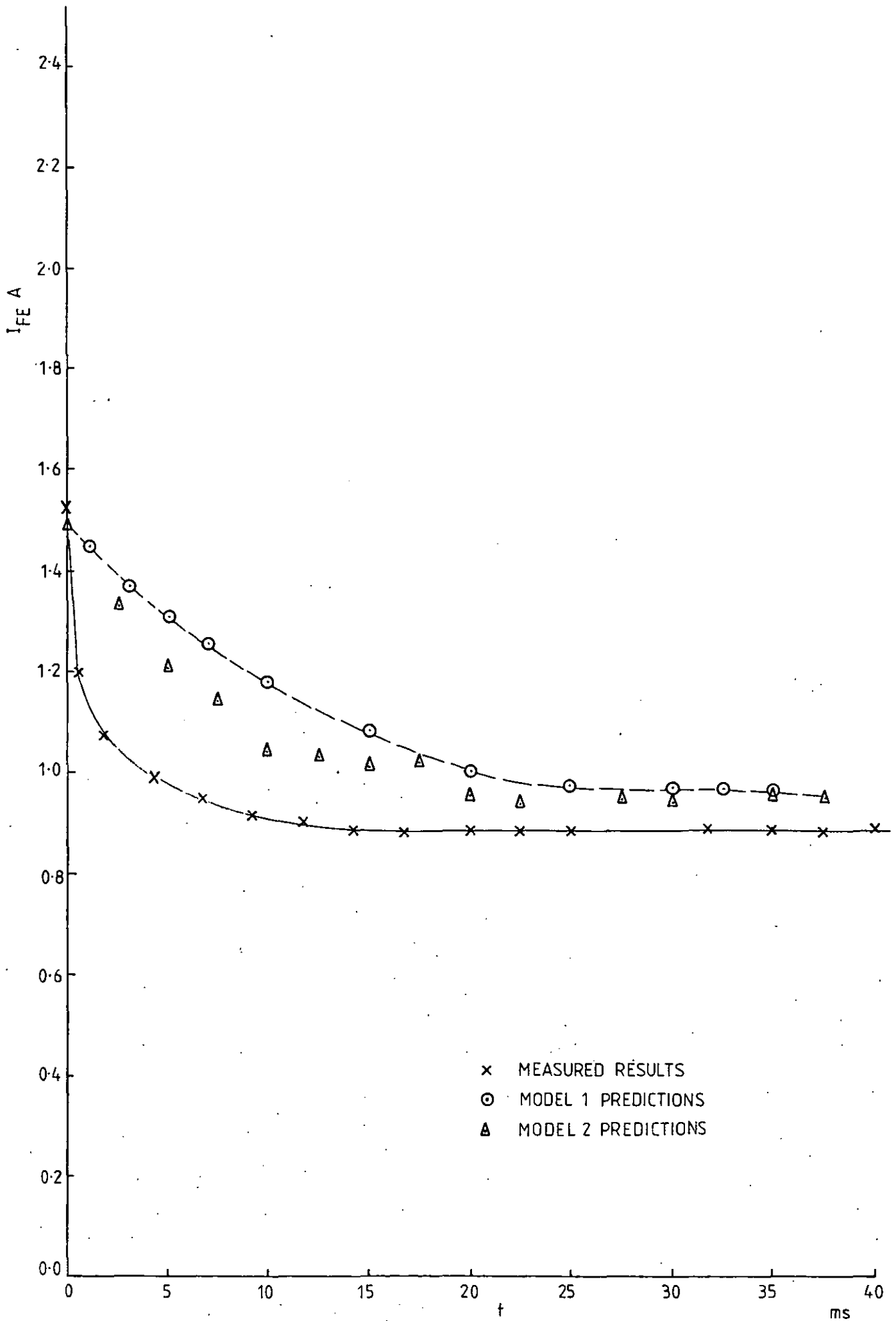


Figure 5.16 40 kVA 1 P.F. LOAD REJECTION TRANSIENT

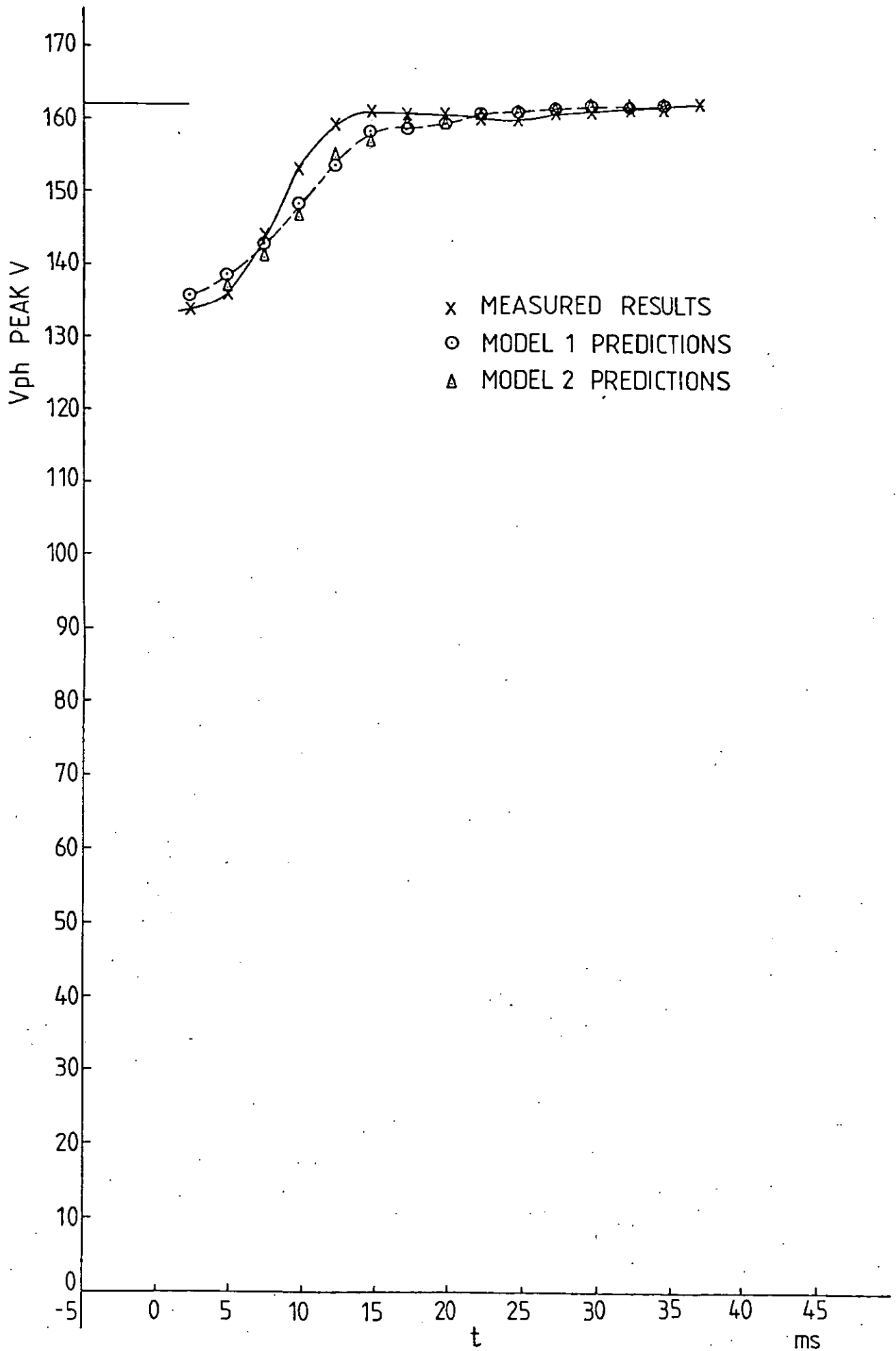


Figure 5.17 40 kVA 0 P.F. LOAD APPLICATION TRANSIENT

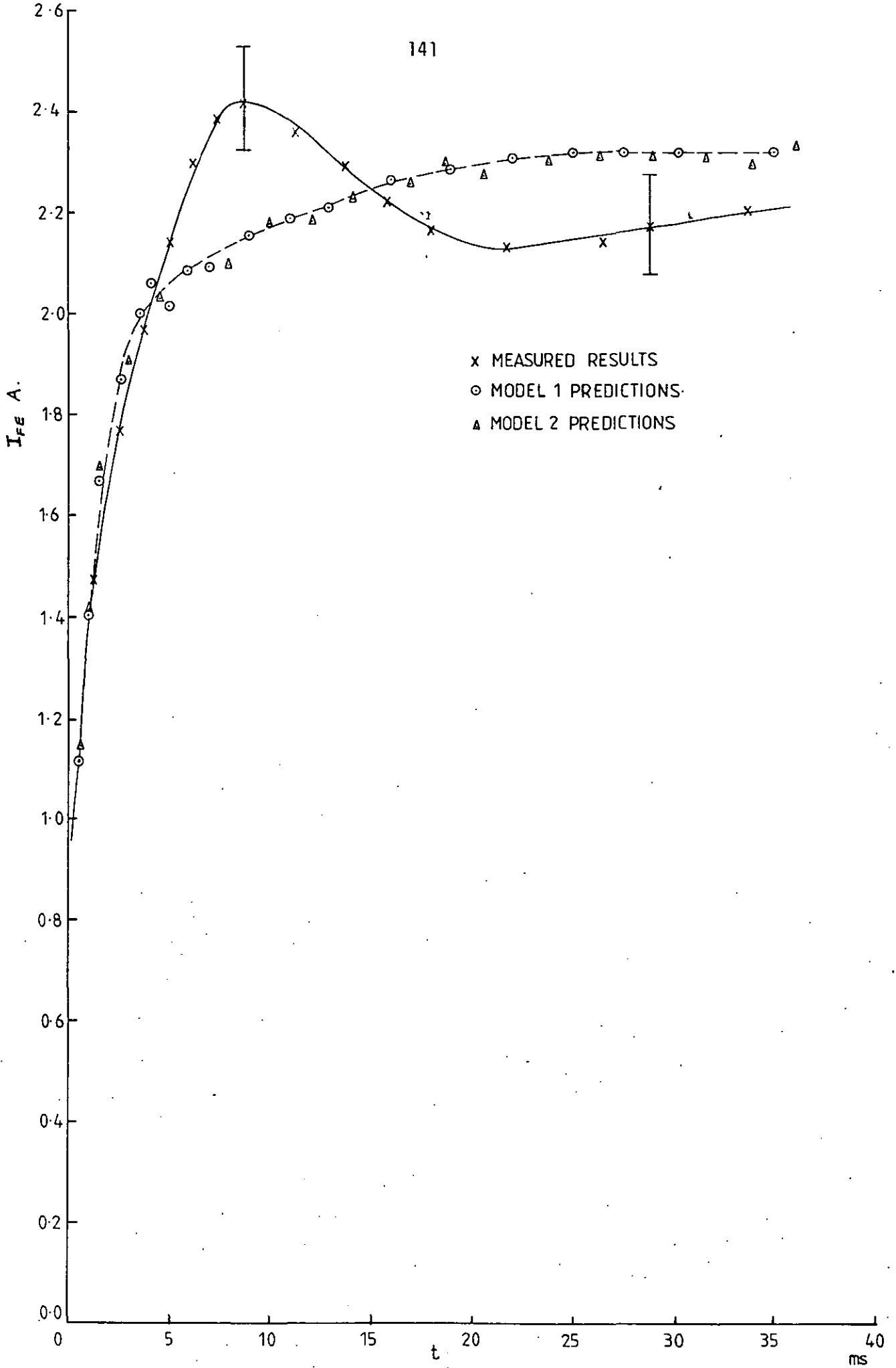


Figure 5.18 40 kVA 0 P.F. LOAD APPLICATION TRANSIENT

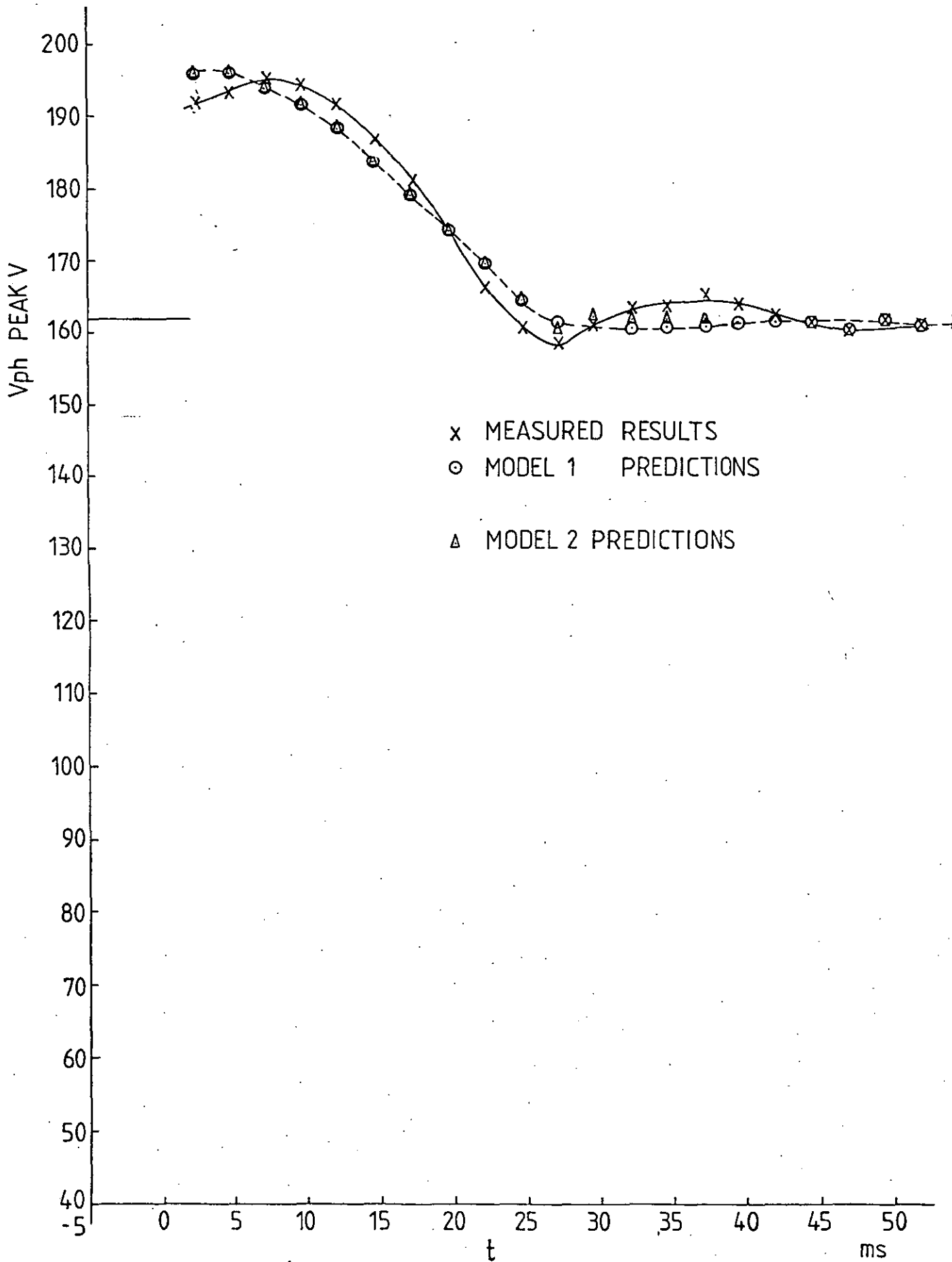


Figure 5.19 40 kVA 0 P.F. LOAD REJECTION TRANSIENT

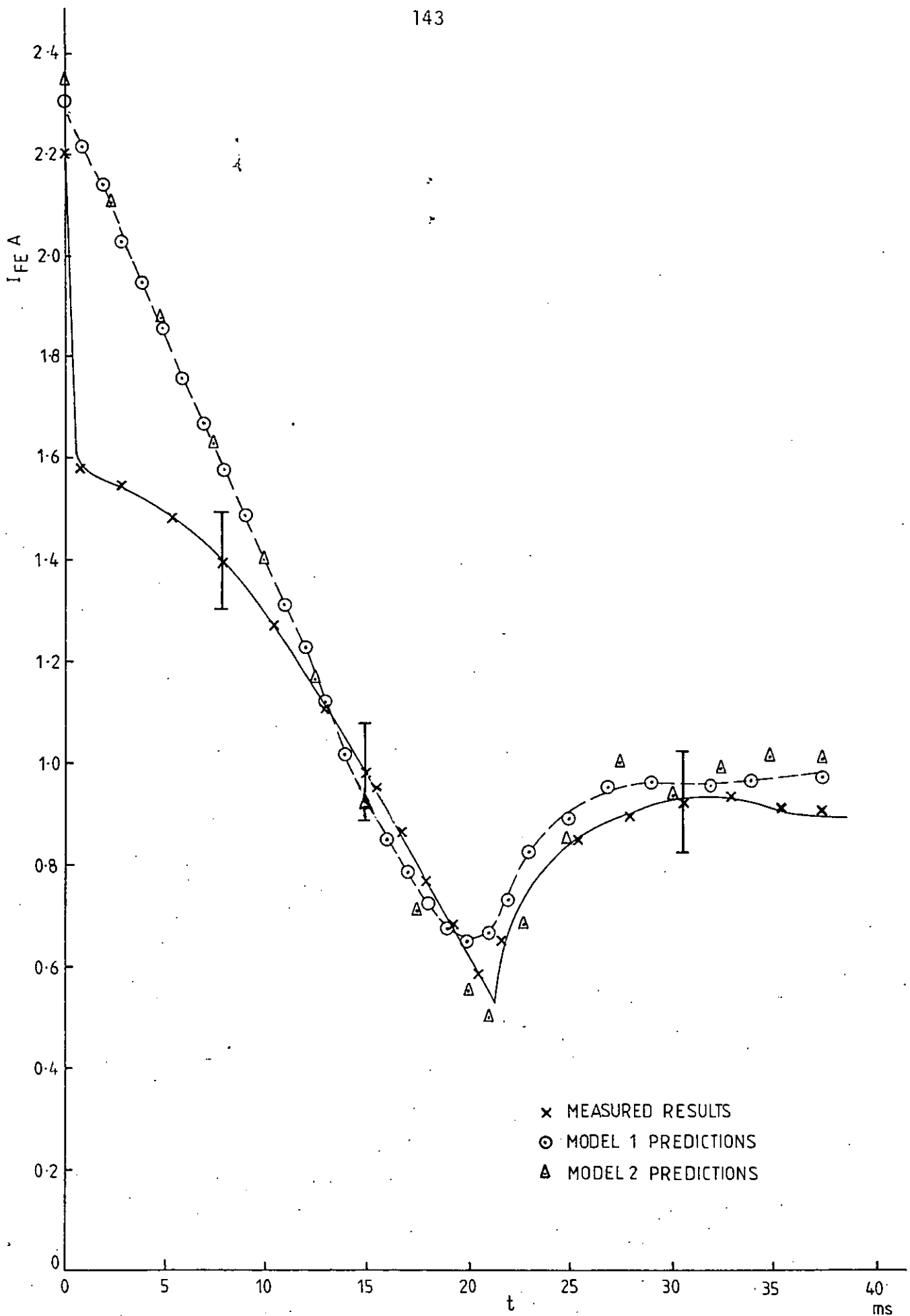


Figure 5.20 40 kVA 0 P.F. LOAD REJECTION TRANSIENT

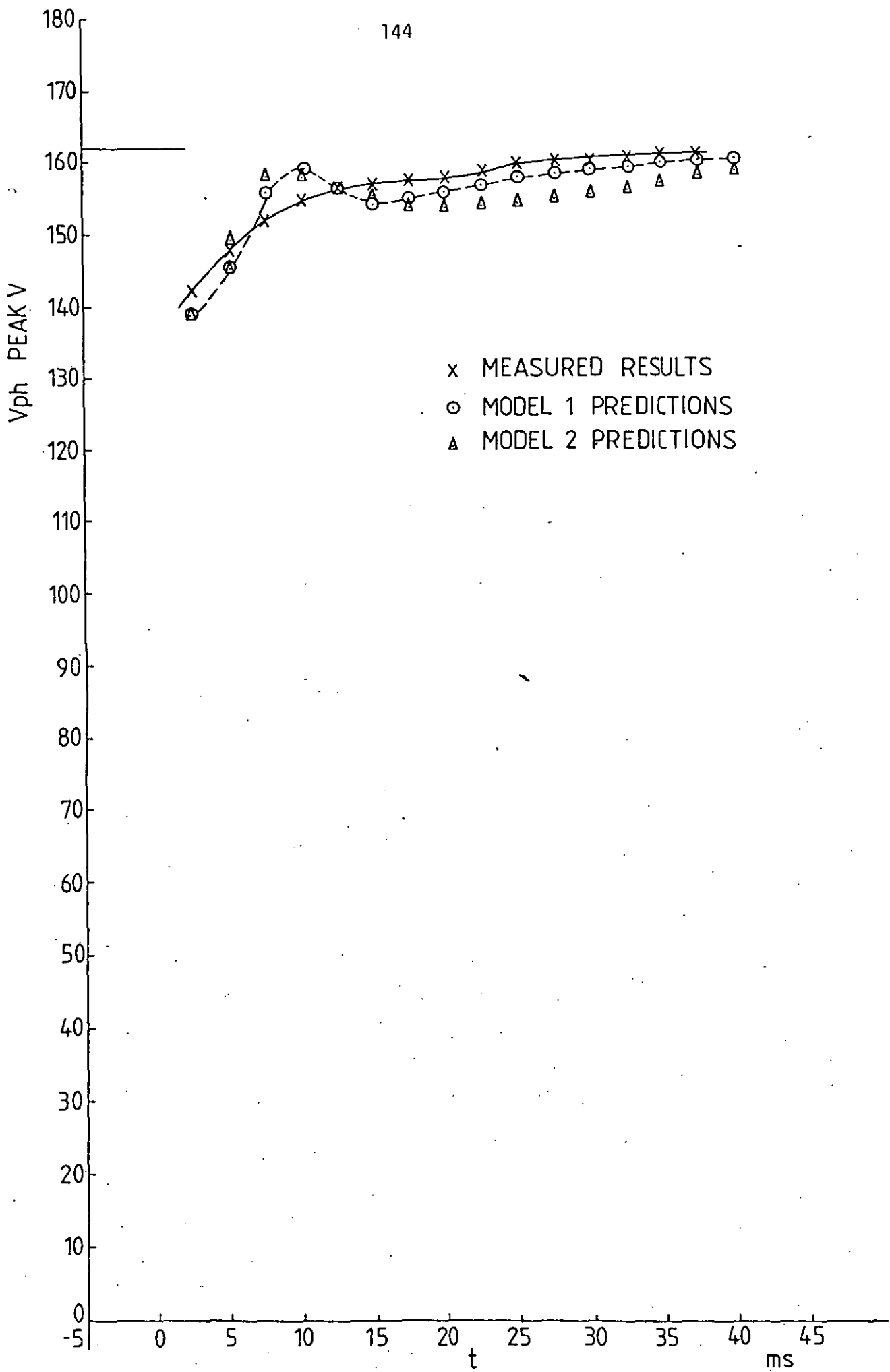


Figure 5.21 60 kVA 1 P.F. LOAD APPLICATION TRANSIENT

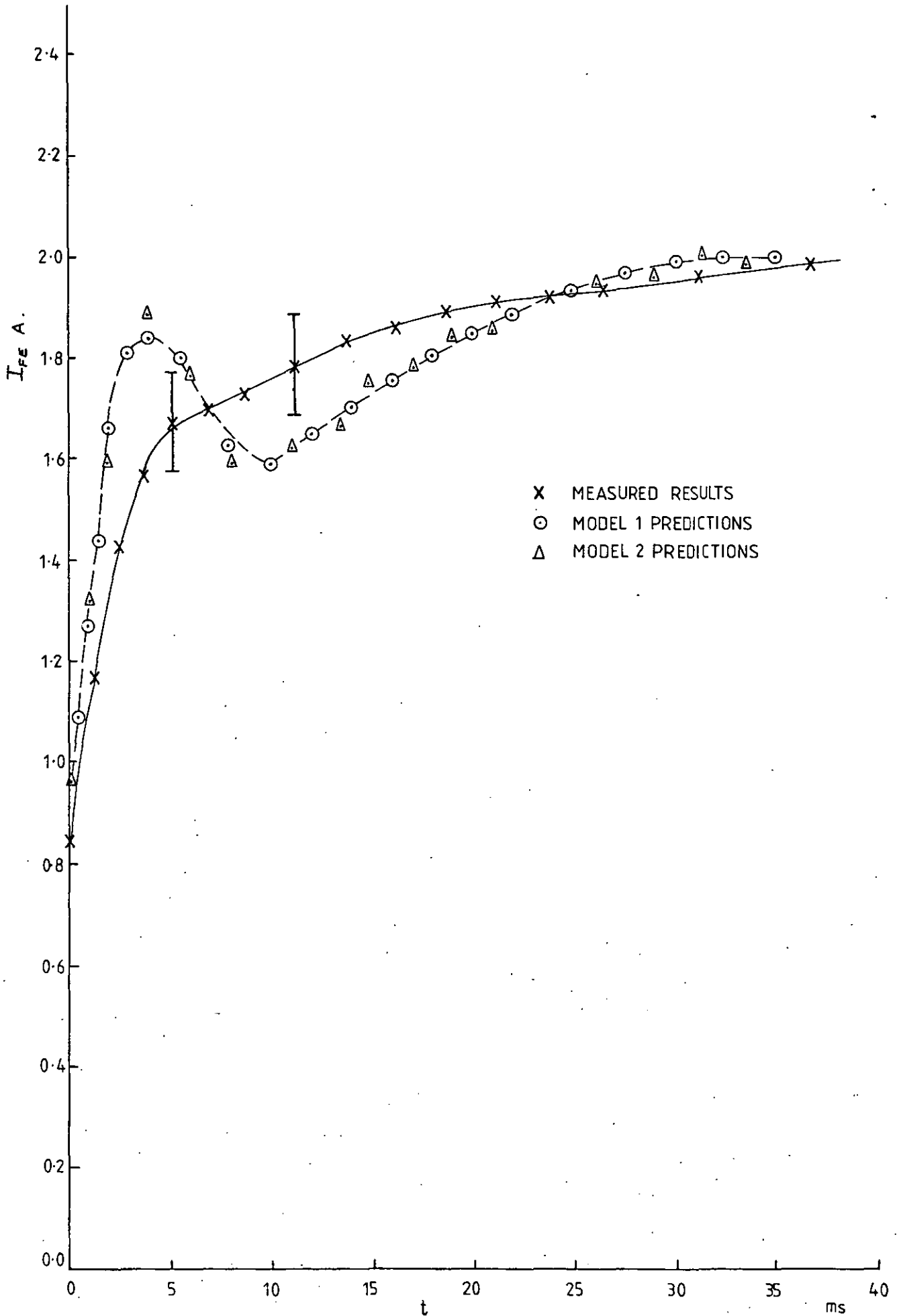


Figure 5.22 60 kVA 1 P.F. LOAD APPLICATION TRANSIENT

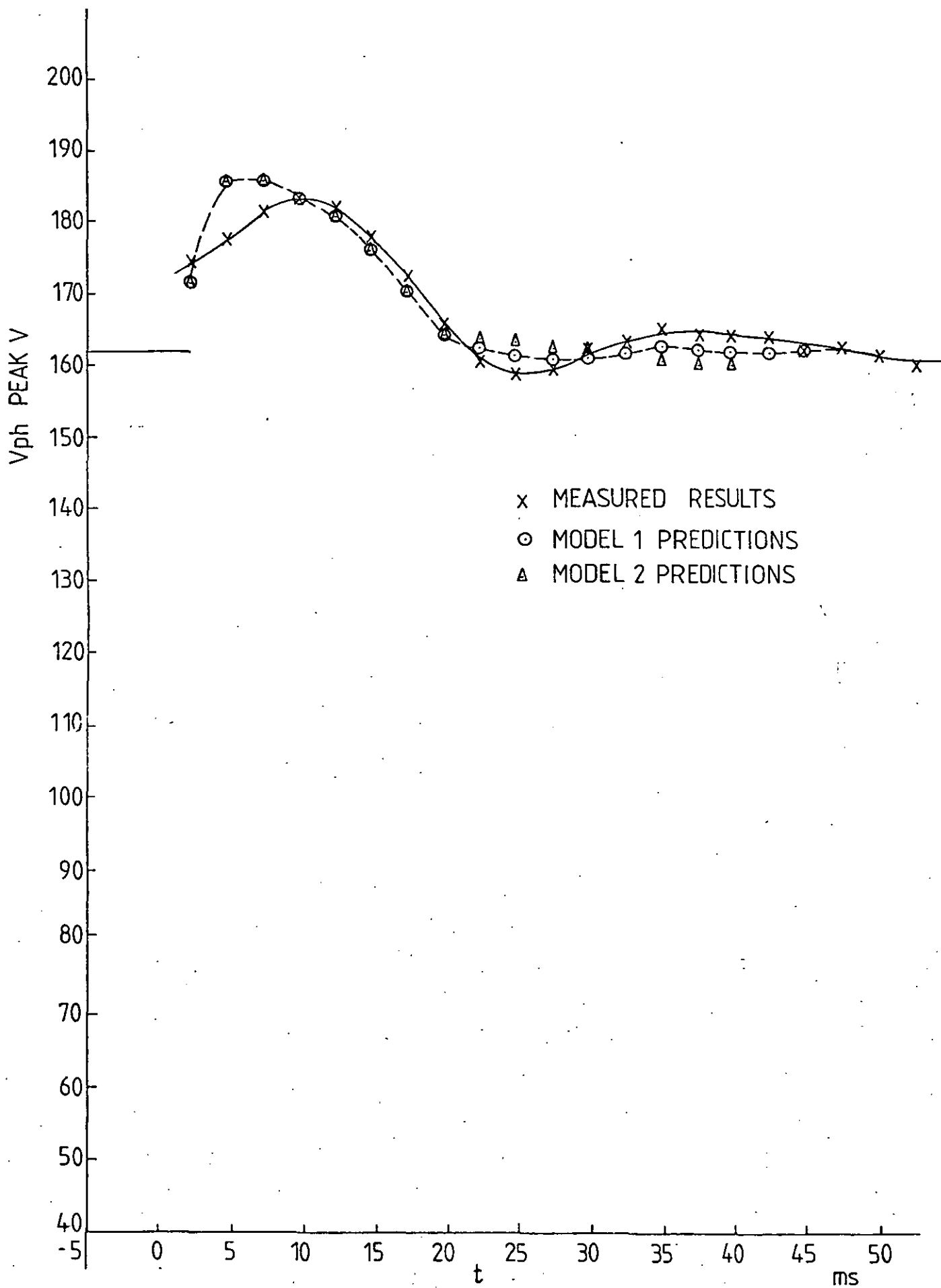


Figure 5.23 60 kVA 1 P.F. LOAD REJECTION TRANSIENT

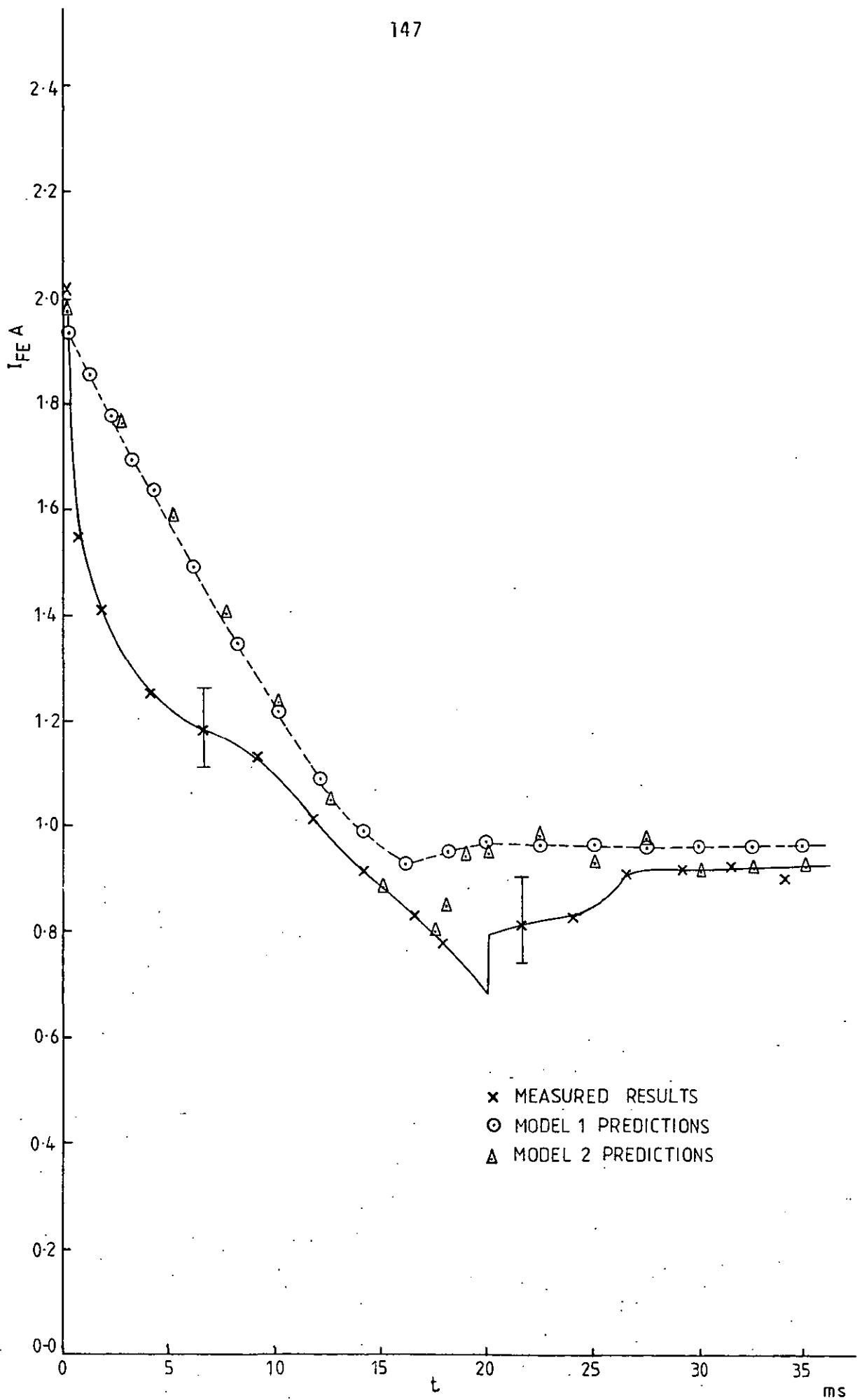


Figure 5.24 60 kVA 1 P.F. LOAD REJECTION TRANSIENT

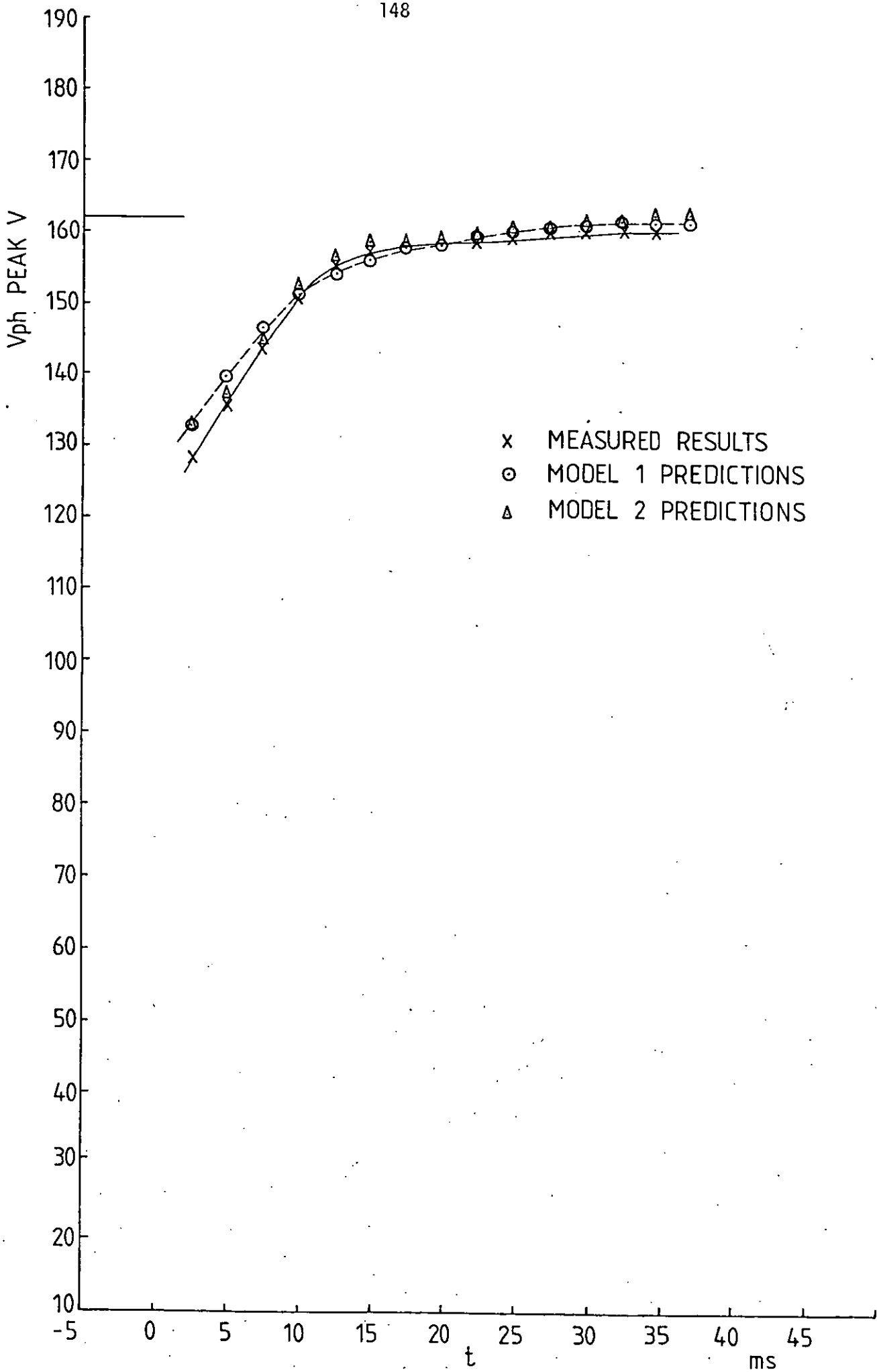


Figure 5.25 60 kVA 0.75 P.F. LOAD APPLICATION TRANSIENT

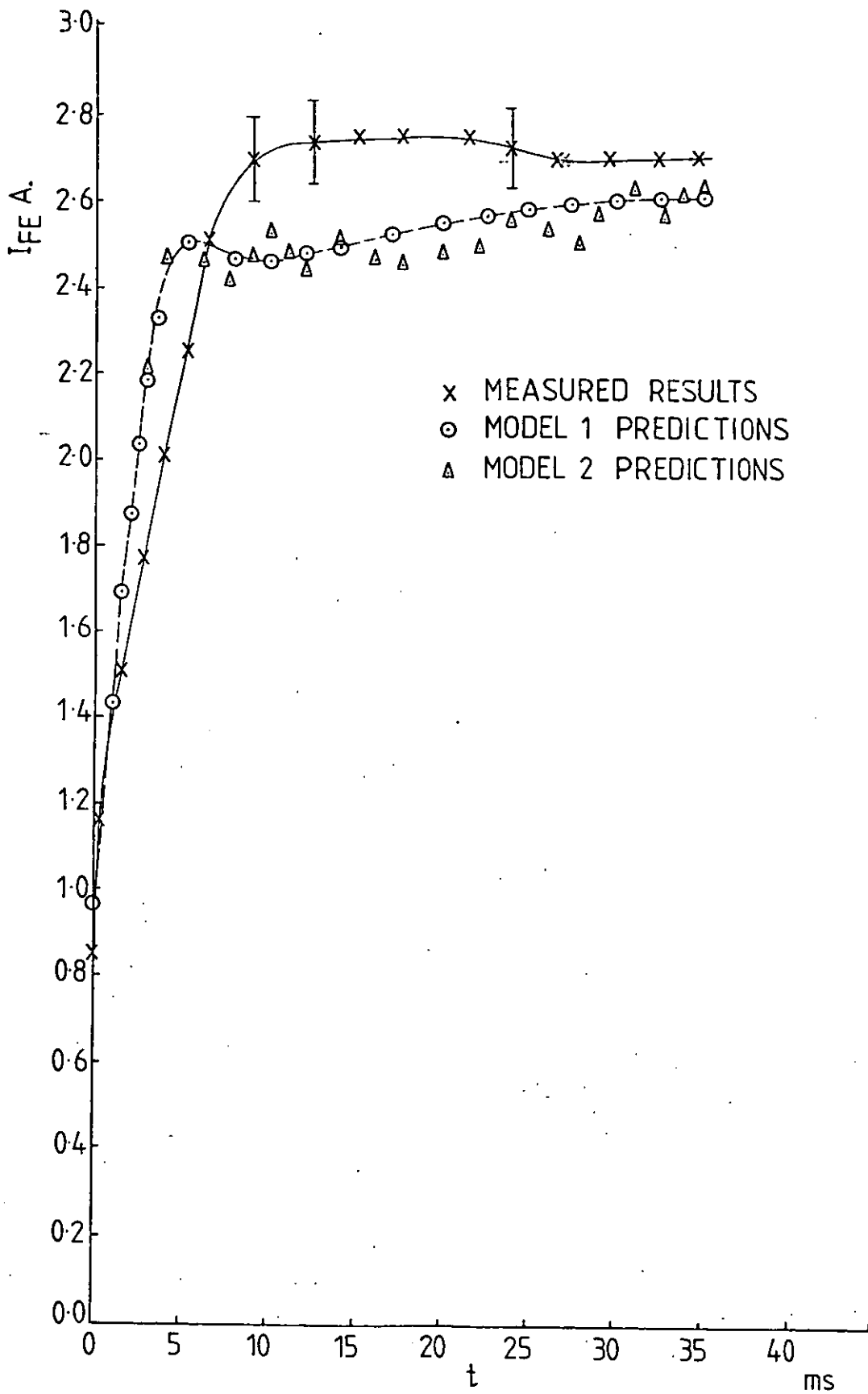


Figure 5.26 60 kVA 0.75 P.F. LOAD APPLICATION TRANSIENT

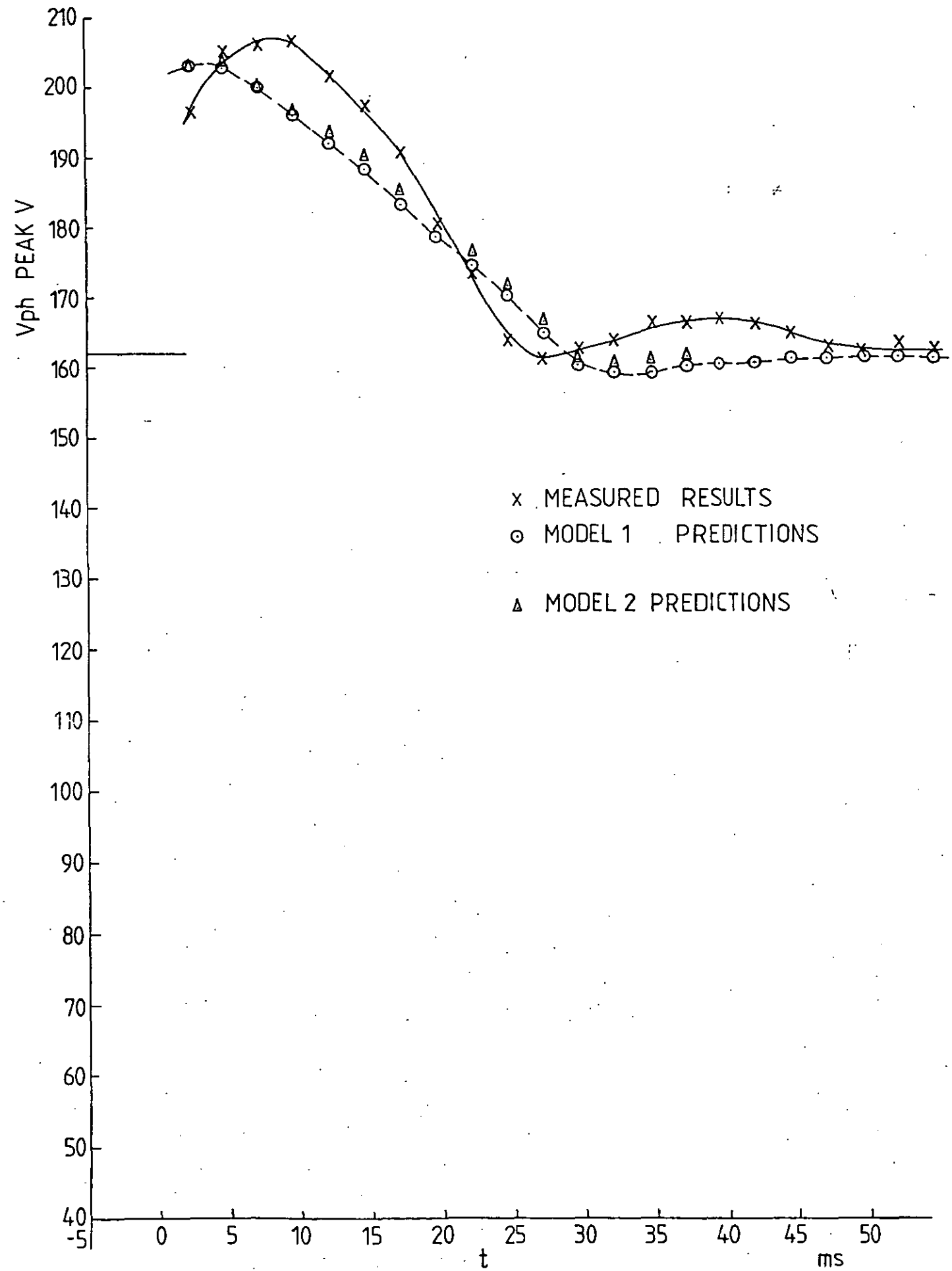


Figure 5.27 60 kVA 0.75 P.F. LOAD REJECTION TRANSIENT

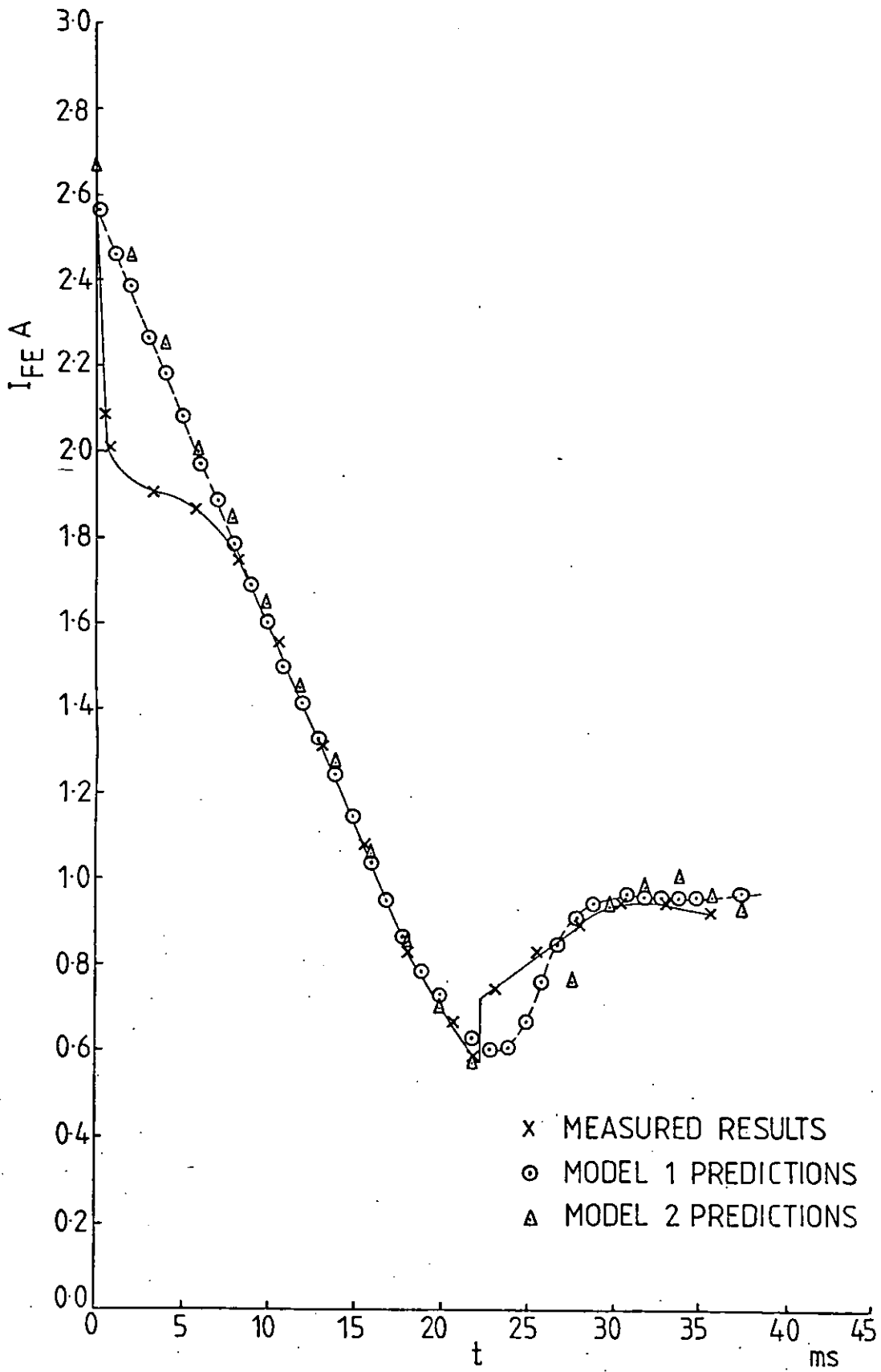


Figure 5.28 60kVA 0.75 P.F. LOAD REJECTION TRANSIENT

CHAPTER 6

THE TRANSFER FUNCTION OF A BRUSHLESS EXCITATION SYSTEM

6.1 Introduction

The modelling of the 3-stage generator unit and the automatic voltage regulator (a.v.r) have been discussed in detail in Chapter 5. It is possible, as shown by the results of the load application and rejection test predictions, that the model of the system is able to predict accurately the response of the exciter, rectifier and the a.v.r. However, from the machine designers viewpoint, this is not an immediately useful exercise, as it does not easily enable him to relate the transient behaviour to the magnitude and power factor of the load change, and the parameters of the main generator and the exciter-rectifier, to arrive at an optimum design for the system. The system model is thus more of an accurate analytical tool than a design tool as far as the exciter-rectifier-generator is concerned. (The a.v.r. design could be optimised by varying the state variables and feedback time constants to obtain a specific transient response on application or rejection of load using the complete model of the system). In this chapter, the transfer function of a synchronous generator is derived which is then used to obtain the complete exciter-rectifier-generator transfer function. The transfer function of the generator is shown to give a clear insight into the effects of varying the parameters of generator and the load.

6.1.1 The Transfer Function of a Synchronous Generator

When a balanced 3-phase load is applied to the terminals of a synchronous generator, it is found that the damper circuits affect only the first cycle or so of the transients, as the time constants of the damper circuits are very much smaller than the transient time constant of the generator. If the effects of the damper windings are neglected, the generator voltage equations⁵⁵ are:

$$e_d = -\psi_q - r i_d + \psi_d p \theta \quad 6.1a$$

$$e_q = \psi_d - r i_q - \psi_q p\theta \quad 6.1b$$

If the further assumption is made that the speed of the rotor does not change on application or rejection of load, equations 6.1 reduce to:

$$e_d = -\psi_q - r i_d \quad 6.2a$$

$$e_q = \psi_d - r i_q \quad 6.2b$$

ψ_d and ψ_q are given by ⁵⁶ :

$$\psi_d = G(p) e_{fd} - x_d(p) i_d \quad 6.3a$$

$$\psi_q = -x_q(p) i_q \quad 6.3b$$

with

$$x_d(p) = \frac{T_{do}' x_d' p + x_d}{T_{do}' p + 1} \quad 6.4a$$

$$T_{do}' = \frac{x_{ffd}}{2\pi f r_{fd}} \quad 6.4b$$

$$x_q(p) = x_q \quad 6.4c$$

where e_{fd} , x_{ffd} , r_{fd} are the field winding voltage, reactance and resistance when referred to the armature d-axis winding.

Also

$$G(p) e_{fd} = \left(\frac{x_{ad}}{r_{fd}} \right) \frac{1}{1 + T_{do} p} e_{fd} \quad 6.5$$

Substituting values of ψ_d , ψ_q from equation 6.3 into equation 6.2 gives

$$e_d = x_q(p) i_q - r i_d \quad 6.6a$$

$$e_q = G(p) e_{fd} - x_d(p) i_d - r i_q \quad 6.6b$$

When the armature is on open circuit, $i_d = i_q = 0$. Therefore:

$$e_d = 0 \quad 6.7a$$

$$e_q = G(p) e_{fd} \quad 6.7b$$

Under steady-state conditions:

$$e_q = e_{q0} = \frac{x_{ad}}{r_{fd}} e_{fd} \quad 6.8$$

If the armature terminals are short-circuited while maintaining the excitation voltage e_{fd} constant,

$$0 = x_q(p) i_q - r i_d \quad 6.9a$$

$$0 = e_{q0} - x_d(p) i_d - r i_q \quad 6.9b$$

Substituting $x_q(p)$ and $x_d(p)$ from equations 6.4 into equations 6.9a and b gives

$$e_{q0} = \frac{(x_d x_q + r^2)}{x_q} \left[\frac{1 + p T'_{dz}}{1 + p T'_{do}} \right] i_d \quad 6.10a$$

$$\text{where } T'_{dz} = T'_{do} \left(\frac{x_q x'_d + r^2}{x_q x_d + r^2} \right) \quad 6.10b$$

The Laplace transform for a short circuit of the armature terminals is $\frac{-e_{q0}}{s}$, when equation 6.10a becomes

$$i_d(s) = \frac{e_{q0}}{s} \frac{x_q}{(x_d x_q + r^2)} \cdot \frac{(1 + s T'_{do})}{(1 + s T'_{dz})}$$

which gives

$$i_d(t) = e_{q0} \frac{x_q}{(x_d x_q + r^2)} \left\{ 1 + \left(\frac{T'_{do}}{T'_{dz}} - 1 \right) e^{-t/T'_{dz}} \right\} \quad 6.12$$

and from equation 6.9a

$$i_q(t) = \frac{r}{x_q} i_d(t) \quad 6.13$$

Using the transformation equation 57

$$[i]_{abc} = [C]_t [i]_{dqo}$$

gives the peak value of armature current as

$$\hat{i}_a = \sqrt{\frac{2(i_d^2 + i_q^2)}{3}} = \sqrt{\frac{2}{3}} \frac{Z_q}{x_q} i_d \quad 6.14$$

$$\text{where } Z_q = \sqrt{x_q^2 + r^2}$$

Substituting for $i_d(t)$ from equation 6.12 into equation 6.14 gives

$$\hat{i}_a = \sqrt{\frac{2}{3}} \frac{Z_q e_{q0}}{(x_d x_q + r^2)} \quad 6.15$$

under steady state condition.

If instead of short circuiting the generator, a 3-phase balanced load of reactance X and resistance R per phase is applied

$$\hat{i}_a = \sqrt{\frac{2}{3}} \frac{Z_{q\Sigma} e_{q0}}{(x_{d\Sigma} x_{q\Sigma} + r_{\Sigma}^2)} \quad 6.16a$$

where Σ signifies the summation of the respective impedances,

$$\text{i.e. } Z_{q\Sigma} = \sqrt{(x_q + X)^2 + (r + R)^2} \quad 6.16b$$

$$x_{d\Sigma} = x_d + X \quad 6.16c$$

$$x_{q\Sigma} = x_q + X \quad 6.16d$$

$$r_{\Sigma} = r + R \quad 6.16e$$

$$x_{d\Sigma}' = x_d' + X \quad 6.16f$$

The transient time constant on load is given by

$$T_{dz}' = T_{do}' \left(\frac{x_{q\Sigma} x_{d\Sigma}' + r_{\Sigma}^2}{x_{q\Sigma} x_{d\Sigma} + r_{\Sigma}^2} \right) \quad 6.16g$$

In terms of the actual field voltage E_f and resistance R_f

$$\frac{e_{fd}}{r_{fd}} = i_{fd} = \sqrt{\frac{2}{3}} \left(\frac{P N_f k_f}{N K_w} \right) \frac{E_f}{R_f} \quad 6.17$$

where $\left(\frac{P N_f k_f}{N K_w} \right)$ is the effective field to armature phase turns ratio ⁵⁸.

Substituting equation 6.17 into equation 6.8 and the result of this into equation 6.16a gives

$$\frac{E_a}{E_f} = K_{go} \frac{Z Z_{q\Sigma}}{(x_{d\Sigma} x_{q\Sigma} + r_{\Sigma}^2)} \quad 6.18$$

where $Z = \sqrt{R^2 + X^2}$, the load impedance per phase and K_{go} is the open circuit gain of the synchronous generator given by

$$K_{go} = \frac{\sqrt{2}}{3} x_{ad} \left(\frac{P N_f k_f}{N K_w} \right) \frac{1}{R_f} \quad 6.19$$

It can be seen from equation 6.18 that the gain of the generator is reduced from its open circuit value of K_{go} by a factor $(Z Z_{q\Sigma} / (x_{d\Sigma} x_{q\Sigma} + r_{\Sigma}^2))$, a load impedance factor which is dependent on both load magnitude and the load power factor. The transient time constant T_{dz}' given in equation 6.16g is also a function of the load impedance and the load power factor.

6.1.2 The Transfer Function of a Brushless Excitation System

The operation of an a.c. exciter - with a full wave rectifier supplying power to a highly inductive load, was discussed in Chapter 5. It was shown that the mode of operation of the exciter rectifier system is dependent on the reactance factor given by $I X_c / E_d$, which if the volt drop across the rectifier is neglected, is very nearly equal to X_c / R_f , where X_c is the commutation reactance of the exciter and R_f , the resistance of the main generator field winding. The mode of operation of the exciter-rectifier *under steady state condition* is independent of the loading on the main generator, as long as X_c and R_f remain constant. It was also shown in Chapter 5 that the rectifier load on the exciter gave rise to non-sinusoidal current flow in the armature windings of the exciter, which can be Fourier analysed to give the in phase and quadrature components of the fundamental-frequency current. The rectifier load therefore presents to the exciter, a load whose magnitude and power factor are dependent on the reactance load factor. If it is assumed that the voltage generated in the phase windings of the exciter is of fundamental frequency, the power flow from the exciter to the generator field winding is associated with the fundamental component of the armature phase current and its phase angle. Therefore considering only the fundamental frequency component of current and voltages in the exciter phase windings:

$$\frac{E_{ae}}{E_{fe}} = K_{eo} \cdot \frac{Z_e Z_{qe}}{(x_{de}^2 + x_{qe}^2 + r_e^2)} \quad 6.20$$

where E_{ae} is the r.m.s. voltage across the effective phase load impedance Z_e given by

$$Z_e = R_e + j X_e = \sqrt{R_e^2 + X_e^2} \quad 6.21a$$

* R_f , depends on the copper losses in the generator field winding and the temperature of the oil spray used for cooling the windings.

Also

$$x_{de\Sigma} = x_{de} + X_e \quad 6.21b$$

$$x_{qe\Sigma} = x_{qe} + X_e \quad 6.21c$$

$$r_{e\Sigma} = r_e + R_e \quad 6.21d$$

$$\text{and } Z_{qe\Sigma} = \sqrt{x_{qe\Sigma}^2 + r_{e\Sigma}^2} \quad 6.21e$$

Also, the open-circuit gain the exciter as given by K_{eo} is

$$K_{eo} = \frac{\sqrt{2} x_{ade}}{3} \left(\frac{P_e N_{fe} k_{fe}}{(N K_w)_e} \right) \frac{1}{R_{fe}} \quad 6.22$$

It is shown in Appendix A10 that the total power supplied to the effective a.c. load equals the d.c. power supplied to the generator field winding.

The exciter transient time constant is given by:

$$T'_{dze} = T_{doe} \left(\frac{x_{qe\Sigma} x_{de\Sigma}' + r_{e\Sigma}^2}{x_{qe\Sigma} x_{de\Sigma} + r_{e\Sigma}^2} \right) \quad 6.23$$

If K_v is the gain of the full-wave rectifier, defined as the ratio of the d.c. output voltage of the rectifier to the a.c. effective load voltage per phase E_{ae} , the gain of the exciter-rectifier system is:

$$\frac{E_f}{E_{fe}} = K_{eo} \frac{Z_e Z_{qe\Sigma}}{(x_{de\Sigma} x_{qe\Sigma} + r_{e\Sigma}^2)} K_v \quad 6.24$$

The overall gain of the exciter-rectifier-generator system is therefore

$$\frac{E_a}{E_{fe}} = K_{eo} K_v K_{go} \frac{Z_e Z_{qe\Sigma}}{(x_{de\Sigma} x_{qe\Sigma} + r_{e\Sigma}^2)} \cdot \frac{Z Z_{q\Sigma}}{(x_{d\Sigma} x_{q\Sigma} + r_{\Sigma}^2)} = G_{eg} \quad 6.25$$

The overall exciter-rectifier-generator transfer function is obtained by including the transient time constants of the generator and the exciter from equations 6.16g and 6.23. This gives

$$\frac{E_a(s)}{E_{fe}(s)} = \frac{G_{eg}}{(1 + s(T_{dz}')_g)(1 + s(T_{dz}')_e)} \quad 6.26$$

It is found from the detailed model of the exciter-rectifier-generator discussed in Chapter 5 that the mode of operation of the rectifier and hence K_v is *not* constant (as is under steady-state condition) during the transient following the application or rejection of a large generator load. Therefore use of equation 6.26 to obtain the transient response of the system for large load transients is grossly in error. However when small loads are applied to or taken from the terminals of the generator, the mode of operation of the rectifier is not substantially altered, and therefore under these conditions equation 6.26 can be used with confidence to predict the transient response.

Furthermore equation 6.26 can be used to study the transient response of the generator with or without load, following a change in the exciter field voltage, as under this condition the mode of operation of the rectifier does not change substantially from that during steady-state operational condition. The gain of the exciter-

rectifier-generator as given by equation 6.25 is very useful, as the effect of the changes in the generator loading can be easily seen as changes in the load impedance factor ($Z Z_{q\Sigma} / (x_{d\Sigma} x_{q\Sigma} + r_{\Sigma}^2)$) of the generator. Assuming the resistance of the generator field winding remains constant (constant temperature of the field winding), the a.c. load as seen by the exciter remains constant, and hence ($Z_e Z_{qe\Sigma} / (x_{de\Sigma} x_{qe\Sigma} + r_{e\Sigma}^2)$) in equation 6.25 is also constant. Therefore the simplified form of this equation

$$\frac{E_a}{E_{fe}} = \frac{Z Z_{q\Sigma}}{(x_{d\Sigma} x_{q\Sigma} + r_{\Sigma}^2)} \times \text{constant} \quad 6.27$$

can be used to calculate the exciter field voltage for different loads applied at the generator terminals. Comparison between the measured and the calculated exciter field current for different steady-state loads applied at the generator terminals while maintaining rated terminal voltage are given in Table 6.1.

Load applied to the generator terminals (p.u)	Measured Value of I_{fe} , A	Calculated Value of I_{fe} , A
Open circuit	0.848	0.872
1 p.u. 0.75 p.f.	1.915	1.996
1.5 p.u. 0.75 p.f.	2.760	2.630

TABLE 6.1

Comparison of measured and predicted values of the exciter field current given in Table 6.1 shows that equations 6.25 and 6.27 can be used to predict the exciter field current accurately over a wide range of values of generator loads.

6.2 The Effect of Changing the Reactance Load Factor and the Generator Field Winding Resistance on the Performance of the Exciter-Rectifier

6.2.1 The Effect of Changing the Reactance Load Factor

The performance of the exciter-rectifier for different values of the reactance load factor (X_c/R_f) were obtained using the rectifier operation equations of Chapter 5. The results obtained are as given in Table 6.2.

The changes in the voltage gain K_v and the current gain K_c with changes in (X_c/R_f) are given in Figure 6.1. The current gain K_c is defined as

$$K_c = \frac{\text{d.c. output current of the rectifier}}{\text{r.m.s. value of the fundamental frequency current}} \quad 6.28$$

It can be seen that as (X_c/R_f) increases and the operation moves into modes II and III, there is a sharp fall in K_v . Accompanying this shift is an increase in the effective power factor angle ϕ_e of the load as shown in Figure 6.2, due to the increase in the reactive component X_e compared with the resistive component R_e . The terms X_e/R_f and R_e/R_f are also shown as a function of reactance load factor in Figure 6.2 to show this increase in the reactive component X_e compared with the resistive component R_e .

6.2.2 The Effect of Changing the Generator Field Winding Resistance

The optimum operating point of the exciter-rectifier system is when it is delivering maximum power to the generator field winding per unit exciter field current. Under this condition, the generator field winding m.m.f. and hence the flux density in the generator air-gap is maximum. This can be proved as follows.

The resistance of the generator field winding R_f is:

$$\begin{aligned}
 R_f &= \frac{\rho \ell_f P N_f}{a_f} \\
 &= \rho \ell_f \frac{P N_f^2}{A_f}
 \end{aligned}
 \tag{6.29}$$

where ρ is the resistivity of copper, ℓ_f is the mean length of turn, P the number of poles, N_f the number of turns per pole, a_f the cross-section area of conductor and A_f the total copper cross-section area of the coil of the generator field winding.

If I_f is the generator field winding current, P_f the total power supplied to the generator field winding is

$$\begin{aligned}
 P_f &= I_f^2 \cdot R_f = \frac{\rho \ell_f P}{A_f} (N_f I_f)^2 \\
 &= \text{constant} \times (N_f I_f)^2
 \end{aligned}
 \tag{6.30}$$

It can be seen from equation 6.30 that $N_f I_f$, the m.m.f. of the generator field winding per pole is maximum when P_f is maximum.

The optimum operating point of the exciter-rectifier system of the 2130 generator unit was found by varying the resistance of the generator field winding while maintaining constant the parameters X_{de} , X_{qe} , X_{de}' , X_c of the exciter.

In terms of the exciter field current, the generator field current is

$$\frac{I_f}{I_{fe}} = \frac{\sqrt{2}}{3} \left(\frac{P_e N_{fe} k_{fe}}{(N K_w)_e} \right) \cdot x_{ade} \cdot \left\{ \frac{Z_{qe\Sigma} K_c}{x_{de\Sigma} x_{qe\Sigma} + r_{e\Sigma}^2} \right\}
 \tag{6.31}$$

and the output power of the exciter-rectifier P_f is

$$P_f = I_f^2 R_f = E_f I_f \quad 6.32$$

As R_f is decreased from the nominal 1.161 ohms to 0.00926 ohms, the mode of operation of the exciter-rectifier changes from mode I to mode II and III. The variations of X_e , R_e , I_f/I_{fe} , E_f/I_{fe} and P_f/I_{fe}^2 with the resulting changes in X_c/R_f are shown in Figure 6.3, and the important intermediate results of the calculations are given in Tables 6.3(a) and 6.3(b).

It will be seen from both Figures 6.1 and 6.3 that the maximum voltage gain K_v and the maximum power transfer to the generator field windings per unit exciter field current (P_f/I_{fe}^2) are obtained by operation of the exciter-rectifier in mode I.

6.3 Discussion and Comments

The transfer function of the complete exciter-rectifier-generator system is derived in terms of the parameters of the system that are usually available from the manufacturers. A useful advantage of an approach using the transfer functions is that it enables the effect of a load applied to the generator terminals to be identified with the corresponding exciter field current required to maintain rated output voltage. The load impedance factor of the generator can be used to determine the effect of both the load and the load power factor on the gain of the generator. The effect of the rectifier load on the exciter is reduced to an effective a.c. load applied to its terminals, which is a function of the reactance load factor. This enables the rectifier load to be represented in the same form as the generator.

The effect of changing the operation of the exciter-rectifier system by changing the reactance load factor and the main generator field resistance are investigated to show that there is an optimum operating point for the exciter-rectifier system used on the 3-stage generator unit in mode I.

The transfer function of the exciter-rectifier-generator system is used to predict the exciter field current for a wide range of loads applied to the generator, as given in Table 6.1. It is shown that the predictions are very close to the actual values of exciter field current obtained from tests on the system.

Mode	$\frac{X_c}{R_f}$ (RLF)	α	μ	ϕ_e	K_v	K_c	$\frac{Z_\Delta}{R_f}$	$\frac{Z_e}{R_f}$
I	0	0	0	0	2.34	1.2825	0	0.5483
Boundary I-II	$\pi/9$	0	60	-39.3°	1.7544	1.3236	0.333	0.7545
Boundary II-III	$\pi/3$	30	60	-59.9°	1.0129	1.4837	1.309	1.4648
III	4.862	30	90	-77.5°	0.6271	1.518	7.636	5.593
III	∞	30	120	-90°	0	1.600	∞	∞

Table 6.2 THE EFFECT OF RLF ON EXCITER-RECTIFIER CHARACTERISTICS

R_f	X_c/R_f	α	μ	Mode	X_e/R_f	X_e	R_e/R_f	R_e
1.161	0.0388	0	21.8°	I	0.1429	0.166	0.5528	0.6418
0.775	0.0582	0	26.5°	I	0.1764	0.1365	0.555	0.4296
0.387	0.1163	0	36.9°	I	0.2550	0.09865	0.5613	0.2172
0.129	0.3491	0	60°	I-II Boundary	0.4779	0.0616	0.5839	0.0753
0.0430	1.0472	30	60°	II-III Boundary	1.2673	0.0545	0.7346	0.0316
0.00926	4.8618	30	90°	III	5.46	0.0506	1.2115	0.0112

Table 6.3(a) EFFECT OF VARYING GENERATOR FIELD RESISTANCE ON
EXCITER-RECTIFIER CHARACTERISTICS

α	μ	I_f/I_{fe}	E_f/I_{fe}	P_f/I_{fe}^2
0	21.8°	14.90	17.30	258
0	26.5°	19.50	15.09	294
0	36.9°	27.49	10.64	292
0	60°	37.02	4.78	177
30	60°	44.56	1.92	86
30	90°	47.05	0.436	20.5

Table 6.3(b) EFFECT OF VARYING GENERATOR FIELD RESISTANCE ON
EXCITER-RECTIFIER CHARACTERISTICS

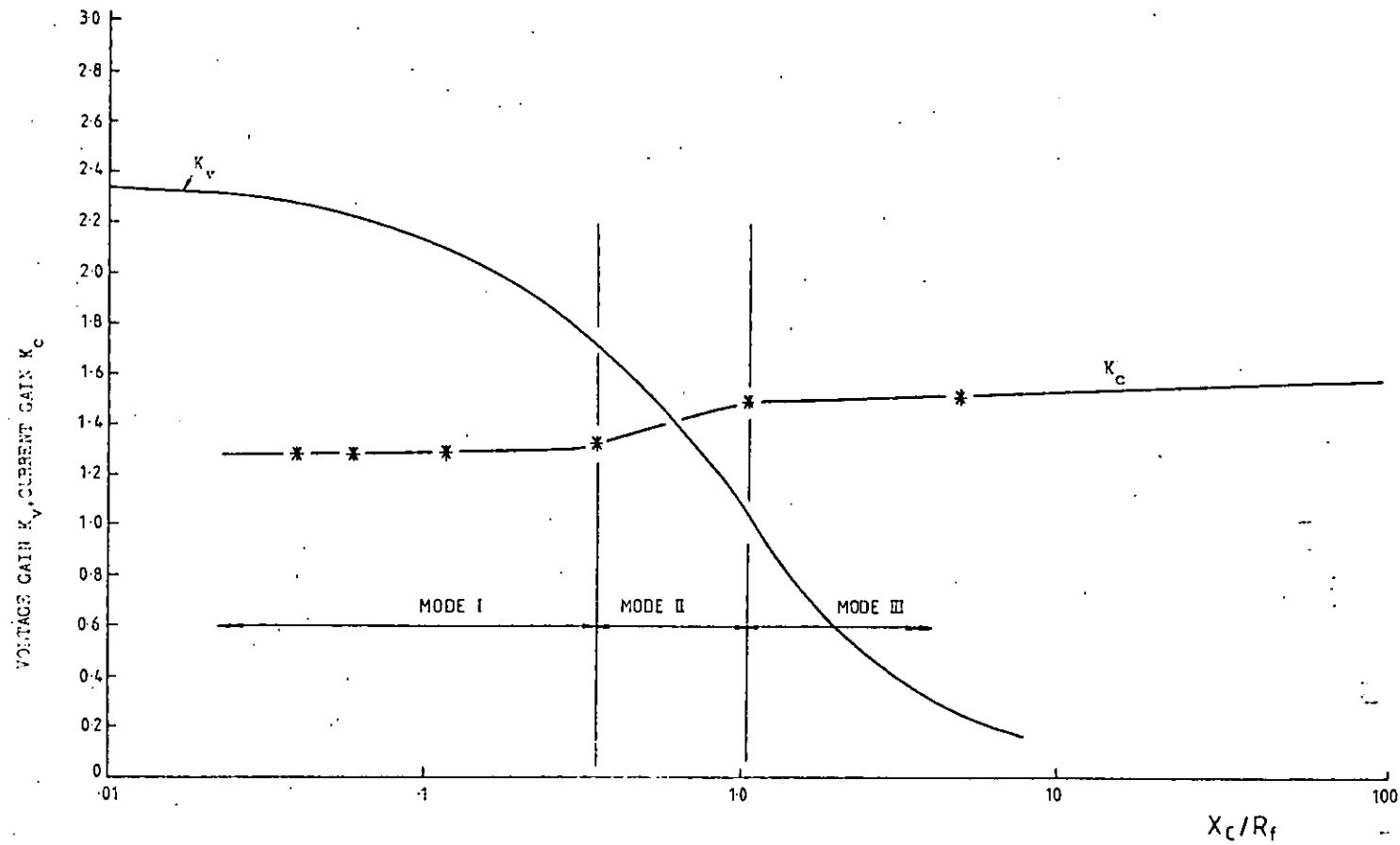


FIGURE 6.1 EXCITER RECTIFIER O/P CHARACTERISTICS

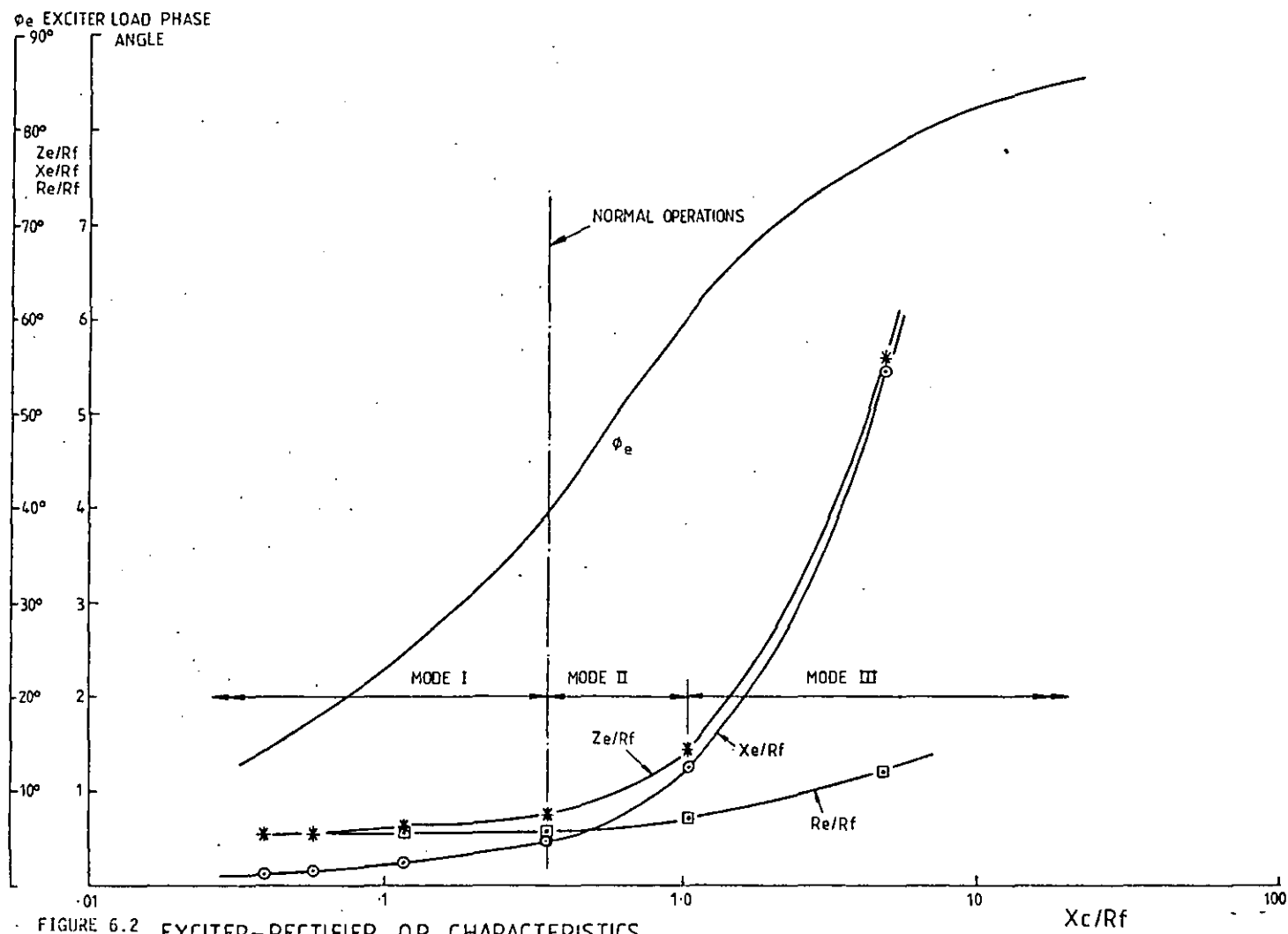


FIGURE 6.2 EXCITER-RECTIFIER O.P. CHARACTERISTICS

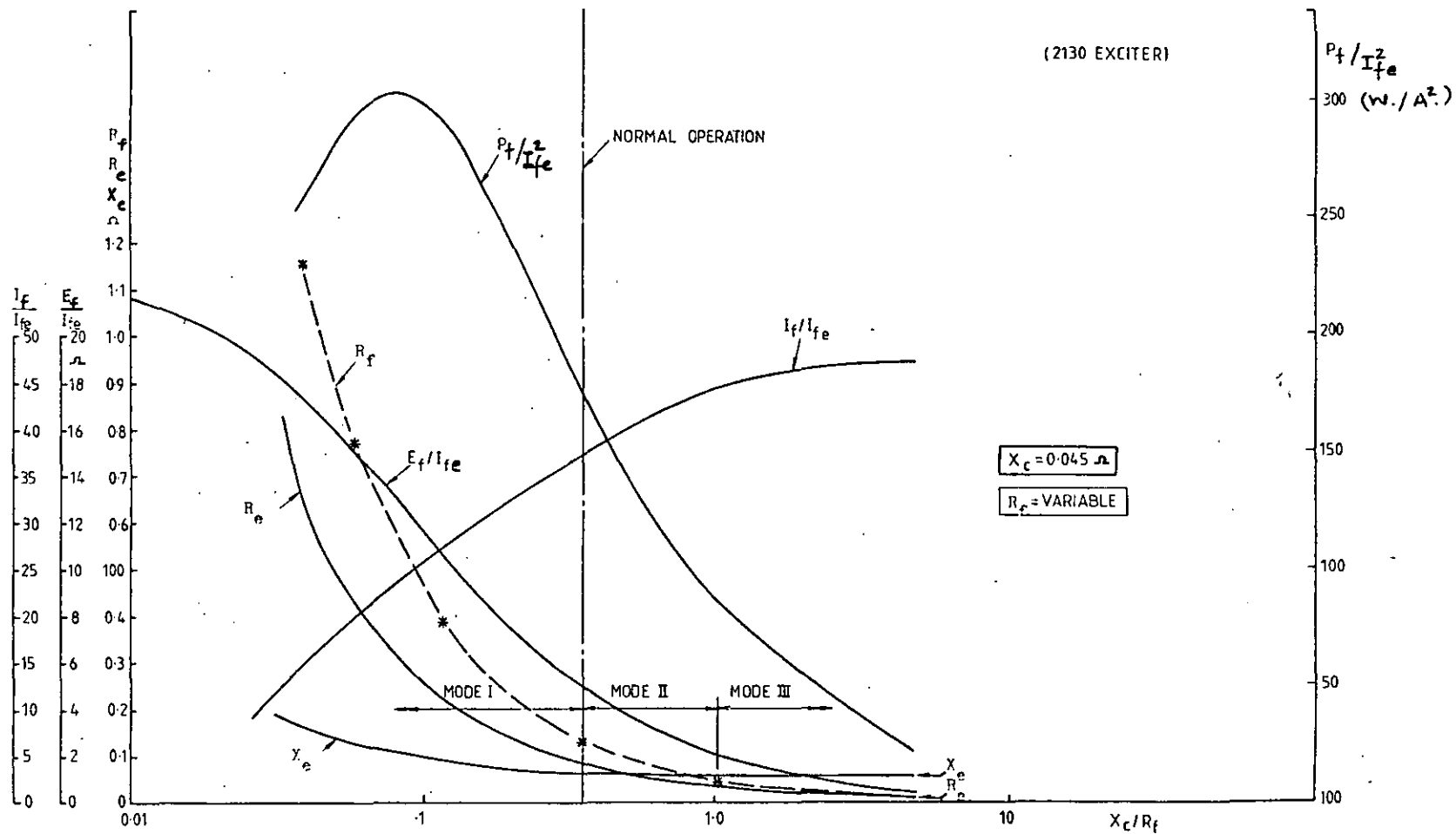


FIGURE 5.3. EXCITER-RECTIFIER O/P CHARACTERISTICS

CHAPTER 7

INDUCTION MOTOR AS AN IMPACT LOAD APPLIED TO THE REGULATED GENERATOR UNIT

The study of induction motors as an impact load on a regulated 3-stage generator unit is very important in the aircraft situation as there are numerous induction motors used to drive air conditioning fans, cooling fans for electronic equipment, pumps etc. Due to the large starting current of an induction motor compared with its full load current, it is important to be able to predict the voltage dip and the settling time when an induction motor is applied to the terminals of the regulated generator unit. A phase model of the induction motor is derived in this chapter and Kron's tensor methods are used to obtain the resultant voltage, impedance and current tensors when the motor is connected to the generator. The characteristics of induction motors switched on to an infinite bus supply and as a load applied to the regulated generator unit are both discussed.

7.1 Modelling of the Induction Motor in Phase Quantities

A number of authors ⁵⁹⁻⁶¹ have derived and used a phase model analysis to study the transients an induction motor experiences when started direct-on-line with either simultaneous or non-simultaneous switching. Further, the induction motor/synchronous generator combination model in phase quantities has been described by Snider and Smith ⁶².

The phase model representation of the induction motor is shown in Figure 7.1 with corresponding primitive branch network representation being given in Figure 7.2. The voltage tensor $[V_{pm}]$ and the current tensor $[I_{pm}]$ for the primitive network of the motor by inspection are:

$$[V_{pm}] = [V_1 \ V_2 \ V_3 \ 0 \ 0 \ 0]_t \quad 7.1$$

$$[I_{pm}] = [I_1 \ I_2 \ I_3 \ I_a \ I_b \ I_c]_t \quad 7.2$$

The impedance tensors $[Z_{pm}]$, $[R_{pm}]$, $[L_{pm}]$, $[G_{pm}]$ for the primitive network of the motor are given by equations 7.3, 7.4, 7.5 and 7.6 respectively

$$[Z_{pm}] = \begin{array}{|c|c|c|c|c|c|} \hline Z_{11} & Z_{12} & Z_{13} & Z_{1a} & Z_{1b} & Z_{1c} \\ \hline Z_{21} & Z_{22} & Z_{23} & Z_{2a} & Z_{2b} & Z_{2c} \\ \hline Z_{31} & Z_{32} & Z_{33} & Z_{3a} & Z_{3b} & Z_{3c} \\ \hline Z_{a1} & Z_{a2} & Z_{a3} & Z_{aa} & Z_{ab} & Z_{ac} \\ \hline Z_{b1} & Z_{b2} & Z_{b3} & Z_{ba} & Z_{bb} & Z_{bc} \\ \hline Z_{c1} & Z_{c2} & Z_{c3} & Z_{ca} & Z_{cb} & Z_{cc} \\ \hline \end{array}$$

7.3

$$[R_{pm}] = \begin{array}{|c|c|c|c|c|c|} \hline R_s & 0 & 0 & 0 & 0 & 0 \\ \hline 0 & R_s & 0 & 0 & 0 & 0 \\ \hline 0 & 0 & R_s & 0 & 0 & 0 \\ \hline 0 & 0 & 0 & R_R & 0 & 0 \\ \hline 0 & 0 & 0 & 0 & R_R & 0 \\ \hline 0 & 0 & 0 & 0 & 0 & R_R \\ \hline \end{array}$$

7.4

$[L_{pm}] =$

L_S	$-M_S$	$-M_S$	$M\cos\theta$	$M\cos(\theta-2\pi/3)$	$M\cos(\theta+2\pi/3)$
$-M_S$	L_S	$-M_S$	$M\cos(\theta+2\pi/3)$	$M\cos(\theta)$	$M\cos(\theta-2\pi/3)$
$-M_S$	$-M_S$	L_S	$M\cos(\theta-2\pi/3)$	$M\cos(\theta+2\pi/3)$	$M\cos\theta$
$M\cos\theta$	$M\cos(\theta+2\pi/3)$	$M\cos(\theta-2\pi/3)$	L_R	$-M_R$	$-M_R$
$M\cos(\theta-2\pi/3)$	$M\cos\theta$	$M\cos(\theta+2\pi/3)$	$-M_R$	L_R	$-M_R$
$M\cos(\theta+2\pi/3)$	$M\cos(\theta-2\pi/3)$	$M\cos\theta$	$-M_R$	$-M_R$	L_R

7.5

$$[G_{pm}] = \frac{d\theta}{dt} \cdot$$

0	0	0	$-M\sin\theta$	$-M\sin(\theta-2\pi/3)$	$-M\sin(\theta+2\pi/3)$
0	0	0	$-M\sin(\theta+2\pi/3)$	$-M\sin\theta$	$-M\sin(\theta-2\pi/3)$
0	0	0	$-M\sin(\theta-2\pi/3)$	$-M\sin(\theta+2\pi/3)$	$-M\sin\theta$
$-M\sin\theta$	$-M\sin(\theta+2\pi/3)$	$-M\sin(\theta-2\pi/3)$	0	0	0
$-M\sin(\theta-2\pi/3)$	$-M\sin\theta$	$-M\sin(\theta+2\pi/3)$	0	0	0
$-M\sin(\theta+2\pi/3)$	$-M\sin(\theta-2\pi/3)$	$-M\sin\theta$	0	0	0

If the voltage source has a source impedance as shown in Figure 7.3, the primitive branch network representation of the source is as in Figure 7.4 and the corresponding voltage, current, impedance tensors are

$$[V_{ps}] = [V_R \quad V_Y \quad V_B]_t \quad 7.7$$

$$[I_{ps}] = [I_R \quad I_Y \quad I_B]_t$$

$$[Z_{ps}] = \begin{bmatrix} Z_R & 0 & 0 \\ 0 & Z_Y & 0 \\ 0 & 0 & Z_B \end{bmatrix} \quad 7.9$$

The primitive voltage, current and impedance tensors for the composite network of Figures 7.3 and 7.5 are given by equations 7.10, 7.11 and 7.12 respectively.

$$[V_p] = [V_R \quad V_Y \quad V_B \quad 0 \quad 0 \quad 0 \quad 0 \quad 0 \quad 0]_t \quad 7.10$$

$$[I_p] = [I_R \quad I_Y \quad I_B \quad I_1 \quad I_2 \quad I_3 \quad I_a \quad I_b \quad I_c]_t \quad 7.11$$

$$[Z_p] = \begin{bmatrix} [Z_{ps}] & 0 \\ 0 & [Z_{pm}] \end{bmatrix} \quad 7.12$$

Similarly

$$[L_p] = \begin{bmatrix} [L_{ps}] & [0] \\ [0] & [L_{pm}] \end{bmatrix} \quad 7.13$$

$$[G_p] = \begin{bmatrix} [0] & [0] \\ [0] & [G_{pm}] \end{bmatrix} \quad 7.14$$

$$[R_p] = \begin{bmatrix} [R_{ps}] & [0] \\ [0] & [R_{pm}] \end{bmatrix} \quad 7.15$$

Since the actual number of independent currents $[I_n]$ depends on the interconnection of the branches, the voltage, current and impedance tensors are transformed to obtain the corresponding tensors for the connected network before they are used for numerical integration (as discussed in Chapter 3). For the 3-wire connection of Figure 7.5 the transformation tensor $[C]$ is

$$[I_p] = [C][I_n] \quad 7.16$$

where

$$[C] = \begin{bmatrix} 1 & 0 & 0 & 0 \\ 0 & 1 & 0 & 0 \\ -1 & -1 & 0 & 0 \\ 1 & 0 & 0 & 0 \\ 0 & 1 & 0 & 0 \\ -1 & -1 & 0 & 0 \\ 0 & 0 & 1 & 0 \\ 0 & 0 & 0 & 1 \\ 0 & 0 & -1 & -1 \end{bmatrix}$$

The impedance tensor $[Z_n]$ for the connected network is

$$[Z_n] = [C]_t [Z_p] [C]$$

$$= \begin{bmatrix} Z_R + Z_B & Z_B + Z_{12} - Z_{32} & Z_{1a} - Z_{3a} & Z_{1b} - Z_{3b} \\ +Z_{11} - Z_{31} & -Z_{13} + Z_{33} & -Z_{1c} + Z_{3c} & -Z_{1c} + Z_{3c} \\ -Z_{13} + Z_{33} & & & \\ Z_B + Z_{21} - Z_{31} & Z_Y + Z_B & Z_{2a} - Z_{3a} & Z_{2b} - Z_{3b} \\ -Z_{23} + Z_{33} & +Z_{22} - Z_{32} & -Z_{2c} + Z_{3c} & -Z_{2c} + Z_{3c} \\ -Z_{23} + Z_{33} & & & \\ Z_{a1} - Z_{c1} & Z_{a2} - Z_{c2} & Z_{aa} - Z_{ca} & Z_{ab} - Z_{cb} \\ -Z_{a3} + Z_{c3} & -Z_{a3} + Z_{c3} & -Z_{ac} + Z_{cc} & -Z_{ac} + Z_{cc} \\ Z_{b1} - Z_{c1} & Z_{b2} - Z_{c2} & Z_{ba} - Z_{ca} & Z_{bb} - Z_{cb} \\ -Z_{b3} + Z_{c3} & -Z_{b3} + Z_{c3} & -Z_{bc} + Z_{cc} & -Z_{bc} + Z_{cc} \end{bmatrix}$$

The $[L_n]$, $[G_n]$, $[R_n]$ tensors are obtained by substituting values of L, G, R in place of Z in equation 7.17. The voltage tensor $[V_n]$ is

$$[V_n] = [C]_t [V_p] = \begin{array}{|c|} \hline V_R - V_B \\ \hline V_Y - V_B \\ \hline 0 \\ \hline 0 \\ \hline \end{array} \quad 7.18$$

The differential equation of the interconnected network, in a form suitable for numerical integration, to obtain $[I_n]$ is

$$[pI_n] = [L_n]^{-1} \{ [V_n] - \{ [R_n] + [G_n] \} [I_n] \} \quad 7.19$$

All the branch currents of the network of Figure 7.5 can be found using equation 7.16 at each time step during numerical integration of equation 7.19.

If the neutral of the supply is connected to the star point of the generator stator winding, the independent currents are as shown in Figure 7.3, and the transformation tensor $[C]$ is

$$[C] = \begin{array}{|c|c|c|c|c|} \hline 1 & 0 & 0 & 0 & 0 \\ \hline 0 & 1 & 0 & 0 & 0 \\ \hline 0 & 0 & 1 & 0 & 0 \\ \hline 1 & 0 & 0 & 0 & 0 \\ \hline 0 & 1 & 0 & 0 & 0 \\ \hline 0 & 0 & 1 & 0 & 0 \\ \hline 0 & 0 & 0 & 1 & 0 \\ \hline 0 & 0 & 0 & 0 & 1 \\ \hline 0 & 0 & 0 & -1 & -1 \\ \hline \end{array} \quad 7.20$$

The corresponding impedance tensor $[Z_n]$ given by $[C]_t [Z_p] [C]$ is

$$[Z_n] = \begin{bmatrix} Z_R + Z_{11} & Z_{12} & Z_{13} & Z_{1a} - Z_{1c} & Z_{1b} - Z_{1c} \\ Z_{21} & Z_Y + Z_{22} & Z_{23} & Z_{2a} - Z_{2c} & Z_{2b} - Z_{2c} \\ Z_{31} & Z_{32} & Z_B + Z_{33} & Z_{3a} - Z_{3c} & Z_{3b} - Z_{3c} \\ Z_{a1} - Z_{c1} & Z_{a2} - Z_{c2} & Z_{a3} - Z_{c3} & Z_{aa} - Z_{ca} - Z_{ac} + Z_{cc} & Z_{ab} - Z_{cb} - Z_{ac} + Z_{cc} \\ Z_{b1} - Z_{c1} & Z_{b2} - Z_{c2} & Z_{b3} - Z_{c3} & Z_{ba} - Z_{ca} - Z_{bc} + Z_{cc} & Z_{ab} - Z_{cb} - Z_{bc} + Z_{cc} \end{bmatrix}$$

7.21

The phase model parameters for the induction motor were obtained from the corresponding equivalent circuit parameters as discussed in Appendix A11. The details of the induction motor used for modelling are also given in Appendix A11. A flow diagram of the computer program for the direct-on-line starting of induction motors is given in Figure 7.6.

As a 3-phase 400 Hz supply was not available for testing direct-on-line starting conditions, the predicted results are given merely to illustrate that the model developed can be used satisfactorily to study induction motor transients. The inertia of the induction motor rotor was reduced to 1/4 of the actual inertia to enable the complete induction motor transient period to be studied without excessive computing time. To simulate the characteristics of the induction motor on load, a fan with the mechanical load torque proportional to the square of the rotational speed was applied to the induction motor shaft. The equations of the simulated load torque of the fan and the electromagnetic torque of the induction motor are given in Appendix A12. Figures 7.7 to 7.11 show the induction motor transient characteristics under no load condition and with the fan load when switched on to a balanced 3-phase

supply. Figure 7.7 shows the transient torque v/s slip characteristics of the induction motor and the fan load. Figure 7.8 shows the induction motor speed build up under no load condition and with the fan load. Figure 7.9 shows the transient torque v/s time characteristic of the induction motor under no load condition and with the fan load. Figures 7.10 and 7.11 show the transient induction motor stator phase current I_1 and the rotor phase current I_a respectively. The induction motor transients under unbalanced supply voltages and non-simultaneous switching on to the supply can also be studied using the computer program described by the flow diagram given in Figure 7.6.

7.2 Modelling of Induction Motor/Synchronous Generator Combination

A schematic representation of the induction motor when connected to the synchronous generator is shown in Figure 7.12, based on the phase model of the synchronous generator given in Chapter 1 and on the induction motor equations 7.1 to 7.6. Inspection of Figure 7.12 enables the primitive network tensors $[V_p]$, $[I_p]$, $[Z_p]$ for the synchronous-generator/induction motor combination to be written down as

$$[V_p] = [V_F \ 0 \ 0 \ 0 \ 0 \ 0 \ 0 \ 0 \ 0 \ 0 \ 0 \ 0]_t \quad 7.22$$

$$[I_p] = [I_F \ I_D \ I_Q \ I_R \ I_Y \ I_B \ I_1 \ I_2 \ I_3 \ I_a \ I_b \ I_c]_t \quad 7.23$$

$[Z_p] =$

Z_{FF}	Z_{FD}	Z_{FQ} $= 0$	Z_{FR}	Z_{FY}	Z_{FB}						
Z_{DF}	Z_{DD}	Z_{DQ} $= 0$	Z_{DR}	Z_{DY}	Z_{DB}						
Z_{QF} $= 0$	Z_{QD} $= 0$	Z_{QQ}	Z_{QR}	Z_{QY}	Z_{QB}						
Z_{RF}	Z_{RD}	Z_{RQ}	Z_{RR}	Z_{RY}	Z_{RB}						
Z_{YF}	Z_{YD}	Z_{YQ}	Z_{YR}	Z_{YY}	Z_{YB}						
Z_{BF}	Z_{BD}	Z_{BQ}	Z_{BR}	Z_{BY}	Z_{BB}						
						Z_{11}	Z_{12}	Z_{13}	Z_{1a}	Z_{1b}	Z_{1c}
						Z_{21}	Z_{22}	Z_{23}	Z_{2a}	Z_{2b}	Z_{2c}
						Z_{31}	Z_{32}	Z_{33}	Z_{3a}	Z_{3b}	Z_{3c}
						Z_{a1}	Z_{a2}	Z_{a3}	Z_{aa}	Z_{ab}	Z_{ac}
						Z_{b1}	Z_{b2}	Z_{b3}	Z_{ba}	Z_{bb}	Z_{bc}
						Z_{c1}	Z_{c2}	Z_{c3}	Z_{ca}	Z_{cb}	Z_{cc}

The transformation tensor $[C]$ for the generator-induction motor combination is.

$$[C] =$$

1	0	0	0	0	0	0
0	1	0	0	0	0	0
0	0	1	0	0	0	0
0	0	0	1	0	0	0
0	0	0	0	1	0	0
0	0	0	-1	-1	0	0
0	0	0	-1	0	0	0
0	0	0	0	-1	0	0
0	0	0	1	1	0	0
0	0	0	0	0	1	0
0	0	0	0	0	0	1
0	0	0	0	0	-1	-1

7.25

The impedance tensor for the connected network $[Z_n]$ is given by $[C]_t [Z_p] [C]$, and the resultant inductance tensor $[L_n]$ and resistance tensor $[R_n]$ as obtained by this technique are given by equations 7.26 and 7.27 respectively. The $[G_n]$ tensor may be found from $\frac{d}{dt} [L_n]$.

$[L_n] =$

L_{FF}	L_{FD}	0	$L_{FR}-L_{FB}$	$L_{FY}-L_{FB}$	0	0
L_{FD}	L_{DD}	0	$L_{DR}-L_{DB}$	$L_{DY}-L_{DB}$	0	0
0	0	L_{QQ}	$L_{QR}-L_{QB}$	$L_{QY}-L_{QB}$	0	0
$L_{FR}-L_{FB}$	$L_{DR}-L_{DB}$	$L_{QR}-L_{QB}$	$L_{RR}-2L_{RB}-L_{BB}$ $+L_{11}-2L_{13}+L_{33}$	$L_{RY}-L_{BY}-L_{RB}+L_{BB}$ $+L_{12}-L_{32}-L_{13}+L_{33}$	$L_{3a}-L_{1a}$ $+L_{1c}-L_{3c}$	$L_{3b}-L_{1b}$ $+L_{1c}-L_{3c}$
$L_{FY}-L_{FB}$	$L_{DY}-L_{DB}$	$L_{QY}-L_{QB}$	$L_{RY}-L_{BY}-L_{RB}+L_{BB}$ $+L_{12}-L_{32}-L_{13}+L_{33}$	$L_{YY}-2L_{BY}+L_{BB}$ $+L_{22}-2L_{23}+L_{33}$	$L_{3a}+L_{2c}$ $-L_{2a}-L_{3c}$	$L_{3b}+L_{2c}$ $-L_{2b}-L_{3c}$
0	0	0	$L_{3a}-L_{1a}+L_{1c}-L_{3c}$	$L_{3a}+L_{2c}-L_{2a}-L_{3c}$	$L_{aa}-2L_{ac}$ $+L_{cc}$	$L_{ab}-L_{ac}$ $-L_{cb}+L_{cc}$
0	0	0	$L_{3b}-L_{1b}+L_{1c}-L_{3c}$	$L_{3b}+L_{2c}-L_{2b}-L_{3c}$	$L_{ab}-L_{ac}$ $-L_{cb}+L_{cc}$	$L_{bb}-2L_{bc}$ $+L_{cc}$

7.26

$$[R_n] = \begin{bmatrix} R_{FF} & 0 & 0 & 0 & 0 & 0 & 0 \\ 0 & R_{DD} & 0 & 0 & 0 & 0 & 0 \\ 0 & 0 & R_{QQ} & 0 & 0 & 0 & 0 \\ 0 & 0 & 0 & R_R + R_B + R_1 + R_3 & R_B + R_3 & 0 & 0 \\ 0 & 0 & 0 & R_B + R_3 & R_Y + R_B + R_2 + R_3 & 0 & 0 \\ 0 & 0 & 0 & 0 & 0 & R_a + R_c & R_c \\ 0 & 0 & 0 & 0 & 0 & R_c & R_b + R_c \end{bmatrix}$$

7.27

$$\text{also } [V_n] = [C]_t [V_p] = [V_f \ 0 \ 0 \ 0 \ 0 \ 0 \ 0]$$

7.28

The differential equations of the generator/induction motor combination in the form for solution by a numerical integration method are the same as equation 7.19, provided that the correct voltage, current and impedance tensors derived for the combination are used.

7.3 Induction Motor as an Impact Load Applied to the Regulated 3-Stage Generator Unit

A block diagram for the regulated 3-stage generator unit with an induction motor load is given in Figure 7.13. The method of analysis is very similar to that discussed in Chapter 5, where the model of the regulated generator unit was derived for a passive load comprising an inductance in series with a resistor. A flow diagram of the program used for calculating the transients on sudden application of the induction motor load to the regulated 3-stage generator is given in Figure 7.14.

The steps in the solution of the transients at each time interval are:

- a) The numerical solution of the differential equation 7.19 together with the electro-mechanical equations of the induction motor given in Appendix A12 .
- b) The calculation of the generator terminal voltage for use in deriving the automatic voltage regulator response.
- c) The solution of the differential equations for the a.v.r. discussed in Chapter 4, to obtain the voltage applied to the exciter field winding.
- d) The solution of the exciter differential equations and the rectifier response to give the new value of the main generator field voltage.

Figure 7.15 shows a comparison between the measured and the predicted phase voltage transient on application of the induction motor load, for the correct value of rotor inertia. Figure 7.16 shows a comparison between the measured and the predicted phase currents of the machines and Figure 7.17 shows the transient electromagnetic torque of the induction motor. It was not possible to measure the transient torque on the motor shaft as the special

equipment that is required was not available. However, since the phase voltage and currents can be fairly accurately predicted, it is felt that the resultant torque predictions are close to the actual values. Figure 7.18 shows the generator field current transient, which is useful to the system design engineer as it shows the effective response of the regulator, and the exciter when the induction motor is switched on to the generator terminals. Figure 7.19 shows a comparison between the measured and predicted exciter field current transients.

7.4 Conclusion and Discussions

The phase model of the induction motor described in this chapter can be used to predict the transients when the motor is switched on to a 3-phase supply. The transient characteristics of the induction motor when switched on to a 3-phase supply, under no load and a simulated fan load condition are given to illustrate the usefulness of a phase model of the motor for such studies. The phase models of the induction motor, and the synchronous generator described in Chapter 2, are combined using Kron's tensor methods to obtain the differential equations for a synchronous-generator/induction-motor combination which are subsequently used in a study of the transients following application of the induction motor as an impact load to the regulated generator unit. Close agreement between the measured and predicted transients for the regulated generator unit is obtained, therefore the model of the regulated generator/induction-motor combination can be used with confidence to predict the voltage dip and the settling time of the generator terminal voltages, and the transient currents of the machines. The predicted transient oscillatory torque of the induction motor is useful for mechanical design of the induction motor/load coupling. The regulated generator/induction-motor model can also be used to adjust the parameters of the a.v.r. for design purposes, to maintain the maximum voltage dip and the settling time of the generator terminal voltages within a specified limit when the induction motor is applied to the generator terminals.

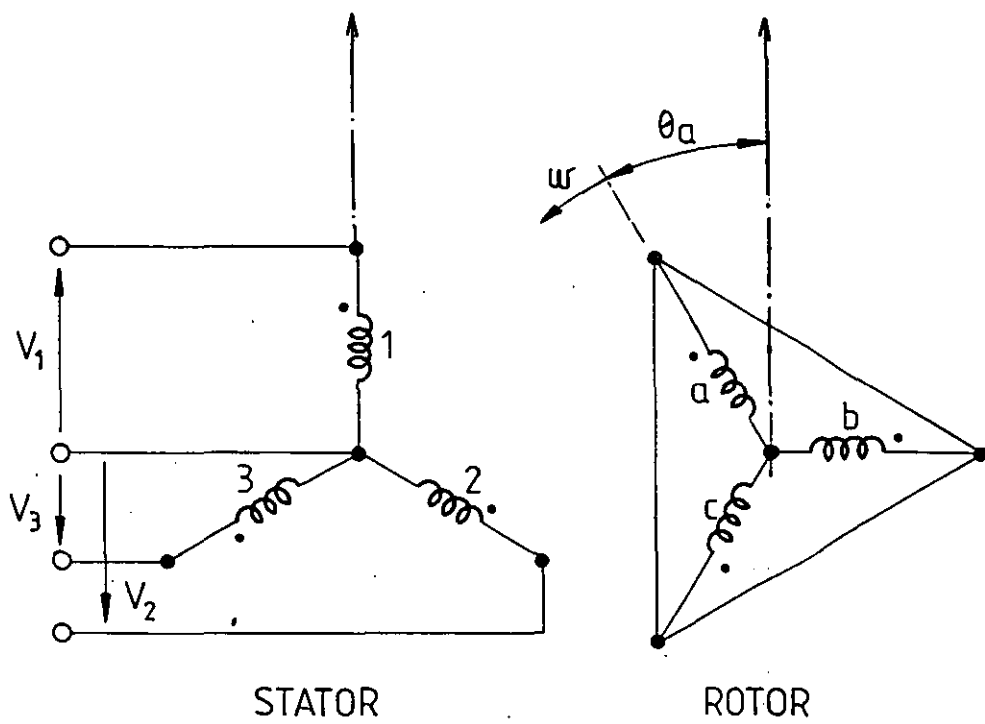


Figure 7.1 PHASE MODEL OF INDUCTION MOTOR

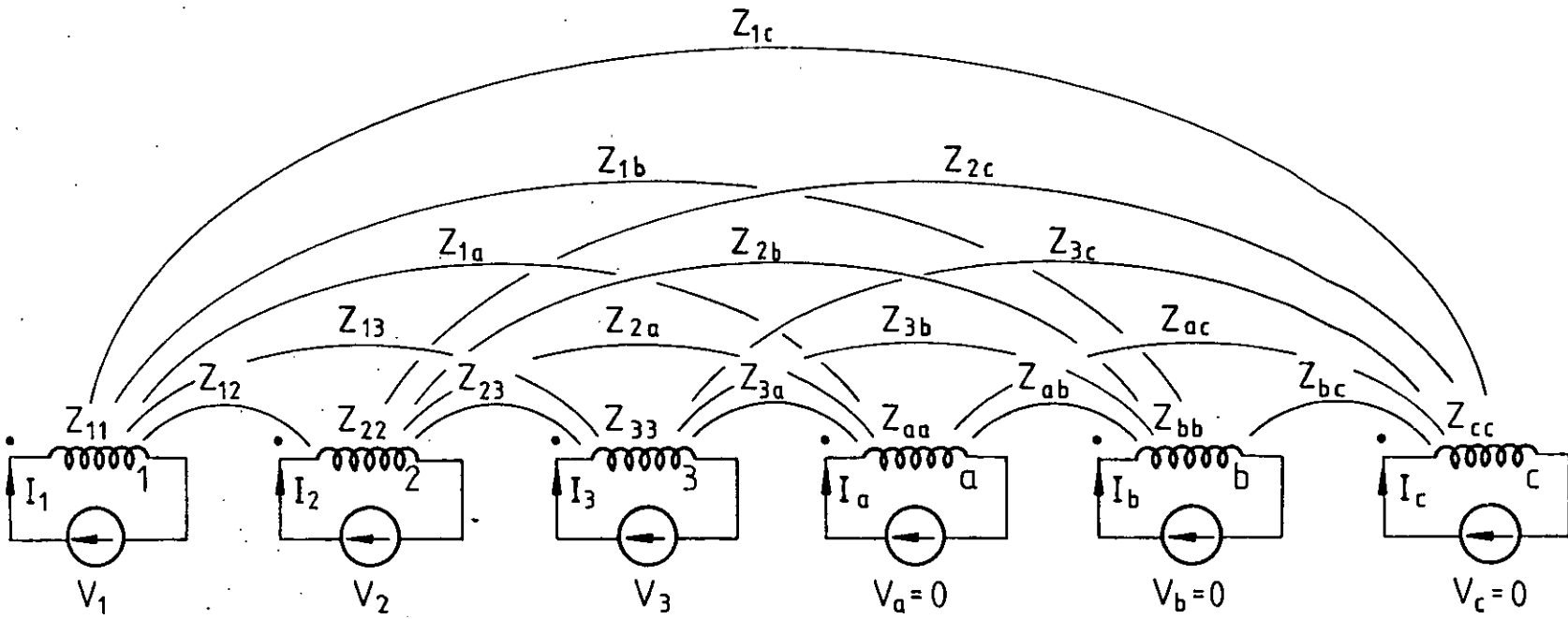


Figure 7.2 PRIMITIVE BRANCH NETWORK OF INDUCTION MOTOR

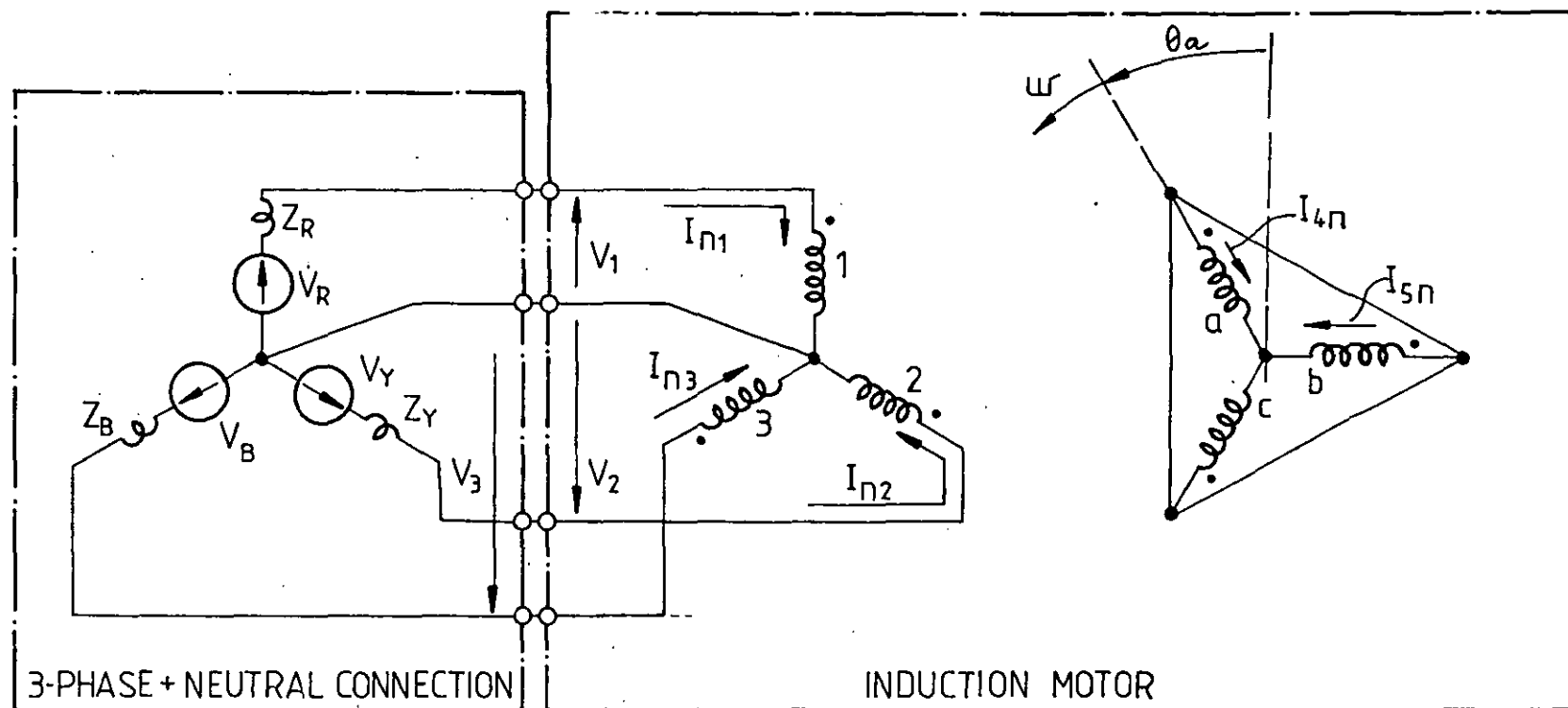


Figure 7.3 INDUCTION MOTOR 4-WIRE CONNECTION

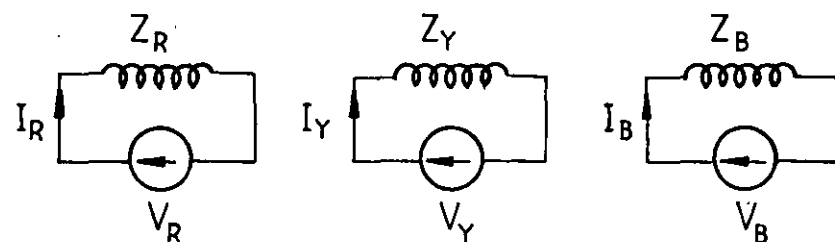


Figure 7.4 PRIMITIVE BRANCH NETWORK OF 3-PHASE SUPPLY

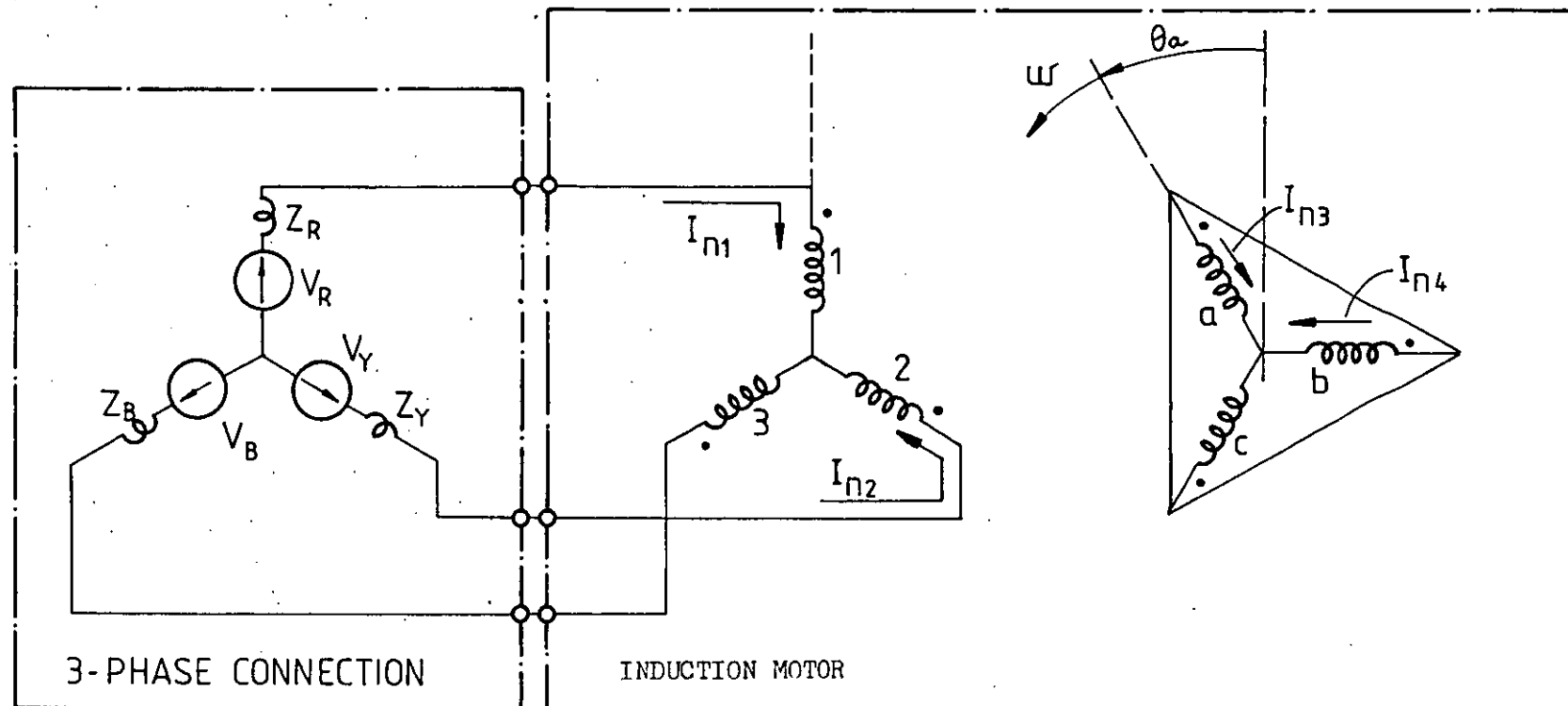


Figure 7.5 INDUCTION MOTOR 3-WIRE CONNECTION

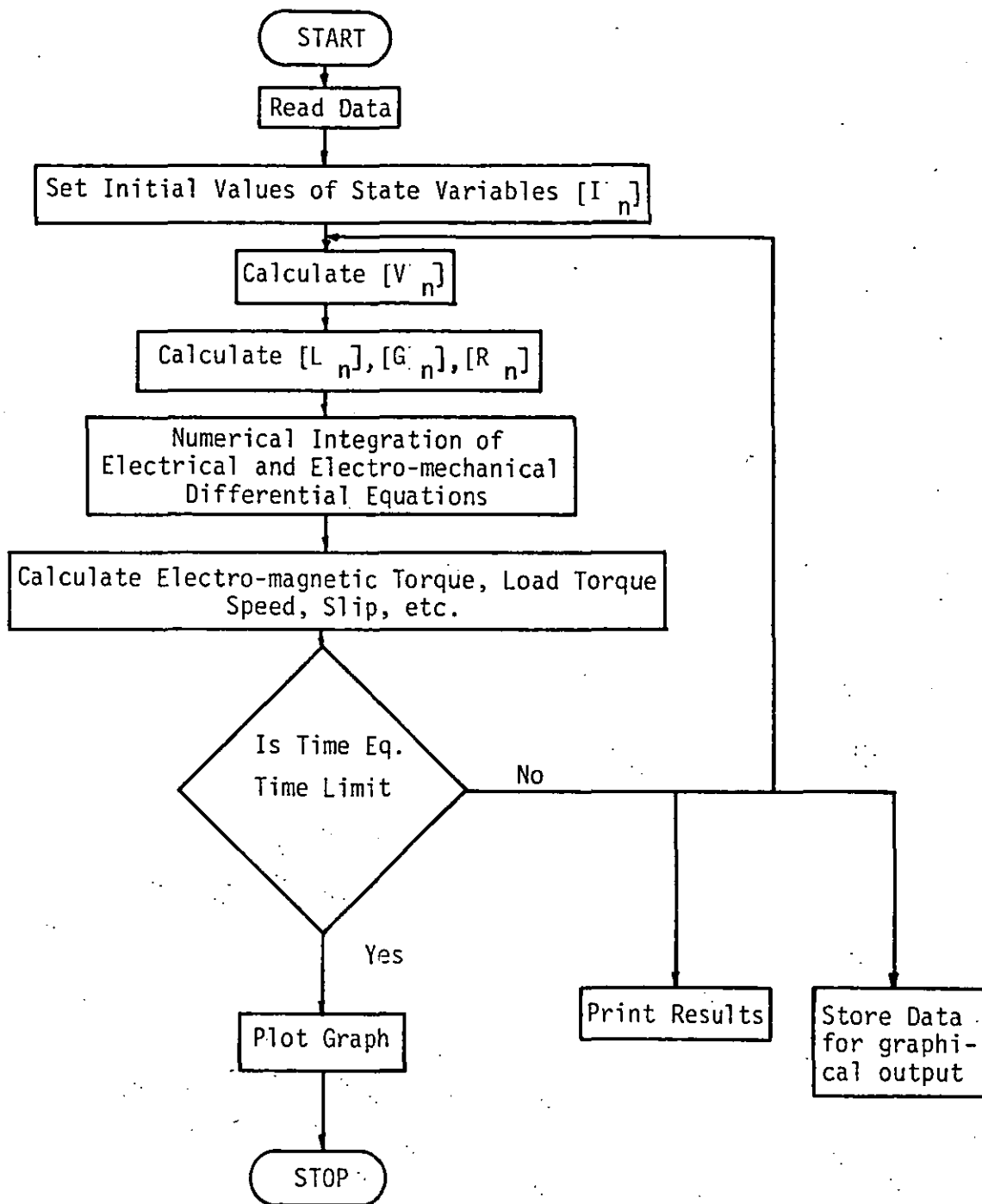


FIGURE 7.6 Direct On-Line Switching of Induction Motor
(Program Flow Diagram)

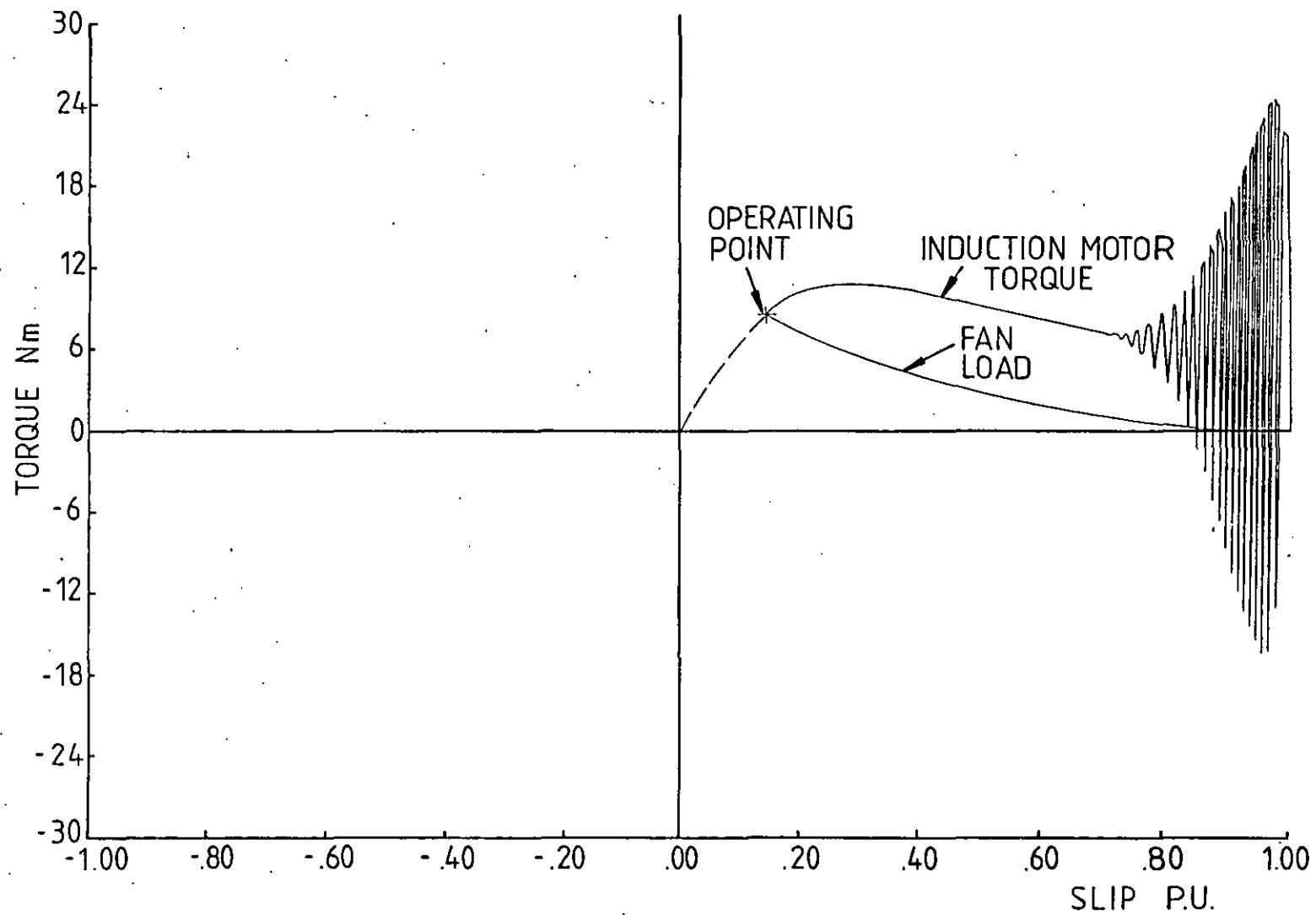


Figure 7.7 INDUCTION MOTOR ON FAN LOAD. TORQUE V/S SLIP CHARACTERISTIC

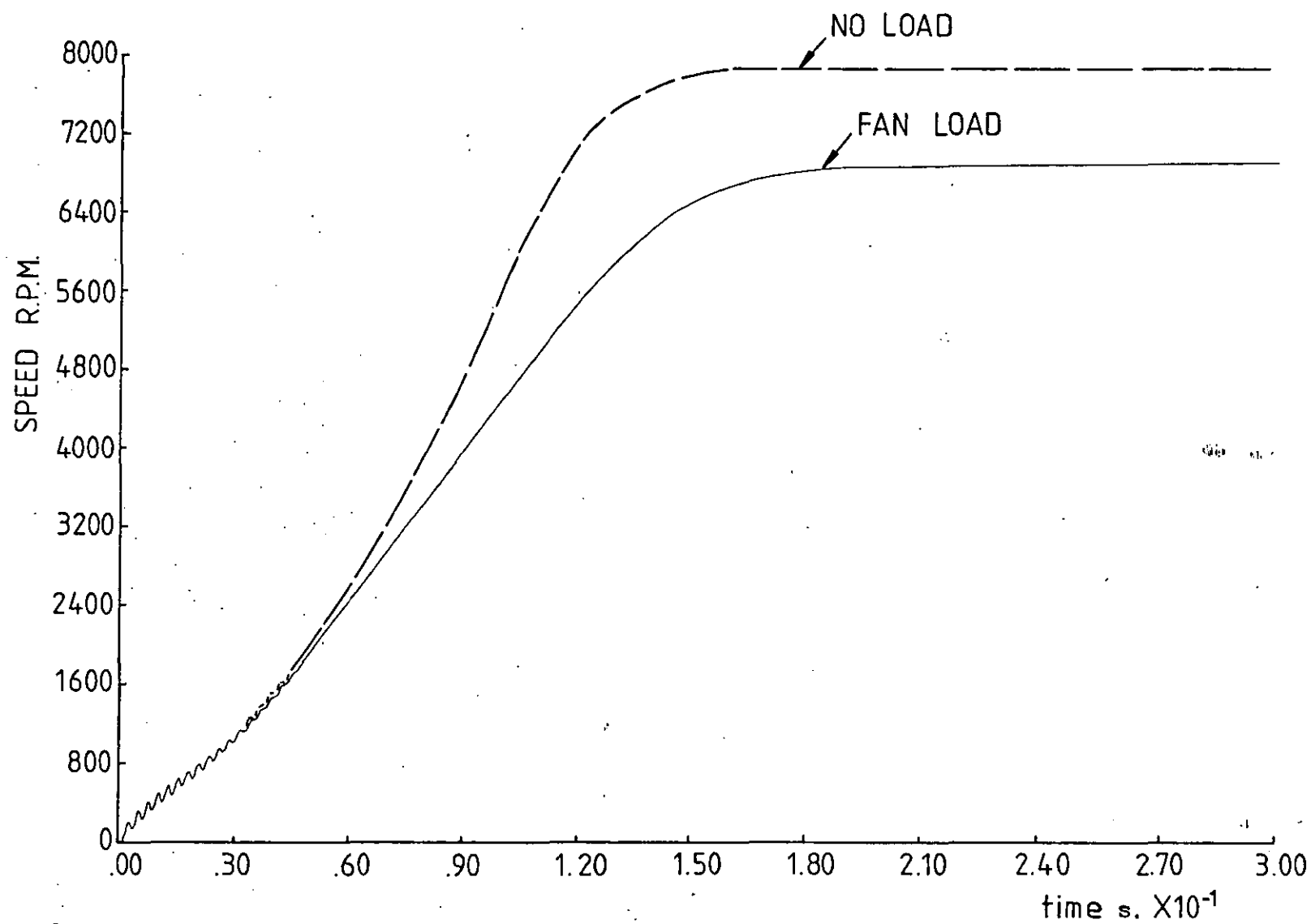


Figure 7.8

INDUCTION MOTOR SPEED BUILD UP V/S TIME

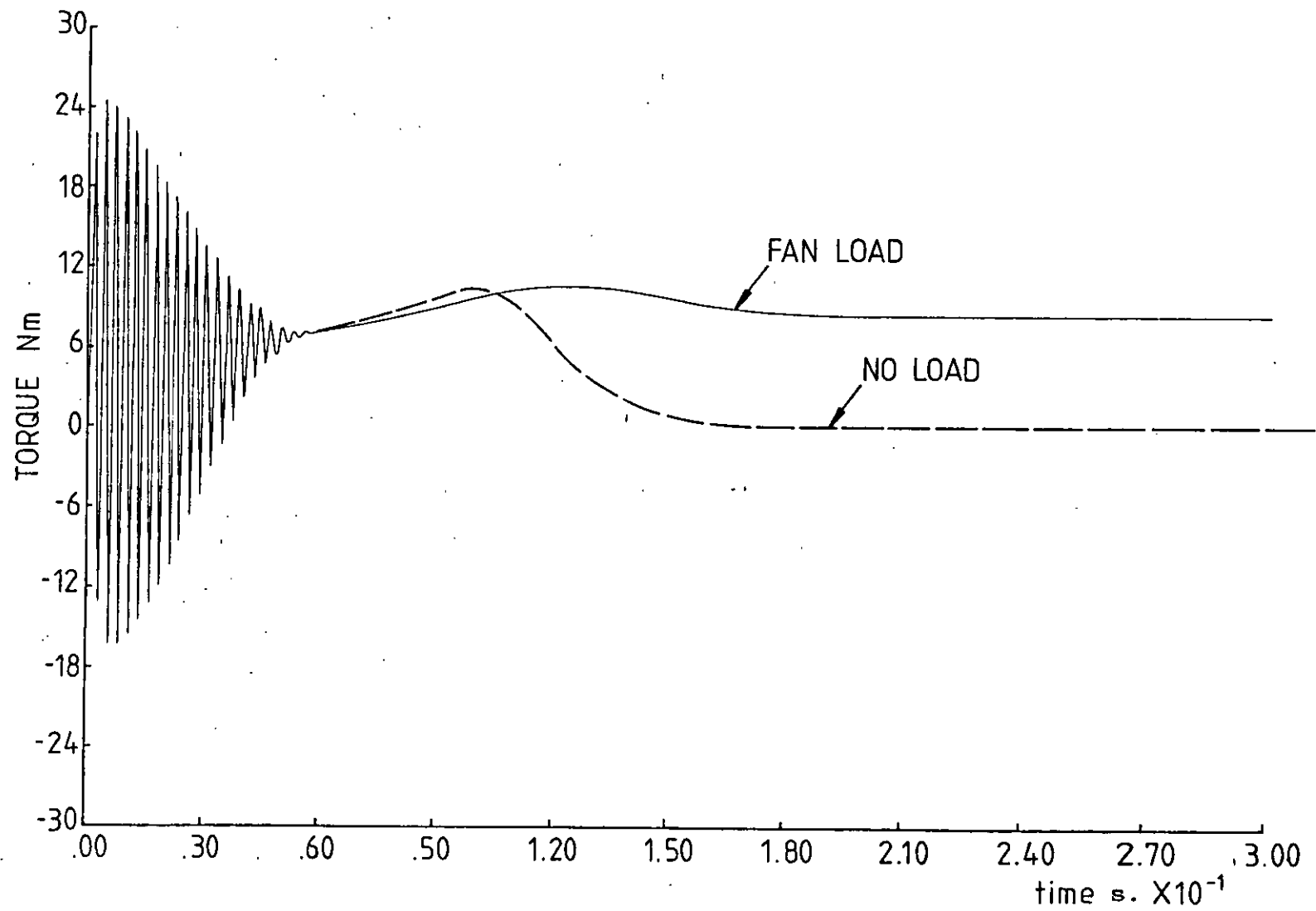


Figure 7.9 INDUCTION MOTOR TORQUE V/S TIME

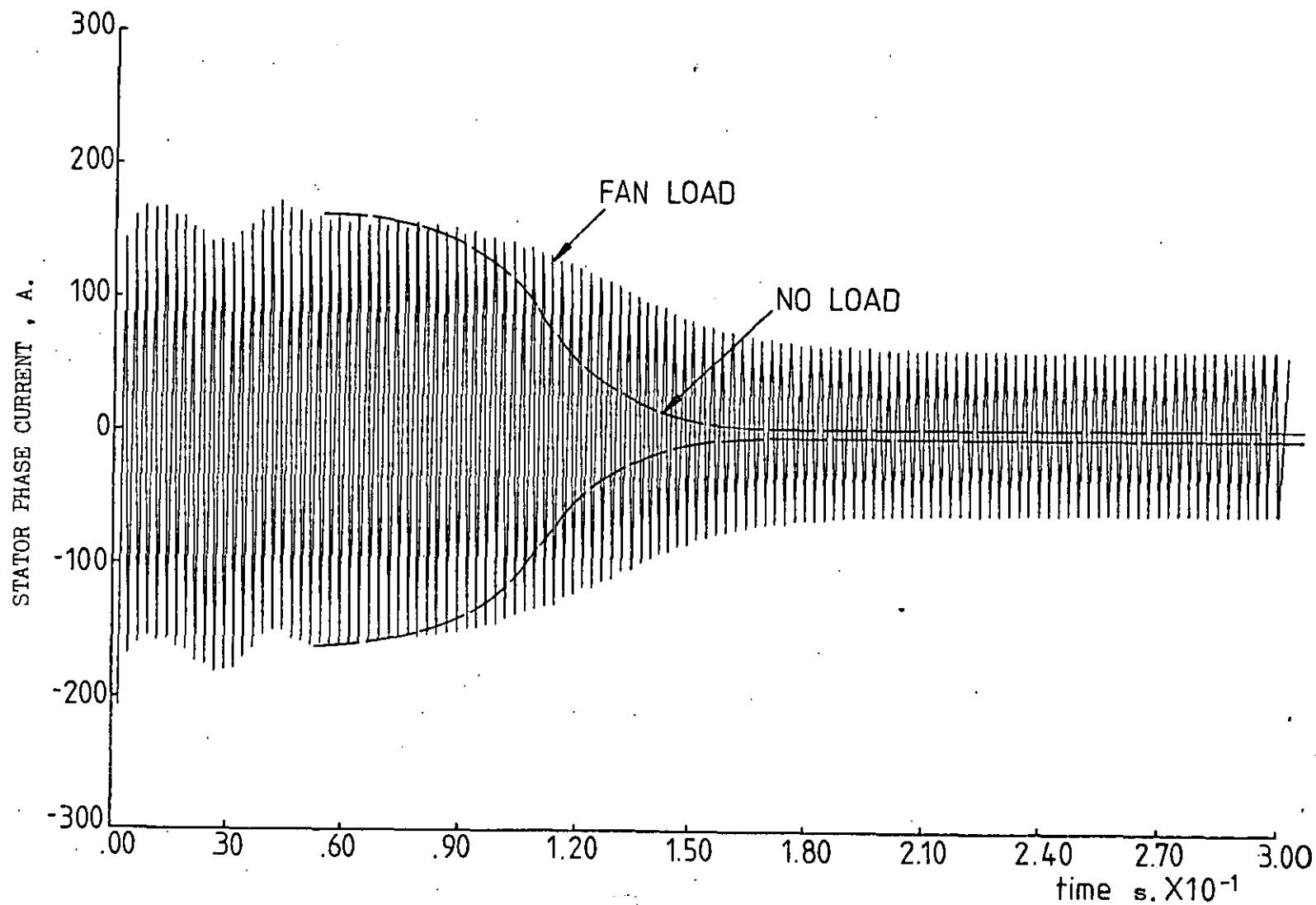


Figure 7.10 INDUCTION MOTOR STATOR PHASE CURRENT V/S TIME

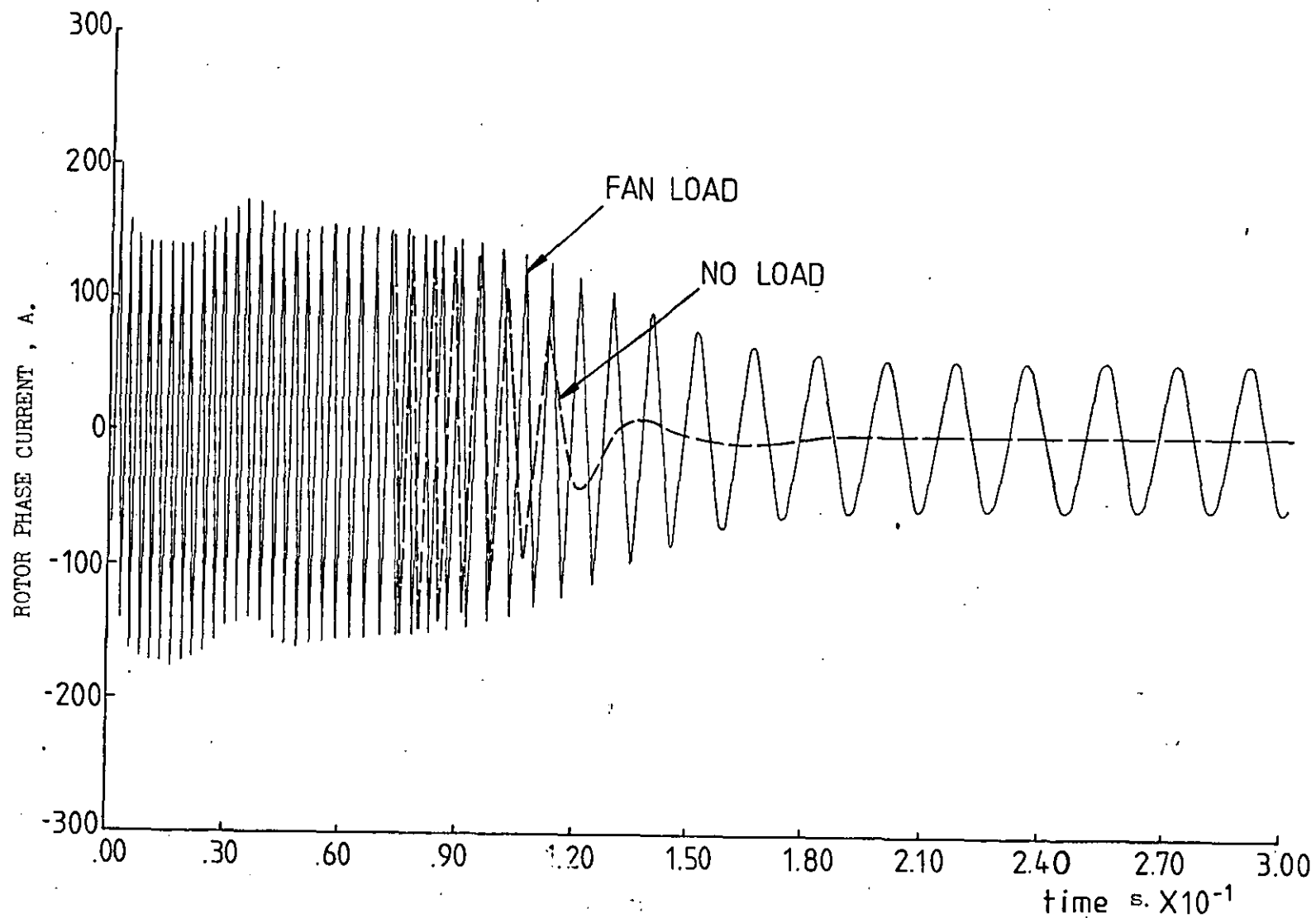


Figure 7.11 INDUCTION MOTOR ROTOR PHASE WINDING CURRENT V/S TIME

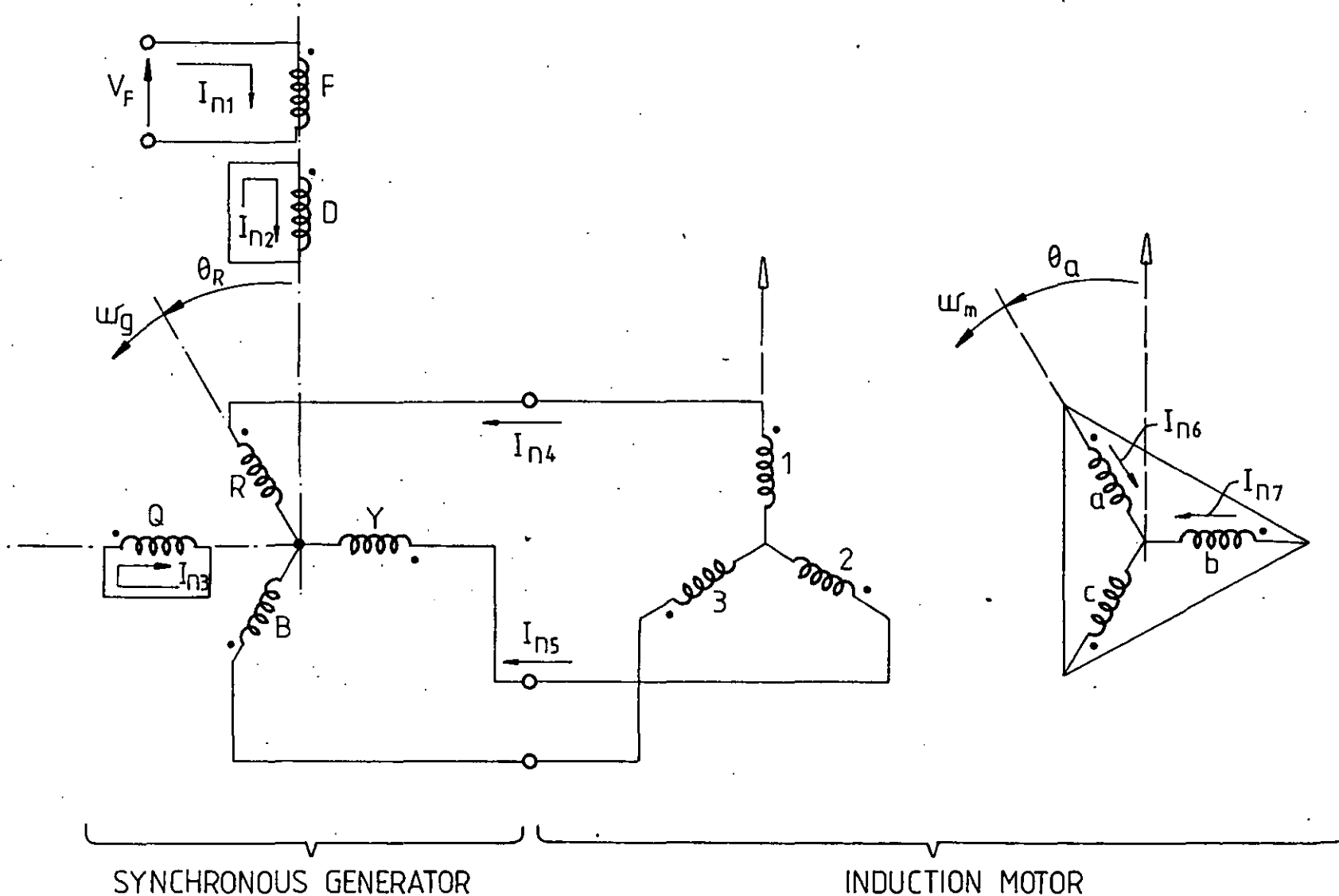


Figure 7.12 INDUCTION MOTOR CONNECTED TO THE SYNCHRONOUS GENERATOR
(NORMAL 3-WIRE CONNECTION)

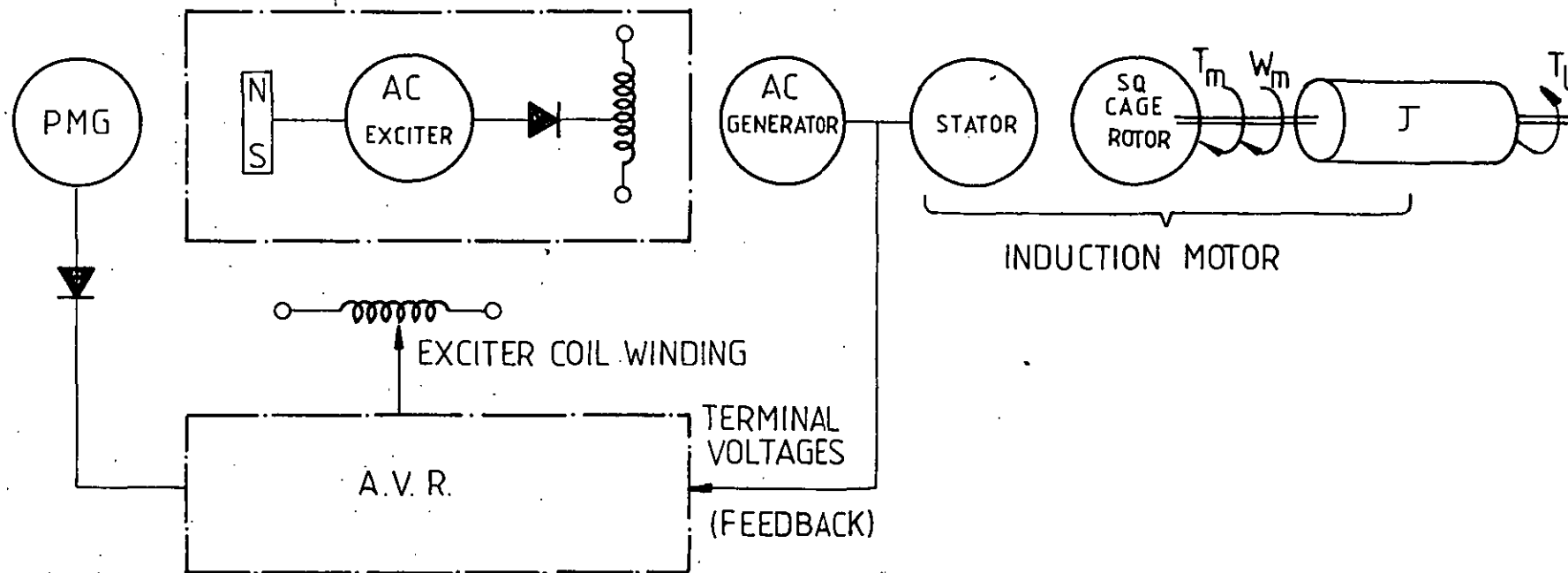


Figure 7.13 BLOCK DIAGRAM OF REGULATED 3-STAGE GENERATOR UNIT WITH INDUCTION MOTOR LOAD

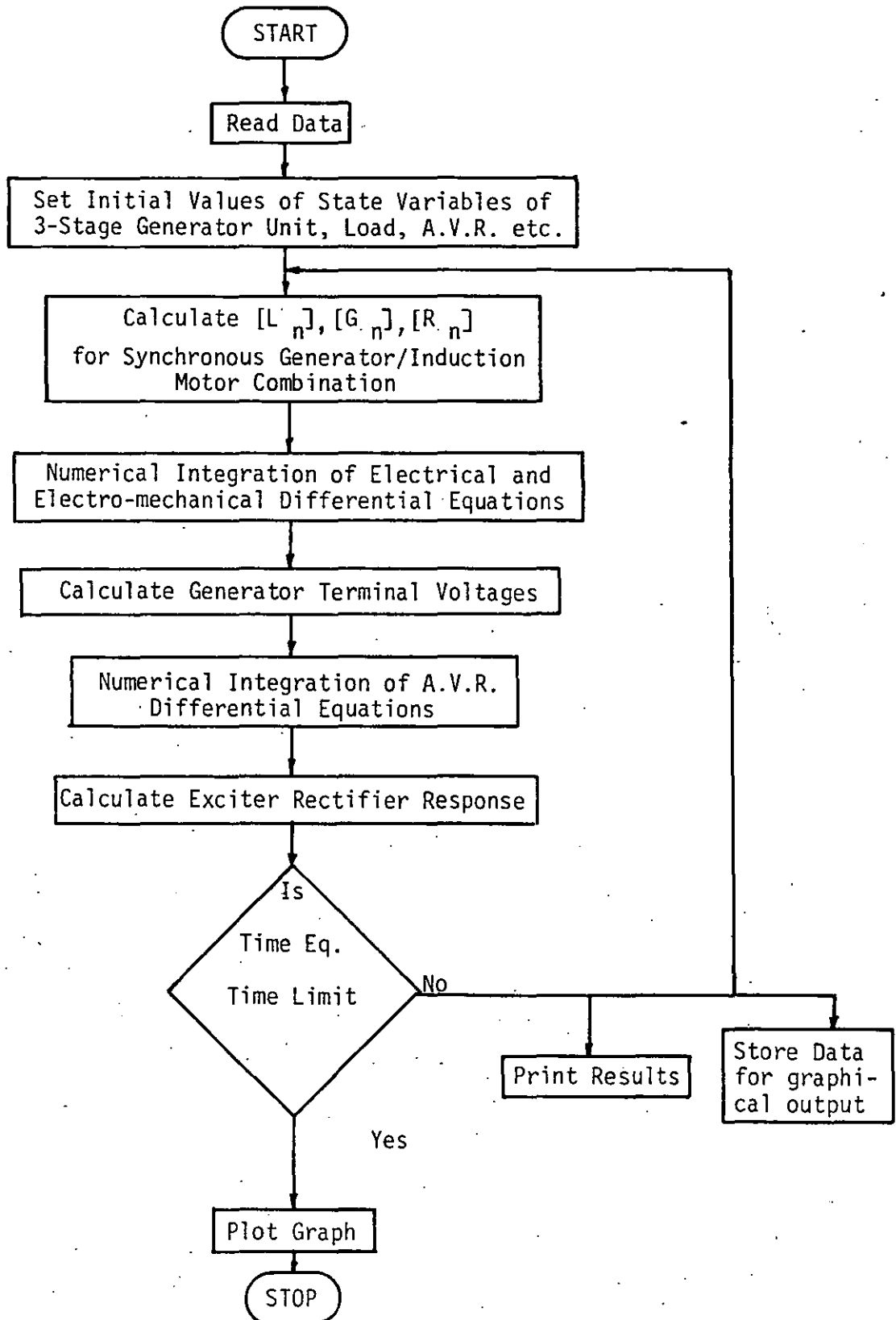


FIGURE 7.14 Induction Motor as an Impact Load Applied to Regulated Generator (Program Flow Diagram)

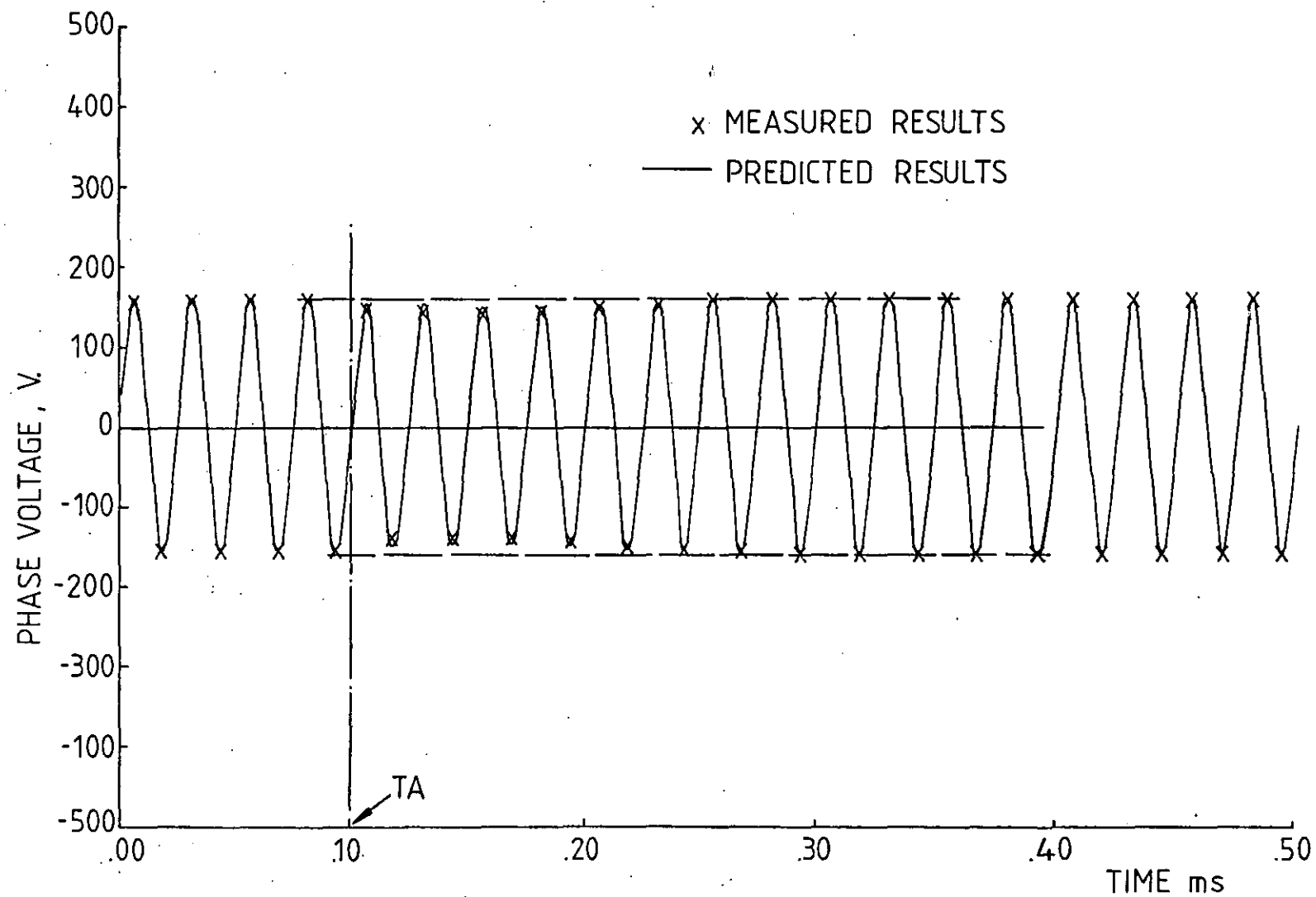


Figure 7.15

GENERATOR PHASE VOLTAGE TRANSIENT ON APPLICATION OF THE INDUCTION MOTOR

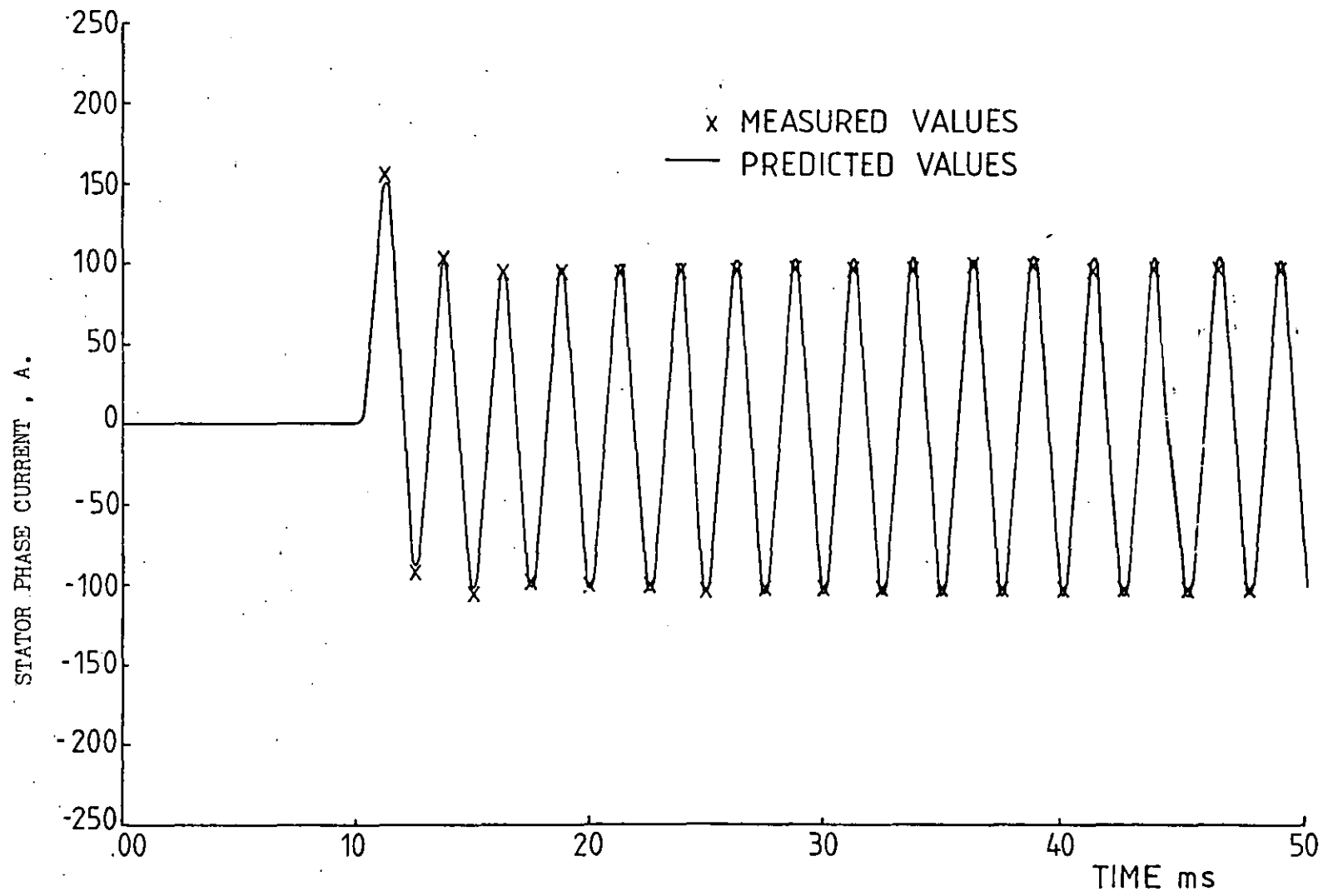


Figure 7.16

GENERATOR AND INDUCTION MOTOR STATOR PHASE CURRENT

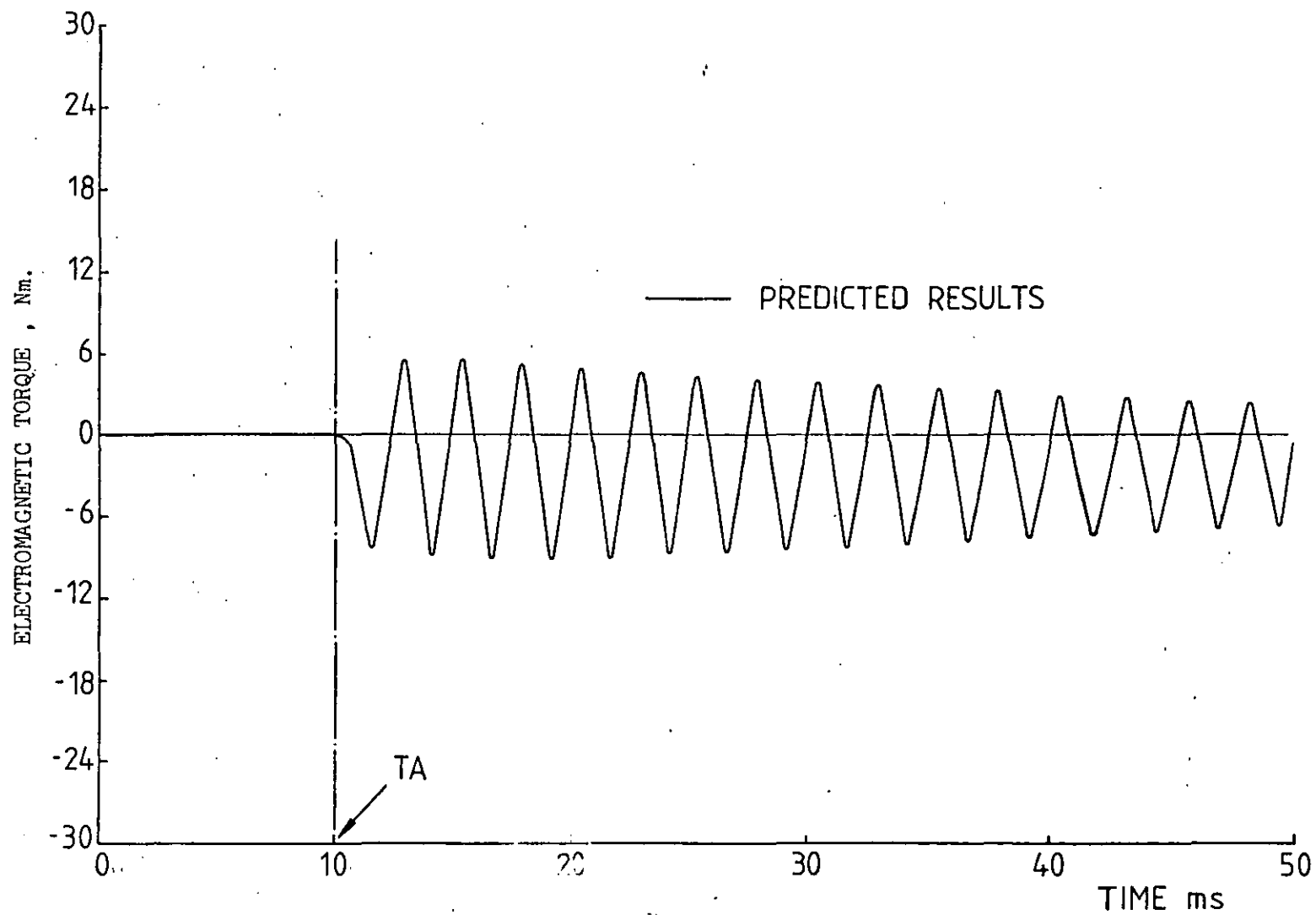


Figure 7.17 INDUCTION MOTOR ELECTROMAGNETIC TORQUE

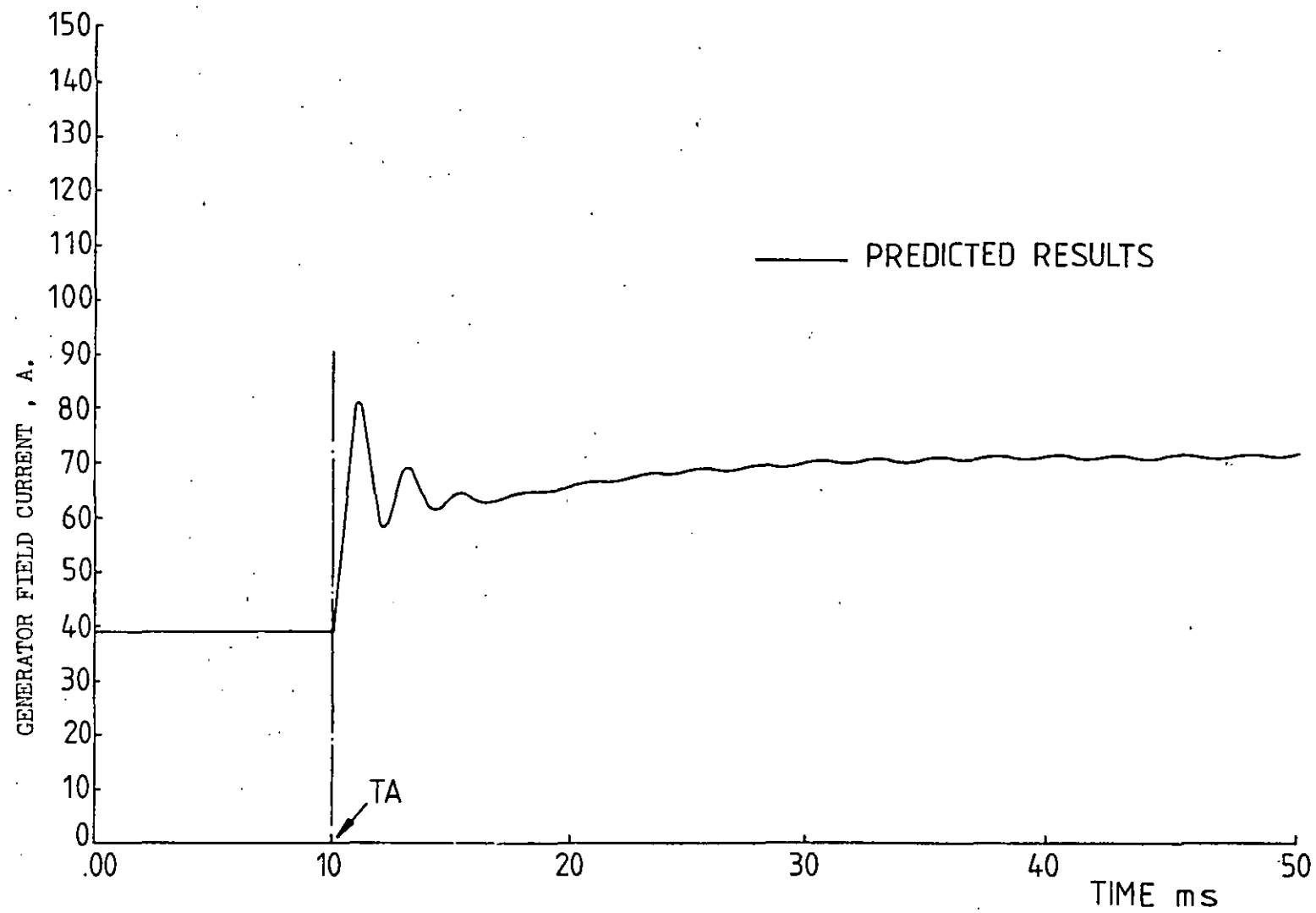


Figure 7.18 GENERATOR FIELD CURRENT TRANSIENT

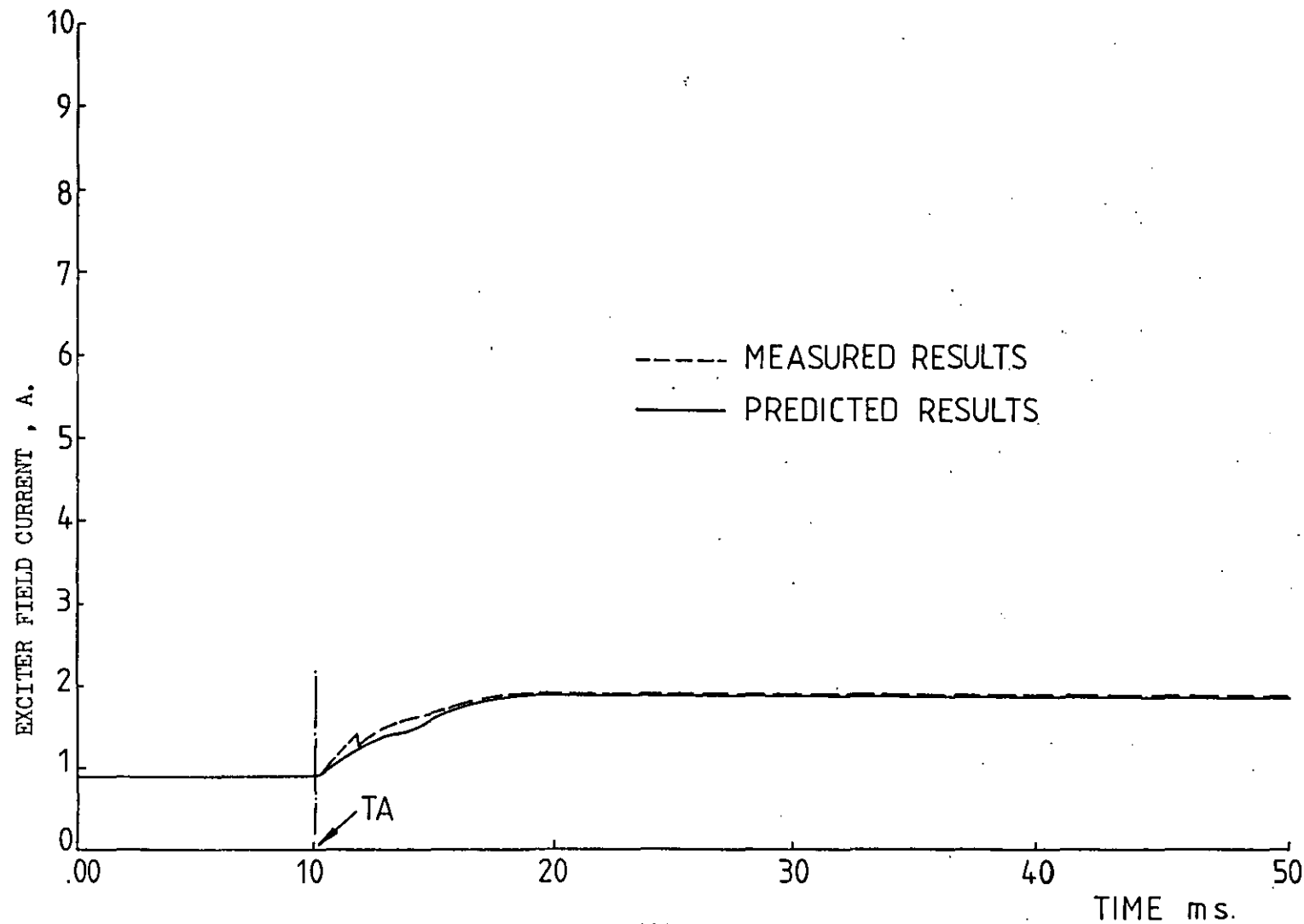


Figure 7.19

EXCITER FIELD CURRENT TRANSIENT

CHAPTER 8

THE MATHEMATICAL MODELLING OF PERMANENT MAGNET GENERATORS

This chapter is concerned with the mathematical modelling of the permanent magnet generator (PMG) used on the 3-stage generator unit. The PMG supplies the power need of the automatic voltage regulator (a.v.r) and the other electronic circuits forming the generator control unit, as well as supplying field current to the main exciter.

Since the PMG is the prime source of electrical power in the unit, it is necessary to know its characteristics both during steady-state operation and following the application of a load. The electronic circuits in the a.v.r. and the exciter field winding both require a d.c. voltage supply, which is obtained from full-wave rectification of the PMG output. The mathematical model of the PMG with its output rectifier was therefore developed as described in this chapter, to obtain a complete model for the first-stage of the generator unit. The PMG is situated at the non-drive end of the generator, as shown in photograph A1.1 (Appendix 1), adjacent to the main stage. Full design details are given in Appendix (A1) and the constructional details are given in Figure 8.1. The mathematical modelling of the PMG is an extension of the main generator model discussed in Chapter 2 to include the characteristics of the rotor magnets. The three armature phase windings are shown in Figure 8.2 (and the rotor is represented as a rotating magnet which induces voltages in the armature windings as it rotates.)

8.1 Calculation of Open Circuit Voltage of PMG from Tests at Standstill

(The open-circuit voltage output of the PMG can be calculated from the measurement of the permanent magnet rotor flux linking a phase winding.) Since the fluxmeter measures the change in flux linkage of a winding connected to it, it was connected across phase A

of the PMG and the rotor magnet turned from 90° to -240° electrical (2 pole pitches) to get the change in flux linkages with phase A over a cycle of PMG output. The results of the measurement are shown in Figure 8.3.

The open circuit voltage output of a phase winding is

$$V_{ph} = 4.44 f N \hat{\phi}$$

Substituting the value of $N \hat{\phi}$ from Figure 8.2 and for f gives

$$V_{ph} = 35 \text{ V}$$

or after rectification assuming no volt-drop in the diodes

$$V_{DC} = 2.34 V_{ph} = 82.0 \text{ V}$$

It was found that the d.c. output voltage of the PMG with a full-wave rectifier and load resistor of 100 ohms when running at 12,000 rpm was 79.5 V. (Hence measurements of the total flux linkages with the phase winding can be used to determine the open circuit voltage without the need for rotation at rated speed.)

8.2 Measurement of the PMG Inductances

The self inductance of the armature phase was measured at different electrical angles (θ_a) by applying an alternating voltage to the terminals and measuring the input power and current. As there is neither a field nor any damper windings on the magnet rotor, the inductance measured is that of the phase winding.

Similarly, the mutual inductance between the phases was measured by applying an alternating current of frequency ω to phase A and measuring the voltage V_{BN} induced in phase B. The mutual inductance L_{ab} between phases A and B is

$$L_{ab} = \frac{V_{BN}}{I_A} \cdot \frac{1}{\omega} \quad 8.1$$

The angular variations of the armature phase A self inductance L_{aa} and the

mutual inductance L_{ab} are shown in Figure 8.4.

To obtain a simplified inductance tensor $[L_{ABC}]$, harmonic inductance terms of the order 40 and above were neglected, resulting in equation 8.2 (see overleaf).

The corresponding rotational inductance tensor $[G_{ABC}]$ is given by equation 8.3 (see overleaf),

$$\text{where } [G_{ABC}] = \frac{d}{dt} [L_{ABC}] \quad 8.4$$

8.3 Model of the PMG on Rectifier Load

The differential equations for the PMG on a rectifier load are obtained in a similar way to that discussed in Chapter 3. The primitive mesh network for Figure 8.5a are given in Figure 8.5b, with the corresponding equations being

$$[V_p] = [Z_p][I_p] \quad 8.5$$

where

$$[V_p] = [E_a \ E_b \ E_c \ 0 \ 0 \ 0 \ 0 \ 0 \ 0]_t \quad 8.6$$

$$[I_p] = [I_a \ I_b \ I_c \ I_L \ I_{D1} \ I_{D2} \ I_{D3} \ I_{D4} \ I_{D5} \ I_{D6}]_t \quad 8.7$$

and $[Z_p]$ is given by equation 8.8 (page 209).

Figure 8.6 shows the independent current variables of the network (assuming all diodes conducting). The transformation tensor $[C_1]$ relating the independent currents to the primitive mesh currents is

$$[I_p] = [C_1][I_n] \quad 8.9$$

$$[L_{ABC}] = \begin{bmatrix} L_{aa} & L_{ab} & L_{ac} \\ L_{ba} & L_{bb} & L_{bc} \\ L_{ca} & L_{cb} & L_{cc} \end{bmatrix} = \begin{bmatrix} A_0 + A_2 \cos(2\theta_a) & -B_0 + B_2 \cos(2\theta_a - 2\pi/3) & -B_0 + B_2 \cos(2\theta_a - 4\pi/3) \\ -B_0 + B_2 \cos(2\theta_a - 2\pi/3) & A_0 + A_2 \cos(2\theta_a - 4\pi/3) & -B_0 + B_2 \cos(2\theta_a) \\ -B_0 + B_2 \cos(2\theta_a - 4\pi/3) & -B_0 + B_2 \cos(2\theta_a) & A_0 + A_2 \cos(2\theta_a - 2\pi/3) \end{bmatrix}$$

8.2

$$[G_{ABC}] = \begin{bmatrix} G_{aa} & G_{ab} & G_{ac} \\ G_{ba} & G_{bb} & G_{bc} \\ G_{ca} & G_{cb} & G_{cc} \end{bmatrix} = \begin{bmatrix} -2A_2 \omega \sin(2\theta_a) & -2B_2 \omega \sin(2\theta_a - 2\pi/3) & -2B_2 \omega \sin(2\theta_a - 4\pi/3) \\ -2B_2 \omega \sin(2\theta_a - 2\pi/3) & -2A_2 \omega \sin(2\theta_a - 4\pi/3) & -2B_2 \omega \sin(2\theta_a) \\ -2B_2 \omega \sin(2\theta_a - 4\pi/3) & -2B_2 \omega \sin(2\theta_a) & -2A_2 \omega \sin(2\theta_a - 2\pi/3) \end{bmatrix}$$

8.3.

$[Z_p] =$

Z_{aa}	Z_{ab}	Z_{ac}							
Z_{ba}	Z_{bb}	Z_{bc}							
Z_{ca}	Z_{cb}	Z_{cc}							
			Z_L						
				Z_D					
					Z_D				
						Z_D			
							Z_D		
								Z_D	
									Z_D

where

$$[C_1] = \begin{bmatrix} -1 & 0 & 0 & -1 & 0 \\ 0 & -1 & 0 & 0 & -1 \\ 1 & 1 & 0 & 1 & 1 \\ 1 & 1 & 1 & 0 & 0 \\ 1 & 0 & 0 & 0 & 0 \\ 0 & 1 & 0 & 0 & 0 \\ 0 & 0 & 1 & 0 & 0 \\ 0 & 0 & 0 & 1 & 0 \\ 0 & 0 & 0 & 0 & 1 \\ -1 & -1 & -1 & -1 & -1 \end{bmatrix} \quad 8.10$$

and

$$[I_n] = [I_1 \ I_2 \ I_3 \ I_4 \ I_5]_t \quad 8.11$$

The voltage tensor $[V_n]$ is

$$[V_n] = [C_1]_t [V_p] \quad 8.12$$

and the impedance tensor $[Z_n]$ is given by equation 8.13 (see overleaf). The resultant equation for the network is

$$[V_n] = [Z_n][I_n] \quad 8.14$$

Since the rectifier diodes are not all conducting at any particular instant, equation 8.14 cannot be used to obtain the required network currents. A transformation tensor $[C_2]$ is therefore obtained as described in Chapter 3, relating the independent currents I_n to the actual currents I_m flowing in the network. The transformation tensor $[C_2]$ depends on the state of the system at any particular instant in time (i.e. the voltage across a diode or the current flowing through it).

$[Z_n] =$

$Z_{aa} - 2Z_{ac} + Z_{cc}$ $+ Z_L$	$Z_{ab} - Z_{ac} - Z_{bc}$ $+ Z_{cc} + Z_L$	Z_L	$Z_{aa} - 2Z_{ac} + Z_{cc}$	$Z_{ab} - Z_{ac} - Z_{bc}$ $+ Z_{cc}$
$Z_{ab} - Z_{ac} - Z_{bc}$ $+ Z_{cc} + Z_L$	$Z_{bb} - 2Z_{bc} + Z_{cc}$ $+ Z_L$	Z_L	$Z_{ab} - Z_{bc} - Z_{ac}$ $+ Z_{cc}$	$Z_{bb} - 2Z_{bc} + Z_{cc}$
Z_L	Z_L	Z_L	0	0
$Z_{aa} - 2Z_{ac} + Z_{cc}$	$Z_{ab} - Z_{ac} - Z_{bc}$ $+ Z_{cc}$	0	$Z_{aa} - 2Z_{ac} + Z_{cc}$	$Z_{ab} - Z_{ac} - Z_{bc}$ $+ Z_{cc}$
$Z_{ab} - Z_{ac} - Z_{bc}$ $+ Z_{cc}$	$Z_{bb} - 2Z_{bc} + Z_{cc}$	0	$Z_{ab} - Z_{bc} - Z_{ac}$ $+ Z_{cc}$	$Z_{bb} - 2Z_{bc} + Z_{cc}$

8.13

$$[I_n] = [C_2][I_m] \quad 8.15$$

Therefore, following the method of analysis of Chapter 3

$$[I_p] = [C_1][C_2][I_m] \quad 8.16$$

$$\text{and if } [C] = [C_1][C_2] \quad 8.17$$

$$[Z_m] = [C]_t \cdot [Z_p][C] \quad 8.18$$

$$[V_m] = [C]_t [V_p] \quad 8.19$$

The resulting differential equation is

$$[pI_m] = [L_m]^{-1} \{ [V_m] - \{ [R_m] + [G_m] \} \cdot [I_m] \} \quad 8.20$$

where $p = \frac{d}{dt}$

Equation 8.20 may be numerically integrated to obtain $[I]_m$ and hence $[I]_n$ and $[I]_p$. The diode currents are calculated at each time step from $[I]_p$ and the corresponding diode voltages are obtained from

$$[V] = [V]_n - [Z]_n [I]_n \quad 8.21$$

where the $[V]$ tensor takes the form

$$[V] = \begin{array}{|c|} \hline V_{D1} - V_{D6} \\ \hline V_{D2} - V_{D6} \\ \hline V_{D3} - V_{D6} \\ \hline V_{D4} - V_{D6} \\ \hline V_{D5} - V_{D6} \\ \hline \end{array} \quad 8.22$$

If D6 is conducting, V_{D6} is zero and all the other diode voltages can be obtained from $[V]$. Similarly if D6 is not conducting, but some other diode, say D2 is, V_{D2} is zero and V_{D6} can be calculated from $[V]$, which enables the voltages across all the other diodes to be calculated.

If a non-conducting diode has a positive voltage across it, or if the current through a conducting diode is negative, the point of discontinuity is calculated by interpolation and the diode voltages and current variables are updated to this point. A new transformation tensor $[C_2]$ is computed relating the independent currents $[I_n]$ to the actual currents $[I_m]$ flowing in the network, which depend on the diodes in ON (conducting) state. A flow diagram for the PMG computer program is given in Figure 8.7.

8.4 Calculation of the PMG Phase Voltages

It is evident from the recording of the open-circuit phase winding voltage given in Figure 8.8, that it has an appreciable harmonic content. However to simplify the model of the PMG, it will be assumed that the voltages generated in the phase windings are sinusoidal. It is found from comparison of the computed and the measured d.c. output voltage of the PMG on rectifier load as shown in Figure 8.9, that the contribution of the harmonic voltages to the d.c. output voltage is less than 5% of that due to the fundamental frequency voltage. Mainer⁶³ has derived the phasor diagram for the PMG, for the steady-state analysis under balanced load conditions. He has shown that a PMG can be regarded as equivalent to a conventional alternator, with a constant field m.m.f., operating in the triangle COD shown in Figure 8.10. (It is found in practice that point D is much closer to B than is shown in the figure, so that even when a short circuit is applied to the generator terminals and removed, the recoil line remains the same as under normal operating condition.) This was confirmed to be the case for the PMG investigated, since when a low resistance load (less than $0.5\Omega/\text{phase}$) was applied and removed, the output voltage recovered to its original open-circuit voltage. (When the PMG is on load, and the armature m.m.f. has a demagnetising component, the operating point (determined

by the working permeance line and the recoil line) moves from E towards B. The flux density in the magnet attributable to the airgap flux (B_{mg}) decreases, while that attributable to the leakage flux ($B_{m\lambda}$) increases as the operating point shifts from E towards B. This fundamental characteristic of the PMG is used in the phase model representation, in which the operating point of the permanent magnet and the peak airgap flux are calculated at each time step by determining the demagnetising m.m.f. due to the armature currents. The generated phase voltages are then calculated from the value of airgap flux density.

The demagnetising m.m.f. F_{ds} in the d-axis due to the armature currents is

$$F_{ds} = N K_w (i_a \cos \theta_a + i_b \cos \theta_b + i_c \cos \theta_c) \quad 8.23$$

The m.m.f. F_{qs} in the q-axis due to the armature currents is

$$F_{qs} = N K_w (i_a \sin \theta_a + i_b \sin \theta_b + i_c \sin \theta_c) \quad 8.24$$

The demagnetising m.m.f. per pole is F_{ds}/P , where P is the number of poles. The airgap flux density is calculated from the B/H characteristic and the permeance lines for Alcomax III using the calculated demagnetising m.m.f.

The voltage generated in the armature phase is

$$e = \frac{d\lambda}{dt} = N K_w \left(\frac{d\phi}{dt} \right) \quad 8.25$$

$$E_{r.m.s.} = 4.44 f N K_w \phi_p \quad 8.26$$

$$\hat{E} = 4 f \hat{B}_g N K_w \cdot l \cdot \tau \quad 8.27$$

The instantaneous generated armature voltages are:

$$\begin{array}{|c|} \hline E_a \\ \hline E_b \\ \hline E_c \\ \hline \end{array} = 4 f N \cdot K_w \cdot l \cdot \tau \cdot \begin{array}{|c|} \hline \hat{B}_g \sin(\theta_a) \\ \hline \hat{B}_g \sin(\theta_b) \\ \hline \hat{B}_g \sin(\theta_c) \\ \hline \end{array} \quad 8.28$$

where:

$$\theta_b = \theta_a - 2\pi/3$$

$$\theta_c = \theta_a - 4\pi/3$$

The voltage tensor $[V_n]$ is calculated at each time step using equation 8.12 and the values of E_a , E_b and E_c obtained from equation 8.28, and $[V_m]$ is calculated using equation 8.19, for use in the numerical integration of equation 8.20.

8.5 Comparison Between the Calculated and the Measured Performance of PMG on Rectifier Load

The measured and predicted steady-state characteristics of the PMG on a purely resistive load are given in Figure 8.9. Figure 8.11 shows the predicted phase voltage V following application of 5Ω (the normal magnitude of load resistance for 2130 PMG) and 0.625Ω resistive load. The corresponding measured voltage waveforms are given in Figures 8.12(a), (b) respectively which also show the measured armature phase current waveforms. The predicted phase current and the d.c. output current on application of the resistive loads are given in Figures 8.13 and 8.14 respectively. The corresponding measured waveforms are given in Figure 8.15(a) and (b) respectively.

Predicted waveforms of the reverse voltage across diode D1 are given in Figure 8.16, with the corresponding measured waveforms being given in Figures 8.17 (a), (b). These figures also show the diode currents and these may be compared with the predicted diode current waveforms given in Figure 8.18.

It is possible to predict the copper loss in the phase windings (and the total copper loss in all the windings) as the program calculates the winding currents at each time steps, as shown in Figure 8.19. The predicted resultant airgap flux density as a fraction of the airgap flux density on no load, on application of resistive loads, is given in Figure 8.20.

Comparison of measured and predicted results shows that the phase model developed for the PMG predicts accurately all its major characteristics. From the machine designer's point of view, this enables him to choose the correct rectifiers, machine size etc. to optimise the design. The data predicted by the program is also useful to the engineer designing the a.v.r., as it can predict the regulation of the d.c. output voltage on application of a load.

Since the settling time of the generator terminal voltage following application or rejection of a load is of the order of 30 ms to 45 ms, it is found that the steady-state characteristics of the PMG are sufficiently accurate for studying the regulated generator transients. It can be seen from the measured and predicted transient response on application of a $5\ \Omega$ resistive load that the PMG response is very fast, as it is essentially steady state after 0.25 ms, or one-tenth of a generator cycle. If the load resistance is very low (0.625 ohms), the PMG output achieves steady state after 1 ms which is still very short when compared with the settling time following application of a 1 p.u. load to the main generator terminals of the order of 30 ms.

8.6 Conclusion

The phase voltage waveform shown in Figure 8.8 clearly implies an airgap flux density distribution of the form

$$B_g = \hat{B}_{g1} \cos\theta + \hat{B}_{g2} \cos(2\theta + \phi_2) + \hat{B}_{g3} \cos(3\theta + \phi_3) +$$

For accurate predictions of the harmonic content of the output voltage and the contribution of the harmonic voltages in the phase windings to the d.c. output voltage, it is necessary to include the harmonic voltages induced in the phase windings. If the ripple voltage on the d.c. output voltage for resistive load of 5 ohms, shown in Figure 8.21(a) is compared with the phase voltage of Figure 8.12(a), it can be seen that the ripple voltage can be accurately predicted if the harmonic voltages in the phase windings are taken into account. Similarly, comparison of the ripple voltage for a resistive load of 0.625 ohms, shown in Figure 8.21(b) with the phase voltage of Figure 8.12(b), show that the ripple voltage is directly dependent^{on} phase voltage waveform. Comparison of the ripple voltages for the two resistive loads (Figures 8.21(a) and (b)) and the corresponding phase voltages (Figures 8.12(a) and (b)) show that they are load dependent, which implies that the harmonic coefficients of equation 8.29 depend on the armature reaction and therefore for a very accurate model, it would be necessary to take this into account.

Close examination of the diode currents of Figure 8.17(a) and (b) show that these do not assume the reverse blocking state until the charges have redistributed inside the diode. A reverse current flows immediately before the diode assumes the blocking state, and a more accurate representation would necessitate consideration of the switching characteristics of the diode⁶⁴. Depending on the circuit parameters, the amount of charge stored in the diode, and its commutation behaviour, the cessation of reverse recovery current may be very abrupt, in which case the diode is said to snap off, or chop; conversely, the reverse recovery current may decrease from its peak value at a slower rate of change, in which case the reverse recovery current is said to tail off. In the former case the very high di/dt in the circuit induces large commutation voltage transients across the inductances in the path of the reverse recovery current. This requires a diode of a sufficient reverse voltage rating. On the other hand, the tail-off type of commutation behaviour may lead to large peak energy dissipation

in the diode as the device assumes reverse voltage simultaneously with the flow of significant reverse current.

Comparison of the measured and predicted performance of PMG on rectifier load discussed in Section 8.5 shows that the model described in this chapter is adequate for most practical purposes. For a study of ripple voltages, it would be necessary to include the harmonic coefficients in the airgap flux density given by equation 8.29. Since the large reverse voltages induced during commutation of diodes gives radio frequency emission of power to the surrounding, it would be necessary to include the switching characteristics of the diode for radio interference studies.

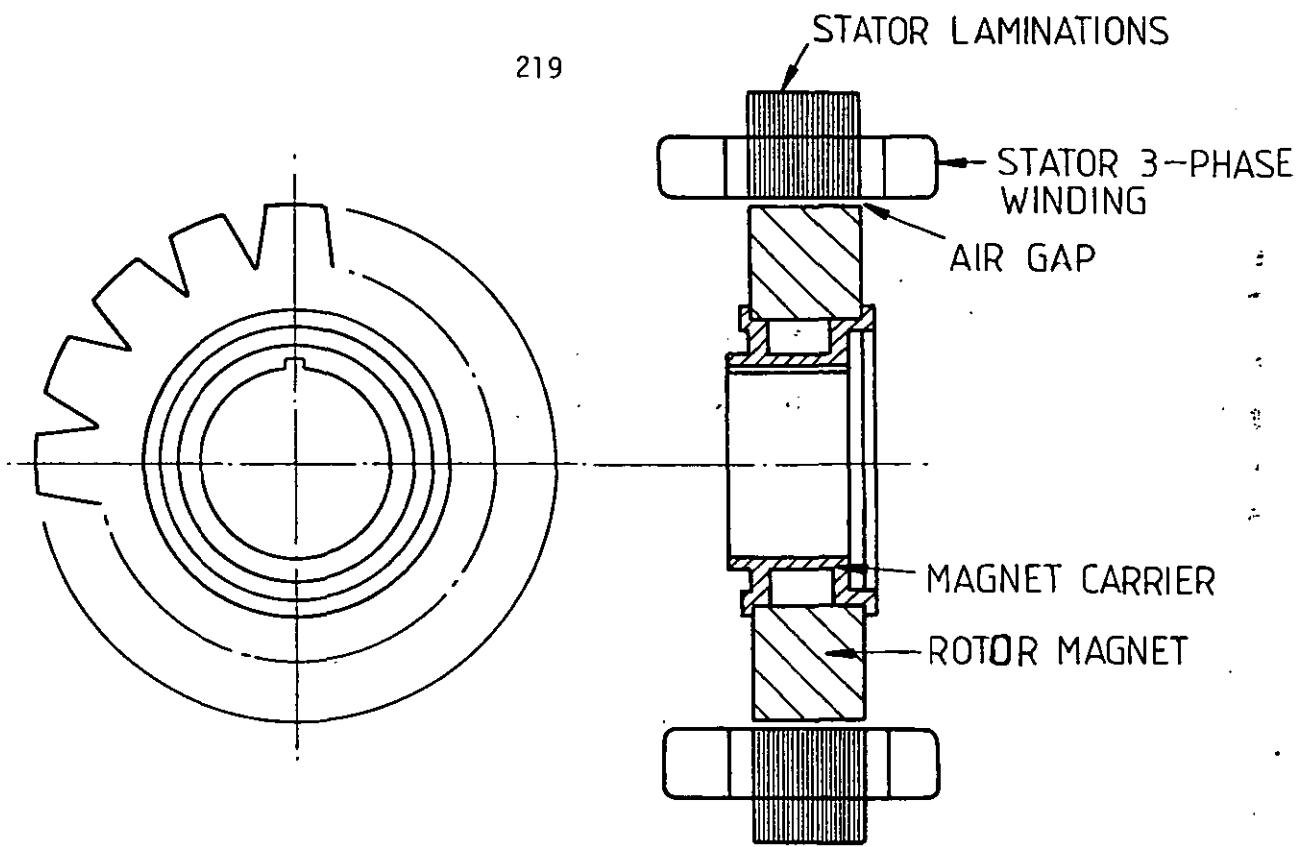


Figure 8.1 PERMANENT MAGNET GENERATOR CONSTRUCTION DETAILS

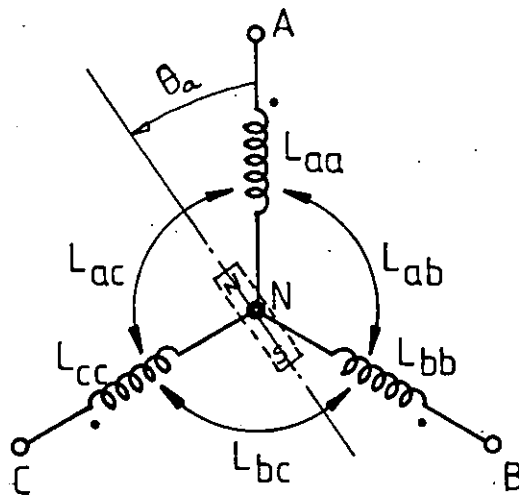


Figure 8.2 THE PHASE MODEL OF THE PERMANENT MAGNET GENERATOR

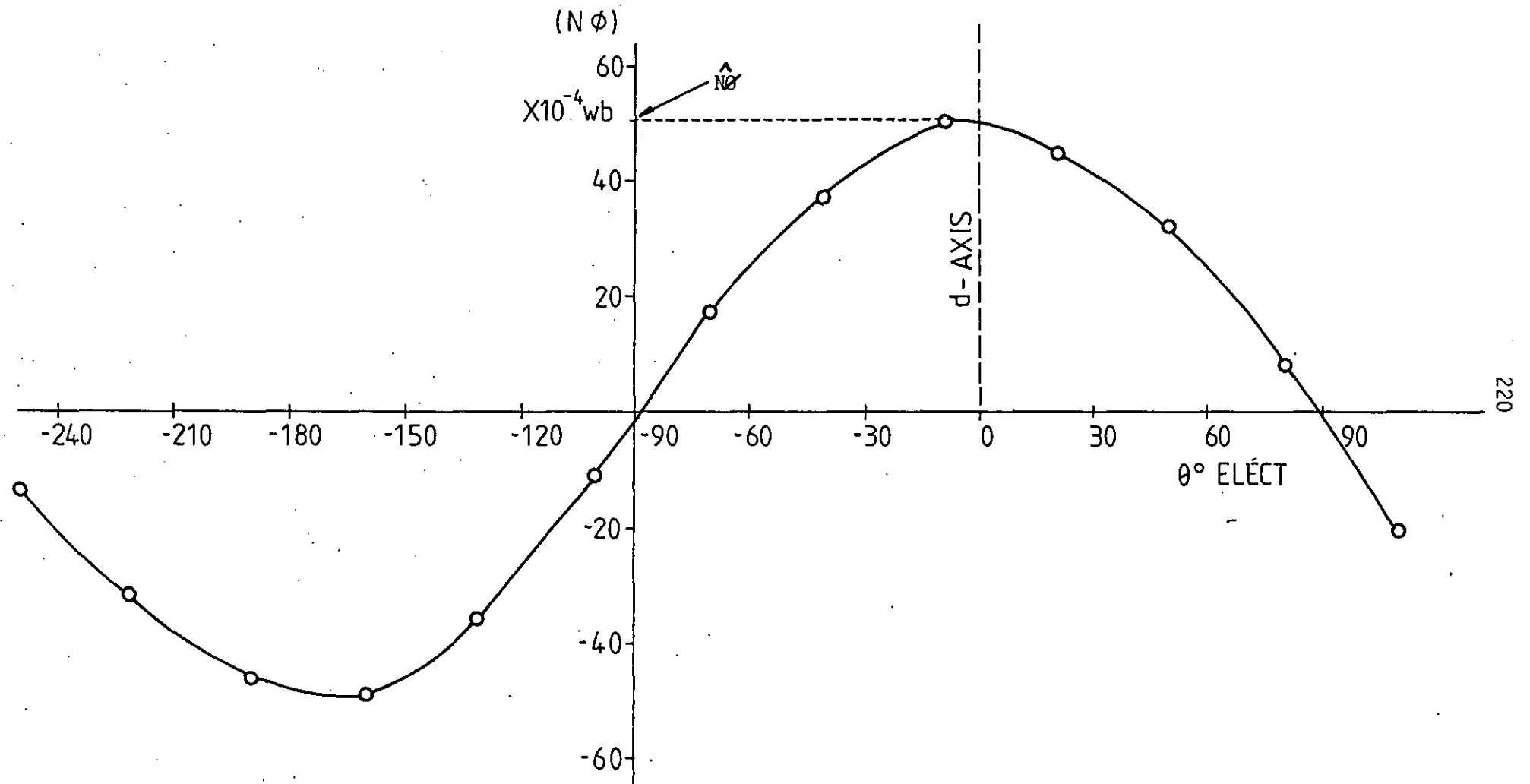


Figure 8.3 P.M.G. PHASE WINDING FLUX LINKAGE V/S θ° (ELECT)

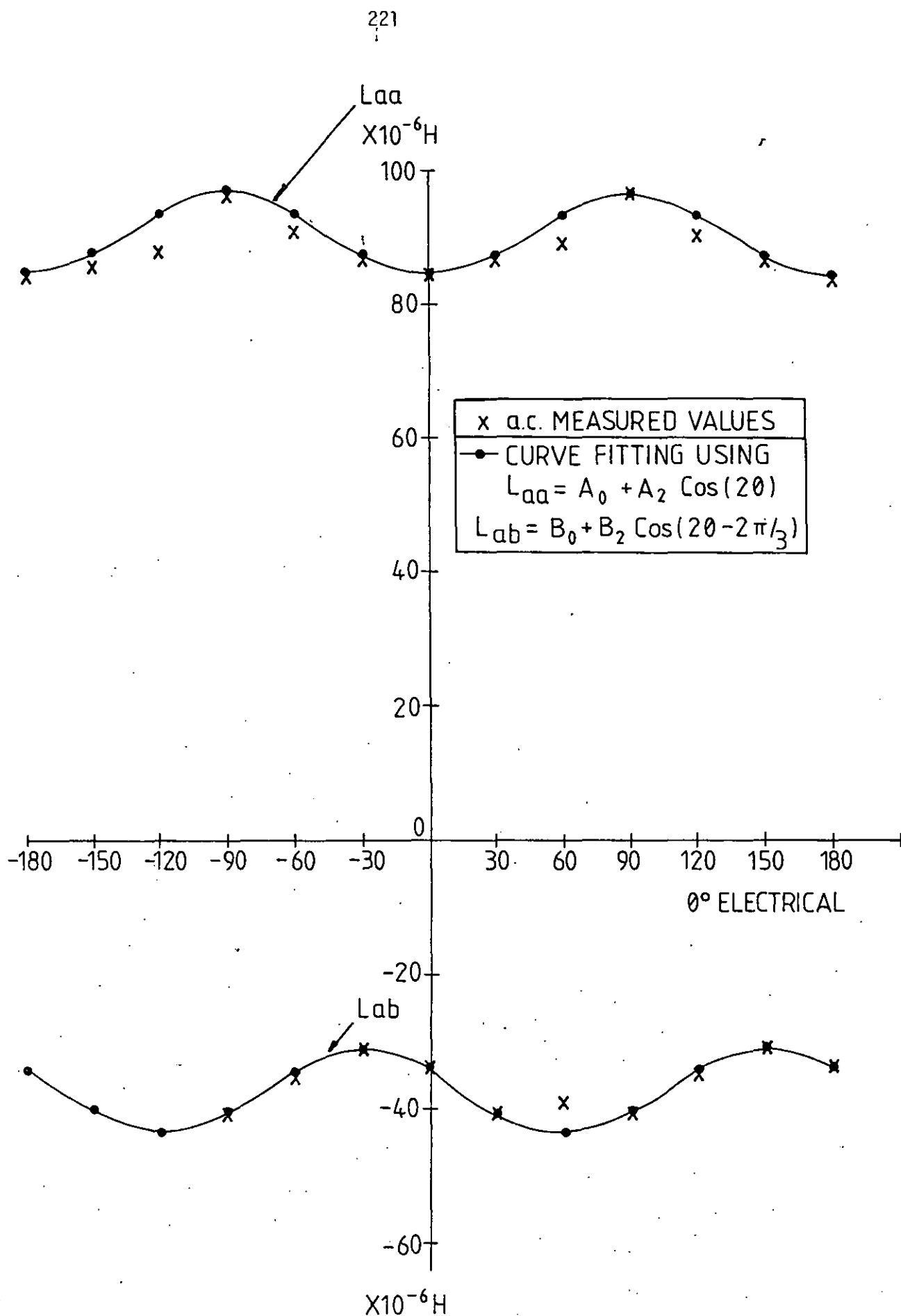


Figure 8.4

ANGULAR VARIATION OF L_{aa} AND L_{ab} PMG INDUCTANCES

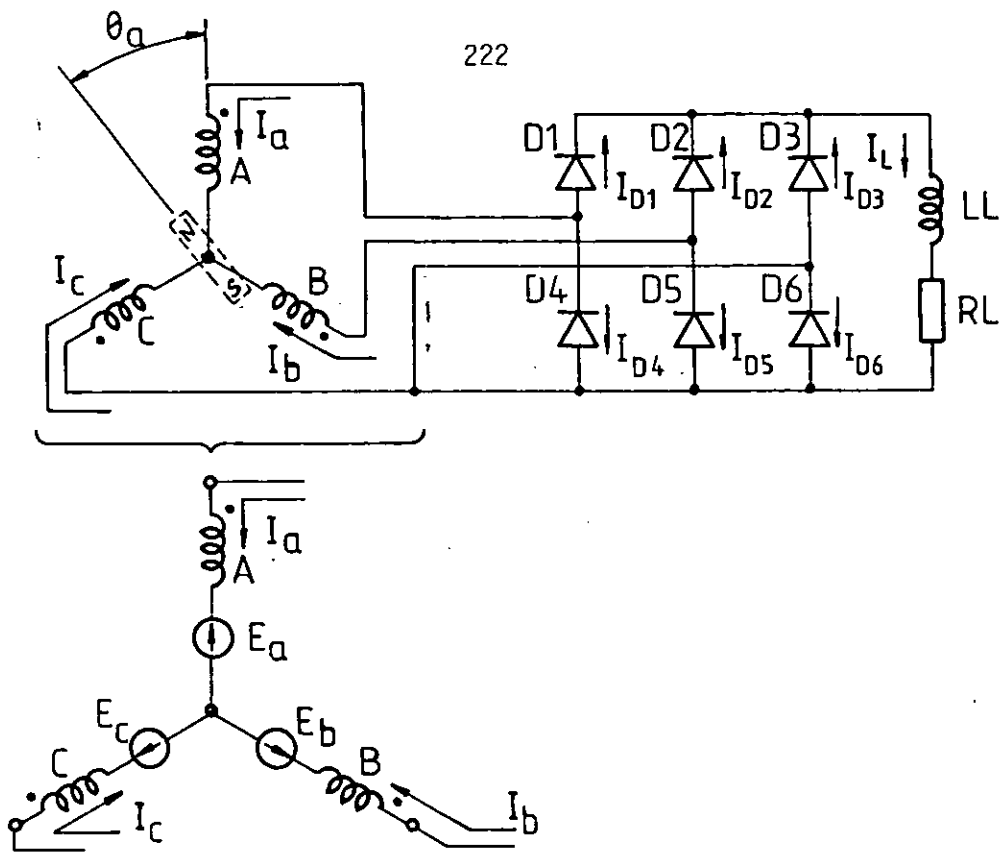


Figure 8.5(a) : PMG WITH RECTIFIER LOAD SHOWING BRANCH CURRENTS

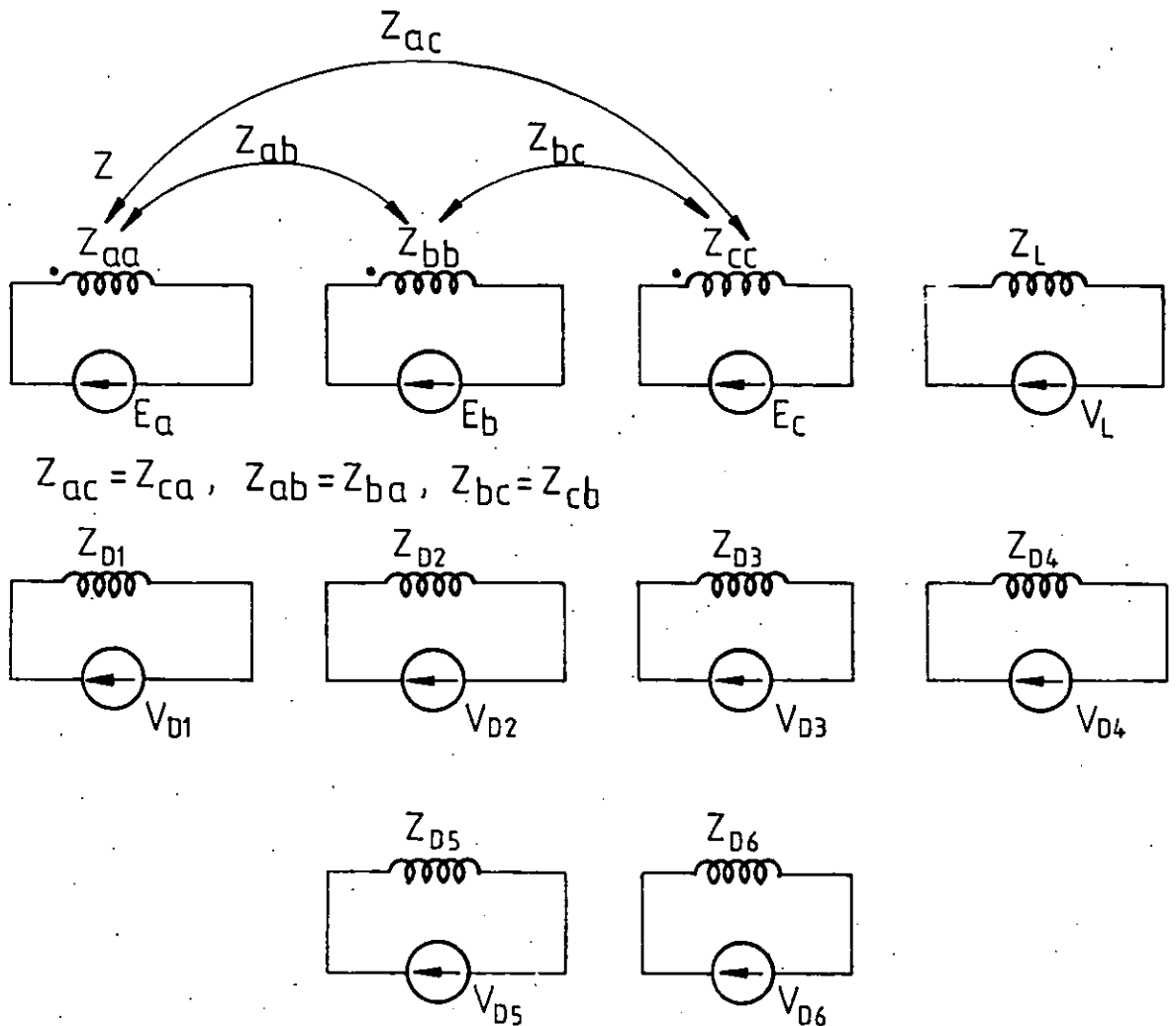


Figure 8.5(b) : PRIMITIVE MESH NETWORKS OF THE PMG WITH THE RECTIFIER LOAD

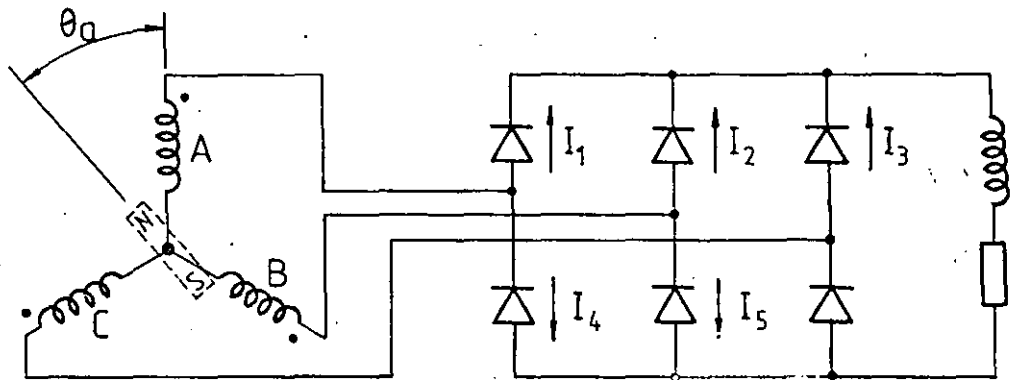


Figure 8.6

PMG WITH RECTIFIER LOAD SHOWING INDEPENDENT
CURRENT VARIABLES

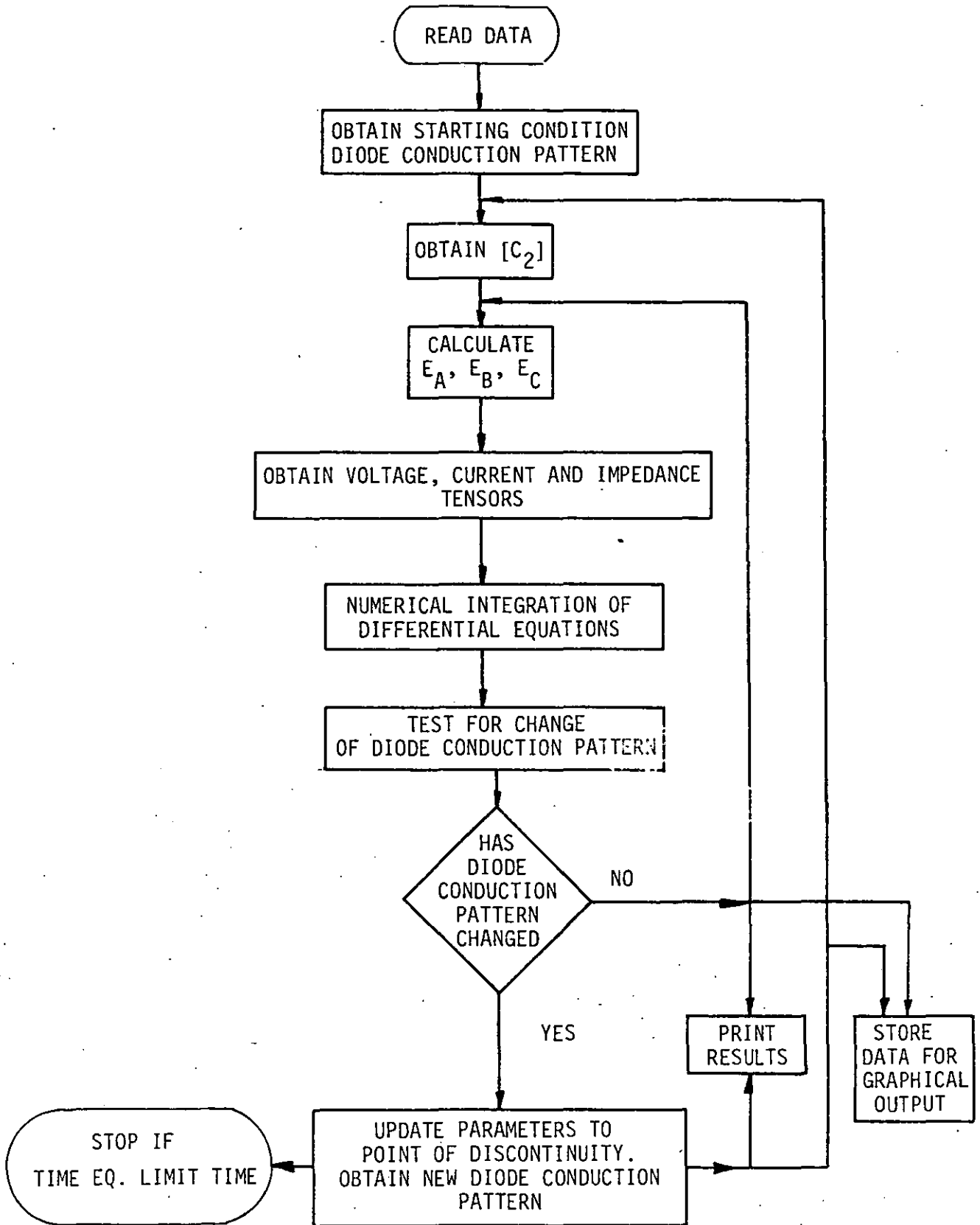


Figure 8.7

PMG with Rectifier Load Computer Program Flow Diagram

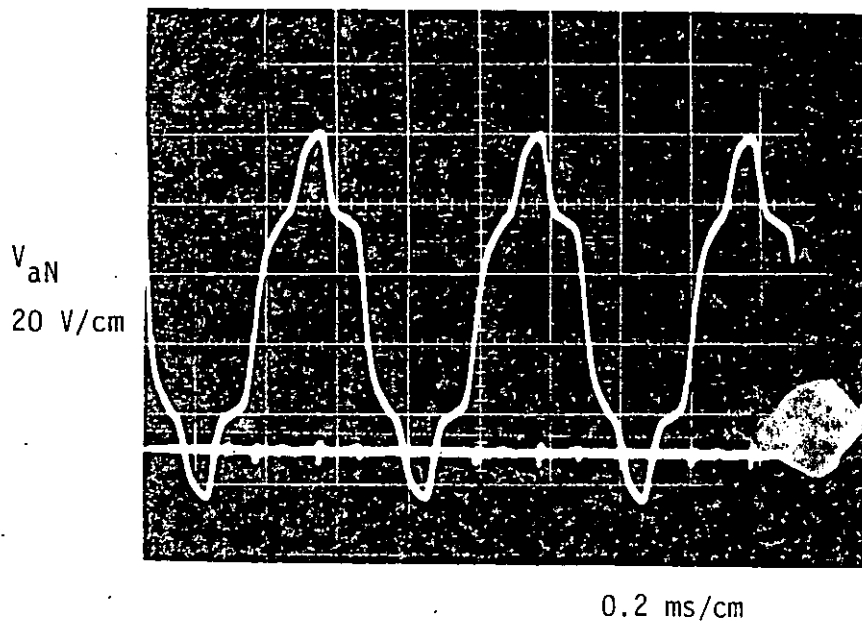


Figure 8.8

OPEN CIRCUIT PHASE VOLTAGE OF P.M.G.
(showing appreciable harmonic content.)

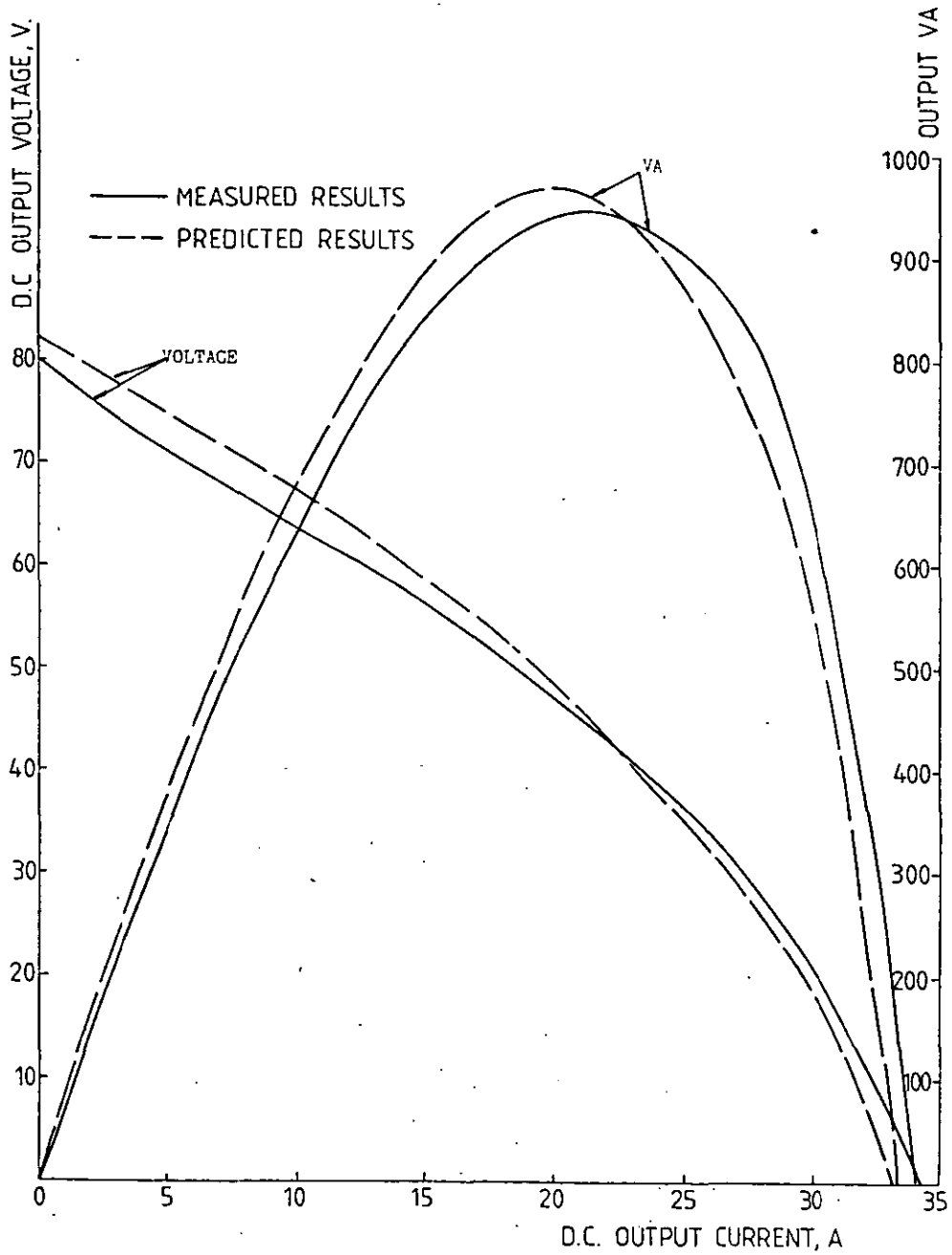


Figure 8.9 PERMANET MAGNET GENERATOR CHARACTERISTICS

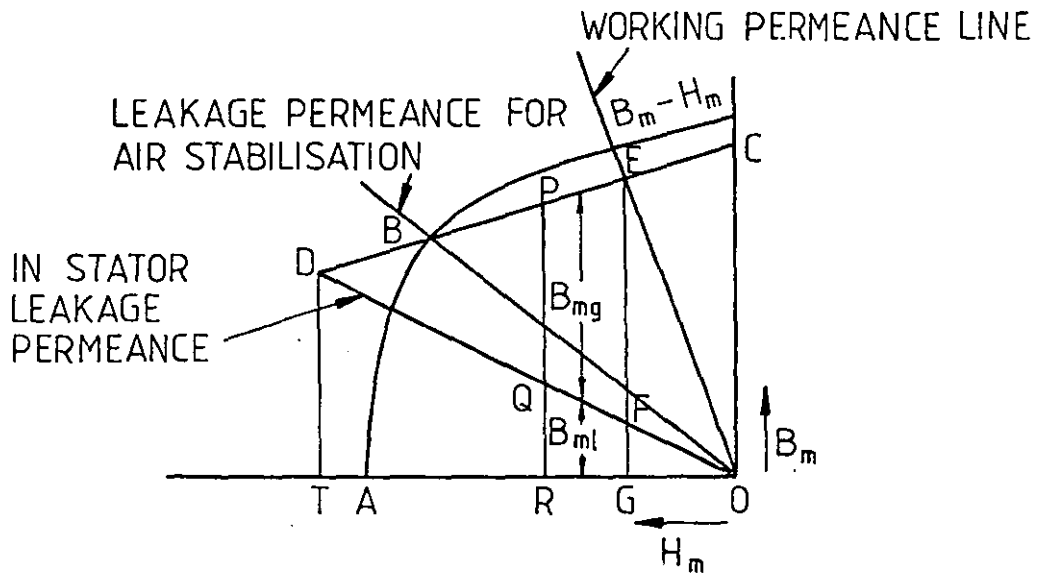


Figure 8.10

DEMAGNETIZATION CHARACTERISTICS OF PERMANENT
MAGNET GENERATOR

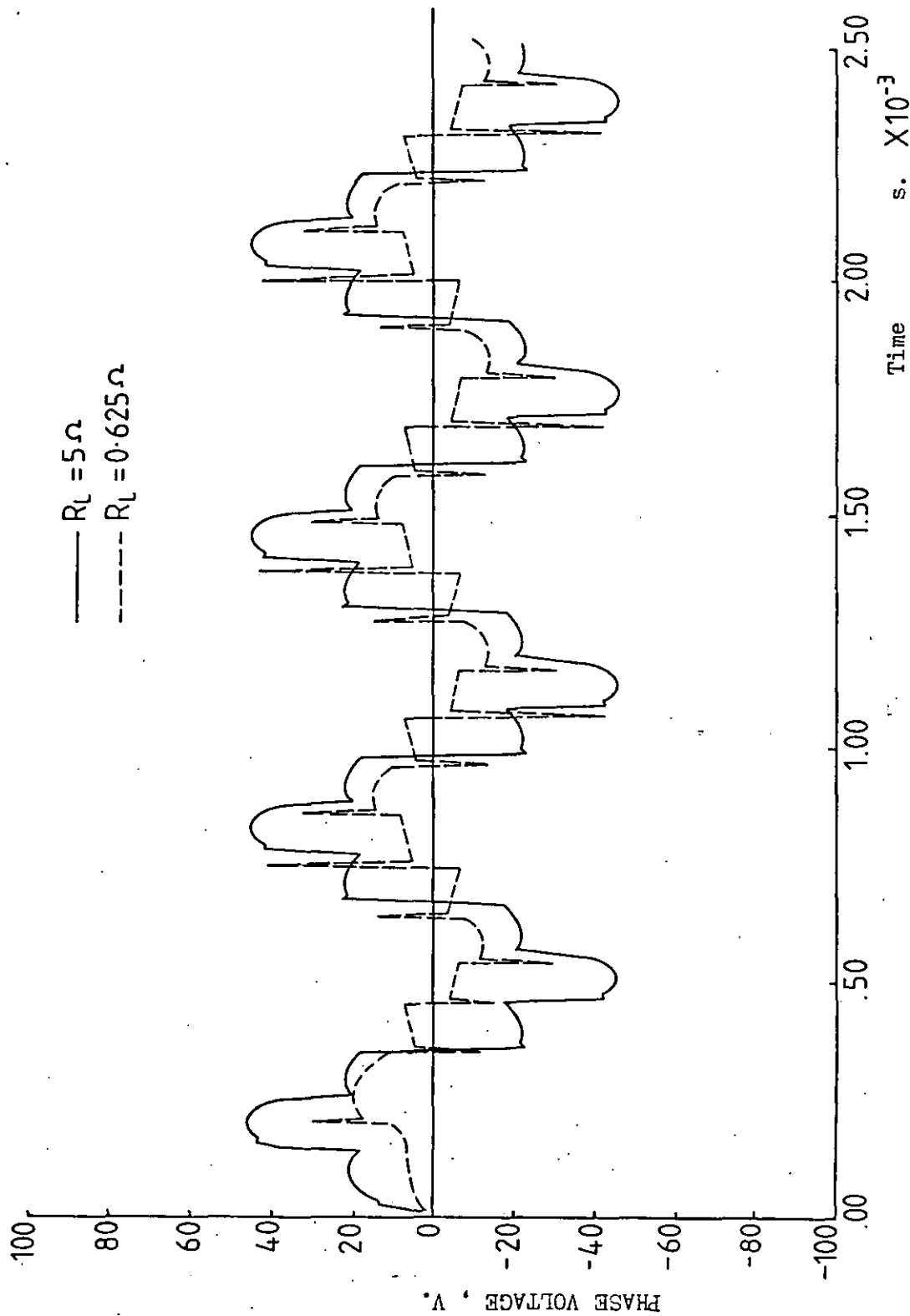


Figure 8.11 PMG PHASE VOLTAGE

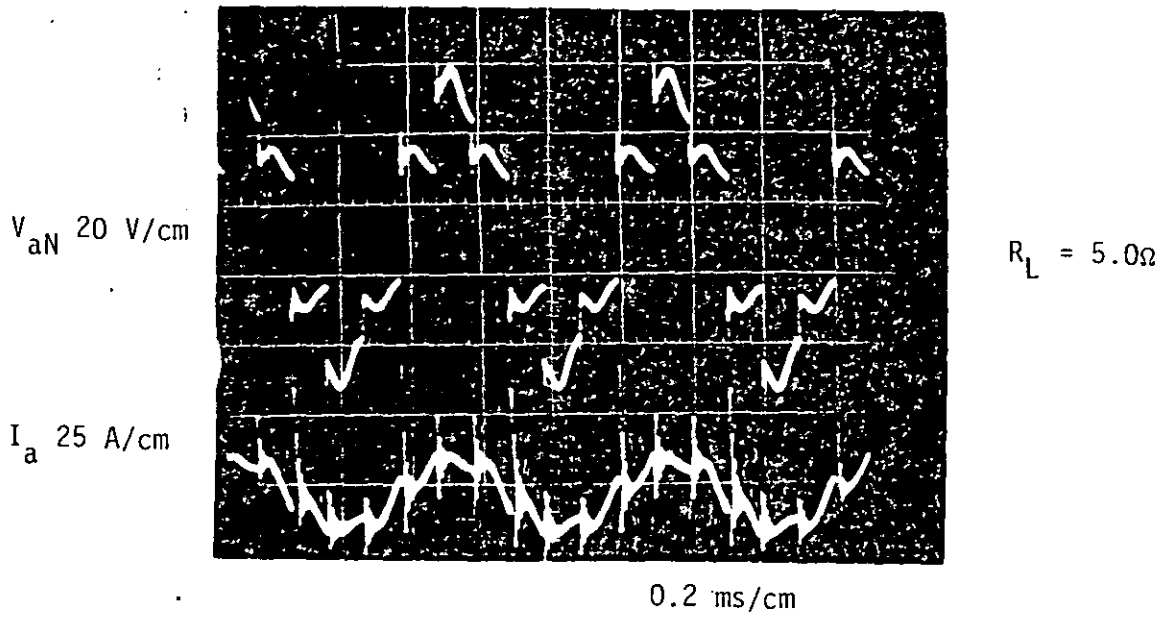


Figure 8.12(a)

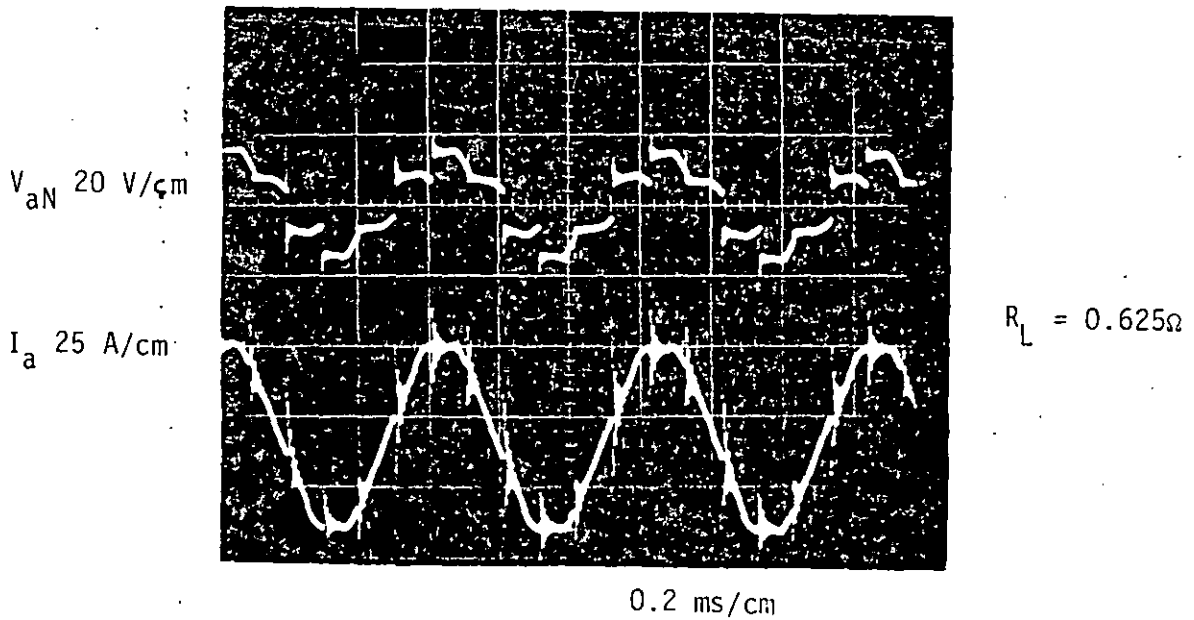


Figure 8.12(b)

A.C. MEASUREMENTS OF P.M.G. ON RECTIFIER LOAD

PHASE VOLTAGES AND CURRENTS

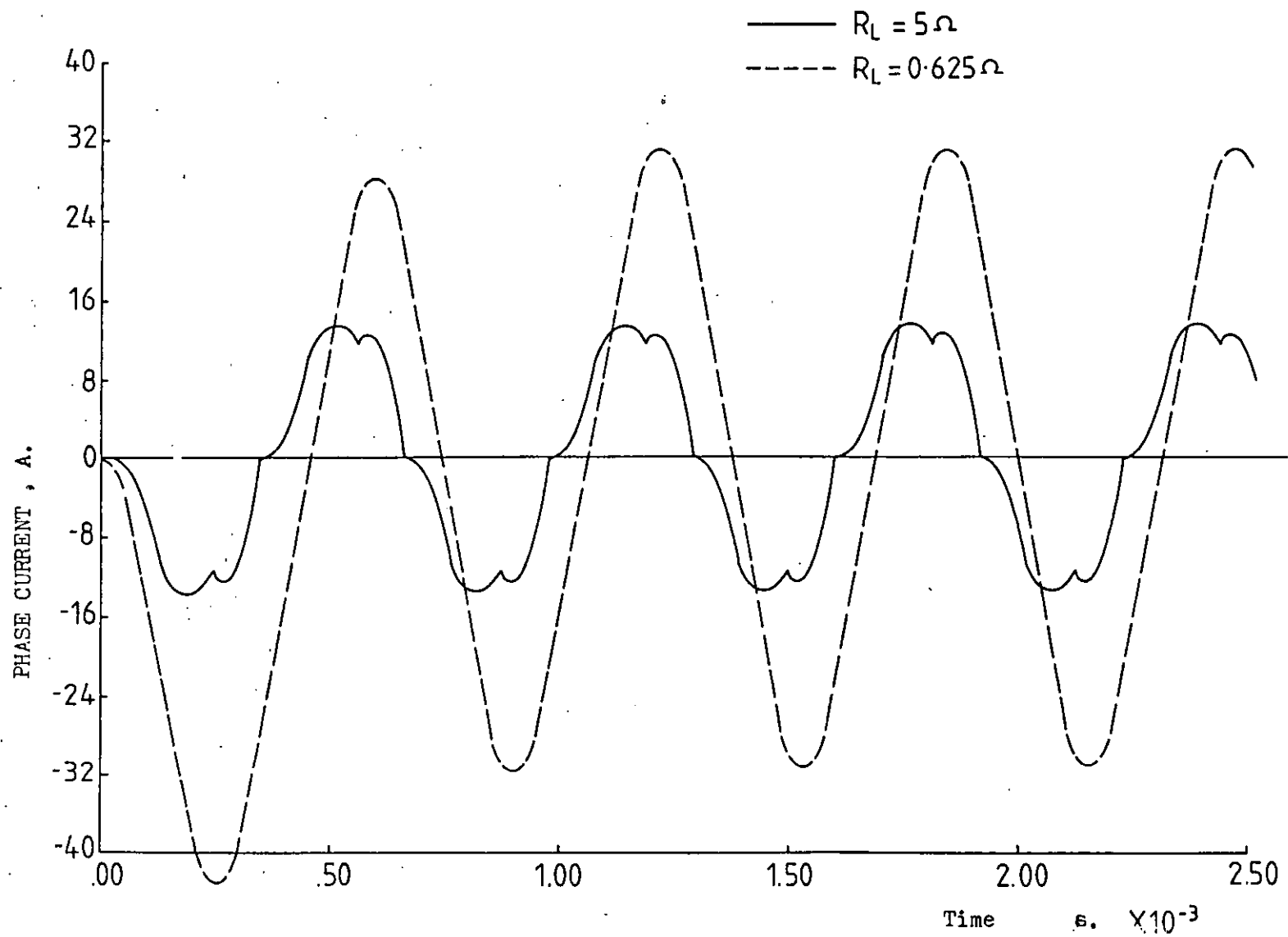


Figure 8.13 P.M.G. PHASE CURRENT

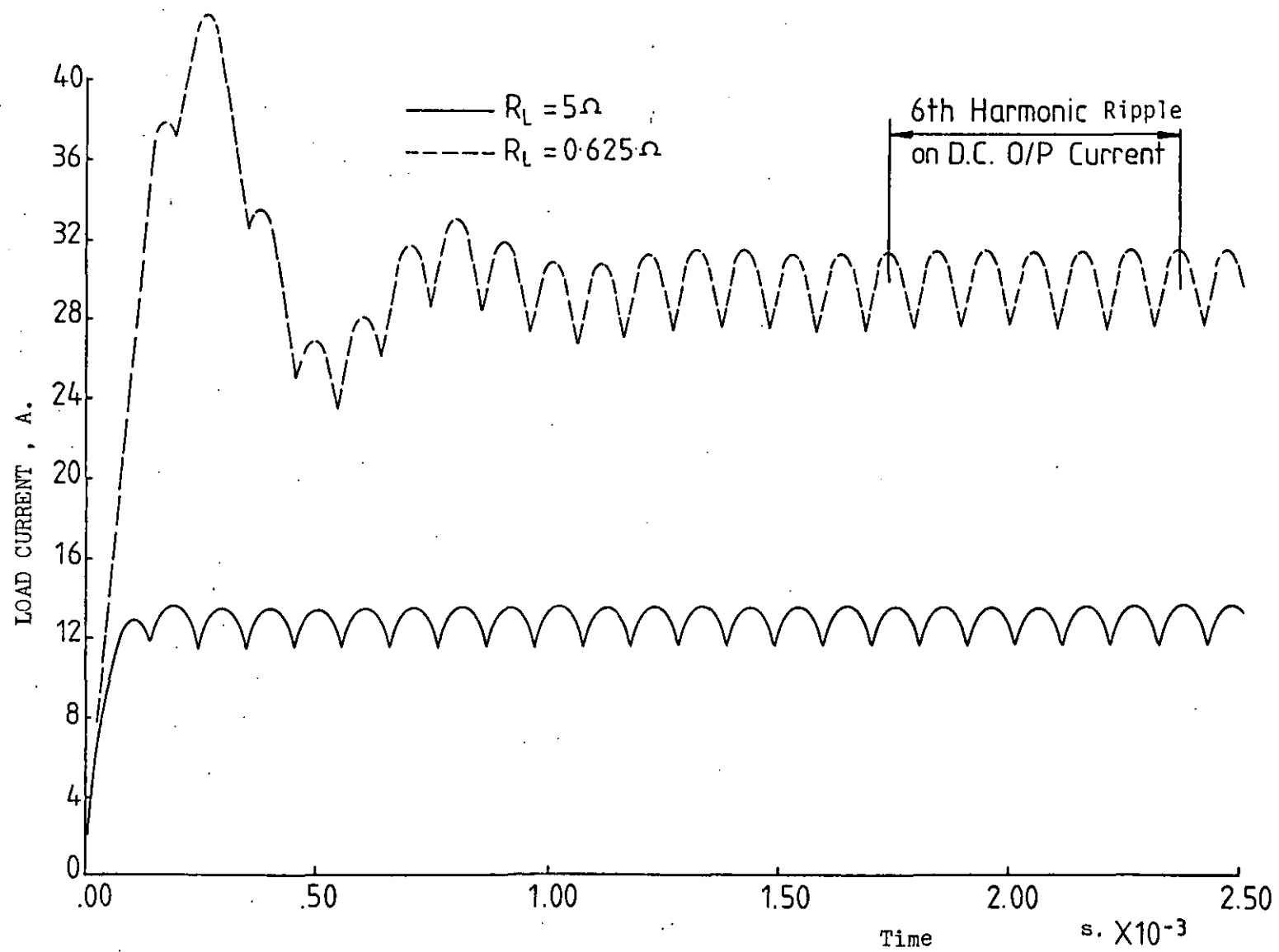


Figure 8.14

LOAD CURRENT SWITCH ON TRANSIENT

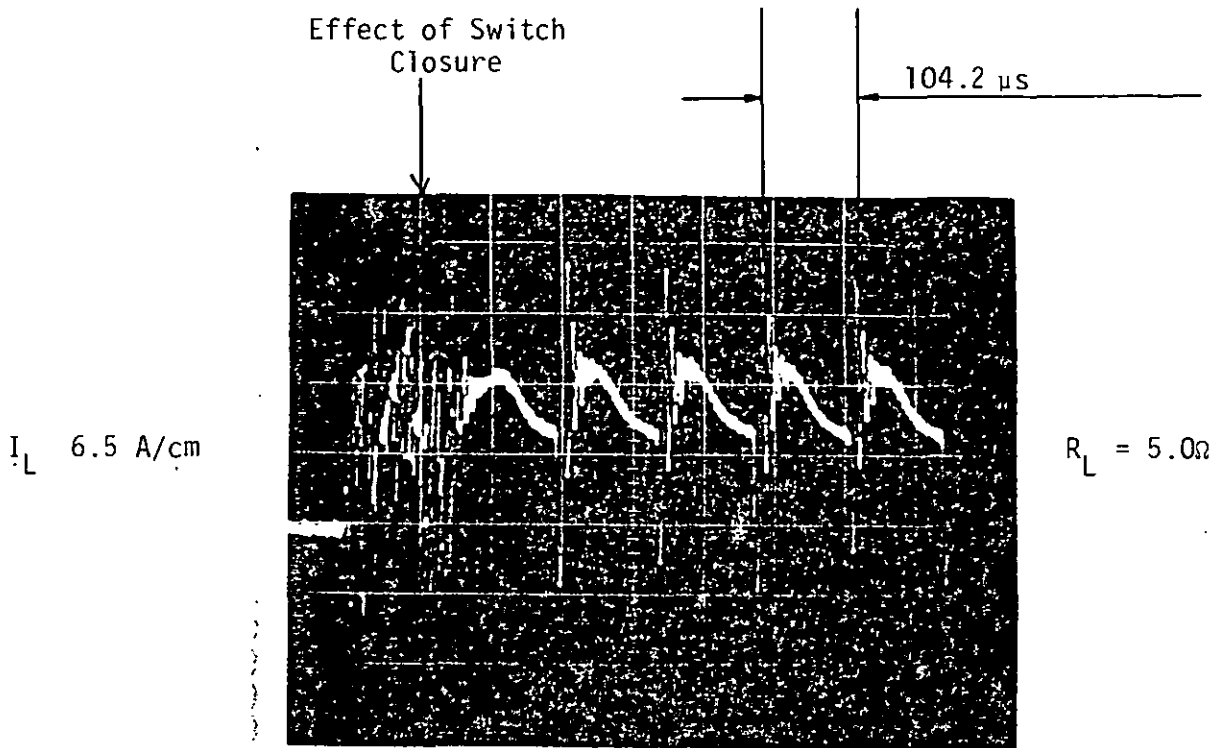


Figure 8.15(a)

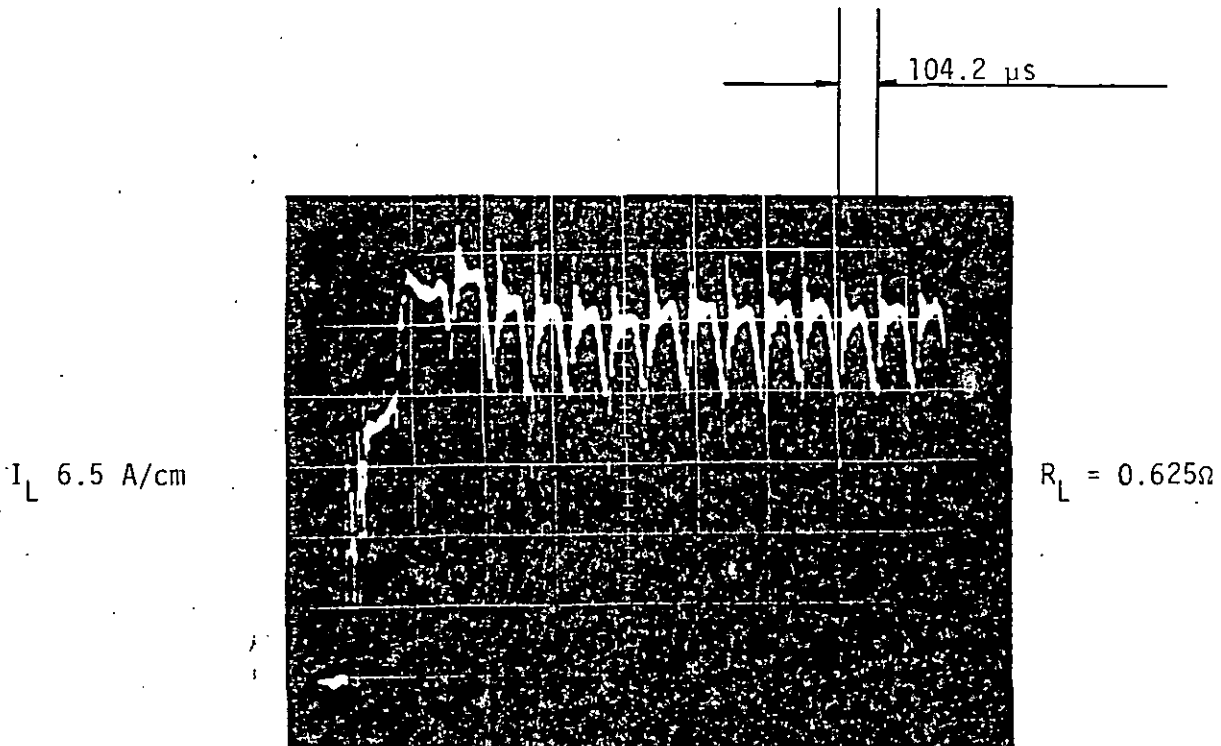


Figure 8.15(b)

TRANSIENT LOAD CURRENT ON APPLICATION OF LOAD (R_L)

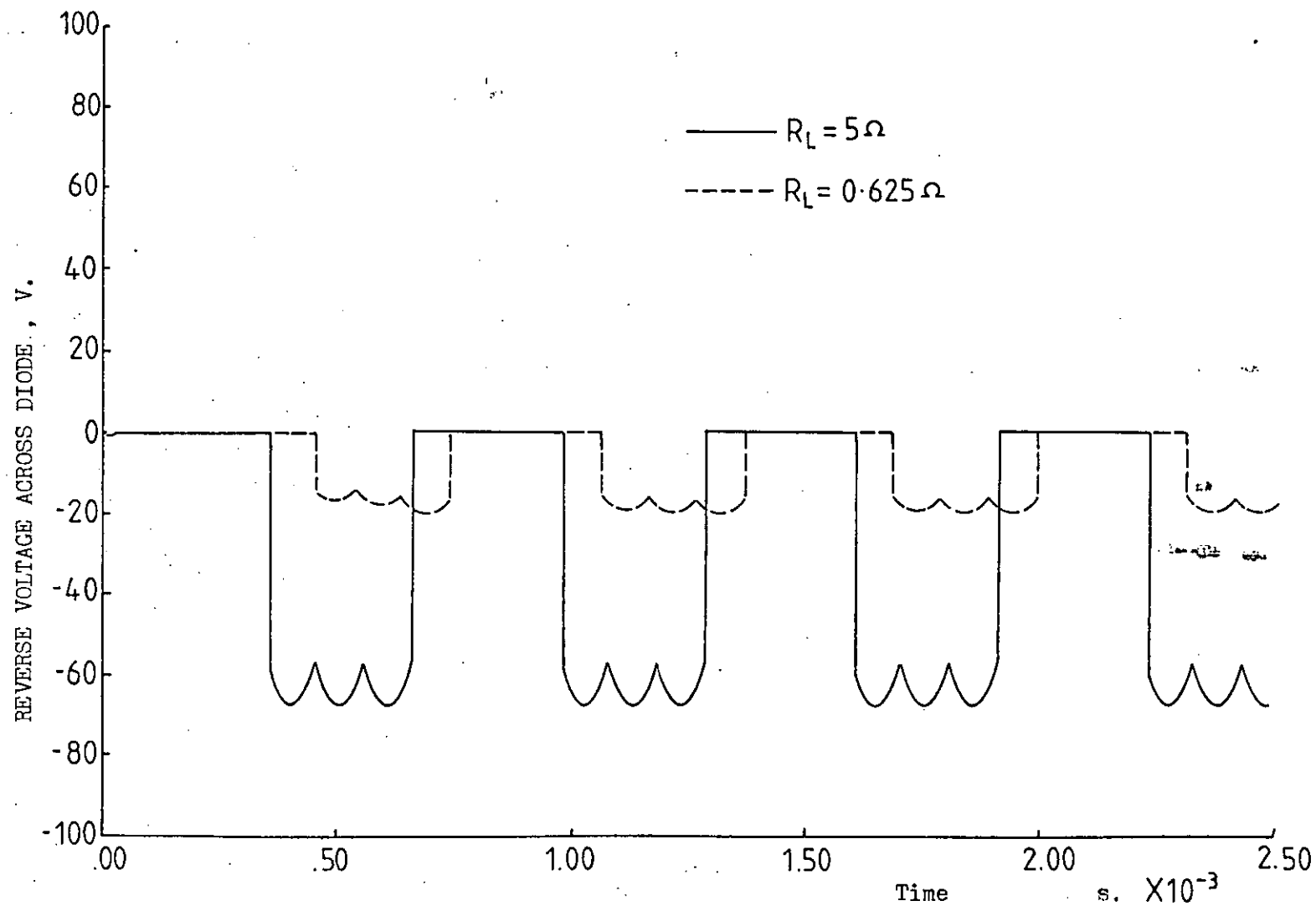


Figure 8.16

REVERSE VOLTAGE ACROSS RECTIFIER DIODE (DI)

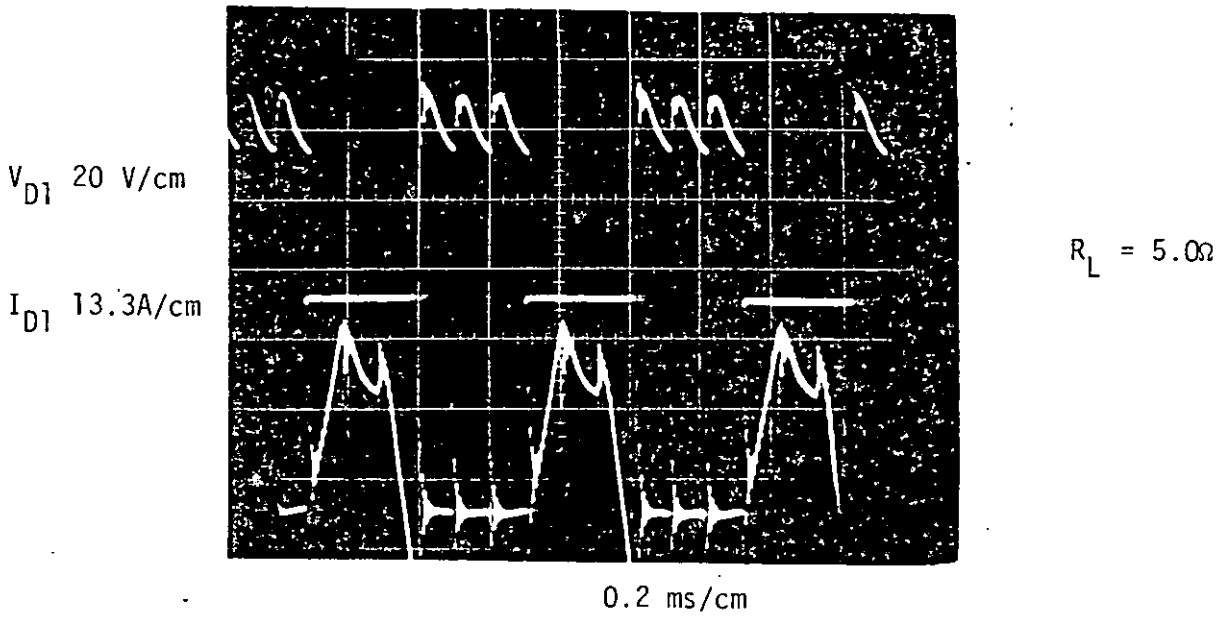


Figure 8.17(a)

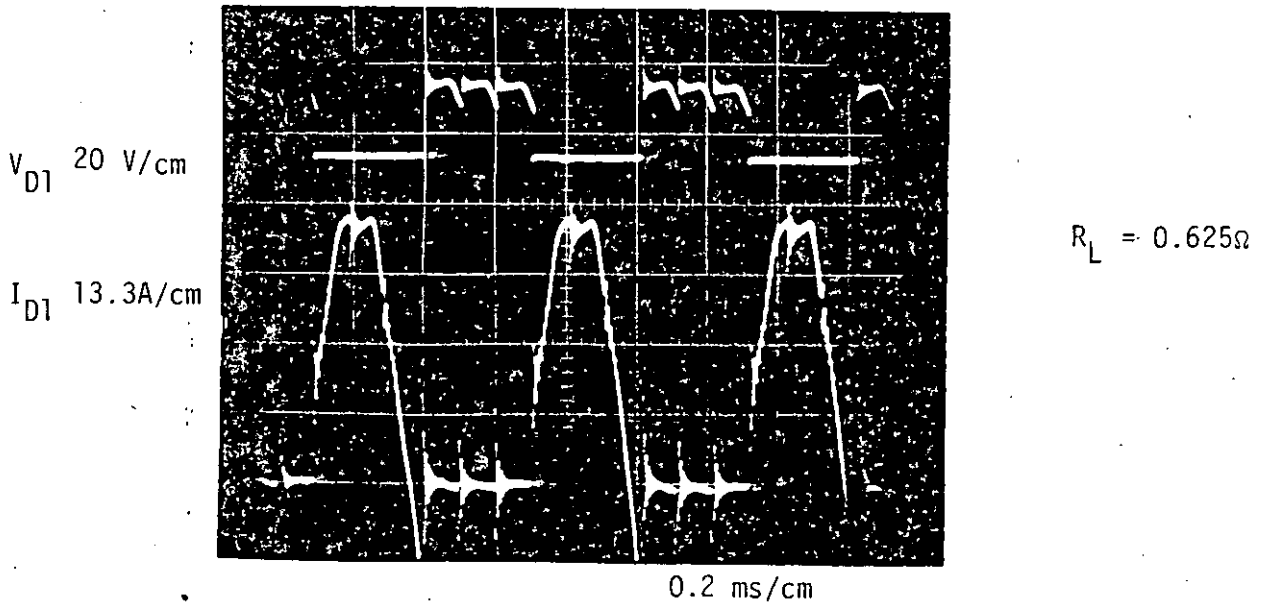


Figure 8.17(b)

RECTIFIER DIODE (D_1), REVERSE VOLTAGES AND FORWARD
CONDUCTION CURRENTS UNDER STEADY STATE LOAD CONDITIONS

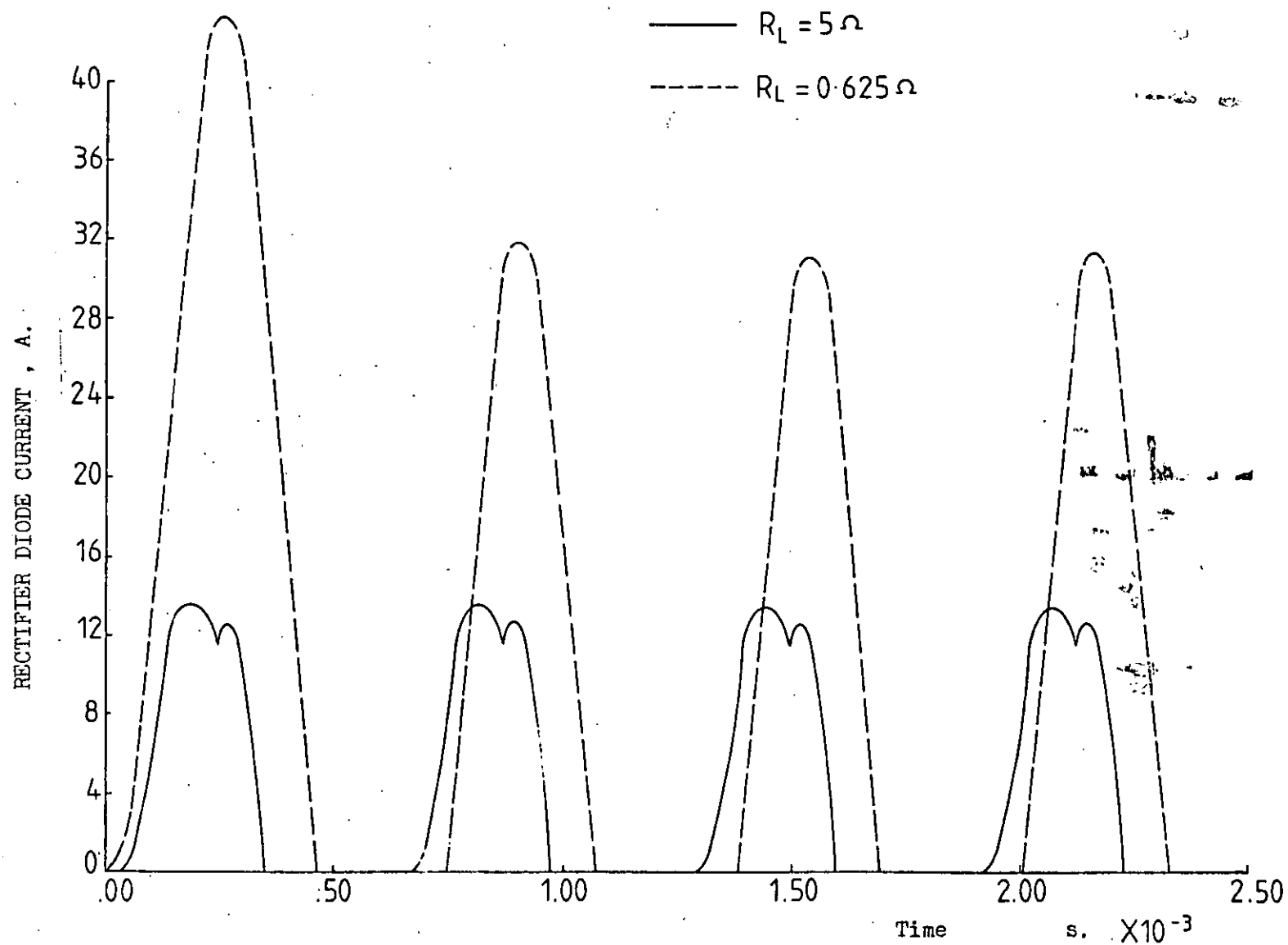


Figure 8.18

(D₁) RECTIFIER DIODE CURRENT

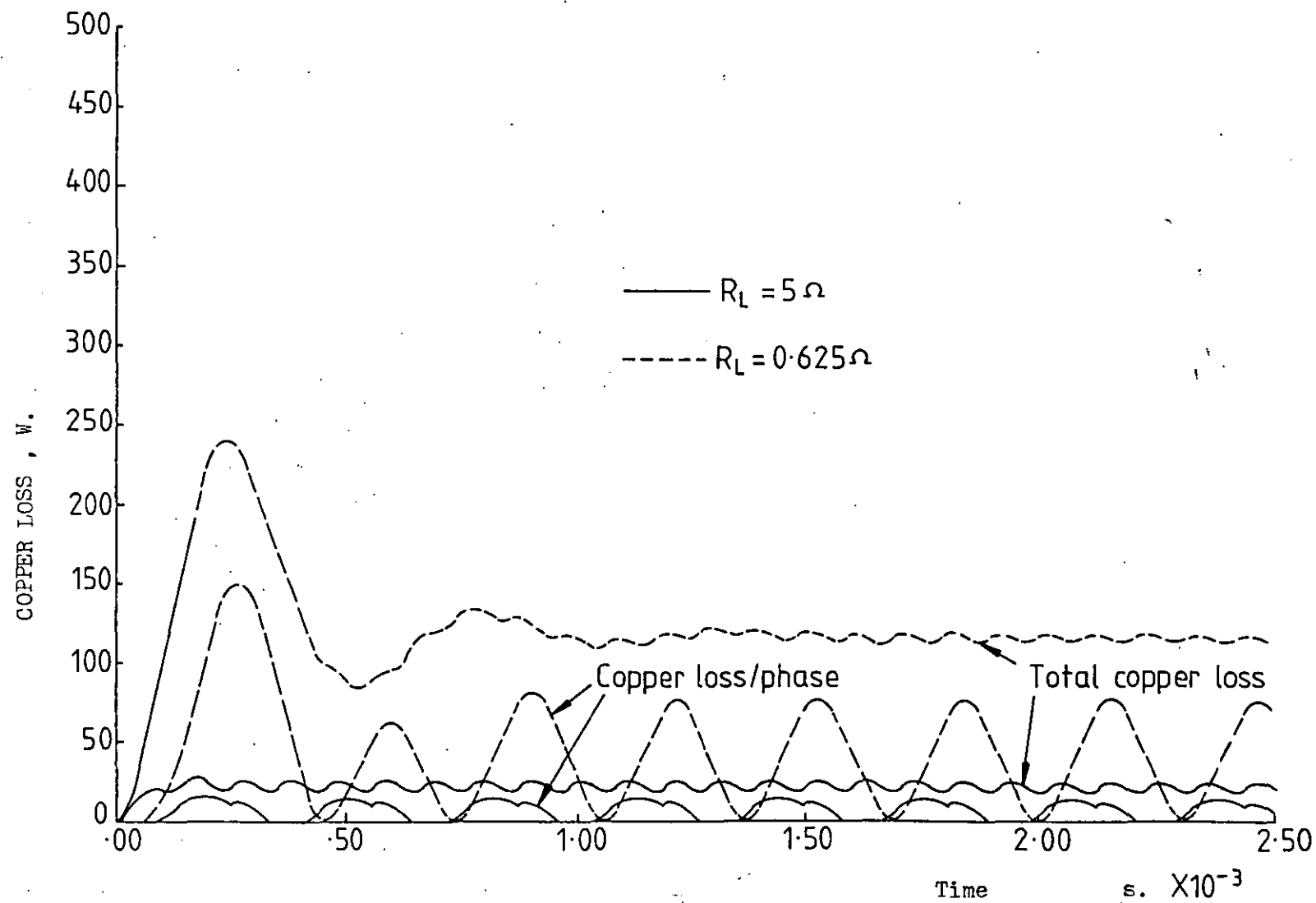


Figure 8.19

POWER DISSIPATION IN P.M.G. PHASE WINDINGS.

AIRGAP FLUX DENSITY/ON LOAD /AIRGAP FLUX DENSITY ON NO LOAD , B_g/B_{go}

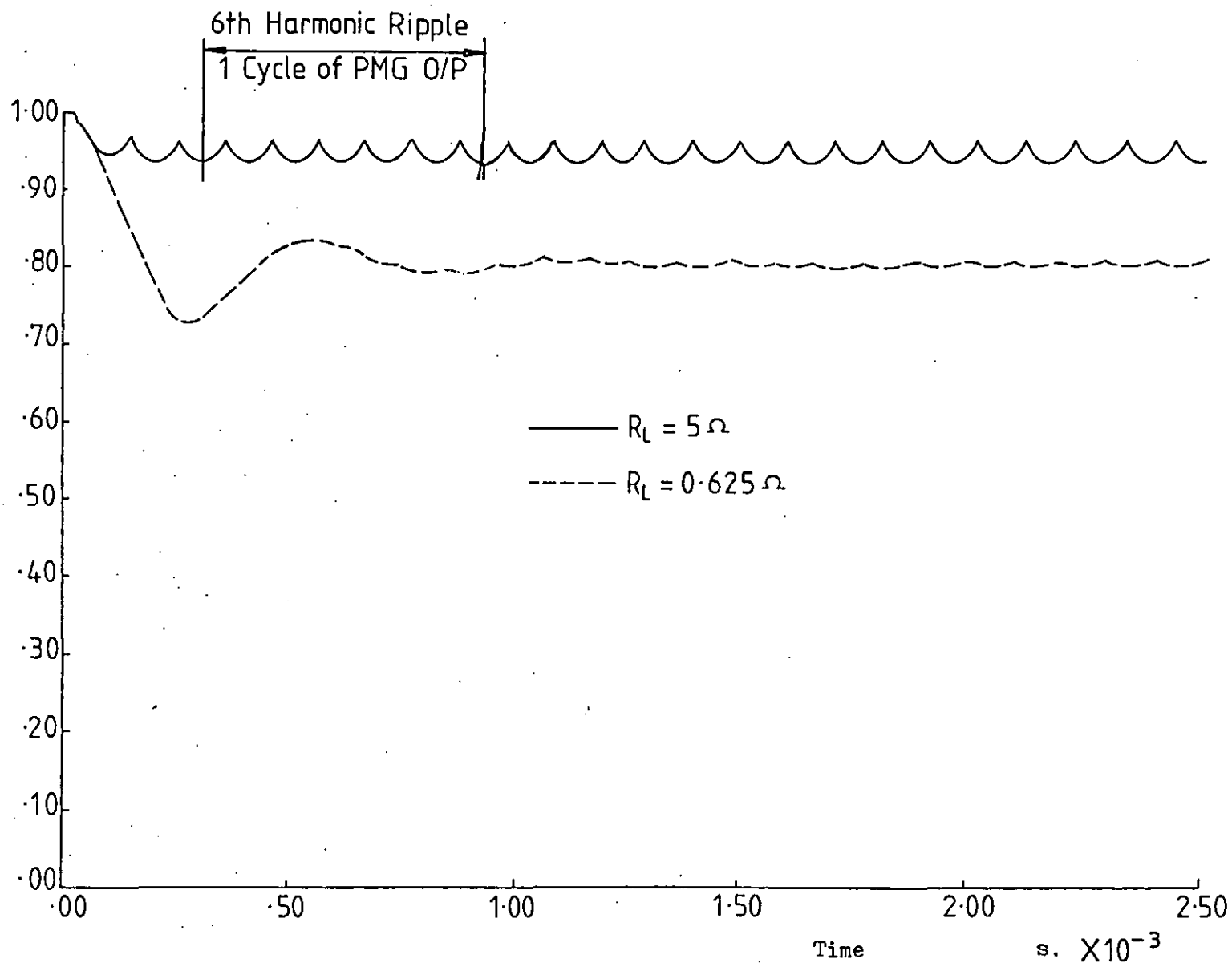


Figure 8.20

AIRGAP FLUX DENSITY (P.U.)

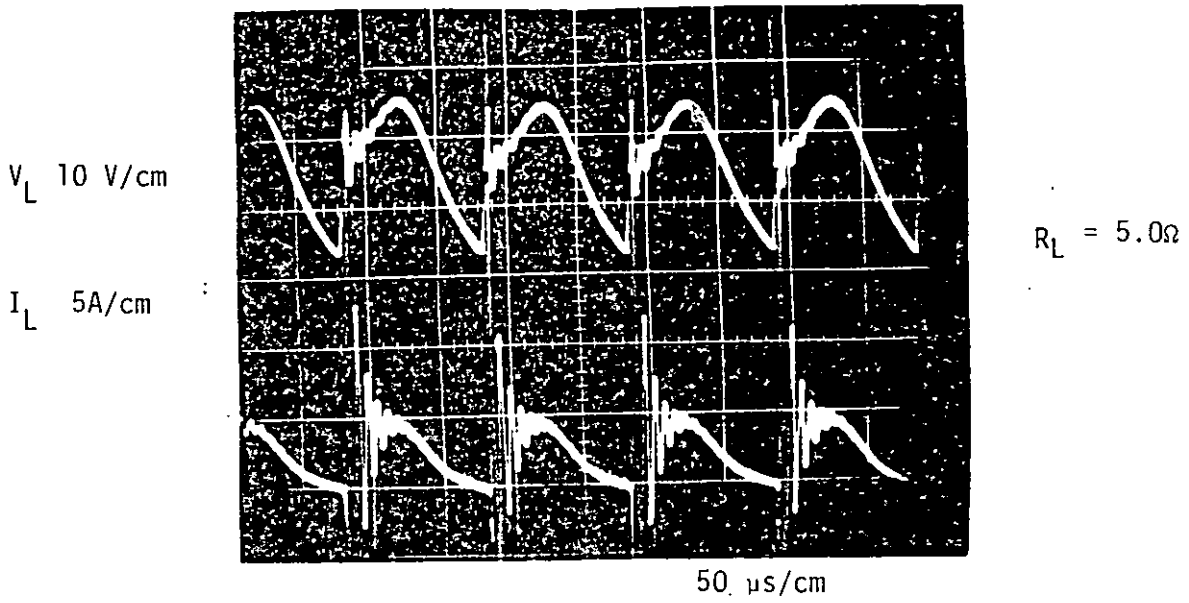


Figure 8.21(a)

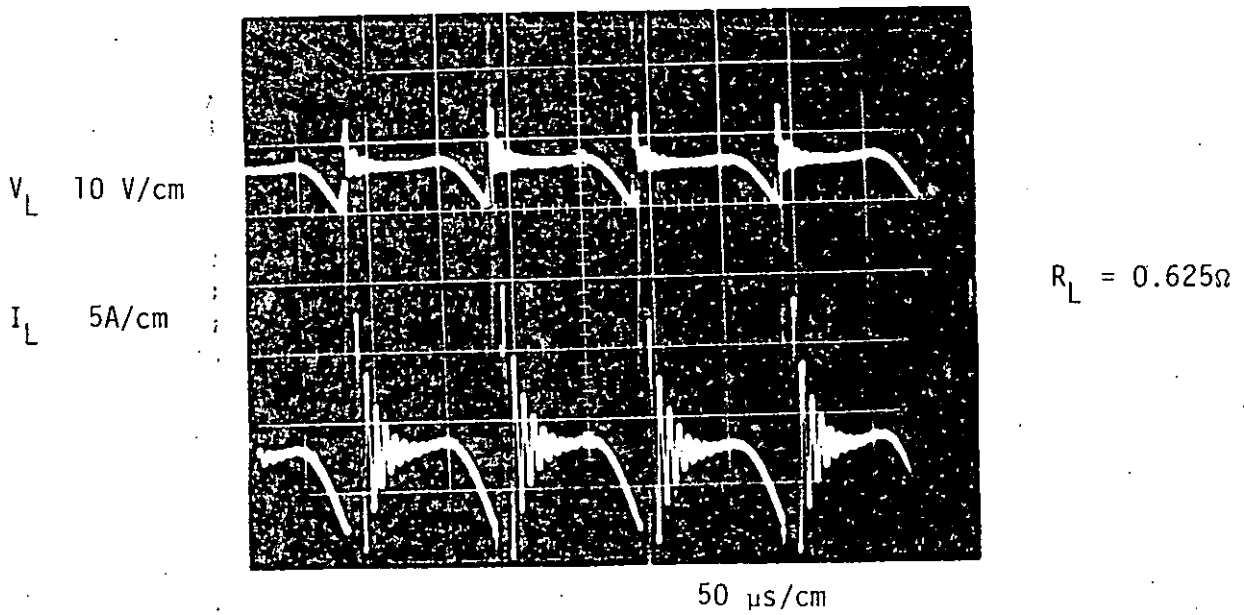


Figure 8.21(b)

D.C. OUTPUT HARMONICS, RECTIFIER LOAD RIPPLE VOLTAGES
AND CURRENTS

CHAPTER 9

CALCULATION OF PHASE MODEL PARAMETERS FROM dqo AND DESIGN PARAMETERS

It is generally found that the synchronous generator manufacturers are able to provide either the dqo parameters or the design parameters of the machines they supply, thus in advance of any facility for measuring phase model parameters, it is useful to be able to determine these parameters from the parameters provided by the manufacturers. If no such parameters are available from the manufacturers, the test procedures by which the dqo parameters of a synchronous generator may be determined are well known⁽⁶⁵⁾. In this chapter, formulae for calculating the inductance coefficients required for a phase model are derived in terms of (a) the dqo parameters and (b) the design parameters of the machine. The conditions under which the dqo to phase model transformation holds, as well as the assumptions inherent in a dqo model, are also discussed. The final part of this chapter shows how the normalised polynomials which account for the saturation in the d-axis (discussed in Chapter 2) are obtained from the open-circuit characteristic of the generator.

9.1 Relationship Between the dqo Model and the ryb -Phase Model Equations

The transformation of the 3-phase (r, y, b) windings into the two windings (d and q) along the direct and quadrature axes respectively is well known⁵⁷. It is arranged that the m.m.f. along the d-axis due to the currents in the r, y, b phases (with N turns per phase) is equal to the corresponding m.m.f. due to a current i_d flowing in the fictitious d-axis winding of N_d turns and the m.m.f. due to the 3-phase currents in the r, y, b phases in the q-axis is equal to the m.m.f. due to a current i_q in the fictitious q-axis winding of N_q turns. There is complete freedom of choice for the ratio of

N_d/N and N_q/N , since both N_d and N_q can assume any value provided appropriate adjustments are made to i_d and i_q respectively. It is assumed in the transformation equations presented here, as it simplifies subsequently derived transformations.⁵⁷

$$N_d = N_q = \sqrt{\frac{3}{2}} N \quad 9.1$$

With a 3-wire load connection, there are only two independent armature phase current variables, and in a dqo model i_d and i_q are sufficient to determine the three phase currents. With a 4-wire load connection there are three independent armature current variables and three variables in the dqo model are necessary for complete correspondence.

The third component involved is the zero-sequence, which produces no fundamental component in the spatial distribution of m.m.f. in the airgap. It can be shown⁵⁷ that the transformation tensor $[C]$ relating the dqo currents to the phase currents shown in Figure 9.1 is:

$$[i_d \ i_q \ i_o]_t = [C][i_r \ i_y \ i_b]_t \quad 9.2$$

where

$$[C] = \sqrt{\frac{2}{3}} \begin{bmatrix} \cos \theta_r & \cos (\theta_r - 120) & \cos (\theta_r + 120) \\ -\sin \theta_r & -\sin (\theta_r - 120) & -\sin (\theta_r + 120) \\ \frac{1}{\sqrt{2}} & \frac{1}{\sqrt{2}} & \frac{1}{\sqrt{2}} \end{bmatrix} \quad 9.3$$

also

$$[C]^{-1} = [C]_t = \sqrt{\frac{2}{3}}$$

$\cos \theta_r$	$-\sin \theta_r$	$\frac{1}{\sqrt{2}}$
$\cos (\theta_r - 120)$	$-\sin (\theta_r - 120)$	$\frac{1}{\sqrt{2}}$
$\cos (\theta_r + 120)$	$-\sin (\theta_r + 120)$	$\frac{1}{\sqrt{2}}$

9.4

$$[i_r \ i_y \ i_b]_t = [C]_t [i_d \ i_q \ i_o]_t$$

9.5

$$[v_d \ v_q \ v_o]_t = [C][v_r \ v_y \ v_b]_t$$

9.6

$$\text{and } [v_r \ v_y \ v_b]_t = [C]_t [v_d \ v_q \ v_o]_t$$

9.7

To obtain the ryb to *dqo* transformation of the impedance tensor, consider the following equation

$$[V_{rybFDQ}]_t = [Z_{rybFDQ}][I_{rybFDQ}]_t$$

9.8

If this equation is partitioned with ryb and FDQ components, it can be written as:

$$\begin{bmatrix} [V_{ryb}]_t \\ [V_{FDQ}]_t \end{bmatrix} = \begin{bmatrix} [Z_{ryb}] & [Z_X] \\ [Z_X]_t & [Z_{FDQ}] \end{bmatrix} \begin{bmatrix} [I_{ryb}]_t \\ [I_{FDQ}]_t \end{bmatrix}$$

9.9

Substituting equations 9.5 and 9.7 in 9.9 gives

$$\begin{bmatrix} [C]_t [V_{dqo}]_t \\ [V_{FDQ}]_t \end{bmatrix} = \begin{bmatrix} [Z_{ryb}] & [Z_X] \\ [Z_X]_t & [Z_{FDQ}] \end{bmatrix} \begin{bmatrix} [C]_t [I_{dqo}]_t \\ [I_{FDQ}] \end{bmatrix}$$

9.10

also

$$\begin{bmatrix} [V_{dQ}]_t \\ [V_{FQ}]_t \end{bmatrix} = \begin{bmatrix} [C] & [0] \\ [0] & [I] \end{bmatrix} \begin{bmatrix} [C]_t [V_{dQ}]_t \\ [V_{FQ}]_t \end{bmatrix} \quad 9.11$$

Substituting equation 9.10 into equation 9.11

$$\begin{bmatrix} [V_{dQ}]_t \\ [V_{FQ}]_t \end{bmatrix} = \begin{bmatrix} [C][Z_{ryb}][C]_t & [C][Z_X] \\ [Z_X]_t [C]_t & [Z_{FQ}] \end{bmatrix} \begin{bmatrix} [I_{dQ}]_t \\ [I_{FQ}]_t \end{bmatrix} \quad 9.12$$

The transformation equations for the impedance tensor $[Z_{ryb}]$ is

$$[Z]_{dQ} = [C][Z_{ryb}][C]_t \quad 9.13$$

It can also be proved that⁵⁷ :

$$[Z_{ryb}] = [C]_t [Z_{dQ}][C] \quad 9.14$$

9.2 Transformation of the Inductance Tensor $[L_{ryb}]$ to $[L_{dQ}]$

The inductance tensor $[L_{ryb}]$ can take a number of forms, with the most commonly used $[L_{ryb}]$ being given by equation 9.15. Snider and Smith²³ defined the inductances of the windings in terms of their d-axis and q-axis components as discussed in Chapter 2. If it is assumed* that the $\frac{K}{3}$ factor discussed in Chapter 2 is negligible, the $[L_{ryb}]$ tensor defined in terms of the d and q axis components is given by equation 9.16. Transformation of the inductance tensor $[L_{ryb}]$

* The dQ model assumes the third harmonic component in the space distribution of armature m.m.f. to be zero. Therefore it is necessary to assume $\frac{K}{3}$ is zero to be able to derive the ryb parameters from dQ parameters.

$$\begin{bmatrix} [L_{ryb}] & [L_x] \\ [L_x]_t & [L_{FDQ}] \end{bmatrix} =$$

$L_{a1} + L_{go}$ $+L_{g2}\cos 2\theta_r$	$-\frac{1}{2} L_{go}$ $+L_{g2}\cos 2(\theta_r-60^\circ)$	$-\frac{1}{2} L_{go}$ $+L_{g2}\cos 2(\theta_r+60^\circ)$	$M_F\cos\theta_r$	$M_{DD}\cos\theta_r$	$-M_{QQ}\sin\theta_r$
$-\frac{1}{2} L_{go}$ $+L_{g2}\cos 2(\theta_r-60^\circ)$	$L_{a1} + L_{go}$ $+L_{g2}\cos 2(\theta_r-60^\circ)$	$-\frac{1}{2} L_{go}$ $+L_{g2}\cos 2(\theta_r)$	$M_F\cos(\theta_r-120)$	$M_{DD}\cos(\theta_r-120)$	$-M_{QQ}\sin(\theta_r-120)$
$-\frac{1}{2} L_{go}$ $+L_{g2}\cos 2(\theta_r+60^\circ)$	$-\frac{1}{2} L_{go}$ $+L_{g2}\cos 2(\theta_r)$	$L_{a1} + L_{go}$ $+L_{g2}\cos 2(\theta_r+120^\circ)$	$M_F\cos(\theta_r+120)$	$M_{DD}\cos(\theta_r+120)$	$-M_{QQ}\sin(\theta_r+120)$
$M_F\cos\theta_r$	$M_F\cos(\theta_r-120)$	$M_F\cos(\theta_r+120)$	L_{FF}	L_{FD}	0
$M_{DD}\cos\theta_r$	$M_{DD}\cos(\theta_r-120)$	$M_{DD}\cos(\theta_r+120)$	L_{FD}	L_{DD}	0
$-M_{QQ}\sin\theta_r$	$-M_{QQ}\sin(\theta_r-120)$	$-M_{QQ}\sin(\theta_r+120)$	0	0	L_{QQ}

$[L_{ryb}] =$

$\frac{L_D+L_Q}{2} + \frac{L_D-L_Q}{2} \cos 2\theta_r$	$- \frac{1}{4} (M_D+M_Q)$ $+ \frac{1}{2} (M_D-M_Q) \cos 2(\theta_r-60^\circ)$	$- \frac{1}{4} (M_D+M_Q)$ $+ \frac{1}{2} (M_D-M_Q) \cos 2(\theta_r+60^\circ)$
$- \frac{1}{4} (M_D+M_Q)$ $+ \frac{1}{2} (M_D-M_Q) \cos 2(\theta_r-60^\circ)$	$\frac{L_D+L_Q}{2} + \frac{L_D-L_Q}{2} \cos 2(\theta_r-120^\circ)$	$- \frac{1}{4} (M_D+M_Q)$ $+ \frac{1}{2} (M_D-M_Q) \cos 2\theta_r$
$- \frac{1}{4} (M_D+M_Q)$ $+ \frac{1}{2} (M_D-M_Q) \cos 2(\theta_r+60^\circ)$	$- \frac{1}{4} (M_D+M_Q)$ $+ \frac{1}{2} (M_D-M_Q) \cos 2\theta_r$	$\frac{L_D+L_Q}{2} + \frac{L_D-L_Q}{2} \cos 2(\theta_r+120^\circ)$

to obtain $[L_{dqo}]$ as given by equation 9.17 is performed as in Appendix A13

$$[L_{dqo}] = [C][L_{ryb}][C]_t \quad 9.17$$

gives

$$[L_{dqo}] = \begin{bmatrix} L_d & 0 & 0 \\ 0 & L_q & 0 \\ 0 & 0 & L_o \end{bmatrix}$$

$$= \begin{bmatrix} L_{a1} & 0 & 0 \\ + \frac{3}{2} (L_{go} + L_{g2}) & & \\ 0 & L_{a1} & 0 \\ & + \frac{3}{2} (L_{go} - L_{g2}) & \\ 0 & 0 & L_{a1} \end{bmatrix} \quad 9.18$$

Therefore from equation (9.18)

$$L_d = L_{a1} + \frac{3}{2} (L_{go} + L_{g2}) \quad 9.19(a)$$

$$L_q = L_{a1} + \frac{3}{2} (L_{go} - L_{g2}) \quad 9.19(b)$$

$$L_o = L_{a1} \quad 9.19(c)$$

Manipulation of equations 9.19(a), (b) and (c) gives:

$$L_{go} = \frac{x_d + x_q - 2x_\ell}{3\omega} = \frac{x_{ad} + x_{aq}}{3\omega} \quad 9.20(a)$$

$$L_{g2} = \frac{x_d - x_q}{3\omega} = \frac{x_{ad} - x_{aq}}{3\omega} \quad 9.20(b)$$

where:

$$x_d = x_{ad} + x_\ell, \quad x_q = x_{aq} + x_\ell$$

$$x_d = \omega L_d, \quad x_q = \omega L_q, \quad x_\ell = \omega L_{a1}$$

Comparison of equations 9.15 and 9.16 gives:

$$L_{a1} + L_{go} + L_{g2} \cos 2\theta_r = \frac{L_D + L_Q}{2} + \frac{L_D - L_Q}{2} \cos 2\theta_r \quad 9.21(a)$$

$$-\frac{1}{2} L_{go} + L_{g2} \cos 2(\theta_r - 60^\circ) = -\frac{1}{4}(M_D + M_Q) + \frac{1}{2}(M_D - M_Q) \cos 2(\theta_r - 60^\circ)$$

Therefore

9.21(b)

$$L_{g2} = \frac{L_D - L_Q}{2} \quad 9.22(a)$$

$$L_{a1} + L_{go} = \frac{L_D + L_Q}{2} \quad 9.22(b)$$

$$-\frac{1}{2} L_{go} = -\frac{1}{4} (M_D + M_Q) \quad 9.22(c)$$

$$L_{g2} = \frac{1}{2} (M_D - M_Q) \quad 9.22(d)$$

Manipulation of equations 9.22(a) to 9.22(d) gives

$$L_D = L_{a1} + L_{go} + L_{g2} = \frac{2 x_d + x_\ell}{3\omega} \quad 9.22(e)$$

$$L_Q = L_{a1} + L_{go} - L_{g2} = \frac{2 x_q + x_\ell}{3\omega} \quad 9.22(f)$$

$$M_D = L_{go} + L_{g2} = \frac{2 (x_d - x_\ell)}{3\omega} \quad 9.22(g)$$

$$M_Q = L_{go} - L_{g2} = \frac{2 (x_q - x_\ell)}{3\omega} \quad 9.22(h)$$

If X_{ad} and X_{aq} are respectively the d-axis and q-axis reactances of the armature phase winding due to flux in the airgap

$$x_d = \frac{m}{2} X_{ad} + x_\ell \quad 9.23$$

$$x_q = \frac{m}{2} X_{aq} + x_\ell$$

where m is the number of phases. For a 3-phase machine therefore

$$L_D = \frac{X_{ad} + x_\ell}{\omega} \quad 9.24(a)$$

$$L_Q = \frac{X_{aq} + x_\ell}{\omega} \quad 9.24(b)$$

$$M_D = \frac{X_{ad}}{\omega} \quad 9.24(c)$$

$$M_Q = \frac{X_{aq}}{\omega} \quad 9.24(d)$$

Therefore all the inductance coefficients for tensor $[L_{ryb}]$ can be calculated using dqo parameters and equations 9.20, 9.22 and 9.24.

9.3 Calculation of the Inductance Coefficients of L_{ryb} from Design Parameters

Talaat⁵⁸ has shown that the dqo parameters of a synchronous machine can be calculated from

$$x_{ad} = X \lambda_a C_{dl} \quad 9.25(a)$$

$$x_{aq} = X \lambda_a C_{ql} \quad 9.25(b)$$

$$\text{where: } X = \frac{4 \text{ mFL } (N K_w)^2}{10^8 P} \quad 9.25(c)$$

Substitution of equations 9.25 into equation 9.20 gives:

$$L_{go} = \frac{2 \text{ mL } (N K_w)^2}{3\pi 10^8 P} \lambda_a (C_{dl} - C_{ql}) \quad 9.26$$

Substitution of equations 9.25 into equation 9.24 gives:

$$L_D = \frac{4 L (N K_w)^2}{\pi 10^8 P} \lambda_a C_{dl} + L_{al} \quad 9.27(a)$$

$$L_Q = \frac{4L (N K_w)^2}{\pi 10^8 P} \lambda_a C_{ql} + L_{al} \quad 9.27(b)$$

$$M_D = \frac{4 L (N K_W)^2}{\pi 10^8 P} \lambda_a C_{d1} \quad 9.27(c)$$

$$M_Q = \frac{4 L (N K_W)^2}{\pi 10^8 P} \lambda_a C_{q1} \quad 9.27(d)$$

A number of authors ⁶⁶⁻⁶⁸ have derived formulae for calculating the leakage inductance L_{a1} , which can be used to obtain the value of L_{a1} required in the calculation of L_D and L_Q .

9.4 Calculation of Armature Phase to Field Mutual Inductance (M_F) and Self Inductance (L_{FF}) of the Field Winding

9.4.1 Calculation of M_F and L_{FF} using dqo parameters

If the resistances of the winding of the generator are neglected, the transient d-axis reactance is given by

$$x_d' = x_d \left(1 - \frac{M_{dF}^2}{L_d L_{FF}} \right) \quad 9.28$$

where M_{dF} is the mutual inductance between the d-axis winding and the field winding.

Since $\frac{N_d}{N} = \sqrt{\frac{3}{2}}$ as given by equation 9.1

$$M_{dF} = \sqrt{\frac{3}{2}} M_F \quad 9.29$$

The d-axis open circuit transient time constant T_{do}' is given by

$$T_{do}' = \frac{L_{FF}}{R_{FF}} \quad 9.30$$

Substituting equations 9.29 and 9.30 into equation 9.28 give:

$$M_F^2 = \frac{2}{3} \left(\frac{x_d - x'_d}{\omega} \right) T'_{do} R_{FF} \quad 9.31$$

Therefore M_F and L_{FF} can be calculated using equations 9.31 and 9.30 respectively.

9.4.2 Calculation of M_F and L_{FF} using design parameters

The self inductance of the field winding is given by⁶⁸

$$L_{FF} = \frac{N_f^2 p L}{10^8} \left[\left(\frac{\pi C_p \lambda_a}{2} \right) + \lambda_F \right] \quad 9.32$$

The phase to field winding mutual inductance M_F is calculated using equation 9.31

$$x'_d = x_\ell + x_{ad} \left(1 - \frac{\lambda_a C_1^2}{C_{d1} \left(2 C_p \lambda_a + \frac{4}{\pi} \lambda_F \right)} \right) \quad 9.33$$

$$x_d = x_\ell + x_{ad} \quad 9.34$$

Therefore from equations 9.33 and 9.34

$$x_d - x'_d = x_{ad} \frac{\lambda_a C_1^2}{C_{d1} \left(2 C_p \lambda_a + \frac{4}{\pi} \lambda_F \right)} \quad 9.35$$

Substituting equation 9.35 and 9.32 into equation 9.31 gives:

$$M_F = \frac{N_f L (N K_w) \lambda_a C_1}{10^8} \quad 9.36$$

9.5 The Effective Constants of the Damper Windings

An a.c. method for measuring the effective d- and q-axis damper windings for use in the phase-model analysis of synchronous generators was discussed in Chapter 2. From the analysis of the measurement technique, it is apparent that the damper winding parameters are not uniquely defined in value, i.e. the parameters that are measured at the terminals of the phase winding (or field winding) reflect the effect of the damper winding on the armature (or field) winding. It is shown here that it is not necessary to know the actual values of the damper winding inductances and resistances (L_{DD} , R_{DD} , M_{DD} , L_{QQ} , M_{QQ} etc) for its representation in the phase model, provided the values chosen to represent the damper windings give the same effect on the generator performance as the actual damper windings in the machine. The coefficients of coupling between the damper windings and the other windings of the machine and the time constants of the damper windings completely account for the effect of the damper windings on the machine performance. Considering the two magnetically coupled windings (1) and (2) shown in Figure 9.2 it follows that:

$$V_1 = R_1 I_1 + j\omega L_{11} I_1 + j\omega M_{12} I_2 \quad 9.37$$

$$0 = j\omega M_{12} I_1 + R_2 I_2 + j\omega L_{22} I_2 \quad 9.38$$

It can be shown by manipulation of equations 9.37 and 9.38 that

$$I_2^2 R_2 = \frac{A V_1^2}{(B \omega^4 + C \omega^2 + D)} \quad 9.38(a)$$

$$\text{where: } A = \omega^2 \left(\frac{M_{12}^2}{R_2} \right) \quad 9.38(b)$$

$$B = \left(\frac{M_{12}^2}{R_2} \right)^2 \quad 9.38(c)$$

$$C = L_{11}^2 + \left(\frac{L_{22}}{R_2} \right)^2 (R_1^2 + \omega^2 L_{11}^2) + 2 \left(\frac{M_{12}^2}{R_2} \right) (R_1 - \omega^2 L_{11}) \left(\frac{L_{22}}{R_2} \right) \quad 9.38(d)$$

$$D = R_1^2 \quad 9.38(e)$$

$$\text{Let } T_2 = \frac{L_{22}}{R_2}, \text{ the time constant of the second winding} \quad 9.39(a)$$

$$\text{and } K = \frac{M_{12}}{\sqrt{L_{11} L_{22}}} \text{ the coupling coefficient between the two windings} \quad 9.39(b)$$

Then if

$$X_{11} = \omega L_{11} \quad 9.39(c)$$

$$\text{and } X_{22} = \omega L_{22} \quad 9.39(d)$$

Substituting equations 9.39 into equations 9.38 and simplifying gives

$$I_2^2 R_2 = \frac{V_1^2 X_{11} K^2 (\omega T_2)}{[R_1^2 + X_{11}^2 + 2R_1 X_{11} (\omega T_2) + (\omega T_2)^2 (R_1^2 + X_{11}^2 (1-K^2)^2)]} \quad 9.40$$

Similarly $I_2^2 X_{22}$ is given by

$$I_2^2 X_{22} = \frac{V_1^2 X_{11} K^2 (\omega T_2)^2}{[R_1^2 + X_{11}^2 + 2R_1 X_{11} (\omega T_2) + (\omega T_2)^2 (R_1^2 + X_{11}^2 (1-K^2)^2)]}$$

It can be seen from equations 9.40 and 9.41 that the power dissipated and the reactance vars in winding (2) are dependent on K and T_2 and independent of the absolute values of L_{22} , M_{12} and R_2 .

If winding (1) is considered to be the armature phase winding and winding (2) as the short circuited damper winding, the effect of the damping winding on the armature phase winding is dependent on K and T_2 .

Once the coefficient of coupling K_{aD} between the armature phase winding (with its axis along the d-axis) and the d-axis damper winding, and the d-axis damper winding time constant T_{DD} are obtained, the mutual inductance coefficient M_{DD} , together with L_{DD} and R_{DD} can be calculated from equations 9.39(a) and 9.39(b) by choosing a value for any one of the three unknowns. Similarly if the coefficient of coupling K_{aQ} between the armature phase winding (with its axis along the q-axis) and the q-axis damper winding, and the q-axis damper winding time constant T_{QQ} are obtained, the mutual inductance coefficient M_{QQ} , together with L_{QQ} and R_{QQ} can be calculated from equations 9.39(a) and 9.39(b) by choosing a value for any one of the three unknowns.

Formulae for calculating K_{aD} , T_{DD} , K_{aQ} and T_{QQ} from the d-q parameters are derived in Section 9.6 which can be used to obtain the damper winding parameters for the phase model. Alternatively, if the design parameters of the generator are known, the formulae given in Section 9.7 can be used to calculate K_{aD} , T_{DD} , K_{aQ} and T_{QQ} .

9.6 Calculation of the Constants of the Damper Windings from d- and q-Axis Reactances and Time Constants

9.6.1 The coefficients of couplings in the d-axis

The d-axis equivalent circuit developed from the d-q model⁶⁹ is shown in Figure 9.3. The corresponding equivalent circuit for the phase winding with its axis lined in the d-axis is shown in Figure 9.4.

It can be shown that

$$x_{ad} = \left(\frac{2}{m}\right) x_{ad} = \left(\frac{2}{m}\right) (x_d - x_\ell) \quad 9.42(a)$$

$$x_{F\ell} = \left(\frac{2}{m}\right) x_{F\ell} = \left(\frac{2}{m}\right) \frac{(x_d - x_\ell)(x'_d - x_\ell)}{(x_d - x'_d)} \quad 9.42(b)$$

$$X_{D\ell} = \left(\frac{2}{m}\right) X_{D\ell} = \left(\frac{2}{m}\right) \frac{(x_d' - x_\ell)(x_d'' - x_\ell)}{(x_d' - x_d'')} \quad 9.42(c)$$

The coefficient of coupling K_{aD} between the phase and the d-axis damper winding with the phase axis lined with the d-axis is

$$K_{aD} = \frac{X_{ad}}{\sqrt{(X_{ad} + X_{D\ell})(X_{ad} + X_\ell)}} \quad 9.43$$

Substituting for X_{AD} and $X_{D\ell}$ from equations 9.42 into equation 9.43 gives:

$$K_{aD} = \frac{1}{\sqrt{\left(1 + \frac{(x_d' - x_\ell)(x_d'' - x_\ell)}{(x_d' - x_\ell)(x_d' - x_d'')}\right)\left(1 + \left(\frac{m}{2}\right)\left(\frac{x_\ell}{x_d' - x_\ell}\right)\right)}} \quad 9.44$$

Similarly, the coefficient of coupling K_{FD} between the field and the d-axis damper winding is

$$K_{FD} = \frac{X_{ad}}{\sqrt{(X_{ad} + X_{D\ell})(X_{ad} + X_{F\ell})}} \quad 9.45$$

hence

$$K_{FD} = \frac{1}{\sqrt{\left(1 + \frac{(x_d' - x_\ell)(x_d'' - x_\ell)}{(x_d' - x_\ell)(x_d' - x_d'')}\right)\left(1 + \frac{(x_d' - x_\ell)}{(x_d' - x_d'')}\right)}} \quad 9.46$$

The coefficient of coupling between the phase and the field winding with the phase axis lined along the d-axis is:

$$K_{aF} = \frac{X_{ad}}{\sqrt{(X_{ad} + X_{F\ell})(X_{ad} + x_\ell)}} \quad 9.47$$

giving

$$K_{aF} = \frac{1}{\sqrt{\left(1 + \frac{(x_d' - x_\ell)}{(x_d - x_d')}\right) \left(1 + \left(\frac{m}{2}\right) \frac{x_\ell}{(x_d - x_\ell)}\right)}} \quad 9.48$$

9.6.2 The Coefficient of Coupling in the q-axis

The q-axis equivalent circuit for the d-q model⁶⁹ is shown in Figure 9.5. The corresponding equivalent circuit for the phase winding with its axis lined along the q-axis is shown in Figure 9.6. It can be shown that

$$X_{aq} = \left(\frac{2}{m}\right) x_{aq} = \left(\frac{2}{m}\right) (x_q - x_\ell) \quad 9.49(a)$$

$$X_{Q\ell} = \left(\frac{2}{m}\right) x_{Q\ell} = \left(\frac{2}{m}\right) \frac{(x_q - x_\ell)(x_q'' - x_\ell)}{(x_q - x_q'')} \quad 9.49(b)$$

The coefficient of coupling K_{aQ} between the phase and the q-axis damper winding with the phase axis lined along the q-axis is

$$K_{aQ} = \frac{X_{aq}}{\sqrt{(X_{aq} + X_{Q\ell})(X_{aq} + x_\ell)}} \quad 9.50$$

Substituting for X_{aq} and $X_{Q\ell}$ from equations 9.49(a), (b) into equation 9.50 gives

$$K_{aQ} = \frac{1}{\sqrt{\left(1 + \frac{(x_q'' - x_\ell)}{(x_q - x_q'')}\right) \left(1 + \left(\frac{m}{2}\right) \left(\frac{x_\ell}{x_q - x_\ell}\right)\right)}} \quad 9.51$$

9.6.3 The d-axis Damper Winding Time Constant

The d-axis damper winding time constant is determined using the d-axis subtransient short-circuit time constant (T_d'') which is given⁷⁰ by

$$T_d'' = \frac{1}{\omega R_{Dd}} \left(x_{Dd} + \frac{x_{ad} x_\ell x_{F\ell}}{x_{ad} x_\ell + x_{ad} x_{F\ell} + x_\ell x_{F\ell}} \right) \quad 9.52$$

By substituting for x_ℓ and x_{ad} , $x_{F\ell}$, x_{Dd} from equations 9.42, R_{Dd} may be calculated from equation 9.52, once the value of T_d'' has been obtained from a short-circuit test on the generator⁷¹.

The d-axis damper winding time constant is then

$$T_{DD} = \frac{x_{ad} + x_{Dd}}{\omega R_{Dd}} \quad 9.53$$

9.6.4 The q-axis Damper Winding Time Constant

The quadrature axis subtransient short circuit time constant⁷⁰ is

$$T_q'' = \frac{1}{\omega R_{Qq}} \left(x_{Qq} + \frac{x_{aq} x_\ell}{x_q} \right) \quad 9.54$$

By substituting for x_ℓ , x_q and x_{aq} , x_{Qq} from equations 9.49, R_{Qq} is calculated from equation 9.54, once the value of T_q'' has been obtained by test on the generator⁶⁵.

The q-axis damper winding time constant is then

$$T_{QQ} = \frac{x_{aq} + x_{Qq}}{\omega R_{Qq}} \quad 9.55$$

9.7 Calculation of the Constants of the Damper Windings from Design Parameters

Talaat ⁵⁸ has derived formulae for calculating the effective damper winding reactances and resistances for distributed damper bars in the poles of a rotor. This is the most widely used form of construction of rotor for synchronous generators and was in fact adopted on the experimental generator 2130. The design formulae derived are for this type of damper windings, with the symbols and units being the same as those used by Talaat.

9.7.1 The Coefficient of Coupling in the d-axis

The reactance of the d-axis damper windings referred to the armature phase winding is

$$X_{DD} = \left(\frac{2}{m}\right) x_{DD} = \left(\frac{2}{m}\right) \cdot X (\lambda_a C_{dl} + \lambda_{LDd}) \quad 9.56$$

where X is given by equation 9.25(c).

If X_{DD} is written as sum of the magnetising reactance (X_{ad}) and the leakage reactance $X_{D\ell}$, then

$$X_{DD} = X_{ad} + X_{D\ell} \quad 9.57(a)$$

$$\text{where } X_{ad} = \left(\frac{2}{m}\right) X \lambda_a C_{dl} \quad 9.57(b)$$

$$X_{D\ell} = \left(\frac{2}{m}\right) X \lambda_{LDd} \quad 9.57(c)$$

The leakage permeance λ_{LDd} of the d-axis damper windings is ⁵⁸

$$\lambda_{LDd} = \frac{2\pi \lambda_{bed}}{n_b (1 - k_b)} \quad 9.58$$

The coefficient of coupling between the d-axis damper winding and the phase winding with the phase winding axis lined in the d-axis is

$$K_{aD} = \frac{X_{ad}}{\sqrt{(X_{ad} + X_{D\ell})(X_{ad} + x_\ell)}} \quad 9.59$$

The leakage reactance of the phase winding is given by

$$x_\ell = X \lambda_{a\ell} \quad 9.60$$

Substituting for λ_{LDd} from equation 9.58 into equation 9.57(c), and for X_{ad} , $X_{D\ell}$ and x_ℓ from equations 9.57(b), 9.57(c) and 9.60 respectively, into equation 9.59 give

$$K_{aD} = \frac{1}{\sqrt{\left(1 + \frac{2\pi \lambda_{bed}}{\lambda_a C_{dl} n_b (1 - k_b)}\right) \left(1 + \frac{m \lambda_{a\ell}}{2 C_{dl} \lambda_a}\right)}} \quad 9.61$$

This formula is very useful as it gives the relationship between the distribution of the damper bars and its effect on the coupling coefficient, which is a measure of the effectiveness of the damper windings.

9.7.2 The Coefficient of Coupling in the q-axis

The reactance of the q-axis damper winding referred to the armature phase winding is

$$X_{QQ} = \left(\frac{2}{m}\right) x_{QQ} = \left(\frac{2}{m}\right) \times (\lambda_a C_{q1} + \lambda_{LQq}) \quad 9.62$$

writing X_{QQ} as the sum of magnetising reactance X_{aq} and the leakage reactance $X_{Q\ell}$

$$X_{QQ} = X_{aq} + X_{Q\ell} \quad 9.63(a)$$

where

$$X_{aq} = \left(\frac{2}{m}\right) \times \lambda_a C_{q1} \quad 9.63(b)$$

and

$$X_{Q\ell} = \left(\frac{2}{m}\right) \times \lambda_{LQq} \quad 9.63(c)$$

The leakage permeance λ_{LQq} of the q-damper windings is ⁵⁸

$$\lambda_{LQq} = \frac{2 \pi \lambda_{beq}}{n_b (1+k_b)} \quad 9.64$$

The coefficient of coupling between the q-axis damper winding and the armature phase winding lined in the q-axis is

$$K_{aQ} = \frac{X_{aq}}{\sqrt{(X_{aq} + X_{Q\ell})(X_{aq} + x_\ell)}} \quad 9.65$$

Substituting for λ_{LQq} from equation 9.64 into equation 9.63(c) and for X_{aq} , X_{Ql} and x_l from equations 9.63(b), 9.63(c) and 9.60 respectively into equation 9.65 give

$$K_{aQ} = \frac{1}{\sqrt{\left(1 + \frac{2\pi\lambda_{beq}}{\lambda_a C_{ql} n_b (1+k_b)}\right) \left(1 + \frac{m}{2} \frac{\lambda_{al}}{C_{ql} \lambda_a}\right)}} \quad 9.66$$

9.7.3 The d-axis Damper Winding Time Constant

The referred value of the d-axis damper winding resistance to the armature phase winding is ⁵⁸

$$R_{DD} = \frac{8 (N k_w)^2}{P n_b (1-k_b)} r_{bed} \quad 9.67$$

The d-axis damper winding time constant T_{DD} is

$$T_{DD} = \frac{X_{DD}}{\omega R_{DD}} \quad 9.68$$

Substituting values of X_{DD} and R_{DD} from equations 9.56 and 9.67 into equation 9.68 gives

$$T_{DD} = \frac{L \cdot h_b (1-k_b)}{2\pi r_{bed} 10^8} \left(\lambda_a C_{dl} + \frac{2\pi \lambda_{bed}}{h_b (1-k_b)} \right) \quad 9.69$$

9.7.4 The q-axis Damper Winding Time Constant

The value of the q-axis damper winding resistance referred to the armature phase winding is ⁵⁸

$$R_{QQ} = \frac{8 (N k_w)^2}{P h_b (1+k_b)} \cdot r_{beq} \quad 9.70$$

The q-axis damper winding time constant T_{QQ} is

$$T_{QQ} = \frac{X_{QQ}}{\omega R_{QQ}} \quad 9.71$$

Substituting values of X_{QQ} and R_{QQ} from equations 9.62 and 9.70 into equation 9.71 gives

$$T_{QQ} = \frac{L h_b (1+k_b)}{2 \pi r_{beq} 10^8} \left(\lambda_a C_{q1} + \frac{2 \pi \lambda_{beq}}{n_b (1+k_b)} \right) \quad 9.72$$

9.8 Determination of Saturation Characteristics for Use in Phase Model Analysis from the Open Circuit Characteristic

It is very important to be able to determine the normalised polynomials C_{rr} , C_{ry} , C_{FF} , C_{DD} , C_{rD} , C_{FD} , C_{rF} which take into account the effect of saturation in the d-axis (as discussed in Chapter 2), if the saturation is to be included in the phase model. The open-circuit characteristics of the generator (open-circuit voltage/field-current) is generally available from the manufacturers. A typical open-circuit characteristic is given in Figure 9.7. It was shown in Chapter 6, that the open-circuit phase voltage $E_{a(r.m.s)}$ in terms of the field excitation voltage E_f is

$$\frac{E_a}{E_f} = K_{go} \quad 9.73(a)$$

$$\text{where } K_{go} = \frac{\sqrt{2}}{3} x_{ad} \left(\frac{P N_f k_f}{N K_w} \right) \cdot \frac{1}{R_f} \quad 9.73(b)$$

Expressing E_a in terms of the generator field current I_f ,

$$E_a = \frac{\sqrt{2}}{3} x_{ad} \left(\frac{P N_f k_f}{N K_w} \right) I_f \quad 9.74$$

To take the effect of saturation into account, x_{ad} is written as

$$x_{ad} = x_{ado} \cdot C_{ad} \quad 9.75$$

where x_{ado} is the unsaturated value of x_{ad} and C_{ad} is a normalised polynomial of the form

$$C_{ad} = 1 + C_1 I_f + C_2 I_f^2 + C_3 I_f^3 + \dots \quad 9.76$$

Since $\frac{\sqrt{2}}{3} \left(\frac{P N_f k_f}{N K_w} \right)$ is constant, equation 9.74 can be written as

$$\frac{E_a}{I_f} = A \cdot x_{ad} \quad 9.78$$

where A is a constant. The values of $A x_{ad}$ can be obtained from the open circuit characteristic for different values of I_f . The normalised saturation function is obtained by dividing $A x_{ad}$ by $A x_{ado}$

the unsaturated value of $A x_{ad}$. The resultant normalised saturation function when plotted as a function of I_f is as in Figure 9.8, which can be represented as a polynomial of the form given by equation 9.76. Once the normalised polynomial C_{ad} is obtained, the normalised polynomials for use in the phase model analysis can be obtained as follows. It was shown in Section (9.6.1), that the d-axis magnetising reactance X_{ad} equals $(2/3) x_{ad}$ for a 3-phase machine, whence multiplying both sides of equation 9.75 by $2/3$ gives:

$$X_{ad} = X_{ado} C_{ad} \quad 9.79$$

L_{Do} , the unsaturated value of L_D , is, from equation 9.24(a),

$$L_{Do} = \frac{X_{ado} + x_\ell}{\omega} \quad 9.80$$

Hence

$$\begin{aligned} C_{rr} &= \frac{L_D}{L_{Do}} = \frac{X_{ad} + x_\ell}{X_{ado} + x_\ell} \\ &= \frac{\left(\frac{x_\ell}{X_{ado}} + C_{ad}\right)}{\left(\frac{x_\ell}{X_{ado}} + 1\right)} \end{aligned} \quad 9.81$$

M_{Do} , the unsaturated value of M_D , is, from equation 9.24(c),

$$M_{Do} = \frac{X_{ado}}{\omega} \quad 9.82$$

Hence

$$C_{ry} = \frac{M_D}{M_{Do}} = \frac{x_{ad}}{x_{ado}} = C_{ad} \quad 9.83$$

The reactance of the field winding, x_{FF} is

$$x_{FF} = x_{ad} + x_{F\ell} \quad 9.84$$

Therefore x_{FF0} , the unsaturated value of x_{FF} is

$$x_{FF0} = x_{ado} + x_{F\ell} \quad 9.85$$

Hence

$$\begin{aligned} C_{FF} &= \frac{x_{FF}}{x_{FF0}} = \frac{x_{ado} C_{ad} + x_{F\ell}}{x_{ado} + x_{F\ell}} \\ &= \frac{\left(\frac{x_{F\ell}}{x_{ado}} + C_{ad} \right)}{\left(\frac{x_{F\ell}}{x_{ado}} + 1 \right)} \quad 9.86 \end{aligned}$$

The reactance of the d-axis damper winding x_{DD} is

$$x_{DD} = x_{ad} + x_{D\ell} \quad 9.87$$

Therefore x_{DD0} , the unsaturated value of x_{DD} is

$$x_{DD0} = x_{ado} + x_{D\ell} \quad 9.88$$

Hence

$$\begin{aligned} C_{DD} &= \frac{x_{ado} C_{ad} + x_{D\ell}}{x_{ado} + x_{D\ell}} \\ &= \frac{\left(\frac{x_{D\ell}}{x_{ado}} + C_{ad} \right)}{\left(\frac{x_{D\ell}}{x_{ado}} + 1 \right)} \quad 9.89 \end{aligned}$$

Since the magnetising reactances of the armature phase in the d-axis, the field winding and the d-damper windings are equal (basic d-q model assumption),

$$C_{rD} = C_{FD} = C_{rF} = C_{ad} \quad 9.90$$

$$\text{i.e. } M_{DD} = M_{DD0} \cdot C_{rD} = M_{DD0} \cdot C_{ad} \quad 9.91(a)$$

$$L_{FD} = L_{FDo} \cdot C_{FD} = L_{FDo} \cdot C_{ad} \quad 9.91(b)$$

$$M_F = M_{Fo} \cdot C_{rF} = M_{Fo} \cdot C_{ad} \quad 9.91(c)$$

where M_{DD0} , L_{FDo} and M_{Fo} are the unsaturated values of M_{DD} , L_{FD} and M_F .

x_{ad} , $x_{F\ell}$, $x_{D\ell}$ are obtained from the dqo parameters from equations 9.42(a), (b), (c), hence all the normalised saturation polynomials

for use in the phase model analysis can be calculated from the open-circuit characteristics presented here.

9.9 Conclusion

Formulae are derived in this chapter which enable all the parameters required for the phase model analysis to be derived from the dqo and design parameters. It is shown that normalised polynomials to include saturation in the phase model can also be derived from the open-circuit characteristic of the generator.

The phase model parameters and the normalised polynomials were calculated from the dqo parameters using the formulae developed in this chapter for a 100 kW 0.8 p.f. 480V, 60 Hz synchronous generator. It was found that realistic short circuit current transients were predicted using the derived phase model parameters. Since the generator was in the U.S.A., it would have required considerable effort to obtain the phase model parameters by measurements using the flux meter method as used for 2130 generators, while the dqo parameters and the open-circuit characteristic were readily available from the manufacturer.

The generator parameters supplied by the manufacturer for the 100 kW generator are given in Table 9.1 and the corresponding calculated phase model parameters are given in Table 9.2. Figures 9.9 and 9.10 show the predicted field current and r-phase current transients respectively when a 3-phase short-circuit is applied to the generator terminals.

Rating: 3-Phase, 100 kW, 0.8 p.f., 480V, 60 Hz		
x_d	4.1200	ohms
x_{q-}	2.2710	ohms
x_ℓ	0.1256	ohms
x'_d	0.2662	ohms
x''_d	0.1878	ohms
x''_q	0.1929	ohms
T'_{do}	1.866	s
T''_d	0.120	s
T''_q	0.035	s
R_{ph}	0.03574	ohms at 20°C
R_F	0.8556	ohms at 20°C

TABLE 9.1: Generator Parameters Supplied by the Manufacturers

L_D	$7.40 \times 10^{-3} \text{ H}$
L_Q	$4.13 \times 10^{-3} \text{ H}$
M_D	$7.06 \times 10^{-3} \text{ H}$
M_Q	$3.79 \times 10^{-3} \text{ H}$
M_F	0.10431 H
M_{DD}	$7.066 \times 10^{-3} \text{ H}$
M_{QQ}	$3.794 \times 10^{-3} \text{ H}$
L_{FF}	1.5965 H
L_{FD}	0.1043 H
L_{DD}	$7.261 \times 10^{-3} \text{ H}$
L_{QQ}	$3.917 \times 10^{-3} \text{ H}$
R_{DD}	$2.622 \times 10^{-3} \text{ ohms}$
R_{QQ}	$9.505 \times 10^{-3} \text{ ohms}$

TABLE 9.2 Calculated Phase Model Parameters for the Generator,
Based on Data Given in Table 9.1

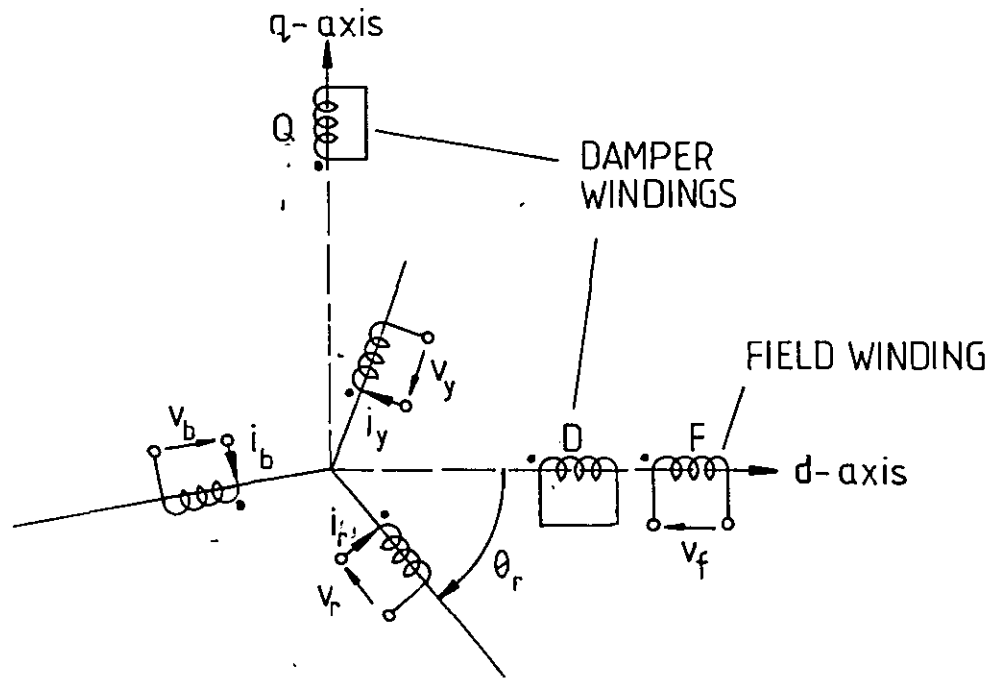


Figure 9.1(a) 3 - PHASE SYNCHRONOUS MACHINE

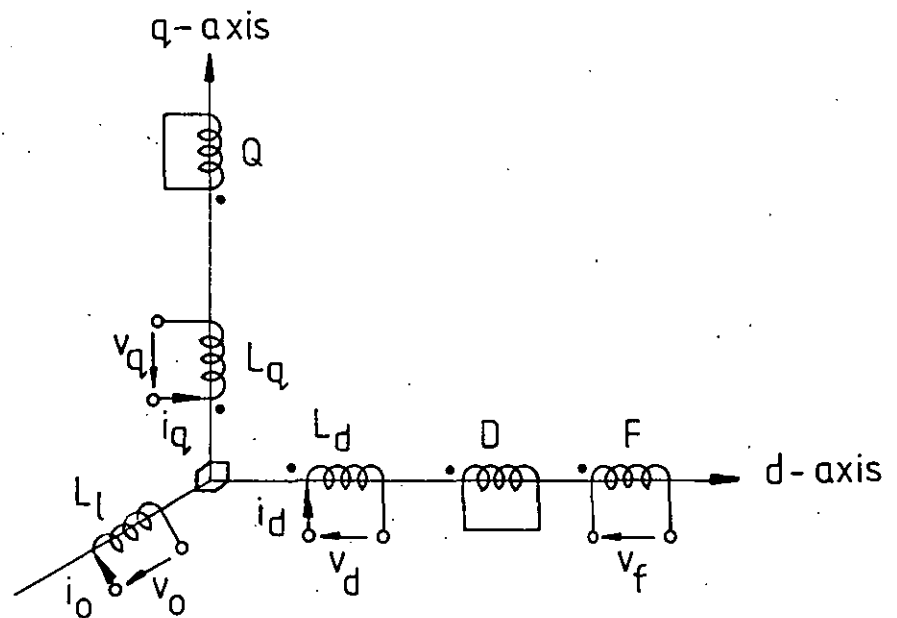


Figure 9.1(b) dqo - EQUIVALENT CIRCUIT OF SYNCHRONOUS MACHINE

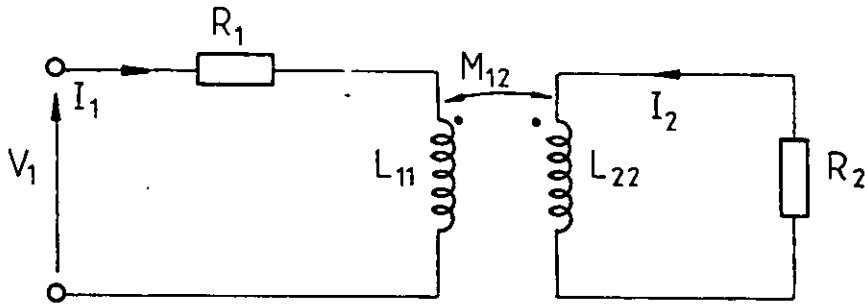
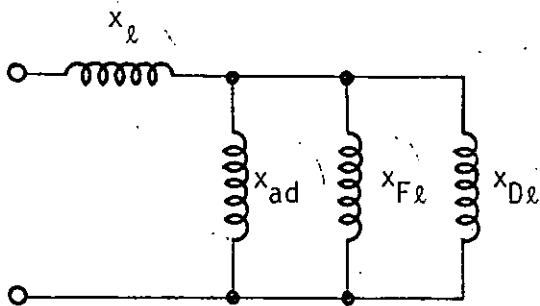
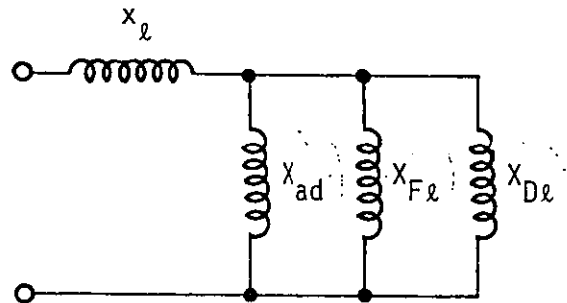


Figure 9.2 MAGNETIC COUPLING BETWEEN TWO WINDINGS



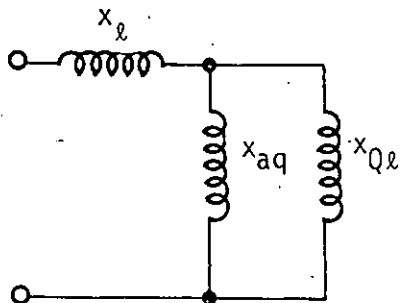
D - AXIS EQUIVALENT CIRCUIT
OF SYNCHRONOUS GENERATOR

Figure 9.3



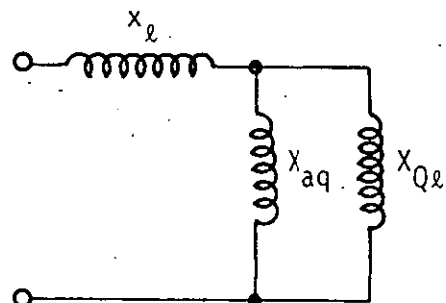
EQUIVALENT CIRCUIT OF ARMATURE
PHASE WINDING IN D - AXIS

Figure 9.4



Q - AXIS EQUIVALENT CIRCUIT
OF SYNCHRONOUS GENERATOR

Figure 9.5



EQUIVALENT CIRCUIT OF ARMATURE
PHASE WINDING IN Q - AXIS

Figure 9.6

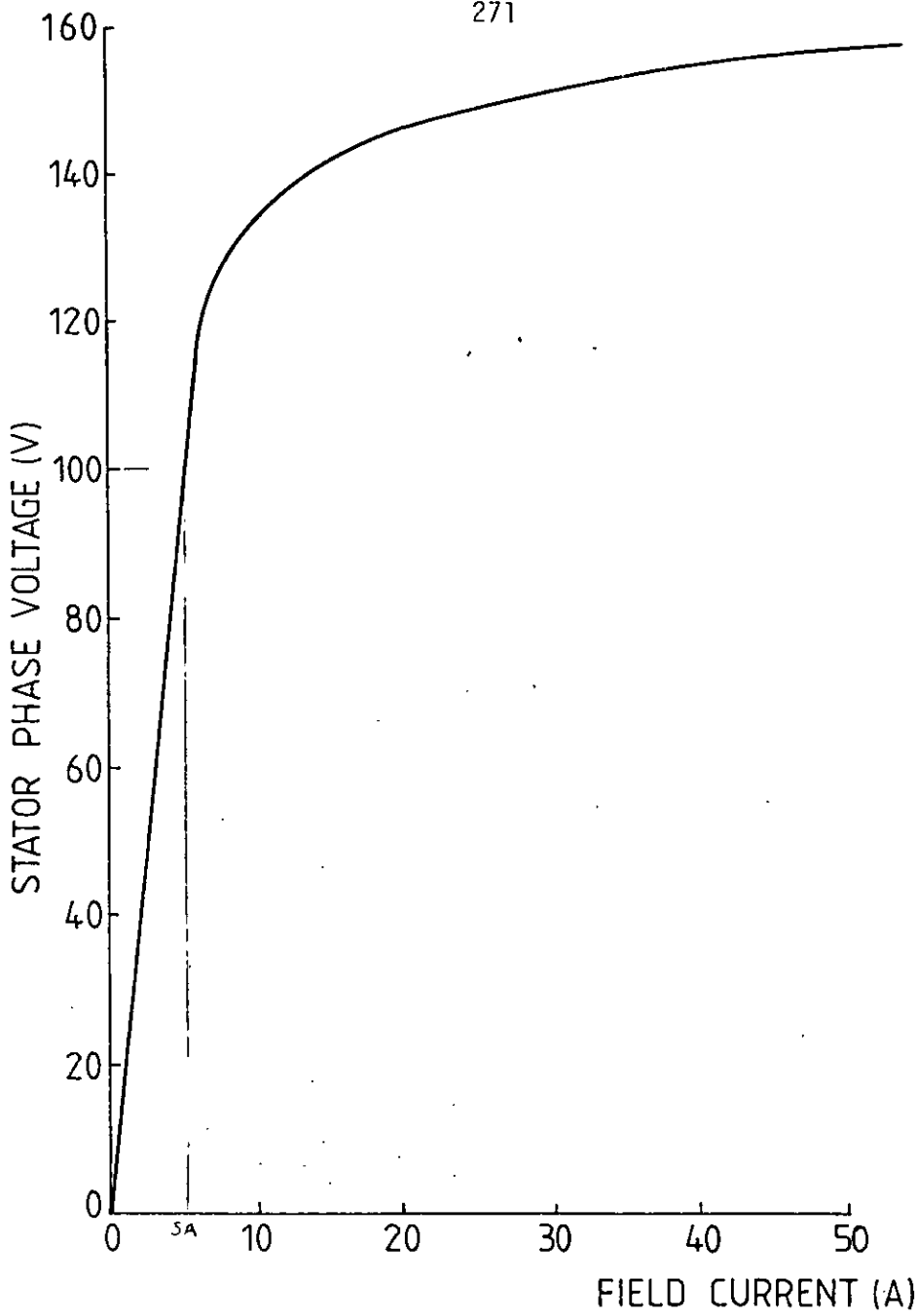


Figure 9.7

OPEN CIRCUIT CHARACTERISTIC OF GENERATOR

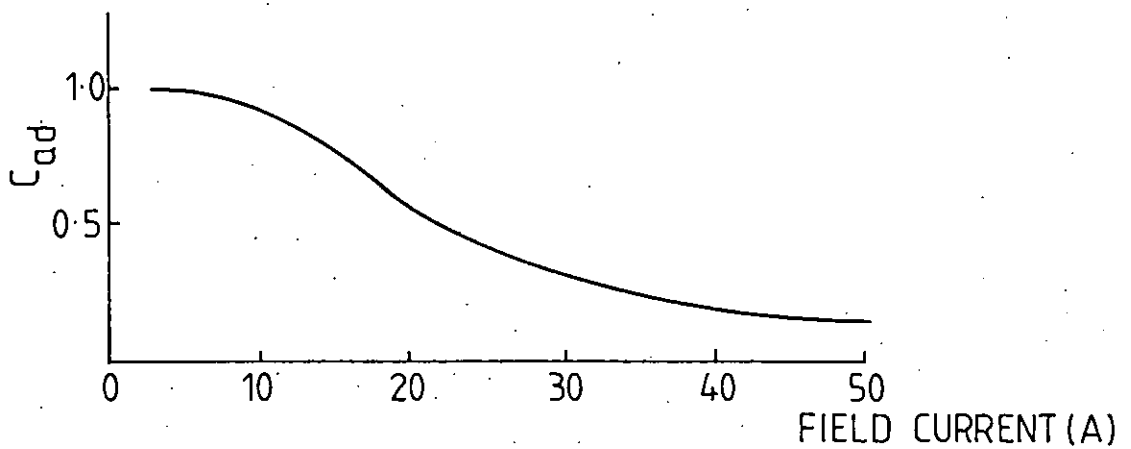


Figure 9.8

NORMALISED POLYNOMIAL C_{ab}

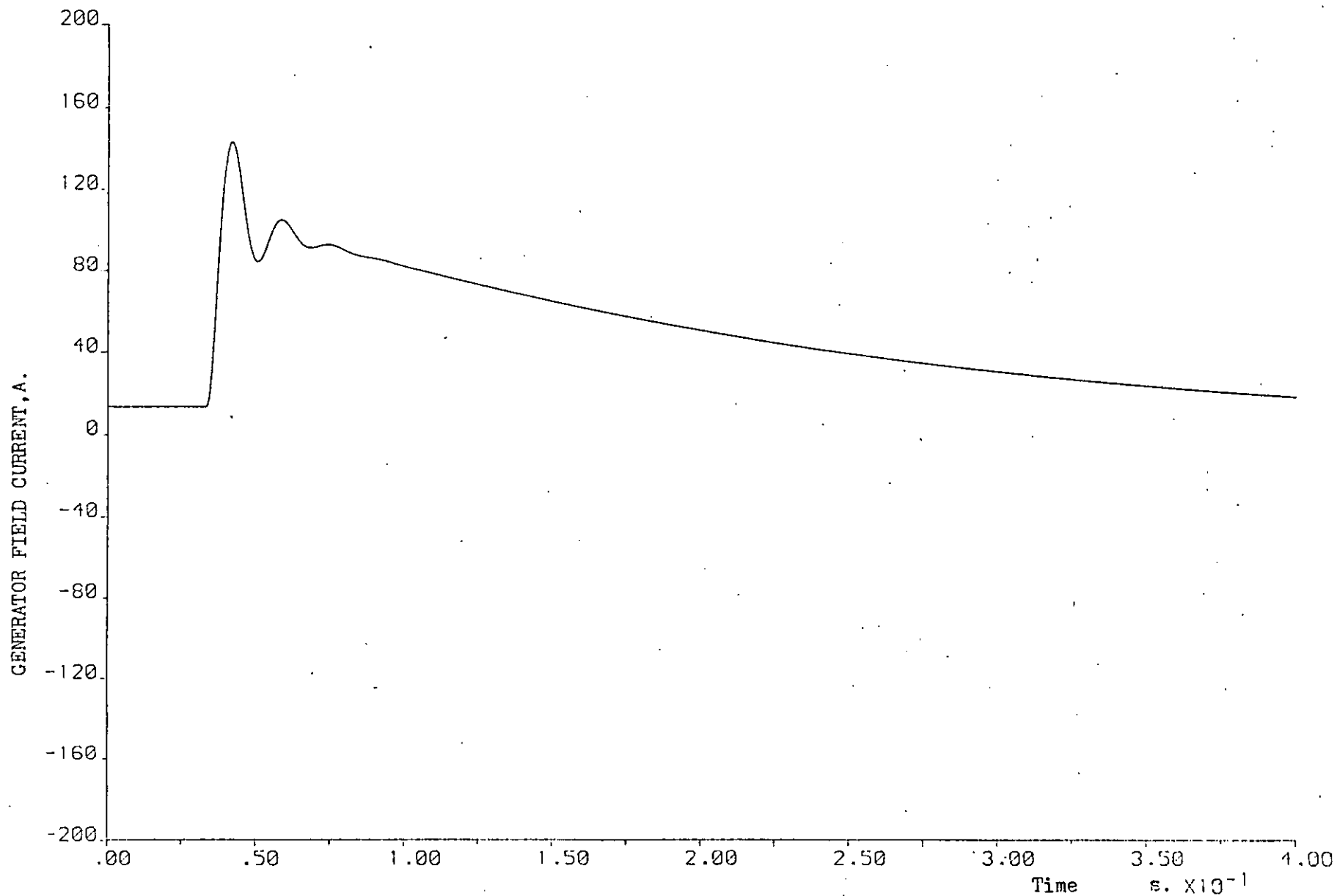


Figure 9.9 GENERATOR FIELD CURRENT TRANSIENT ON APPLICATION OF A 3 - PHASE SHORT CIRCUIT

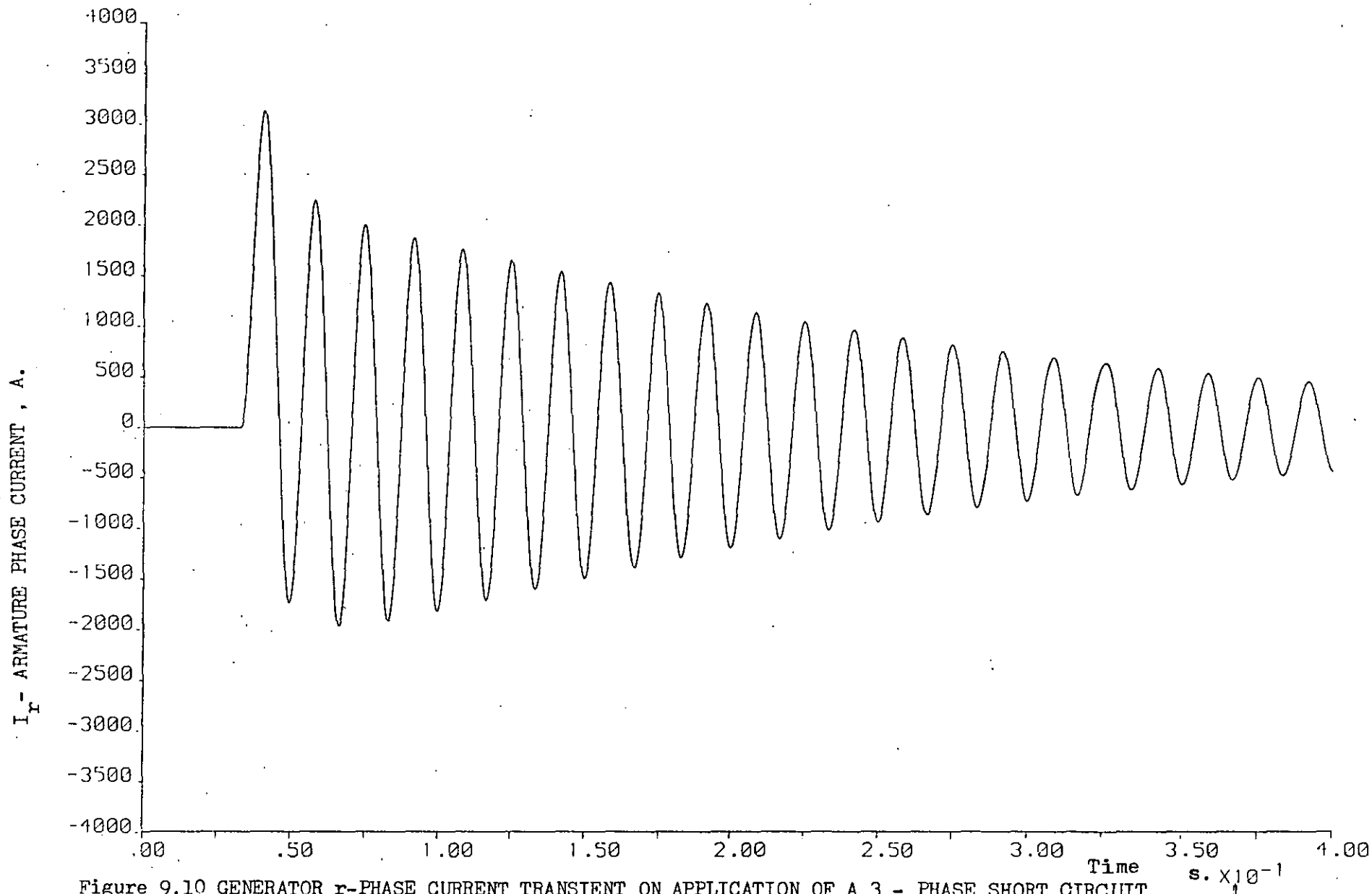


Figure 9.10 GENERATOR r-PHASE CURRENT TRANSIENT ON APPLICATION OF A 3 - PHASE SHORT CIRCUIT

CHAPTER 10

AREAS OF FURTHER RESEARCH

The mathematical models developed in this thesis can be used to investigate the following areas of interest related to electrical systems on the aircraft

1. The effect of changes in the temperature inside the 3-stage generator unit on the performance of the regulated generator. Under no-load conditions, this temperature is typically 40°C , while under full load condition it could be in excess of 120°C . The effective increase in the resistances of the generator unit windings not only affects the steady-state operating point of the system, but also the transients on application and rejection of load. Sollecito and Swann³ investigated the effects of temperature changes by modelling on an analogue computer. Similar investigations can also be carried out using the mathematical models described in this thesis, on a digital computer.
2. There are often a number of regulated generator units operating in parallel on board an aircraft, when the proper sharing or division of the load between the generator units is very important. The a.v.r. and other electrical systems are used to ensure a proper division of reactive load between the units, while the drive systems determine the division of real load between the units. Therefore a complete model of the electro-mechanical system using the model of the regulated generator unit described in this thesis could be developed for such studies.
3. The optimisation of the transient response of the regulated generator unit can be investigated using the model of the regulated generator unit on the digital computer, in place of the analogue computer method² used in the past. Some work in this direction is described by Kabriel⁷² who has derived formulae

for predicting the gain and time constants of the a.v.r. to obtain different transient response.

4. The design of optimum excitation controller using the Matrix Riccati Algorithm as applied to the turbogenerators is described by Humpage and Smith⁷³. They used the synchronous generator equation of the form

$$[V] = [L][pI] + \{[R] + [G]\}[I]$$

to determine the optimum excitation controller. Since the generator equation described in this thesis is of the same form, the method can be extended to the 3-stage generator unit to determine an optimum excitation controller which gives the desired transient response of the generator.

5. The effect of varying the a.v.r. parameters on the stability of the generator was investigated by Grainger and Ahmari⁷⁴ using Lyapunov's first method. The method could be used to investigate the stability of the regulated generator unit.

Additional areas of further research are discussed where applicable, in Chapters 2-9.

CHAPTER 11

CONCLUSION

In this thesis, mathematical models of the 3-stage generator unit and the automatic voltage regulator which form a primary part of an aircraft electrical power system have been described.

Starting with the phase model of the synchronous generator, a phase model for a brushless excitation system has been developed and used to predict accurately the exciter armature currents, the rectifier diode currents, the reverse voltages across the diodes etc. This model is suited for investigation in depth, the performance of the exciter-rectifier system.

Two models for the automatic voltage regulator have been described, and used to predict the transient response of the regulated 3-stage generator. It was shown that both models predict very nearly the same transient response, following the switching of balanced 3-phase loads. The state-variable model of the AVR can be used to investigate the transient response following unbalanced load switching, as discussed in Chapter 5. A simplified model of the exciter-rectifier, adequate for the system model, is also described.

The transfer function of the exciter-rectifier generator system was developed to show that it can be used to predict the steady-state exciter field current required when different loads are applied to the generator terminals. The effect of operating the exciter-rectifier in its different modes of operation is investigated, to show that, for optimum d.c. power output, it should be designed to operate in Mode 1. The phase model of the induction motor and the synchronous-generator/induction-motor combination were developed to investigate the direct-on-line switching of the induction motor and the effect of the induction motor as an impact load applied to the regulated generator unit. The phase model of the permanent magnet generator with the rectifier load was developed to investigate the performance of the first stage of the 3-stage generator unit.

At all stages of the thesis the theoretical work was substantiated by an extensive experimental investigation. It was shown that the mathematical models of the aircraft electrical power system predict accurately the characteristics of the system.

Theoretical methods for calculating the phase model parameters from the design and the dqo parameters were described, together with a method of obtaining the normalised polynomials to include saturation in the d-axis from the open-circuit characteristic of the generator. Theoretical formulae can be used in place of actual measurements if it is not possible to do the measurements due to a lack of test facilities, etc. The theoretical formulae were found to predict all the inductance coefficients of 2130 main generator within 5% error from those of the measured values. The formulae were also used to predict the performance of a 100 kW-480V-60 Hz-3-phase generator using the phase model of the generator. The inductance coefficients and the normalised saturation polynomials were calculated from the dqo parameters and the open-circuit characteristic of the generator supplied by the manufacturers in the USA.

Areas of further research in the modelling of the aircraft electrical power systems are discussed in Chapter 10.

REFERENCES

1. Breedon, D B and Ferguson, R W, "Fundamental equations for analogue studies of synchronous machines", Trans. A.I.E.E., June 1956, pp. 297-305.
2. James, H B, "The use of an analogue computer to optimise the transient response of an aircraft type generator regulator system", Trans. A.I.E.E., Nov. 1953.
3. Sollecito, W E and Swann, D A, "Computer evaluation of high temperature ^{aircraft} A-C electrical system design", Trans. A.I.E.E., Jan. 1960, pp. 434-444.
1959 UoI 78
4. Park, R H, "Two reaction theory of synchronous machines - Part I", Trans. A.I.E.E., 1929, 48, pp. 716-730.
5. Park, R H, "Two reaction theory of synchronous machines - Part II", Trans. A.I.E.E., 1933, 52, pp. 352.
6. ^{معرّف} Park, R H, "Definition of an ideal synchronous machine and formula for the flux linkages", G E Review, 1928, 31, pp. 332-334.
7. Blondel, A E, "Synchronous machines and converters", McGraw-Hill Book Co., 1913.
8. Doherty, R E and Nickle, C A, "Synchronous machines, an extension to Blondel's two-reaction theory", Trans. A.I.E.E., 1926, Vol. 45, pp. 974-987.
9. Hwang, H H, "Unbalanced operation of a.c. machines", I.E.E.E. Trans., PAS-84, 1965, pp. 1054-1066.
10. Hwang, H H, "Mathematical analysis of double line to ground short circuit of an alternator", I.E.E.E. Trans., PAS-86, 1967, pp. 1254-1257.

- + 11.

Hwang, H H, "Transient analysis of unbalanced short circuit of synchronous machines", I.E.E.E. Trans., PAS-88, 1969, pp.67-72.
- K + 12.

Hwang, H H, "Unbalanced operation of three phase machines with damper windings", I.E.E.E. Trans., PAS-88, 1969, pp.1588-1693.
- + 13.

Jones, C V, "The unified theory of electrical machines", Butterworth, 1967.
- 14.

Dunfield, J C and Barton, T H, "Inductances of a practical slip ring primitive II - An experimental study", I.E.E.E., PAS-85, 1966, pp. 145-151.
- 15.

Snider, L A, and Smith, I R, "Ballistic techniques for the measurement of self and mutual inductance of windings with a ferromagnetic core", J. of Physics E: Scientific Instruments 1971, Vol. 4, pp. 733-736.
- 16.

Kron, G, "Tensor analysis of networks", Macdonald (1955).
- K 17.

Kron, G, "Tensors for circuits". Dover Publication, 1959.
- K 18.

Kron, G, "The application of tensors to the analysis of rotating electrical machinery", G E Review, Pt. I - Part XIII (1935-1939).
- 19.

Kron, G, "Tensorial analysis of the integrated transmission system, Part I - The 6 basic frames", A.I.E.E. Trans., 1951, Vol. 70, pp. 1239-1248.
- +20.

Subramaniam, P and Malik, O P, "Digital simulation of a synchronous generator in direct-phase quantities", Proc. I.E.E. Vol. 118, 1971, pp. 153-160.
- K 21.

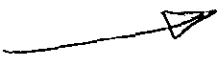

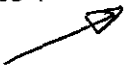
Dash, P K, Menzies, R W and Mathur, R M, "Digital simulation of a rectifier loaded synchronous machine", Electrical Machines and Electromechanic, Vol. 1, 1977, pp. 281-294.

22. El-Serafi, A M and Shehata, S A, "Digital simulation of an AC/DC system in direct phase quantities", I.E.E.E. PAS-95, 1976, pp. 731-742.
- + 23. Smith, I R and Snider, L A, "Predictions of the performance of an isolated, saturated synchronous generator", Proc. I.E.E., Vol. 119, 1972, pp. 1309-1318.
24. Snider, L A and Smith, I R, "Measurement of inductance coefficients of saturated synchronous machines", Proc. I.E.E. Vol. 119, 1972, pp. 597-602.
25. Pender, H and Delmar, W A, "Electrical engineer's handbook", John Wiley and Sons, Inc. (Publishers), Section 3, Article 25.
- + 26. Prescott, J C and El-Kharashi, A K, "A method of measuring self-inductances applicable to large machines", Proc. I.E.E. 1959, 106A, pp. 169-173.
- K 27. "Prediction of Saturated Steady-State Inductances of Aircraft Generators Using Finite-Element Field Solutions", GEC Power Engineering Ltd., Stafford, Report NEP 247 (Electrical Division) August 1979.
28. Zienkiewicz, O C, "The finite-element method in engineering science", McGraw Hill Publication, 1971.
29. Segerlind, L G, "Applied finite element analysis" John Wiley Publication, 1976.
30. Silvester, P and Chari, M V, "Finite-element solution of saturated magnetic field problems", I.E.E.E. Trans., PAS-90, N02, 1971, pp. 454-464.
- K 31. Easton, V, "Excitation of large turbogenerators", Proc. I.E.E., Vol. 111, No. 5, 1964, pp. 1040-1049.

- K 32. Smith, R E, "A brushless aircooled aircraft AC generator", A.I.E.E. Trans., Pt. II, Vol. 76, 1957, pp. 189-192.
33. Gayek, H W and Kyzer, S T, "Effect of regulation inversion on performance of brushless aircraft-generating systems", A.I.E.E. Conference paper CP62-1214, June 1962.
34. Merhof, W, "Brushless excitation of synchronous machines by rotating semiconductors", The Brown Boveri Review, Sept. 1967, pp. 539-553.
35. Goto, M, Isono, A and Okuda, K, "Transient behaviour of synchronous generator with shunt connected thyristor exciter under system faults", I.E.E.E. PAS-89, 1970, pp.2218-2227.
36. Rao, K V, "Fault studies on synchronous generators with rectifier excitation", Ph.D. Thesis, University of London, 1970.
37. Rao, K V, "Peak inverse voltages in the rectifier excitation system of synchronous machines", I.E.E.E. P/S-93, 1974, pp. 1685-1692.
- +38. Franklin, W, "Theory of the three phase salient pole type generator with bridge rectifier output - Part I", I.E.E.E. PAS 72, 1972, pp. 1960-1967, "Part II", I.E.E.E. PAS 72, pp.1968-1975.
- +39. Williams, S and Smith, I R, "Fast digital computation of 3-phase thyristor bridge circuits", Proc. I.E.E., Vol. 120, No. 7, 1973, pp.791-795.
- +40. Htsui, J S, Shepherd, W, "Method of digital computation of thyristor switching circuits", Proc. I.E.E., Vol. 118, 1971, pp.993-998.
41. Smith, M J, "Modelling and analysis of non-ideal polyphase diode converters", Simulation (U.S.A), 1971, 17, pp.237-243.

42. William, S and Smith, I R, "SCR bridge converter computation using tensor methods", I.E.E.E. Trans., 1976, Computers-25, pp.1-6.
43. (a) Gayek, H W, "Behaviour of brushless aircraft generating systems", I.E.E.E. Trans. on Aerospace, Vol. AS-1, No. 2, Aug. 1963, pp. 594-622.
 (b) Gayek, H W, "Transfer characteristics of brushless aircraft generator systems", ibid, Vol. 2, No. 2, April 1964, pp. 913-928.
44. "Excitation system dynamic characteristics", I.E.E.E. Committee Report, I.E.E.E., PAS-91, 1972, pp.64-75.
45. "Computer representation of excitation systems", I.E.E.E. PAS-87, 1968, pp. 1460-1464.
46. Witzke, R L, Kresser, J V and Dillard, J K, "Influence of a.c. reactance on voltage regulation of 6-phase rectifiers", A.I.E.E. Trans., July 1953, pp. 244-252.
47. Schmidt, A, "Power factor of rectifiers", A.I.E.E. Trans. May 1958, pp. 53-57.
48. Shilling, W J, "Exciter armature reaction and excitation requirements in a brushless rotating rectifier aircraft alternator", A.I.E.E. Trans., Nov. 1960, pp. 394-402.
49. Smith, R T, "Excitation requirements for rectified output A.C. generators", I.E.E.E. Trans. PAS-89, pp. 1910-1914, 1970.
50. Stepina, J, "Calculation of the effective loading per unit of rotor periphery in the synchronous machine under rectifier load", ACTA Technica CSAV, No. 3, 1964.

51. Fenwick, D R and Wright, W F, "Review of trends in excitation systems and possible future trends", Proc. I.E.E., Vol. 123, 1976, pp. 413-420.
52. Maslin, A J, "Three phase rectifier circuits", Electronics, pp. 28-31, Dec. 1936.
53. Christensen, E F, Willis, C H and Herskind, C C, "Analysis of rectifier circuits", A.I.E.E. Trans., Vol. 63, 1944, pp.1048-1058.
54. Stinemen, R W, Voss, J M, King, W S, "Analysis of aerospace electric power system dynamics with a digital computer", I.E.E.E. Trans. on Aerospace, Vol. 2, 1964, pp. 630-641.
55. Anderson, H C, "Voltage variation of suddenly loaded generators", General Electric Review, Aug. 1945, pp. 25-33.
- + 56. Concordia, C, "Synchronous machines", John Wiley and Sons, Inc. New York, 1951.
57. O'Kelly, D and Simmons, S, "Introduction to generalized electrical machine theory", McGraw Hill Publishing Co. Ltd., London.
58. Talaat, M E, "A new approach to the calculation of synchronous machine reactances - Part I", Trans. A.I.E.E. 1955, pp. 176-183. "Part II", Trans. A.I.E.E., 1956, pp. 317-327.
59. De Sarkar, A K and Berg, G J, "Digital simulation of three-phase induction motors", I.E.E.E. Trans., PAS-89, 1970, pp.1031-1036.
60. Stanley, H C, "An analysis of the induction machine", A.I.E.E. Trans., Vol. 57, pp. 751-757, 1938.

- + 61. Rafian, M and Laughton, M A, "Aspects of induction and synchronous motor analysis using dynamic phase coordinate theory" Proc. I.E.E., Vol. 126, 1979, pp. 749-758.
- + 62. Snider, L A and Smith, I R, "Prediction of the performance of an induction motor/synchronous generator combination", Proc. I.E.E., Vol. 120, 1973, pp.79-86.
- 63. Mainer, O E, "Theoretical treatment of permanent magnet alternators", Int. J. Elect. Engn. Educ., Vol. 6, pp. 417-425.
- 64. Von Zastrow, E E and Galloway, J H, "Commutation behaviour of diffused high current rectifier diodes", I.E.E.E. International Convention Record Part 4, 1964, pp. 106-118.
- + 65. "Test procedures for synchronous machines", I.E.E.E. Publ. 115, 1965. 
- + 66. Liwshitz-Garik, M and Whipple, C C, "Alternating current machines". D Van Norstrand Co., Princeton, New Jersey (Publishers).
- + 67. Alger, P L, "Nature of polyphase induction machines", Wiley, 1951.
- + 68. Kilgore, L A, "Calculation of synchronous machine constants", A.I.E.E. Trans., Dec. 1931, pp. 1201-1214. 
- + 69. Venikov, V, "Transient processes in electrical power systems", Mir Publishers, Moscow.
- + 70. Adkins, B and Harley, R G, "The general theory of alternating current machines", Chapman and Hall, London, 1975.
- + 71. Wright, S W, "Determination of synchronous machine constants by test", A.I.E.E. Trans., 1931, Vol. 50, pp. 1331-1351. 

72. (a) Kabriel, B J, "Simple formulae for voltage regulation gains for best alternator stability", Proc. I.E.E., Vol. 116, 1969, pp. 1907-1914.

(b) Kabriel, B J, "Choosing power system voltage regulator parameters by use of standard forms", Proc. I.E.E., Vol. 117, 1970, pp. 1809-1814.
- ~~73.~~ Humpage, W D and Smith, J R, "Application of dynamic optimisation to synchronous generator excitation controller", Proc. I.E.E., Vol. 120, 1973, pp. 87-93.
- ~~74.~~ Grainger, J T and Ahmari, R, "Effect of non-dynamic parameters of excitation system on stability performance", I.E.E.E., PAS-91, 1972, pp. 1-8.
75. Golding, E W, "Electrical measurements and measuring instruments", Pitman, 3rd Edition, 1946.
76. Jones, C V, "An analysis of commutation for the unified-machine theory", Proc. I.E.E., 1958, 105C, pp. 476-480.
- +77. Wylie, C R, "Advanced engineering mathematics", McGraw Hill Book Co.
78. Runge, C, "Über die numerische Lösung von Differentialgleichungen", Math. Ann., 1895, pp. 167-178.
79. Kutta, W, "Beitrag zur näherungsweise Integration totaler Differentialgleichungen", Z. Math. Phys., 1901, 46, pp. 435-453.
80. Gill, S, "A process for the step-by-step integration of differential equations in an automatic digital computing machine", Proc. Cambridge Phil. Soc., 1951, 47, pp. 96-108.

81. Ralston, A, "Runge-Kutta methods with minimum error bounds", M.A.T.C., 1962, 16, (80), pp. 431-437.
82. Milne, W E, "Numerical integration of ordinary differential equations", Amer. Math. Monthly, 1931, 38, pp. 455-460.
83. Hamming, R, "Stable predictor-corrector methods for ordinary differential equations", J. Assoc. Computing Machinery", 1959, 6, (1), pp.37-47.

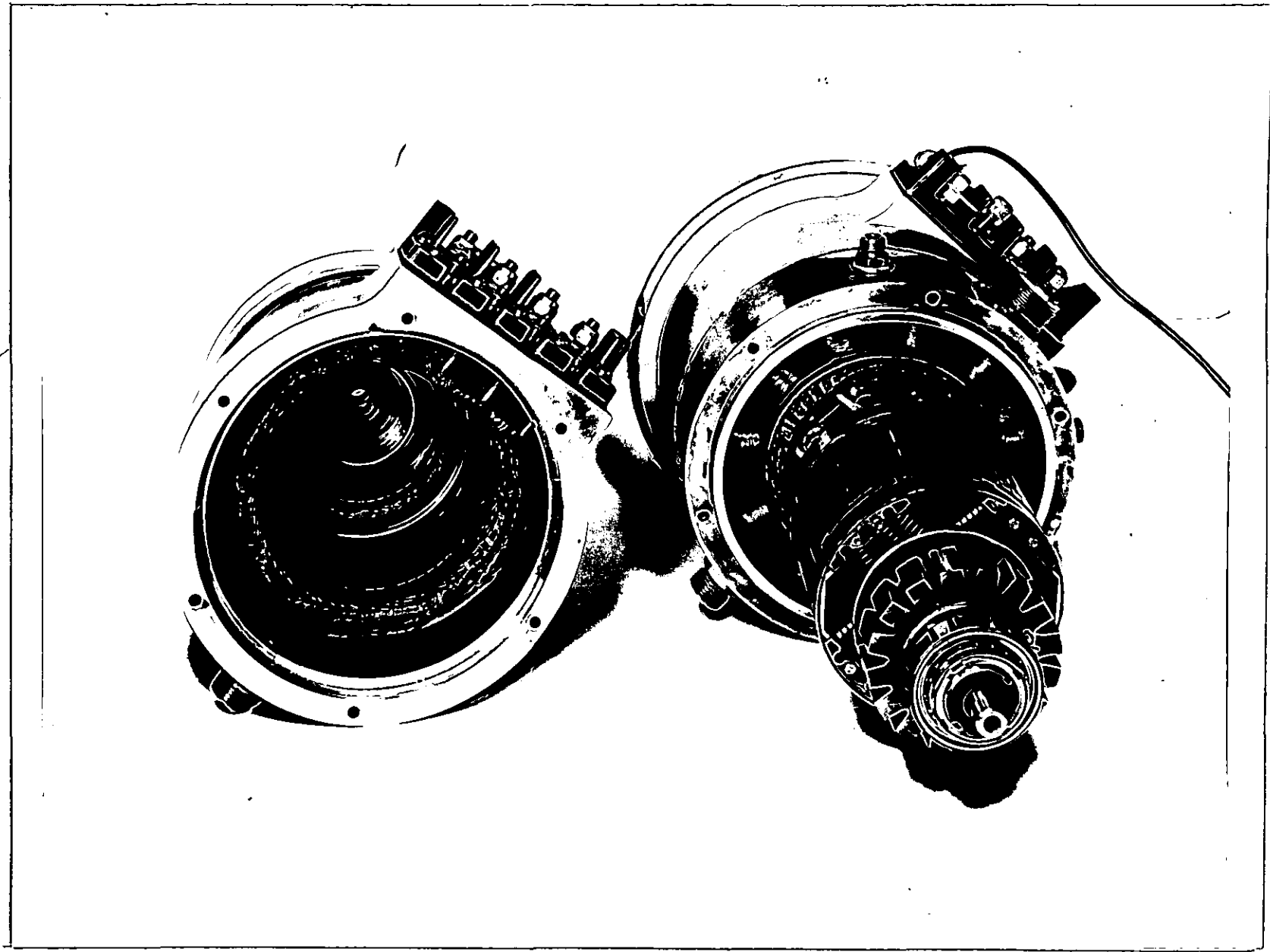
APPENDIX A1

A1.1 Construction of 2130 3-Stage Generator Unit

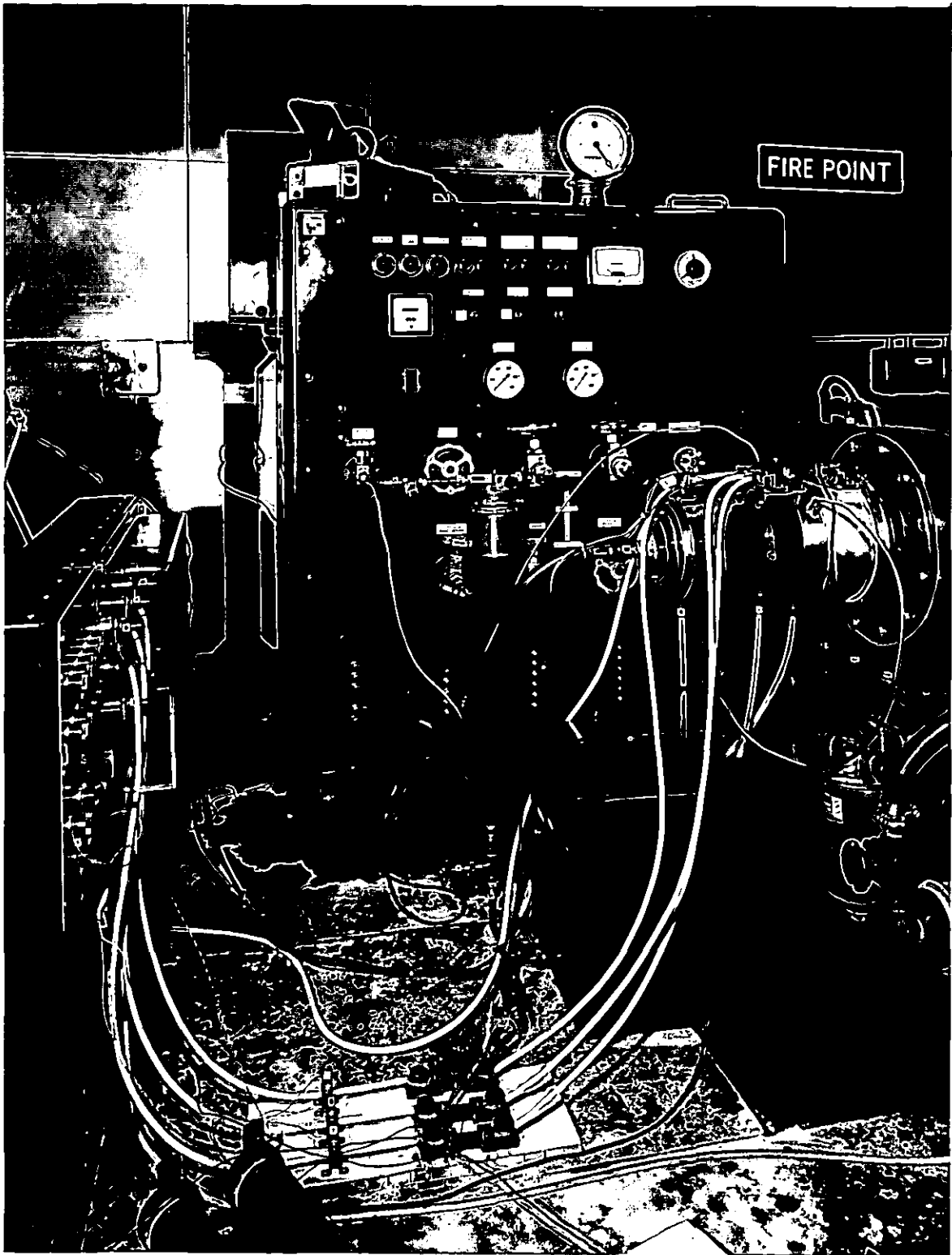
Photograph A1.1 shows the 3-stage generator unit rotor and stator detail . The stator on the left of the photograph shows the main generator and pilot exciter phase windings. The rotor on the right of the photograph shows the PMG rotor magnet, the main generator rotor and the main exciter phase windings. The part of the stator with the main exciter field windings is shown with the rotor.

A1.2 3-Stage Generator Unit Connected for Load Tests

Photograph A1.2 shows the 3-stage generator unit connected to the d.c. drive via a gearbox. The cables connecting the generator to the load via the current shunts and the transfer boards are also shown. To maintain the temperature of the generator unit within close limits, oil spray cooling is used. The oil pump unit to cool and circulate the oil can be seen in the background. Figure A1.3 shows the electrical circuit used for measuring the load application and rejection transients discussed in Chapter 5. Photograph A1.4 shows the control station for the d.c. drive and the load selection switches. The automatic voltage regulator (a.v.r) is also shown connected to the system.



Photograph A1.1



Photograph A1.2

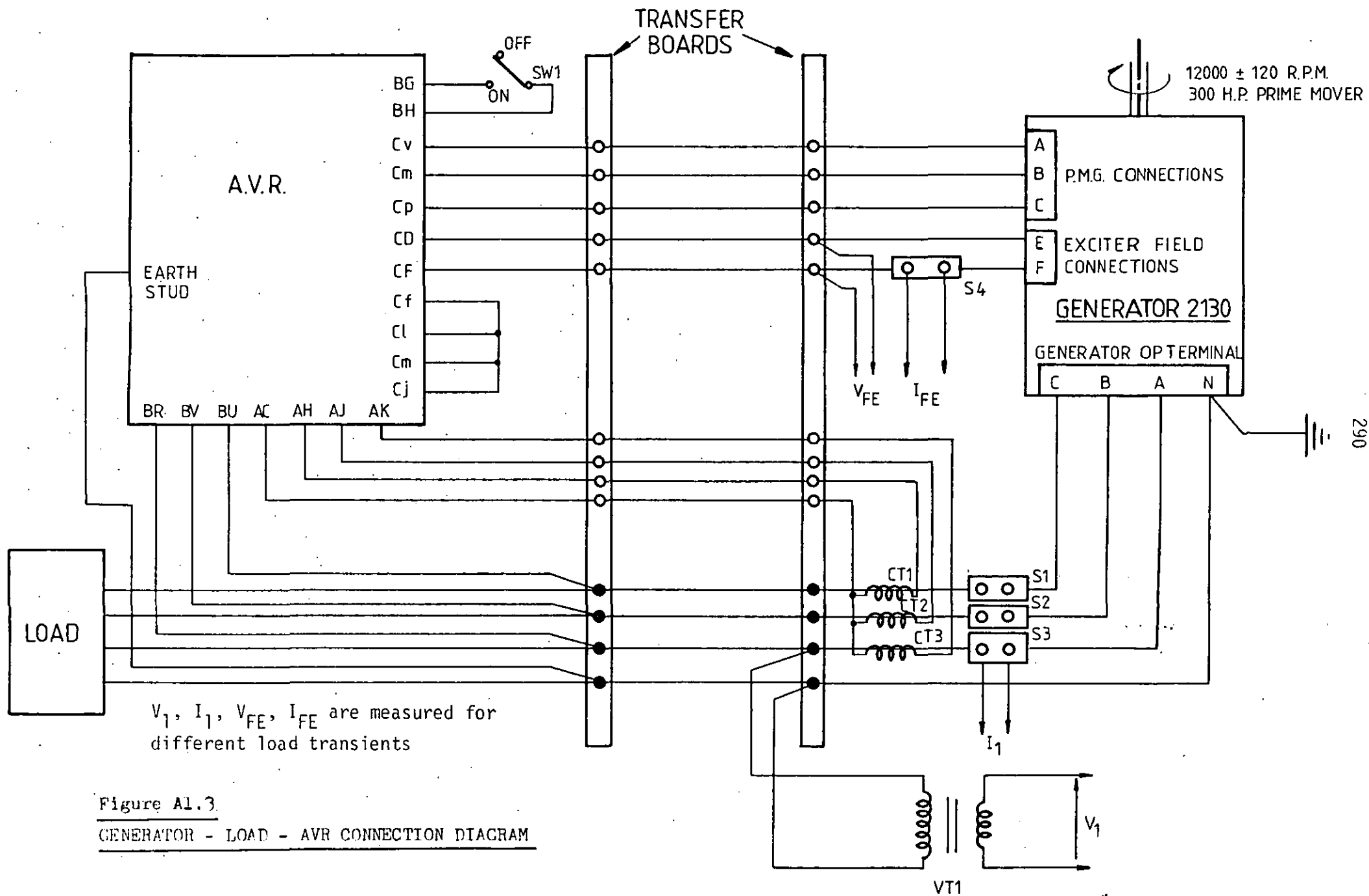
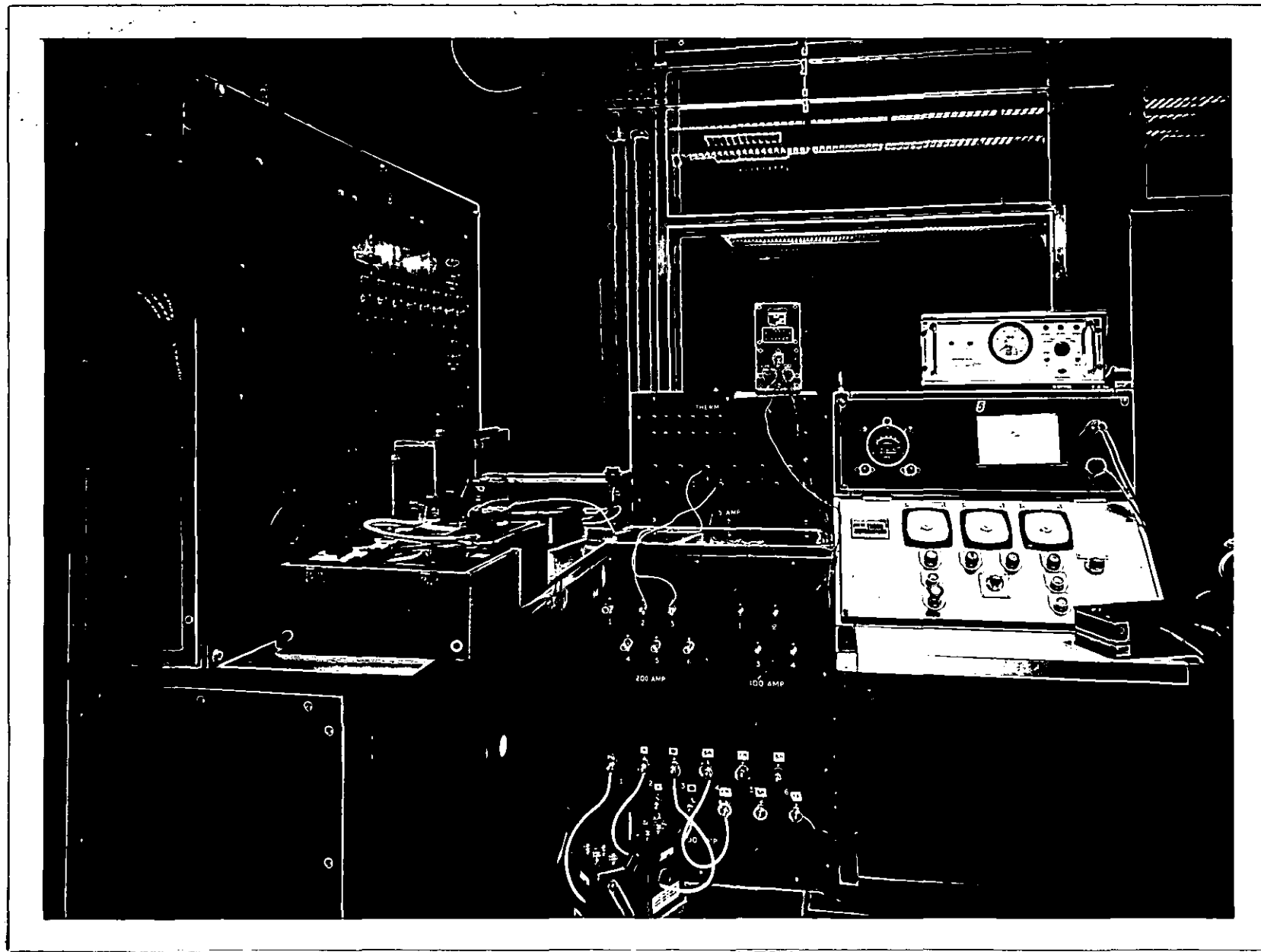


Figure A1.3

GENERATOR - LOAD - AVR CONNECTION DIAGRAM



Photograph A1.4

A1.3 Main Generator Design Parameters (based on 0.030" airgap)

Rating: 40 kVA 400 Hz. 115V (phase voltage)

Parameter			
x_d		1.6572	ohms
x_q		0.7813	ohms
x_l	leakage	0.0670	ohms
x'_d		0.1429	ohms
x''_d		0.1313	ohms
x''_q		0.1184	ohms
x_2	we. seq.	0.1249	ohms
x_0	zero seq.	0.0193	ohms
R_{ph}		0.0251	ohms at 20°C
R_F		0.1191	ohms at 20°C
R_2	rotor	0.0405	ohms at 20°C
R_0	zero seq.	0.0251	ohms at 20°C
T_A	arm. time	0.00198	s. at 20°C
T'_d	T. arm. seq.	0.01376	s. at 20°C
T'_{do}	T. rotor d.c.	0.15957	s. at 20°C
P		4	
N		22	
K_w	w. f.	0.7810	
K_G : stator		1.0474	
K_G : rotor	rotor conf.	1.0303	
N_f		25	

A1.4 Main Exciter Design Parameters

Parameter		
x_d	0.246	ohms
x_q	0.184	ohms
x_c	0.063	ohms
x_ℓ	0.046	ohms
x'_d	0.077	ohms
R_{ph}	0.0116	ohms at 20°C
R_F	8.129	ohms at 20°C
T'_{do}	0.03198	s at 20°C
P	10	
N	18	
K_w	0.949	
K_G	1.0811	

A1.5 Permanent Magnet Generator (PMG) Design Parameters

Parameter	
x_d	0.7662 ohms
x_q	1.1574 ohms
x_ℓ	0.2138 ohms
R_{ph}	0.1471 ohms at 20°C
Tan (δ)	18.1789
Tan (β)	25.0671
Tan (γ)	85.8304
P	16 (Alcomax III)
N	64
K_w	0.8660
K_G	1.1789

APPENDIX A2.

The ballistic techniques for measuring the inductances of the windings of a machine in the presence of short-circuited windings are well known. Golding⁷⁵ used a bridge technique for measurement of self-inductance. Snider and Smith¹⁵ have shown that the method can be extended to the measurement of inductances in the presence of other short-circuited coils, for example an explicit damper winding on a synchronous machine rotor or the eddy current paths in the iron and the solid pole tips of a generator rotor.

A Norma model 251F fluxmeter was used to measure the self and mutual inductance between the armature and field windings. This consists of a D'Arsonval galvanometer, the movement of which is measured by the deflection of the light spot on a glass screen marked in scale divisions. The relationships between the voltage V applied to the galvanometer for a time T and the distance x moved by the light spot is given by

$$\int_0^T V \cdot dt = c \cdot x \quad \text{A2.1}$$

where c is the scale constant.

A2.1 Measurement of Self-Inductance of a Coil

The bridge circuit used to measure the self-inductance of a coil in the presence of other coupled coils is shown in Figure A2.1. It consists of a test coil with winding resistance R_2 and three non-inductive resistances R_1 , R_3 , R_4 connected as shown. The resistance R_4 must be capable of taking the maximum test coil current.

Under balanced bridge conditions, the voltage V_0 applied to the fluxmeter coil is zero and

$$\frac{R_1}{R_3} = \frac{R_2}{R_4}$$

A2.2

If the test coil current I_2 is reversed using the reversing switch S, it can be shown¹⁵ that the relationship between the inductance of the coil L'_{22} , the deflection x and the constant c of the flux-meter is

$$L'_{22} = \left(1 + \frac{R_2}{R_4}\right) \cdot \frac{c \cdot x}{2I_2}$$

A2.3

$$= \left(1 + \frac{R_1}{R_3}\right) \cdot \frac{c \cdot x}{2I_2}$$

i) Secant Self-inductance

In the absence of any external bias current (I_1), the measurements made by reversal of the current through the coil is termed the secant inductance L_{22} .

ii) Incremental Self-inductance

The incremental self-inductance is measured, with a constant bias current (I_1) in coil (1), by reversing a small current I_2 in the test coil. The inductances of any coupled coils and their mutuals have no effect on the measurement of the self-inductance of the coil.

If the secant inductance L_{22} of the test coil (2) is plotted against the current I_2 for different values of I_2 , a graph similar to that shown in Figure A2.2(a) is obtained. If ψ_2 , the flux linkage of coil (2) is plotted against I_2 , a graph similar to that shown in figure A2.2(b) is obtained. The incremental inductance L_{22} at any current I_{22} is given by the slope of this graph at I_{22} .

$$\psi_2 = L_{22} I_{22} \quad \text{A2.4}$$

$$L'_{22} = \frac{d\psi_2}{dI_{22}} \quad \text{A2.5}$$

The incremental inductance of the test coil can be measured for different values of bias current I_1 in coil (1). If the incremental inductance L'_{22} is plotted against I_1 , a graph similar to figure A2.2(c) is obtained. If coil (1) is in the same axis as coil (2), the bias current I_1 can be replaced by an equivalent bias current I_2 flowing in test coil (2). As the quiescent point is established by the total ampere turns in the axis of the coil (2)

$$N_1 I_1 = N_2 I_2 \quad \text{A2.6(a)}$$

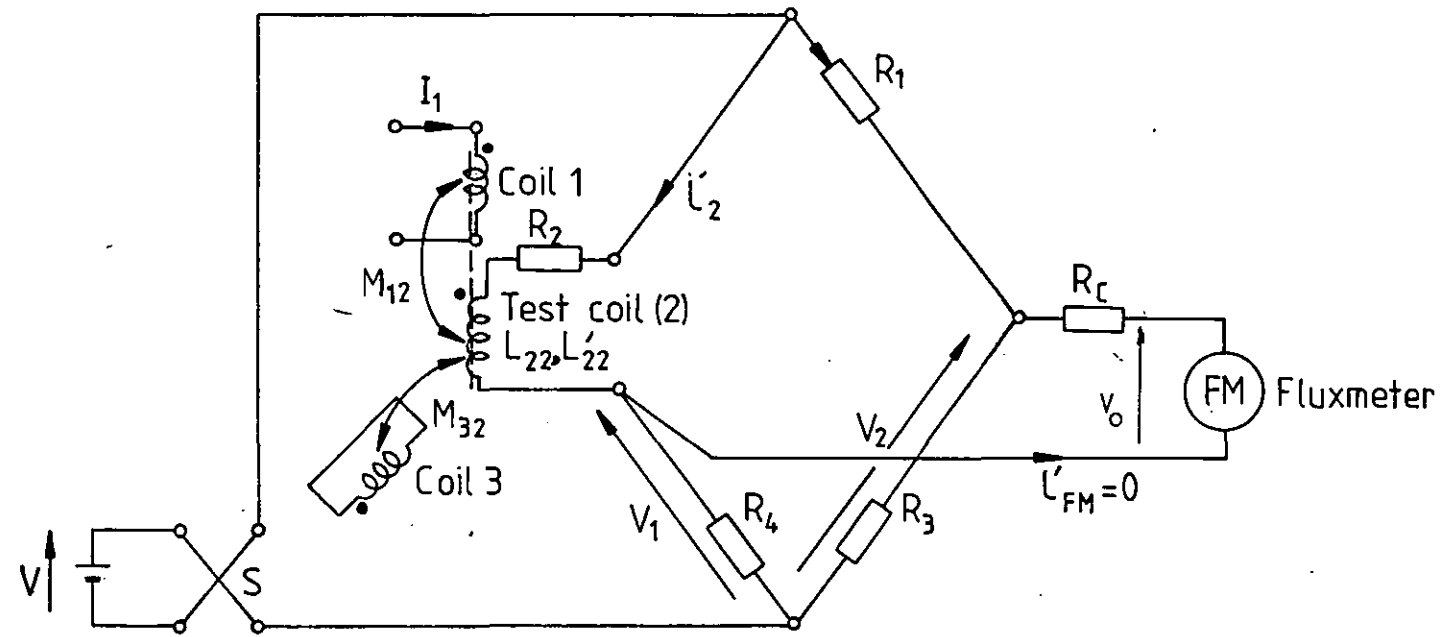
$$\therefore I_2 = \left(\frac{N_1}{N_2}\right) I_1 \quad \text{A2.6(b)}$$

The x-axis scale of Figure A2.2(c) can be changed to that of the equivalent bias current I_2 , by multiplying by the turns ratio between coil (1) and the test coil (2). The secant inductance corresponding to any current I_{22} can hence be found by

$$\begin{aligned} L_{22} &= \frac{1}{I_{22}} \int_0^{I_{22}} \left(\frac{dL_{22}}{dI_2}\right) \cdot dI_2 \\ &= \frac{1}{I_{22}} \int_0^{I_{22}} L'_{22} dI_2 \end{aligned} \quad \text{A2.7(a)}$$

$$\text{or } L_{22} = \frac{\text{Area under } L'_{22} \text{ curve from } I_2 = 0 \text{ to } I_2 = I_{22}}{I_{22}}$$

$$L_{22} = \frac{\bar{A}}{I_{22}} \quad \text{A2.7(b)}$$



TEST CIRCUIT FOR MEASURING SELF INDUCTANCE OF
A COIL (2) WITH SECANT INDUCTANCE L_{22} AND INCREMENTAL
INDUCTANCE L'_{22}

Figure A2.1

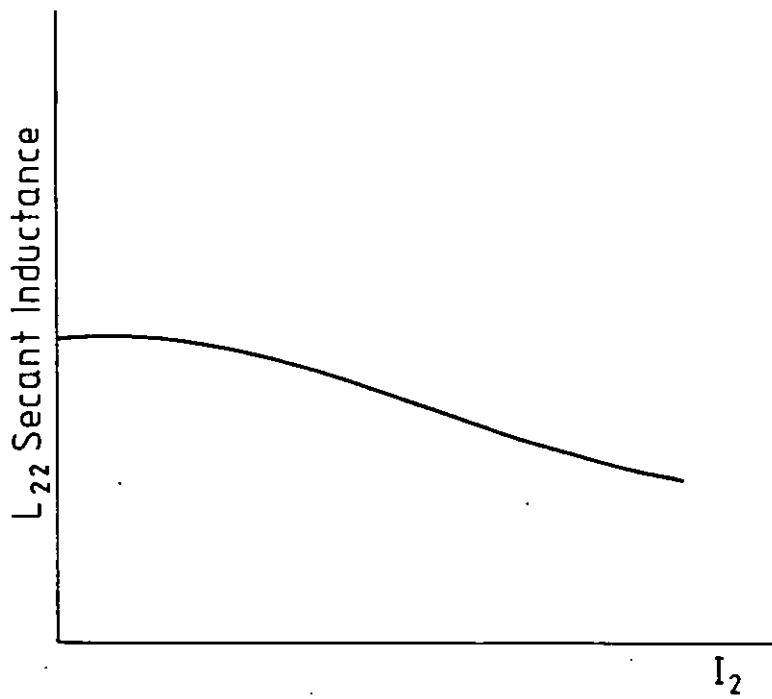


Figure A2.2(a) SECANT INDUCTANCE L_{22} AS A FUNCTION OF I_2

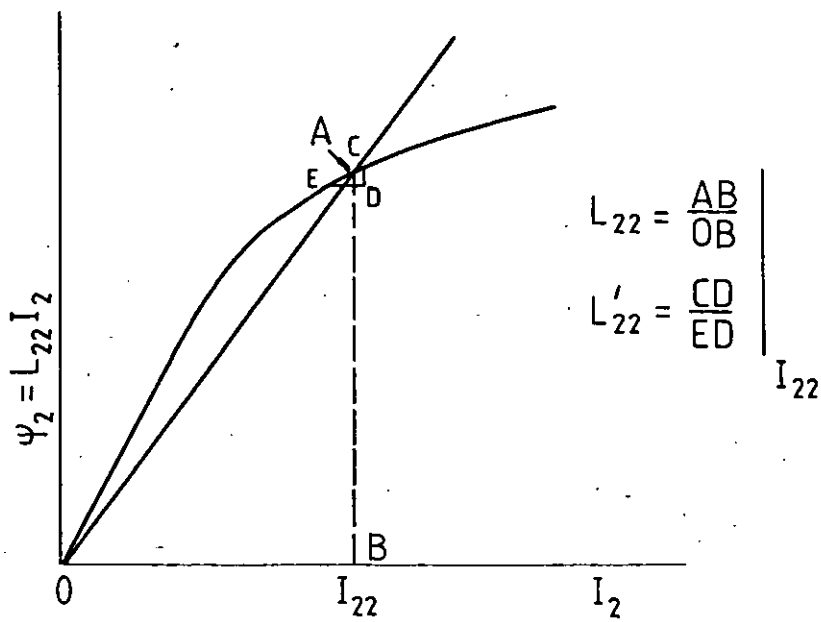


Figure A2.2(b) FLUX LINKAGE AS A FUNCTION OF I_2

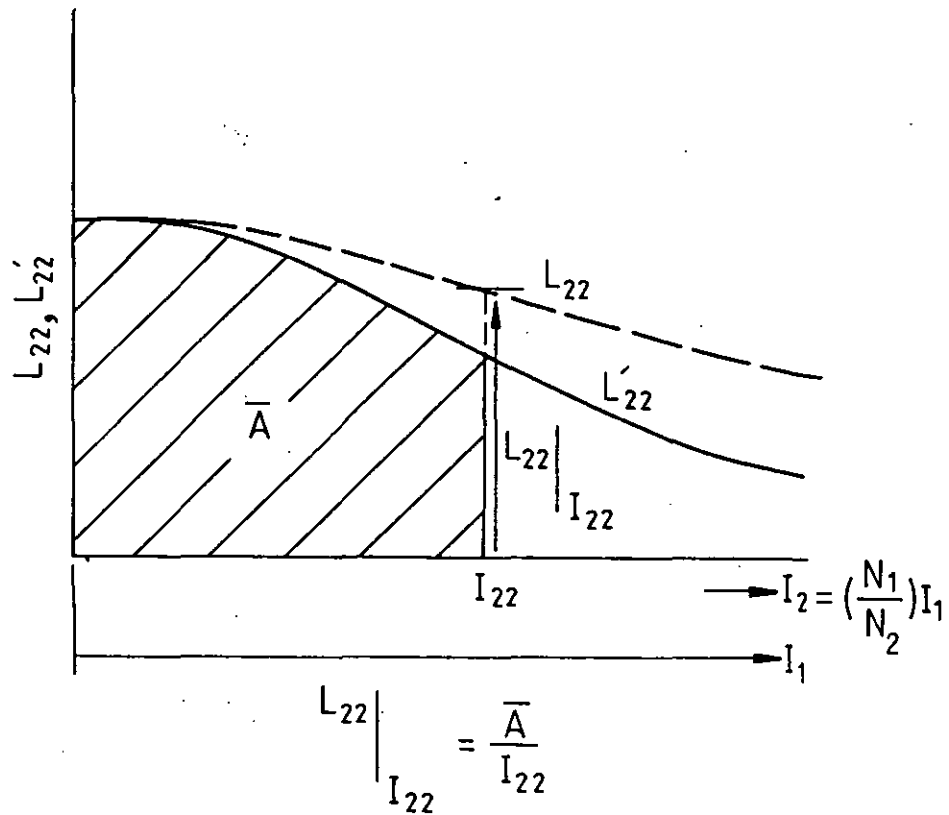


Figure A2.2(c) SECANT INDUCTANCE L_{22} AND INCRIMENTAL INDUCTANCE L'_{22}
AS FUNCTIONS OF I_1, I_2

APPENDIX A3MEASUREMENT OF MUTUAL INDUCTANCES BETWEEN TWO COILS

The circuit used to measure the mutual inductance between coils 1 and 2 in the presence of other coupled coils is shown in Figure A3.1. Coil 1 is connected to the fluxmeter via the resistance R_c which is adjusted to give the required source resistance for the fluxmeter. When the current I_2 in coil 2 is reversed, the voltage induced in coil 1 is given by

$$V_1 = M_{12} \frac{di_2}{dt} + M_{13} \frac{di_3}{dt} \quad A3.1$$

Therefore

$$\int_0^{\infty} V_1 dt = M_{12} \int_{-I_2}^{+I_2} di_2 + M_{13} \int_0^0 di_3 \quad A3.2$$

If C is the constant of the fluxmeter and x the deflection of light spot, then

$$M_{21} = \frac{C \cdot x}{2I_2} \quad A3.3$$

The value of mutual inductance obtained in the absence of any bias current is a secant value. The mutual inductance between two coils 1 and 2 can be measured for different values of I_2 and plotted as shown in Figure A3.2(a).

The mutual inductance between coils 1 and 2 can also be obtained by reversing current in coil 1 and measuring the voltage integral

$$\int_0^{\infty} V_2 dt \text{ across coil 2.}$$

$$M_{21} = \frac{C \cdot X}{2I_1}$$

A3.4

The mutual inductance between coils 1 and 2 can be measured for different values of I_1 and plotted as shown in Figure A3.2(b). As mutual inductance is reciprocal under the same level of saturation⁷⁶, the current ratio to produce the same saturation level in the mutual flux path can be found from the ratio of I_1 and I_2 for the same value of mutual inductance. From Figures A3.2(a) and A3.2(b), if I_{20} and I_{10} correspond to a mutual inductance value, it follows that

$$N_1 I_{10} = N_2 I_{20}, \text{ if } (M_{120} = M_{210})$$

$$\text{or } \frac{N_1}{N_2} = \frac{I_{20}}{I_{10}}$$

A3.5

It is found that the M_{21} curve of Figure A3.2(b) is a close fit to the M_{12} curve of Figure A3.2(a) if the x-axis scale of Figure A3.2(b) is multiplied by a scaling factor equal to the turns ratio $\left(\frac{N_1}{N_2}\right)$.

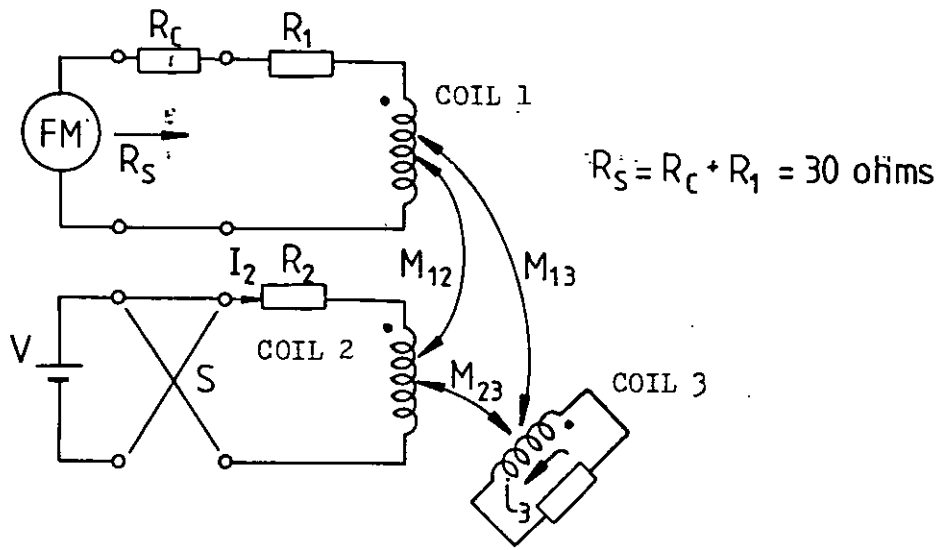


Figure A3.1 CIRCUIT FOR MEASURING MUTUAL INDUCTANCE BETWEEN TWO COILS
IN PRESENCE OF OTHER COUPLED COILS

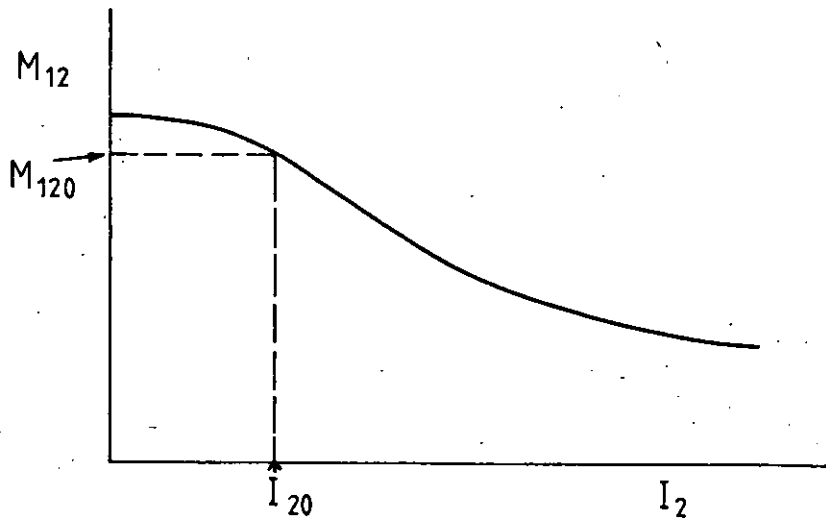


Figure A3.2(a) MUTUAL INDUCTANCE M_{12} AS A FUNCTION OF I_2

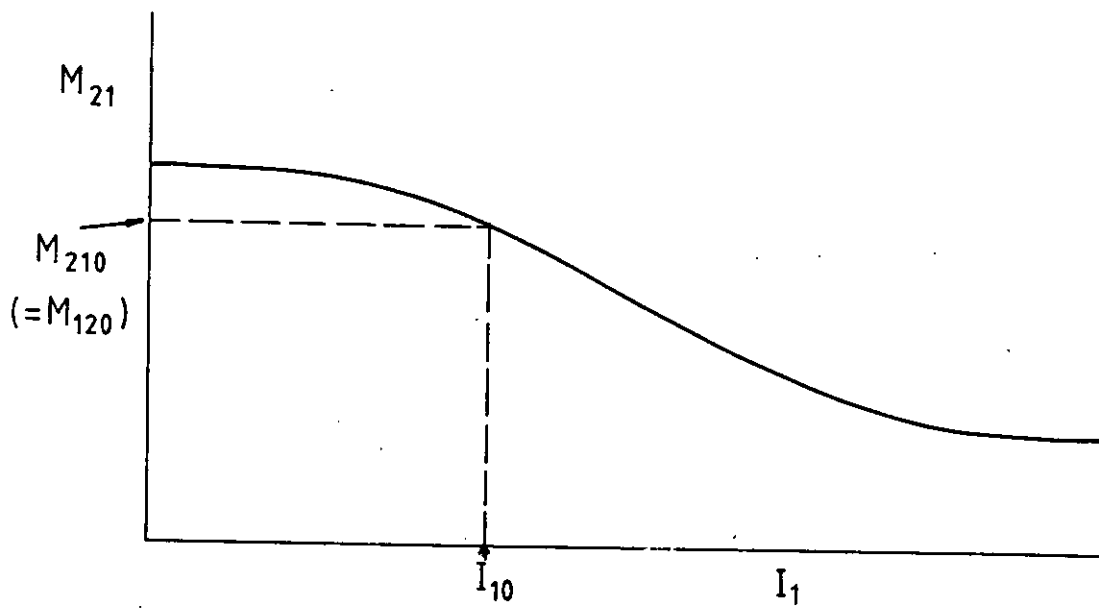


Figure A3.2(b) MUTUAL INDUCTANCE M_{21} AS A FUNCTION OF I_1

APPENDIX A4

MEASUREMENT OF MUTUAL INDUCTION BETWEEN TWO COILS HAVING A COMMON RESISTIVE PATH

It is common practice in synchronous generators for the phase windings to have their star point brought out via a single copper wire of relatively small resistance. In these circumstances no two phases of an armature winding are electrically isolated, and if the arrangement shown in Figure A4.1 is used to measure the mutual inductance between any two phases a considerable error in measurement is introduced by the voltage V_R . There are two methods of reducing the error due to V_R .

i) Method (1)

Consider switch S_1 closed and S_2 open, to establish the current I through coil. If S_2 is closed and S_1 is open simultaneously, the mutual inductance between windings 1 and 2 is given by

$$M_{12} = \frac{\int_0^{\infty} V_0 dt}{I} = \frac{c \cdot x}{I} \quad \text{A4.1}$$

If however there is a small time interval ΔT between closure of switch S_2 and opening of S_1

$$M_{12} = \frac{\int_0^{\infty} V_0 dt + RI \Delta T}{I} \neq \frac{c \cdot x}{I} \quad \text{A4.2}$$

This introduces an error term $RI \Delta T$, although it is possible to minimise this by making ΔT as small as possible.

If the ferromagnetic structure of the magnetic circuit exhibits a hysteresis effect, it is necessary to reverse the current I

in order to obtain a more accurate value of M_{12} . If S_2 is closed at $t=0$, followed by the reversal of current I after a time interval ΔT ,

$$\int_0^{\infty} V_o dt = -RI \Delta T + RI \int_{\Delta T}^{\infty} DT + 2I M_{12} \quad A4.3$$

The results show that the fluxmeter deflection is due to three components, resulting in a continuous movement of the light spot due to V_R . Any attempt to measure the deflection due to $2I M_{12}$ is always in error due to these additional components.

ii) Method (2)

The method that was used to measure the phases to phase mutual inductance employs a bridge circuit shown in Figure A4.2. If this is balanced such that under steady-state conditions V_o is zero and

$$\frac{R_1}{R} = \frac{R_2}{R_3} \quad A4.4$$

The measurement consists of closing S_1 to establish the current I through coil 1. Take the deflection of light spot position as zero with I established. Then open switch S_1 and measure the deflection (x_1), and close S_1 with supply reversed and measure the deflection (x_2).

It can be shown that

$$C.x_1 = -I M_{12} + \frac{(R_3 + R) L_{11} I}{(R + R_1 + R_2 + R_3)} \quad A4.5$$

$$C.x_2 = -I M_{12} + \frac{R I L_{11}}{(R + R_1)} \quad A4.6$$

If it is arranged so that $R_2 \gg R_1$ and $R_3 \gg R$, while still maintaining balanced bridge condition, adding equation A4.5 and A4.6 gives

$$M_{12} - L_{11} \left(\frac{R}{R + R_1} \right) = \frac{-C (x_1 + x_2)}{2I} \quad A4.7$$

Generally, if the resistance of the phase winding R_1 is very much greater than that of the wire used for bringing out the star point (R), the correction factor on the left hand side of the equation is small and under these circumstances

$$M_{12} = \frac{-C (x_1 + x_2)}{2I} \quad A4.8$$

The bridge circuit described fully compensates for V_R and steady-state deflections are found using the fluxmeter. Any integrating circuit can also be used with the bridge circuit in place of the fluxmeter.

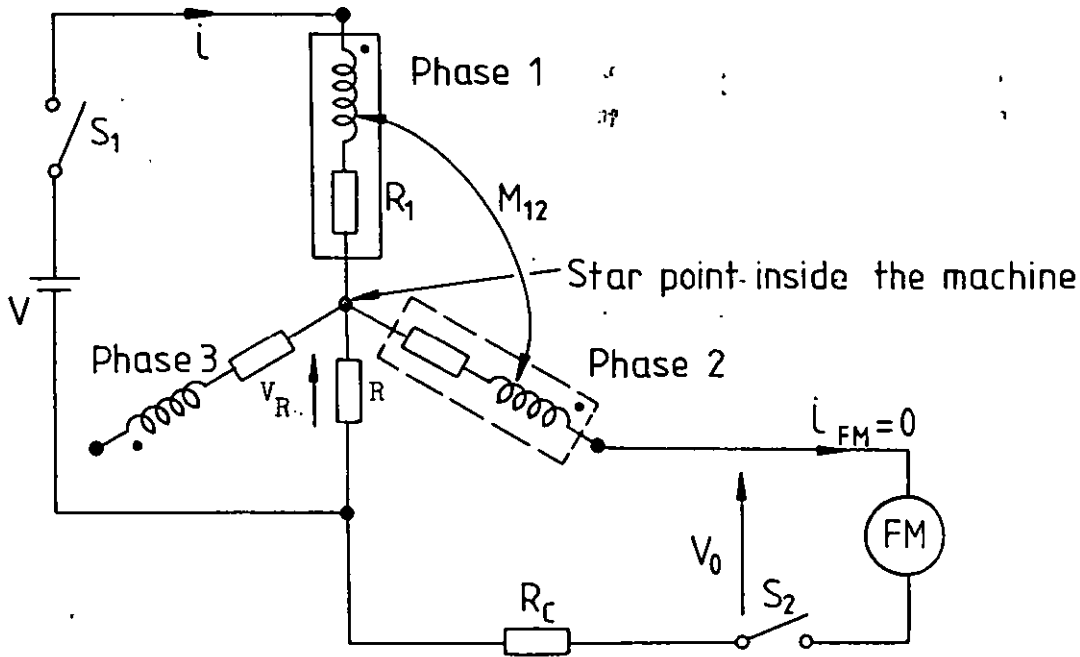


Figure A4.1 MEASURING PHASE TO PHASE MUTUAL INDUCTANCE OF A MACHINE WITH STAR CONNECTED PHASES

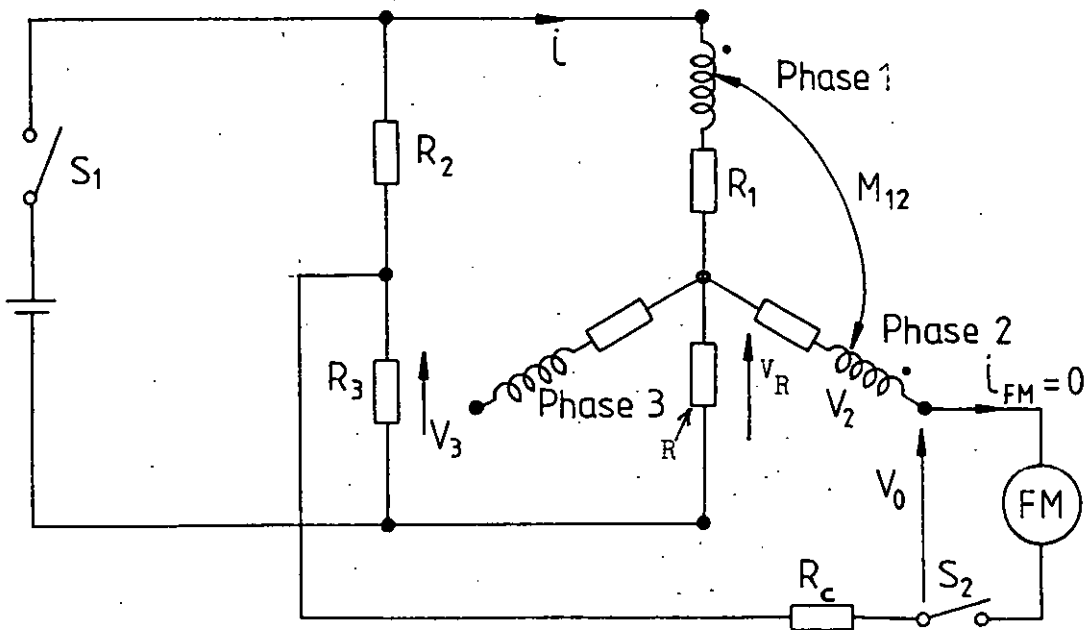


Figure A4.2 BRIDGE CIRCUIT FOR MEASURING PHASE TO PHASE MUTUAL INDUCTANCE

APPENDIX A5

A5.1 Computation of Operational Impedance Tensor $[Z_m]$

The independent impedance tensors $[L_n]$, $[G_n]$, $[R_n]$ are computed at each step during the numerical integration. To save computing time $[L_n]$ and $[G_n]$ are computed from equations 3.50, 3.51 or 3.56, 3.57 instead of performing a $[C_1]_t \cdot [Z_p][C_1]$ transformation at each step. To save computing time when obtaining $[Z_m] = [C_2]_t [Z_n][C_2]$, the following simplification to the actual multiplication is made.

$$[C_2] = \begin{bmatrix} [C_{21}] & [C_{22}] \\ [C_{23}] & [C_{24}] \end{bmatrix} \quad \text{A5.1.}$$

$$[C_2]_t = \begin{bmatrix} [C_{21}]_t & [C_{23}]_t \\ [C_{22}]_t & [C_{24}]_t \end{bmatrix} \quad \text{A5.2}$$

$$\text{Let } [Z_n] = \begin{bmatrix} [Z_{11n}] & [Z_{12n}] \\ [Z_{21n}] & [Z_{22n}] \end{bmatrix} \quad \text{A5.3}$$

Then

$$[Z_m] = \begin{bmatrix} [C_{21}]_t & [C_{23}]_t \\ [C_{22}]_t & [C_{24}]_t \end{bmatrix} \begin{bmatrix} [Z_{11n}][C_{21}] + [Z_{12n}] \cdot [C_{23}] & [Z_{11n}][C_{22}] + [Z_{12n}][C_{24}] \\ [Z_{21n}][C_{21}] + [Z_{22n}] \cdot [C_{23}] & [Z_{21n}][C_{22}] + [Z_{22n}][C_{24}] \end{bmatrix}$$

$$= \begin{bmatrix} [A] & [B] \\ [C] & [D] \end{bmatrix} \quad \text{A5.4}$$

where

$$\begin{aligned}
 [A] &= [C_{21}]_t \cdot \{ [Z_{11n}] \cdot [C_{21}] + [Z_{12n}] \cdot [C_{23}] \} \\
 &+ [C_{23}]_t \cdot \{ [Z_{21n}] \cdot [C_{21}] + [Z_{22n}] \cdot [C_{23}] \} \\
 [B] &= [C_{21}]_t \cdot \{ [Z_{11n}] \cdot [C_{22}] + [Z_{12n}] \cdot [C_{24}] \} \\
 &+ [C_{23}]_t \cdot \{ [Z_{21n}] \cdot [C_{22}] + [Z_{22n}] \cdot [C_{24}] \} \\
 [C] &= [C_{22}]_t \cdot \{ [Z_{11n}] \cdot [C_{21}] + [Z_{12n}] \cdot [C_{23}] \} \\
 &+ [C_{24}]_t \cdot \{ [Z_{21n}] \cdot [C_{21}] + [Z_{22n}] \cdot [C_{23}] \} \\
 [D] &= [C_{22}]_t \cdot \{ [Z_{11n}] \cdot [C_{22}] + [Z_{12n}] \cdot [C_{24}] \} \\
 &+ [C_{24}]_t \cdot \{ [Z_{21n}] \cdot [C_{22}] + [Z_{22n}] \cdot [C_{24}] \}
 \end{aligned} \tag{A5.5}$$

Referring to equation 3.59

$$\begin{aligned}
 [C_{22}] &= [0] \\
 [C_{23}] &= [0] \\
 [C_{21}] &= [I]
 \end{aligned} \tag{A5.6}$$

Therefore

$$\begin{aligned}
 [C_{22}]_t &= [0] \\
 [C_{23}]_t &= [0] \\
 [C_{21}]_t &= [0]
 \end{aligned}$$

Substituting results of equations A5.6 into equations A5.5 gives

$$\begin{aligned}
 [A] &= [Z_{11n}] \\
 [B] &= [Z_{12n}] \cdot [C_{24}] \\
 [C] &= [C_{24}]_t \cdot [Z_{21n}] \\
 [D] &= [C_{24}]_t \cdot [Z_{22n}] \cdot [C_{24}]
 \end{aligned} \tag{A5.7}$$

Matrix $[C_{24}]$ is computed at each step and $[Z_m]$ is obtained using equations A5.7.

A5.2 Computation of Independent Currents $[I_n]$ from Computed Values of $[I_m]$

$[I_n] = [C_2][I_m]$ can be written as

$$\begin{bmatrix} [I_{1n}] \\ [I_{2n}] \end{bmatrix} = \begin{bmatrix} [C_{21}] & [C_{22}] \\ [C_{23}] & [C_{24}] \end{bmatrix} \begin{bmatrix} [I_{1m}] \\ [I_{2m}] \end{bmatrix} \quad \text{A5.8}$$

as $[C_{21}] = [I]$

$[C_{22}] = [0]$

$[C_{23}] = [0]$

equation A5.8 becomes

$$\begin{bmatrix} [I_{1n}] \\ [I_{2n}] \end{bmatrix} = \begin{bmatrix} [I_{1m}] \\ [C_{24}] \cdot [I_{2m}] \end{bmatrix} \quad \text{A5.9}$$

The independent currents $[I_n]$ are obtained by using equation A5.9

A5.3 Computation of Diode Currents

Having obtained $[I_{2n}]$, the diode currents $[I_D]$ are obtained from equation A5.10

$$[I_D] = [C_{14'}][I_{2n}] \quad \text{A5.10}$$

A5.4 Computation of the Voltages Across the Diodes $[V_D]$

The computation of the diode voltage is in two steps:

- i) $[VY]$ is computed from $[VX]$ where

$$[VX] = [V_n] - \{[R_n] + [G_n]\} \cdot [I_n] - [L]_n [pI_n] \quad A5.11$$

If

$$[VX] = \begin{bmatrix} [VX_1] \\ [VX_2] \end{bmatrix}$$

$[VY] = [VX_2]$ as $[VX_2]$ is $\Sigma(V - ZI)$ around the diode conduction paths.

- ii) The diode voltages $[V_D]$ are found using values of $[VY]$.
(The diode voltages in the lower limits are reversed for test purposes).

APPENDIX A6
NUMERICAL METHODS FOR THE SOLUTION OF THE
DIFFERENTIAL EQUATIONS ON A DIGITAL COMPUTER

A Taylor Series expansion can be used in the solution of many of the differential equations associated with electrical systems. The solution of the differential equation of the form $y' = f(x,y)$, at the $(n+1)$ th point is given by

$$y_{n+1} = y_n + h y'_n + h^2 \frac{y''_n}{2!} + h^3 \frac{y'''_n}{3!} + \dots \quad A6.1$$

where $y'_n = \frac{d y_n}{dx}$

$$y''_n = \frac{d^2 y}{dx^2}$$

$$y'''_n = \frac{d^3 y}{dx^3}$$

This method is of little practical value, due to the difficulty of calculating the higher derivatives. The most generally used numerical method for solution of the differential equations, is the fourth-order Runge Kutta method.

A6.1 Runge-Kutta Methods

The Runge-Kutta methods are based on the solution of the differential equations by means of successive substitutions. They approximate to the Taylor Series solution without requiring the evaluation of any derivative beyond the first. The general form of Runge-Kutta method is given in references 77-79 .

The fourth-order Runge-Kutta formula for solving the differential equation $y' = f(x,y)$ is

$$y_{n+1} - y_n = \frac{1}{6} (K_1 + 2K_2 + 2K_3 + K_4) \quad A6.2$$

where

$$K_1 = h \cdot f(x_n, y_n) \quad A6.3$$

$$K_2 = h.f \left(x_n + \frac{1}{2} h, y_n + \frac{1}{2} K_1 \right) \quad A6.4$$

$$K_3 = h.f \left(x_n + \frac{1}{2} h, y_n + \frac{1}{2} K_2 \right) \quad A6.5$$

$$K_4 = h.f \left(x_n + h, y_n + K_3 \right) \quad A6.6$$

The fourth-order Runge-Kutta method was used for the solution of most of the differential equations described in the thesis.

Gill⁸⁰ and Ralston⁸¹ have suggested methods for reducing the memory space required and the truncation errors respectively, by modifying the fourth-order Runge-Kutta solution.

Predictor-corrector methods^{82,83} can also be used for the numerical solutions of differential equations, but because they require a knowledge of previous points of the solution, they are not self starting, and other methods (such as the Runge-Kutta method) have to be used to start the solution. They are therefore not suitable for the solution of networks involving change of topology in this thesis.

APPENDIX A7STATE VARIABLE MODEL OF AVR
(DIGITAL COMPUTER PROGRAM)

A7.1: The digital computer program for obtaining the response of the Automatic Voltage Regulator (AVR) to changes in the terminal voltages of the generator is given on pages 316 to 319. The differential equations in the state variable form, as discussed in Chapter 4 are used.

JOB AVR4PLOT,FLPP,VVV3295
 FORTRAN ,PDS
 JOBCORE 45K
 VOLUME 15000
 RUN ,990

FORTRAN COMPILATION BY #XFAT MK SB DATE 19/03/79 TIME 21/26/10

0001 SEND TO (ED,SEMICOMPUSER,AXXX)
 0002 DUMP ON (ED,PROGRAM USER)
 0003 WORK (ED,WORKFILEUSER)
 0004 RUN
 0005
 0006 LIBRARY (ED,SUBGROUPGINO)
 0007 PROGRAM(MAVR1)
 0008 OUTPUT 2=LPO
 0009 COMPRESS INTEGER AND LOGICAL
 0010 TRACE 0
 0011 END

0012 MASTER ANALYSIS
 0013 CAVR TRANSIENT PERFORMANCE
 0014 DIMENSION TT(1500),A1(1500),A2(1500),A3(1500),A4(1500)
 0015 DIMENSION A5(1500),A6(1500),A7(1500)
 0016 R1=5.0E3
 0017 C2=0.1E-6
 0018 R3=150.0E3
 0019 R4=20.0E3
 0020 R5=4.7E6
 0021 R6=5.1E3
 0022 C7=0.47E-6
 0023 R8=R1+R3
 0024 R9=R5+R6
 0025 R10=75.0E3
 0026 R11=24.3E3
 0027 R12=5.11E3
 0028 C13=0.033E-6
 0029 C14=0.22E-6
 0030 VPEAK=150.0
 0031 VDC=60.0
 0032 PI=3.14159
 0033 F=400.0
 0034 OMEGA=2*PI*F
 0035 H=1.66666/E-5
 0036 TL=1.00001
 0037 T1=1.0/(C2*R8)
 0038 T2,T5=T1
 0039 T3=1.0/(C7*R8)
 0040 T4=1.0/C7*(1.0/R4+1.0/R8+1.0/R9)
 0041 T6=T3
 0042 T7=1.0/(C7*R4)

```

043      T8=1.0/(C15*R10) 317
044      T9=1.0/(C15*R11)
045      T10=1.0/(C14*R11)
046      T11=1.0/(C14*R12)+T10
047      T12=T8
048      TA=0.25
049      TB=0.050
050      TC=0.075
051      TD=0.100
052      JJ=0
053      TZ1=0.50
054      VIX,XV=0.0
055      XO,XY,V2X,V7X,V13X,V14X,V00,VXX=0.0
056      V2,V7,V13,V14,V,V70,V20,V130,V140,U8=0.0
057      M=0
058 700 CONTINUE
059      IF(T.GT.TL) GO TO 99
060      VA=VPEAK*SIN(OMEGA*T)
061      TX=2.0*PI/3.0/OMEGA
062      TY=4.0*PI/3.0/OMEGA
063      IF(T.LE.TX)VB=0.0
064      IF(T.GT.TX)VB=VPEAK*SIN(OMEGA*(T-TX))
065      IF(T.LE.TY)VC=0.0
066      IF(T.GT.TY)VC=VPEAK*SIN(OMEGA*(T-TY))
067      IF(VA.GT.VB)V=VA
068      IF(VA.LT.VB)V=VB
069      IF(VA.EQ.VB)V=VA
070      IF(V.LE.VC)V=VC
071      VREF=-6.5
072      VS=(VREF+V14)/2.0
073      U8=(VS-V7-V2)/R8
074      VX=VS-U8*R1-V7*R6/R9
075      IF(VX.LT.0,0)V0=VDC
076      IF(VX.GE.0,0)V0=0.0
077 600 CONTINUE
078      DV2=-T1+V2-T2*V7+T5*VS
079      DV7=-T3+V2-T4*V7+T6*VS+T7*V0
080      DV13=-T8+V13-T9*V13+T9*V14+T12*V
081      DV14=T10+V13-T11*V14
082      M=M+1
083      IF(M.GE.5) GO TO 99
084      GO TO (100,101,102,103),M
085 100 CONTINUE
086      DV21=H*DV2
087      DV71=H*DV7
088      DV131=H*DV13
089      DV141=H*DV14
090      V2=V20+DV21*0.5
091      V7=V70+DV71*0.5
092      V13=V130+DV131*0.5
093      V14=V140+DV141*0.5
094      T=T+0.5*H
095      GO TO 700
096 101 CONTINUE
097      DV22=H*DV2
098      DV72=H*DV7
099      DV132=H*DV13
100      DV142=H*DV14
101      V2=V20+DV22*0.5
102      V7=V70+DV72*0.5
103      V13=V130+DV132*0.5
104      V14=V140+DV142*0.5

```

```

105      GO TO 600
106      CONTINUE
107      DV23=H*DV2
108      DV73=H*DV7
109      DV133=H*DV13
110      DV143=H*DV14
111      V2=V20+DV23
112      V7=V70+DV73
113      V13=V130+DV133
114      V14=V140+DV143
115      T=T+0.5*H
116      GO TO 700
103      CONTINUE
118      DV24=H*DV2
119      DV74=H*DV7
120      DV134=H*DV13
121      DV144=H*DV14
122      DV20=(DV21+2.0*DV22+2.0*DV23+DV24)/6.0
123      DV70=(DV71+2.0*DV72+2.0*DV73+DV74)/6.0
124      DV130=(DV131+2.0*DV132+2.0*DV133+DV134)/6.0
125      DV140=(DV141+2.0*DV142+2.0*DV143+DV144)/6.0
126      V20=V20+DV20
127      V70=V70+DV70
128      V130=V130+DV130
129      V140=V140+DV140
130      X0=X0+1.000
131      VIX=VIX+V
132      V00=V00+V0
133      VXX=VXX+VX
134      NX=X0/50.0
135      XNX=FLOAT(NX)
136      X1=X0-XNX*50.0
137      V2X=V2X+V20
138      V7X=V7X+V70
139      V13X=V13X+V130
140      V14X=V14X+V140
141      IF (ABS(X1).LT.1.0E-6) GO TO 400
142      GO TO 401
400      CONTINUE
144      JJ=JJ+1
145      XY=XY+1.00
146      XX1=50.0
147      XV=VIX/XX1
148      XV2=V2X/XX1
149      XV7=V7X/XX1
150      XV13=V13X/XX1
151      XV14=V14X/XX1
152      XV0=V00/XX1
153      VXV=VXX/XX1
154      TZ2=T
155      TT(JJ)=(TZ2+TZ1)/2.0
156      A1(JJ)=XV
157      A2(JJ)=XV13
158      A3(JJ)=XV14
159      A4(JJ)=XV7
160      A5(JJ)=XV2
161      A6(JJ)=XVX
162      A7(JJ)=XV0
163      TZ1=TZ2
164      WRITE(2,999)XY,XV2,XV7,XV13,XV14,VXV,XV0,XV
165      V2X,V7X,V13X,V14X,V00,VXX=0.0
166      VIX=0.0

```

```

167 401 CONTINUE
168 V2=V20 319
169 V7=V70
170 V13=V130
171 V14=V140
172 M=0
173 IF (ABS(T-TA).LT.1.0E-6) GO TO 201
174 GO TO 600
175 999 FORMAT(1H0 ,12F10.5)
176 201 CONTINUE
177 VPEAK=164.5
178 GO TO 600
179 99 CONTINUE
180 CALL LU1934
181 CALL UNITS(1,0)
182 CALL WINDOW(2)
183 CALL DEVPAP(500,200,1)
184 CALL AXISCA(3,10,0.,1.00,1)
185 CALL AXISCA(3,10,0.,200.,2)
186 CALL AXIDRA(1,1,1)
187 CALL AXIDRA(-1,-1,2)
188 CALL GRAPOL(TT,A1,JJ)
189 CALL PICCLE
190 CALL AXISCA(3,10,0.,50.,2)
191 CALL AXIDRA(1,1,1)
192 CALL AXIDRA(-1,-1,2)
193 CALL GRAPOL(TT,A2,JJ)
194 CALL PICCLE
195 CALL AXISCA(3,10,0.,10.,2)
196 CALL AXIDRA(1,1,1)
197 CALL AXIDRA(-1,-1,2)
198 CALL GRAPOL(TT,A3,JJ)
199 CALL PICCLE
200 CALL AXISCA(3,6,0.,60.,2)
201 CALL AXIDRA(1,1,1)
202 CALL AXIDRA(-1,-1,2)
203 CALL GRAPOL(TT,A4,JJ)
204 CALL PICCLE
205 CALL AXISCA(2,6,0.,-60.,2)
206 CALL AXIDRA(1,1,1)
207 CALL AXIDRA(-1,-1,2)
208 CALL GRAPOL(TT,A5,JJ)
209 CALL PICCLE
210 CALL AXISCA(2,10,-0.5,0.5,2)
211 CALL AXIDRA(1,1,1)
212 CALL AXIDRA(-1,-1,2)
213 CALL GRAPOL(TT,A6,JJ)
214 CALL PICCLE
215 CALL AXISCA(2,6,0.,60.,2)
216 CALL AXIDRA(1,1,1)
217 CALL AXIDRA(-1,-1,2)
218 CALL GRAPOL(TT,A7,JJ)
219 CALL PICCLE
220 CALL DEVEND
221 STOP
222 END

```


A7.2 Calculation of non-linear gain of the AVR for use in transfer function model of AVR

The digital computer program for obtaining the response of the AVR to changes in the terminal voltage of the generator given in Section A7.1 was used to obtain the effective non-linear gain of the AVR. Figure A7.1 shows the change in the voltage applied to the voltage sensing circuit following a step change in the terminal voltage (phase voltage) of the generator from 150 V (peak) to 164.5 V (peak). Figures A7.2, A7.3, A7.4 and A7.5 show the corresponding changes in the state variables of the AVR. Figure A7.6 shows the change in the voltage difference ($V_X - V_Y$) applied to the amplifier A and Figure A7.7 shows the corresponding change in the output voltage (V_O) of the amplifier, which is the voltage applied to the exciter field winding.

It can be seen from Figures A7.6 and A7.7 that there is a large change in the output voltage for small changes in the voltage difference ($V_X - V_Y$) from 0 volts. Figure A7.8 shows the output voltage V_O as a function of difference voltage $V_X - V_Y$ for different generator terminal voltage changes. When the terminal voltage is far below the reference voltage (162 V peak), the output voltage V_O is 60 V (i.e. the full rectified PMG voltage is applied to the exciter field winding). When the terminal voltage is far above the reference voltage, the output voltage V_O is zero, (i.e. the voltage applied to the exciter field winding is zero). The output voltage V_O is anywhere between zero and full volts for small changes in the terminal voltage (typically 1-2 V) about its reference voltage.

Referring to Figure 4.1

$$V_{E2} = \frac{V_S + V_{REF(-)}}{2} + V_{F1} - V_{F2} \quad \text{A7.1}$$

Differentiating equation A7.1,

$$\dot{V}_{E2} = \frac{\dot{V}_S}{2} + \dot{V}_{F1} + \dot{V}_{F2} \quad (\text{as } V_{REF(-)} \text{ is constant}) \quad \text{A7.2}$$

Since V_o is the voltage applied to the exciter field winding (V_{FE})

$$V_{FE} = V_o \quad A7.3$$

and the difference voltage applied to the non-linear amplifier is V_{E2} , therefore

$$V_{E2} = V_X - V_Y \quad A7.4$$

Since the shape of the V_o V/S ($V_X - V_Y$) graph is of the arctan form, the approximate gain curve given in Figure A7.8 was obtained as

$$V_{FE} = \frac{V_{DC}}{\pi} \left[\frac{\pi}{2} - A \tan \left(\frac{V_{E2}}{A} \right) \right] \quad A7.5$$

where V_{DC} = rectified output voltage of PMG (= 60 V)

$$A = 5.7735 \times 10^{-3} \text{ (constant)}$$

Differentiating equation A7.5 gives

$$\dot{V}_{FE} = \frac{V_{DC}}{\pi} \cdot A \cdot \dot{V}_{E2} \cdot \left[\frac{1}{A^2 + V_{E2}^2} \right] \quad A7.6$$

Equations A7.1, A7.2, A7.5, A7.6 are used to obtain the effective non-linear gain of AVR in the transfer function model of the AVR.

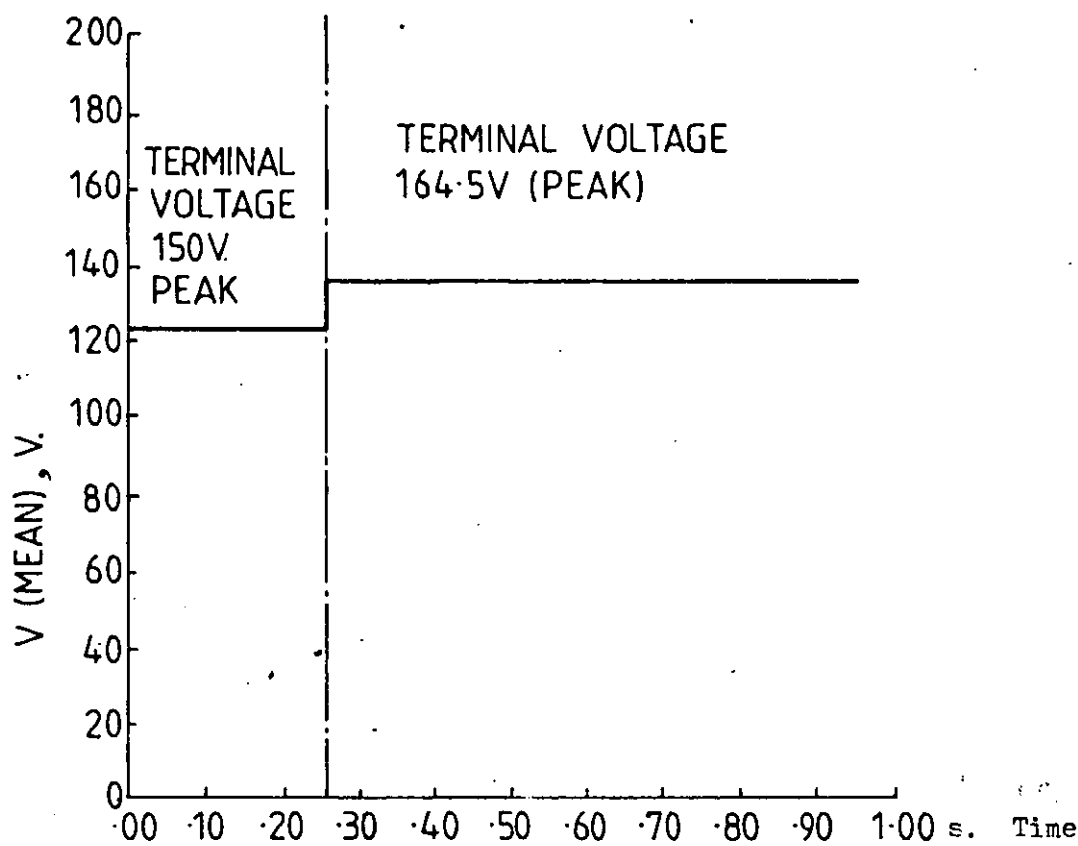


Figure A7.1 VOLTAGE (V) APPLIED TO VOLTAGE SENSING CIRCUIT

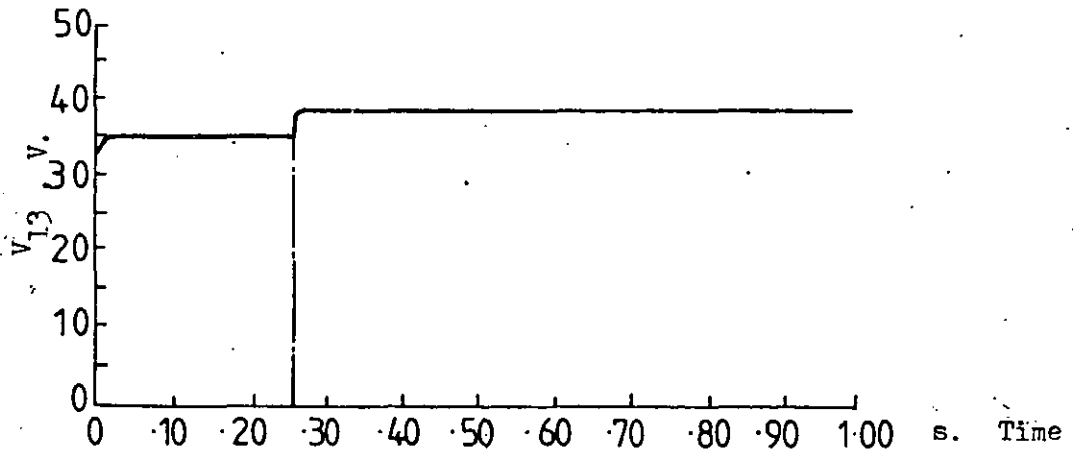


Figure A7.2 VOLTAGE ACROSS CAPACITOR C_{13}

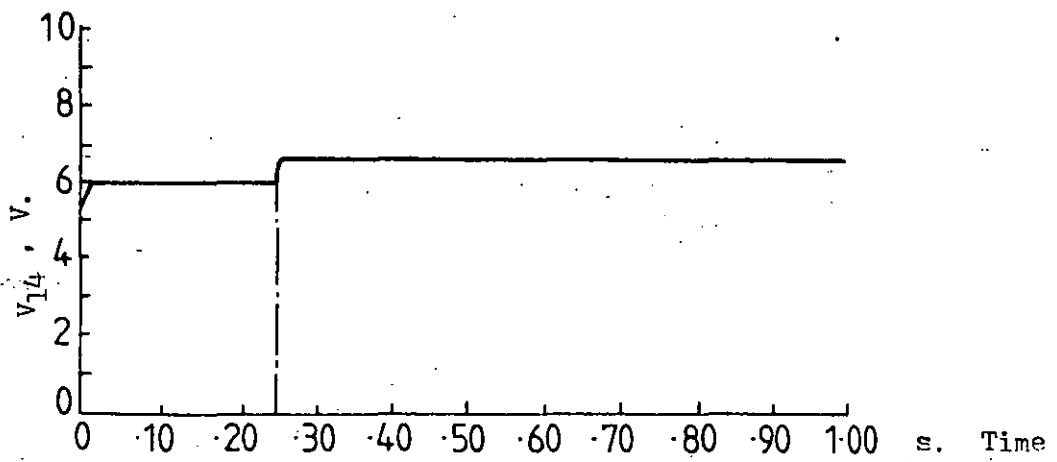


Figure A7.3 VOLTAGE ACROSS CAPACITOR C_{14}

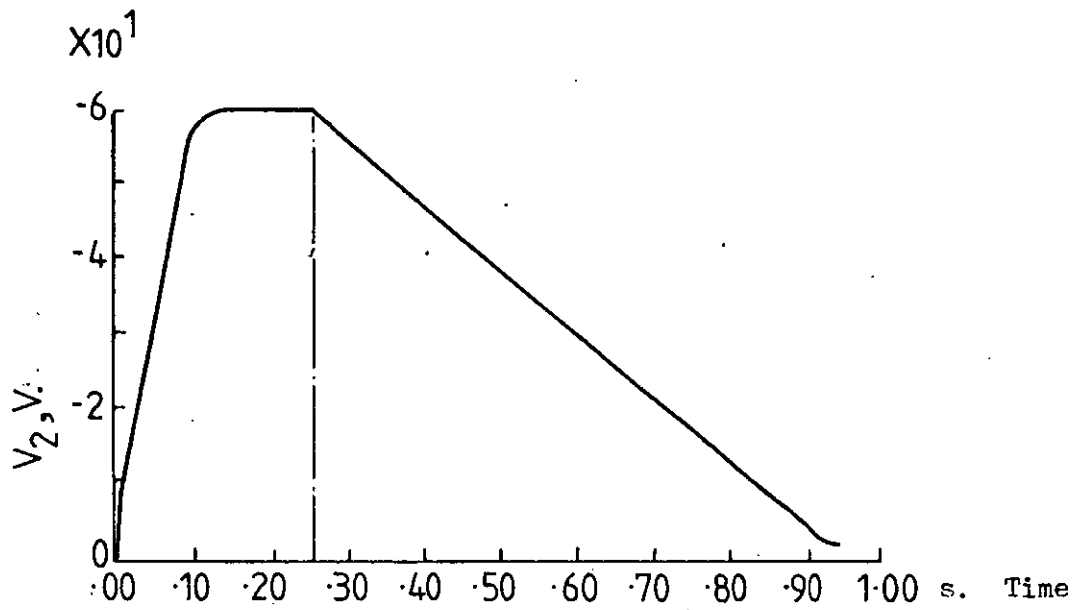


Figure A7.4 VOLTAGE ACROSS CAPACITOR C_2

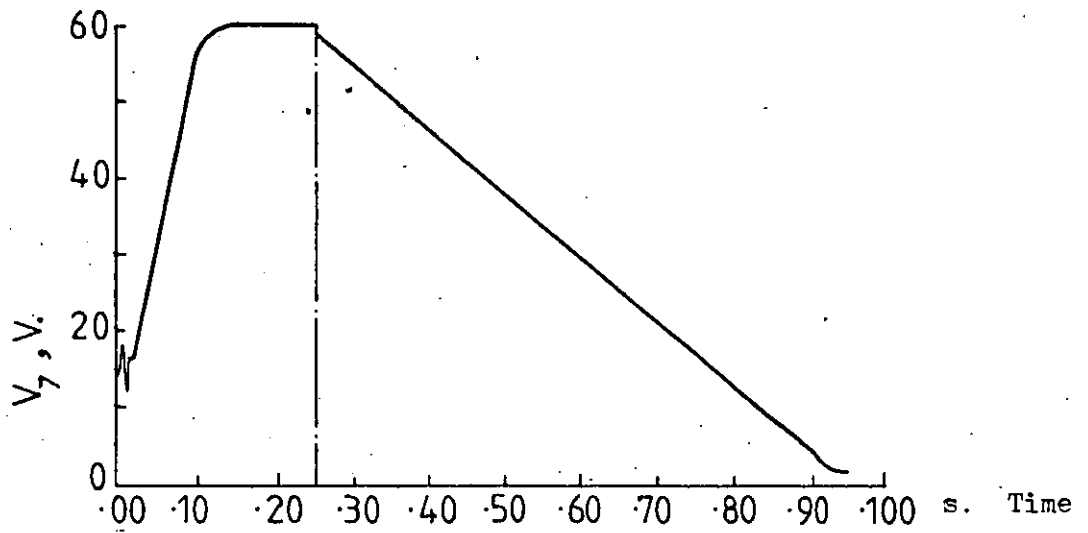


Figure A7.5 VOLTAGE ACROSS CAPACITOR C_7

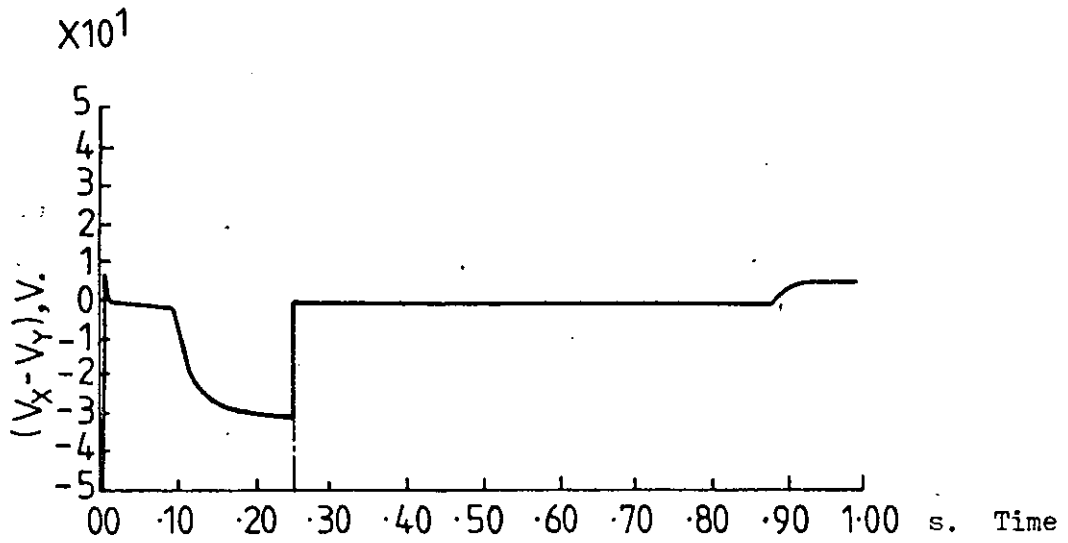


Figure A7.6 VOLTAGE DIFFERENCE ($V_x - V_y$)

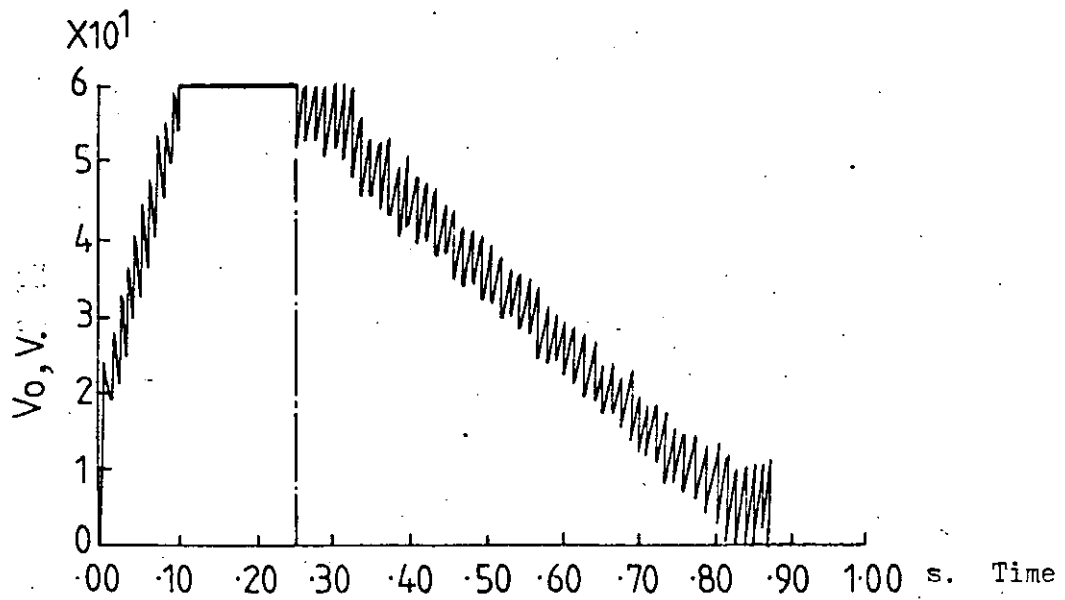


Figure A7.7 A.V.R. OUTPUT VOLTAGE

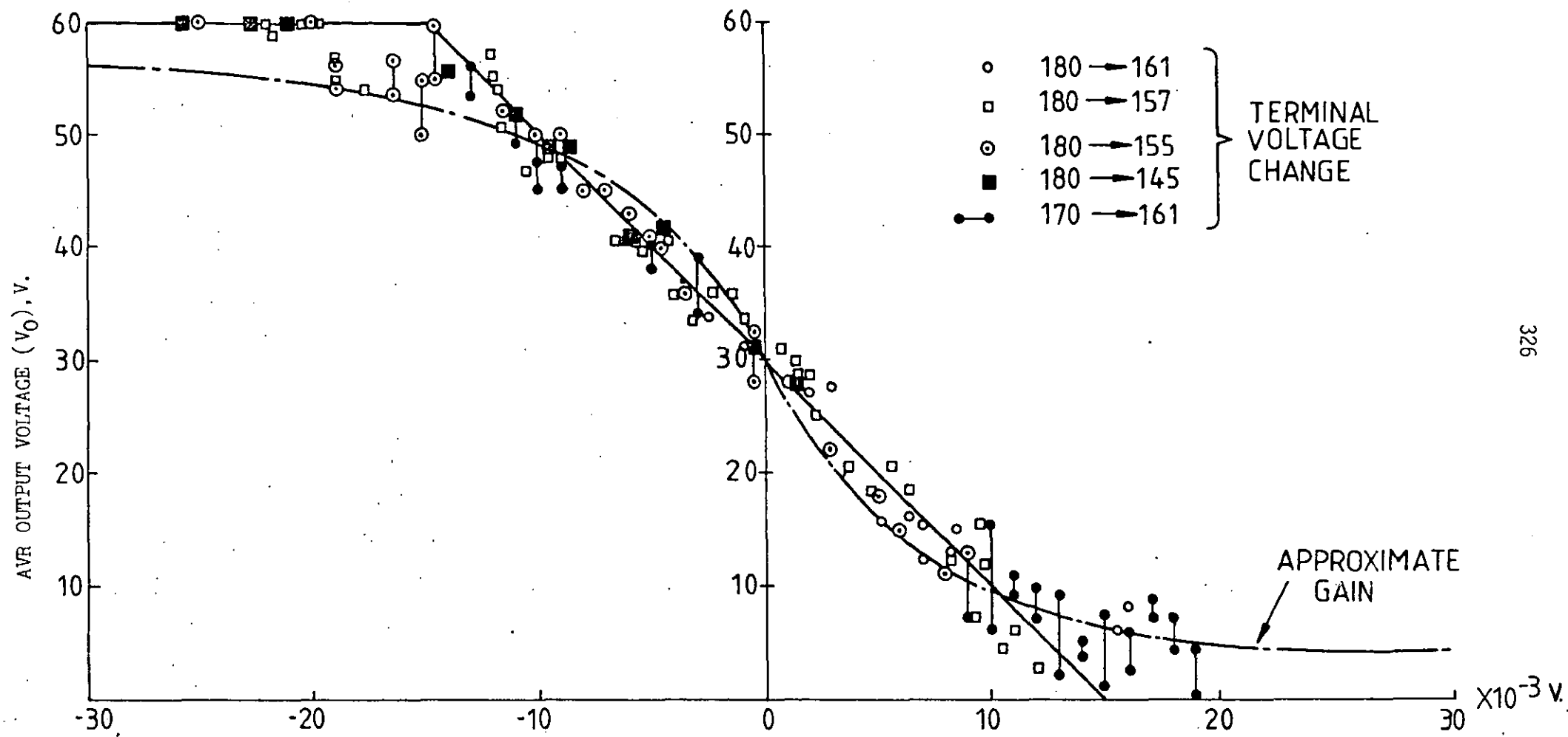


Figure A7.8 A.V.R. OUTPUT VOLTAGE V/S $(V_x - V_y)$ VOLTS

$$V_x - V_y = V_{E2}$$

APPENDIX A8
TRANSFER FUNCTION ANALYSIS OF AVR

A8.1 Voltage Sensing Circuit

The effective voltage applied to the voltage sensing circuit is as shown in Figure A8.1(a), and the transfer function of the circuit may be deduced as:

$$\frac{V_s}{V_m} = \frac{Z_2 Z_4}{Z_1 (Z_2 + Z_3 + Z_4) + Z_2 (Z_3 + Z_4)} \quad \text{A8.1}$$

where V_s is the mean output voltage of the voltage sensing circuit, and V_m is the mean voltage applied to the voltage sensing circuit. In terms of the individual components of this circuit

$$\frac{V_s}{V_m} = \frac{R_{12}}{R_{10}R_{11}R_{12}C_{13}C_{15}s^2 + [R_{10}(R_{11}+R_{12})C_{13} + R_{12}(R_{10}+R_{11})C_{14}]s + (R_{10}+R_{11}+R_{12})} \quad \text{A8.2}$$

Substituting the values of resistances and capacitances given in Figure 4.4(a)

$$\frac{V_s}{V_m} = \frac{4.89417 \times 10^{-2}}{(0.64754 \times 10^{-6} s^2 + 1.76631 \times 10^{-3} s + 1)} \quad \text{A8.3}$$

In terms of the peak line to neutral voltage V_T ,

$$\frac{V_s}{V_T} = \frac{4.0475 \times 10^{-2}}{(0.64754 \times 10^{-6} s^2 + 1.76631 \times 10^{-3} s + 1)} \quad \text{A8.4}$$

as $\frac{V_m}{V_T} = 0.827$.

If the denominator of equation A8.3 is factorised this equation can be written as

$$\frac{V_s}{V_T} = \frac{K_R}{(1 + sT_{R1})(1 + sT_{R2})} \quad \text{A8.5}$$

where

$$K_R = 4.0475 \times 10^{-2} \quad \text{A8.6(a)}$$

$$T_{R1}T_{R2} = 0.64754 \times 10^{-6} \text{ s}^2 \quad \text{A8.6(b)}$$

$$T_{R1} + T_{R2} = 1.76631 \times 10^{-3} \text{ s} \quad \text{A8.6(c)}$$

The peak value of the line to neutral voltage on application or rejection of a balanced load is obtained from the instantaneous values of phase voltages as

$$V_D = \frac{2}{3} [(V_R \cos(\theta_R) + V_Y \cos(\theta_R - 2\pi/3) + V_B \cos(\theta_R + 2\pi/3))] \quad \text{A8.7(a)}$$

$$V_Q = \frac{2}{3} [(V_R \sin(\theta_R) + V_Y \sin(\theta_R - 2\pi/3) + V_B \sin(\theta_R + 2\pi/3))] \quad \text{A8.7(b)}$$

$$V_T = \sqrt{V_D^2 + V_Q^2} \quad \text{A8.7(c)}$$

Use of equations A8.7 eliminates the need to include the variation of the individual phase voltage, as V_T gives the envelope of the peak line to neutral voltage as this changes in time.

A8.2 Negative Feedback Circuit

The mean voltage applied to the field winding is V_{FE} as shown in Figure A8.2(a). The feedback RC-network can be represented as in Figure A8.2(b).

The values of the resistances are:

$$R_9 = R_5 + R_6 = 4.7 \times 10^6 + 5.1 \times 10^3 = 4.7051 \times 10^6 \Omega$$

$$R_4 = 20 \times 10^3 \Omega$$

$$R_8 = R_1 + R_3 = 5 \times 10^3 + 150 \times 10^3 = 0.155 \times 10^6 \Omega$$

Since $R_9 \gg R_8$ and $R_9 \gg R_4$, the resistance R_9 is effectively a potential divider to give the positive feedback voltage V_{F2} ; also since the input impedance of the operational amplifier is very high ($> 10^6 \Omega$) the corresponding current input is negligible. This reduces the feedback circuit to that shown in Figure A8.2(c).

The resulting equations which apply for this simplified network are

$$Z = \frac{R_4}{(1 + s R_4 C_7)} \quad \text{A8.8}$$

$$V = \frac{V_{FE}}{(1 + s R_4 C_7)} \quad \text{A8.9}$$

$$I_1 = \frac{V_{E1} - V_X}{R_1} \quad \text{A8.10}$$

and

$$I_2 = \frac{V - V_X}{Z + \frac{1}{sC_2} + R_3} \quad \text{A8.11}$$

Substituting for Z and V from equations A8.8 and A8.9 into equation A8.11 gives

$$I_2 = \frac{V_{FE} sC_2 - V_X sC_2 (1 + sR_4C_7)}{(R_3R_4C_2C_7 s^2 + (R_4C_2 + R_3C_2 + R_4C_7) s + 1)} \quad \text{A8.12}$$

Since $I_1 + I_2 = 0$, as the current input to the operational amplifier is negligible, addition of equation A8.10 and A8.12 gives

$$\frac{V_{E1} - V_X}{R_1} + \frac{V_{FE} s C_2 - V_X s C_2 (1 + s R_4 C_7)}{(R_3 R_4 C_2 C_7 s^2 + (R_4 C_2 + R_3 C_2 + R_4 C_7) s + 1)} = 0 \quad A8.13$$

$$\begin{aligned} \frac{V_X}{R_1} + \frac{V_X s C_2 (1 + s R_4 C_7)}{[R_3 R_4 C_2 C_7 s^2 + (R_4 C_2 + R_3 C_2 + R_4 C_7) s + 1]} \\ = \frac{V_{E1}}{R_1} + \frac{V_{FE} s C_2}{[(R_3 R_4 C_2 C_7 s^2 + (R_4 C_2 + R_3 C_2 + R_4 C_7) s + 1)]} \end{aligned} \quad A8.14$$

On multiplying both sides of equation A8.14 by R_1 , substituting the values of the components and then simplifying, it is found that

$$\frac{V_X s C_2 R_1 (1 + s R_4 C_7)}{[R_3 R_4 C_2 C_7 s^2 + (R_4 C_2 + R_3 C_2 + R_4 C_7) s + 1]} = \frac{6.45 \times 10^{-6} V_X s (s + 106.4)}{(s + 51.58)(s + 133.05)} \ll V_X \quad A8.15$$

$$V_X = V_{E1} + V_{FE} \cdot \frac{0.5 \times 10^{-3} s}{(145.7 \times 10^{-6} s^2 + 26.9 \times 10^{-3} s + 1)} \quad A8.16$$

Therefore

$$V_{F1} = V_{FE} \cdot \frac{0.5 \times 10^{-3} s}{(145.7 \times 10^{-6} s^2 + 26.9 \times 10^{-3} s + 1)} \quad A8.17$$

$$\frac{V_{F1}}{V_{FE}} = \frac{K_F s}{(1 + s T_{F1})(1 + s T_{F2})} \quad A8.18$$

where

$$K_F = 0.5 \times 10^{-3} \text{ s}^{-1} \quad \text{A8.19(a)}$$

$$T_{F1} T_{F2} = 145.7 \times 10^{-6} \text{ s}^2 \quad \text{A8.19(b)}$$

$$T_{F1} + T_{F2} = 26.9 \times 10^{-3} \text{ s} \quad \text{A8.19(c)}$$

A8.3 Positive Feedback Circuit

The positive feedback voltage V_{F2} is obtained by calculating the voltage V_C across capacitor C_7 (referring to Figure A8.2(c)). As $V_X = 0$ (virtual earth potential),

$$\begin{aligned} V_C &= \frac{V}{Z + \frac{1}{sC_2} + R_3} \left(\frac{1}{sC_2} + R_3 \right) \\ &= \frac{V_{FE}}{(1 + sR_4C_7)} \cdot \frac{(1 + sR_3C_2)}{sC_2} \cdot \frac{1}{\left[\frac{R_4}{(1 + sR_4C_7)} + \frac{(1 + sR_3C_2)}{sC_2} \right]} \\ &= \frac{V_{FE} (1 + sR_3C_2)}{[R_4sC_2 + (1 + sR_4C_7)(1 + sR_3C_2)]} \quad \text{A8.20} \end{aligned}$$

Therefore

$$V_C = \frac{V_{FE} (1 + sR_3C_2)}{(1 + s(R_4C_7 + R_3C_2 + R_4C_2) + s^2 R_3R_4C_2C_7)} \quad \text{A8.21}$$

$$\text{hence: } V_{F2} = \left(\frac{R_6}{R_5 + R_6} \right) \frac{V_{FE} (1 + sR_3C_2)}{(1 + s(R_4C_7 + R_3C_2 + R_4C_2) + s^2 R_3R_4C_2C_7)}$$

A8.22

Substituting the values of resistances and capacitances in equation A8.22 and simplifying gives

$$\frac{V_{F2}}{V_{FE}} = \frac{K_1 (1 + sT_{A1})}{(1 + sT_{F1})(1 + sT_{F2})} \quad \text{A8.23}$$

$$\text{where } K_1 = 1.084 \times 10^{-3} \quad \text{A8.24(a)}$$

$$T_{A1} = 0.0150 \text{ s} \quad \text{A8.24(b)}$$

and T_{F1} , T_{F2} are given in equations A8.19(a) and (b).

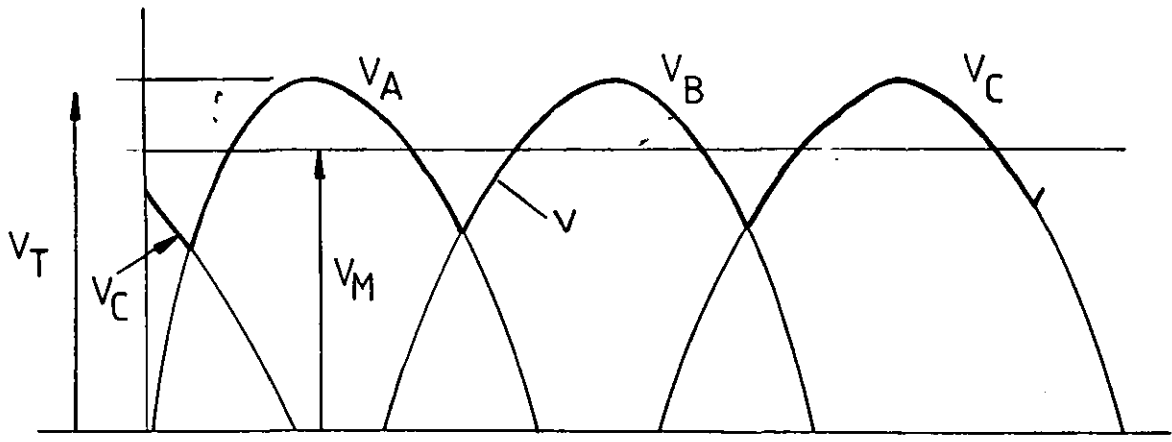


Figure A8.1(a) VOLTAGE APPLIED TO AVR VOLTAGE SENSING CIRCUIT

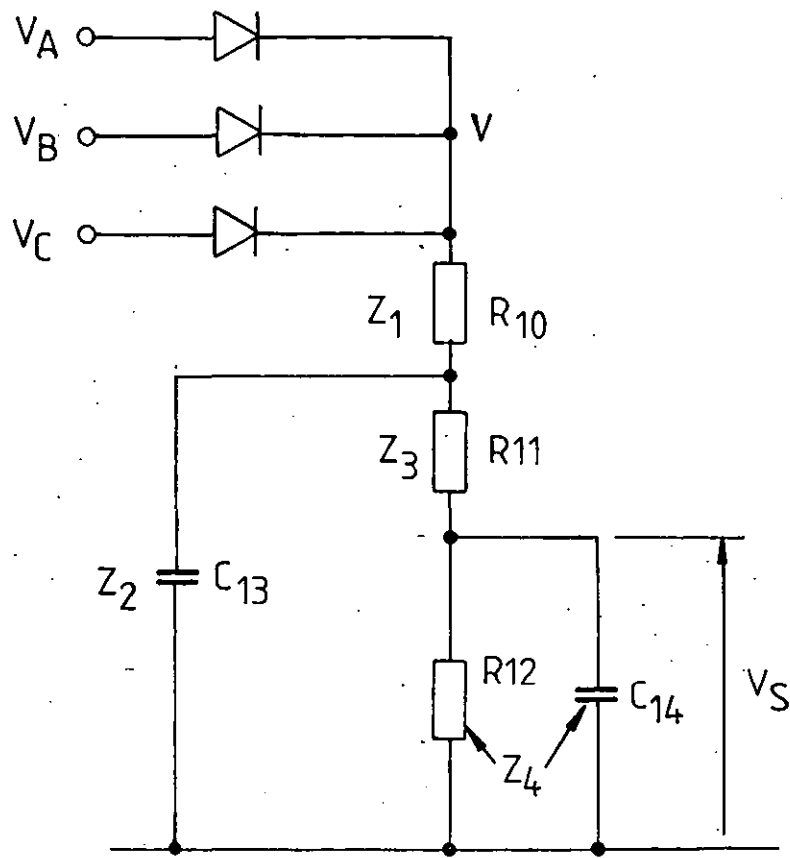


Figure A8.1(b) AVR VOLTAGE SENSING CIRCUIT

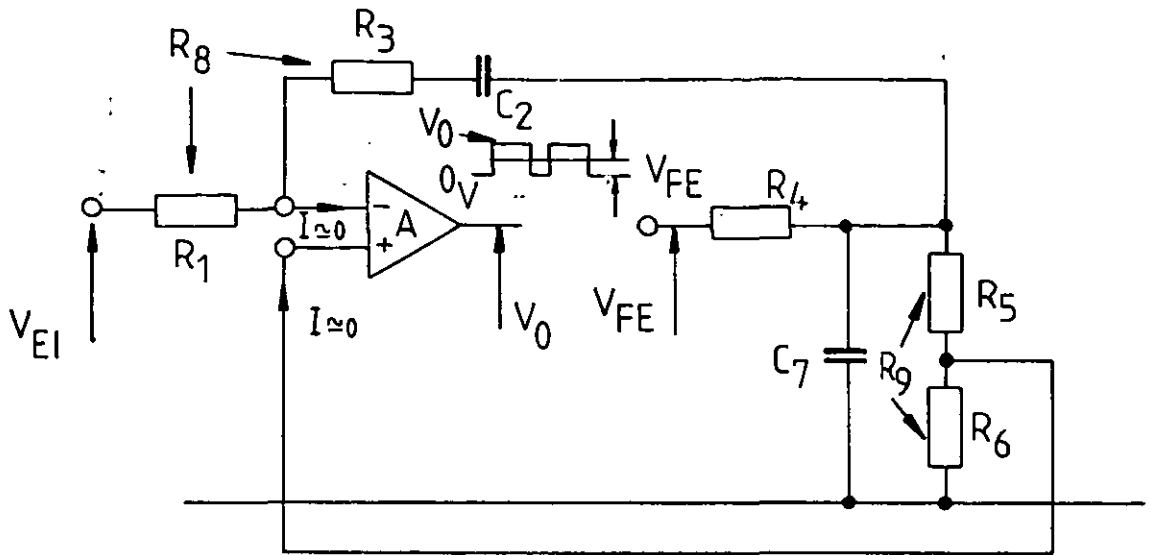


Figure A8.2(a) AVR AMPLIFIER AND FEEDBACK CIRCUITS

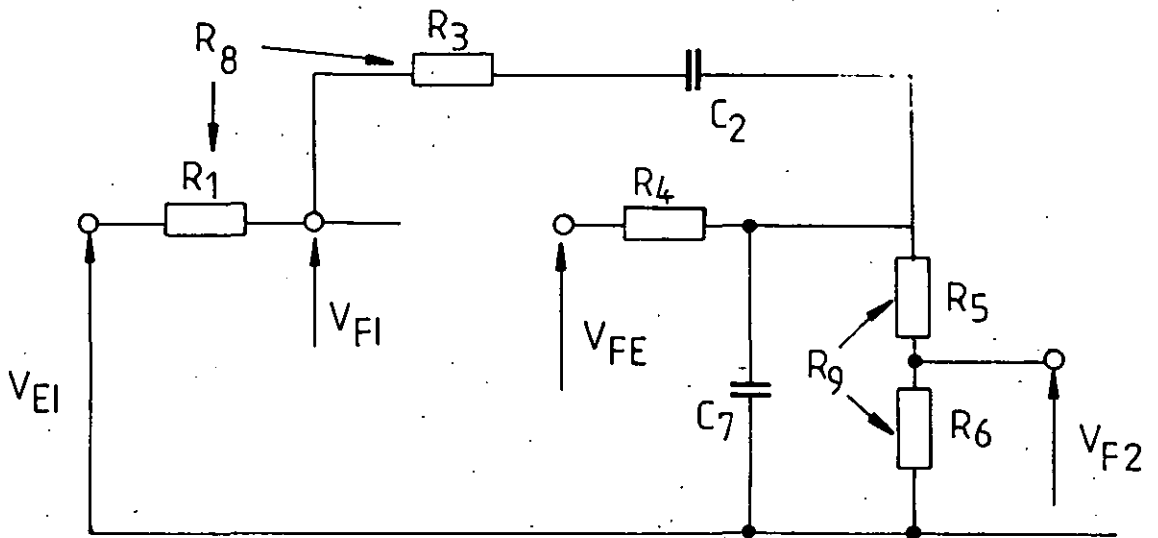


Figure A8.2(b) SIMPLIFICATION OF FEEDBACK CIRCUITS

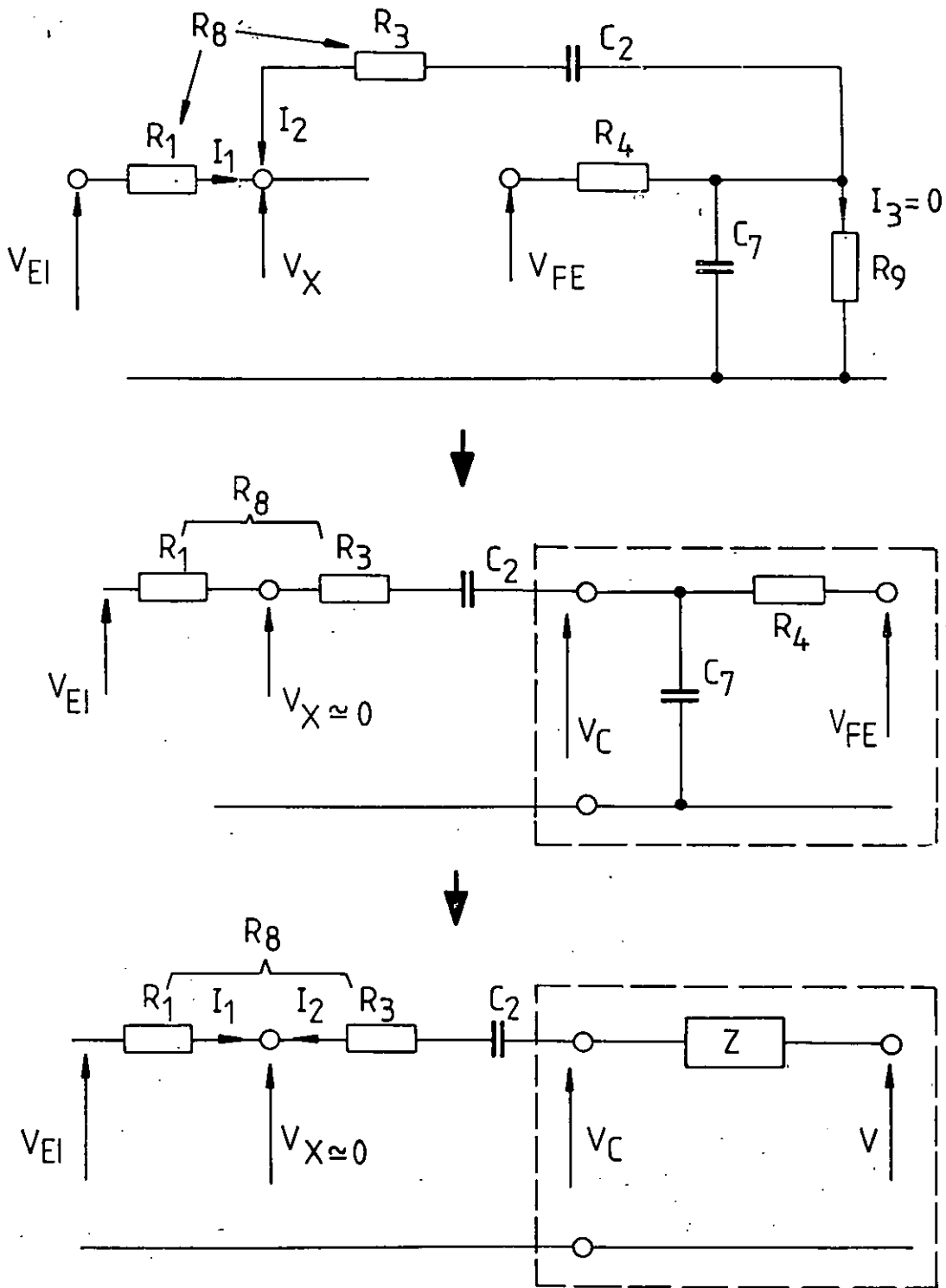


Figure A8.2(c) FURTHER SIMPLIFICATION, IN STAGES, OF FEEDBACK CIRCUITS

APPENDIX A9
SATURATION CHARACTERISTICS OF THE EXCITER

The effect of saturation due to exciter field current on the self inductance L_{FFE} of the exciter field winding is given in Figure A9.1 . This is obtained by measuring the secant self-inductance of the field winding as discussed in Chapter 2. Similarly, the effect of saturation due to the exciter field current on the gain K_E of the exciter is obtained from measurement of the secant mutual inductance between the armature phase and the field winding, as discussed in Chapter 2. This is given in Figure A9.2 . The saturation characteristic of Figure A9.2 can also be obtained from the open-circuit characteristic of the exciter, if this is available. Comparison of the normalised polynomials C_1 and C_2 show that these are very nearly equal, and they can therefore both be obtained from the open-circuit characteristic of the exciter. Therefore:

$$L_{FFE} = L_{FFE(0)} \cdot C_1 = f_1 (I_{FFE} - I_{dr}) \quad A9.1$$

$$K_E = K_{E(0)} \cdot C_2 = f_2 (I_{FFE} - I_{dr}) \quad A9.2$$

$$C_1 = C_2 \quad A9.3$$

where $L_{FFE(0)}$ and $K_{E(0)}$ are the unsaturated values of the self-inductance and gain of the exciter.

From open-circuit characteristic of the exciter, the gain of the exciter at any exciter field current is

$$K_E = \frac{E_{ph}}{I_{FFE}} \quad A9.4$$

where E_{ph} is the exciter phase voltage (R.M.S). Hence values of K_E can be calculated for different values of I_{FFE} , and a normalised

polynomial obtained, expressing K_E in terms of I_{FFE} as given by equation A9.2.

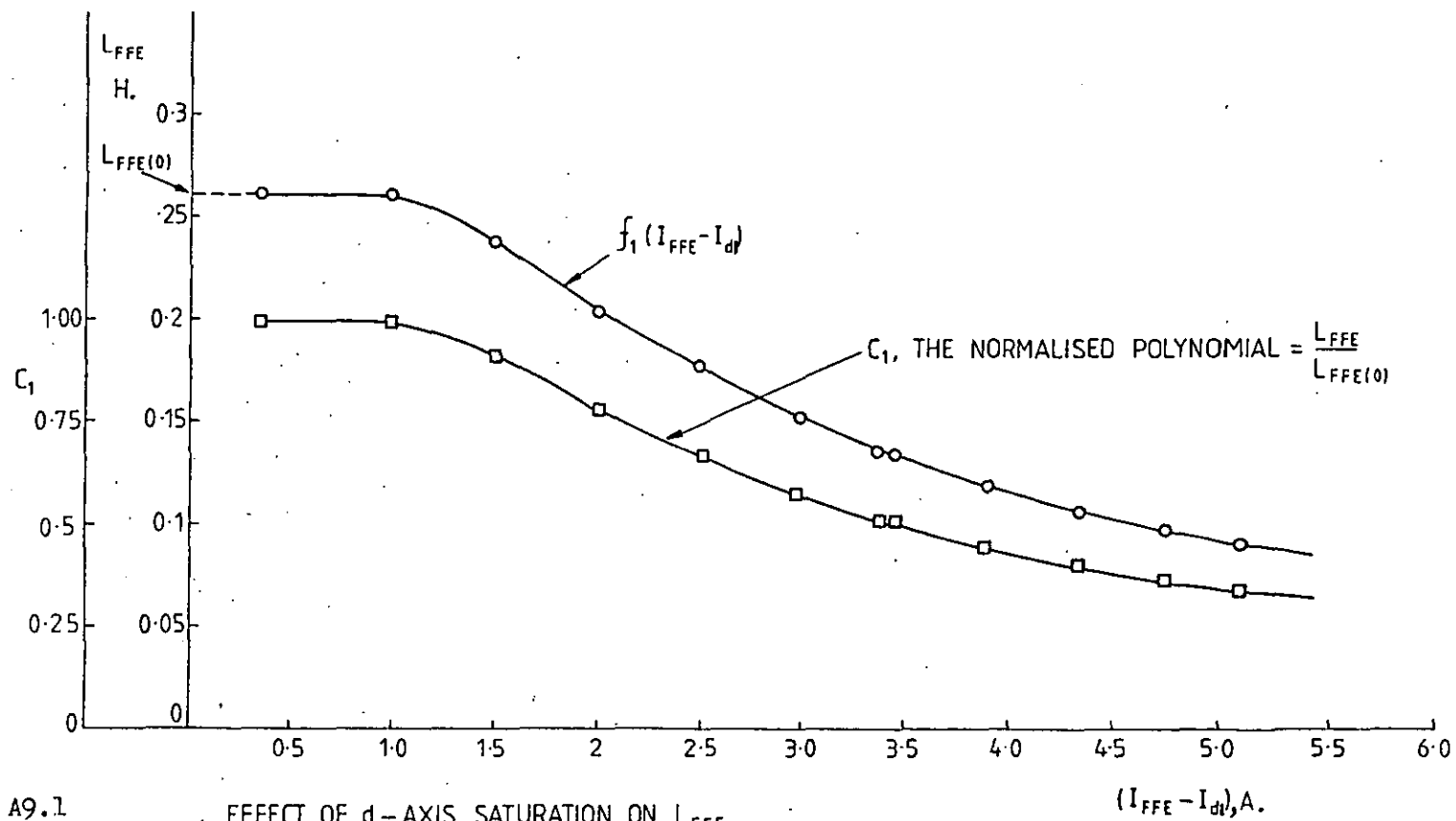


Figure A9.1 EFFECT OF d-AXIS SATURATION ON L_{FFE}

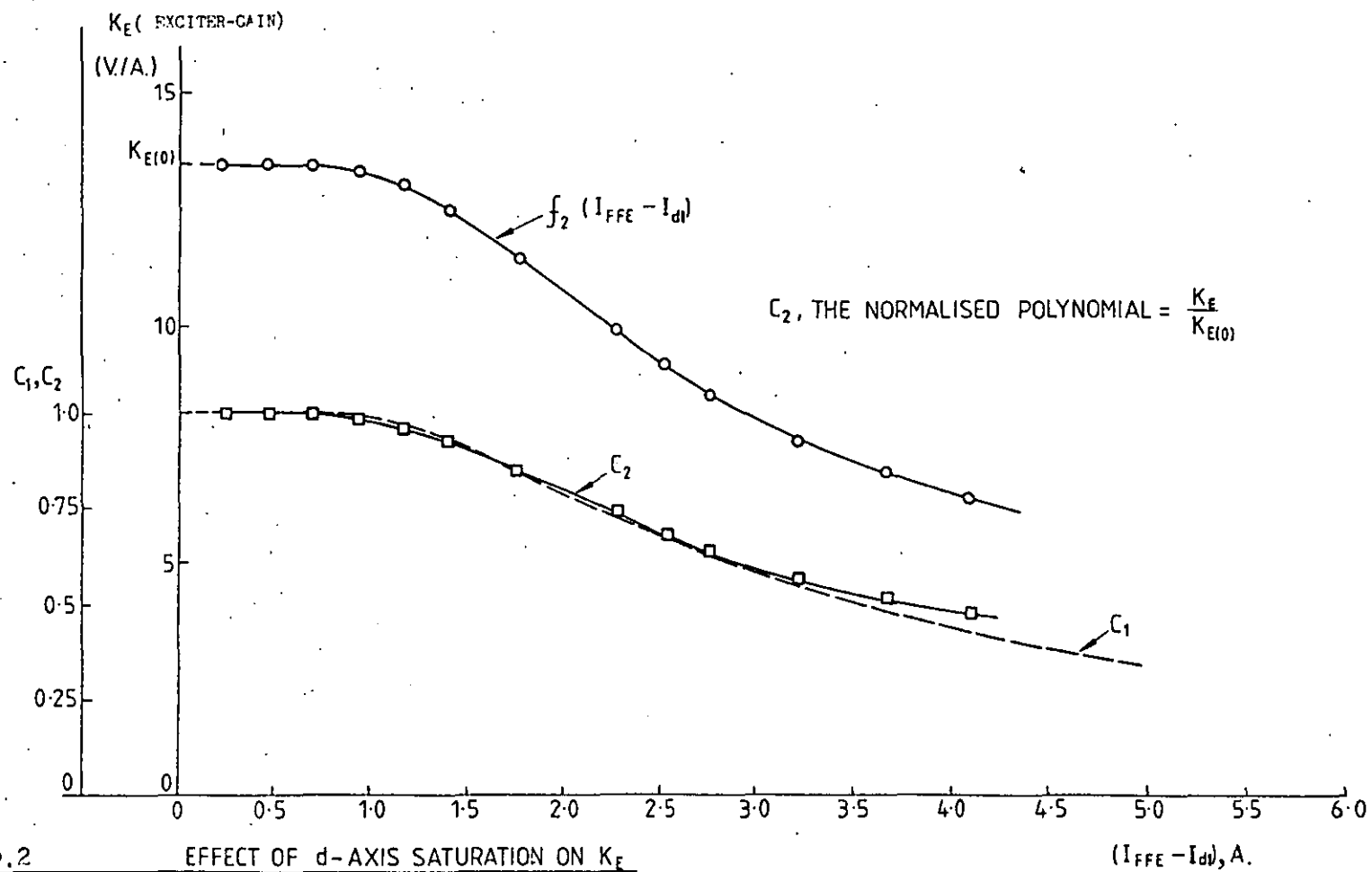


Figure A9.2 EFFECT OF d-AXIS SATURATION ON K_E

APPENDIX A10RELATIONSHIP BETWEEN D.C. POWER OUTPUT AND
EFFECTIVE A.C. POWER SUPPLIED BY THE EXCITER

The d.c. power output P_{dc} of the exciter rectifier is

$$P_{dc} = \frac{E_d^2}{R_d} = E_d I_d \quad A10.1$$

The a.c. power $P_{ac(f)}$ supplied by the fundamental frequency component of the armature phase current is

$$\begin{aligned} P_{ac(f)} &= 3 E_1 I_1 \cos \phi \\ &= 3 \cdot \left(\frac{E_d}{K_v} \right) \left(\frac{I_d}{K_c} \right) \cos \phi \end{aligned}$$

$$\text{or } P_{ac(f)} = P_{dc} \left[\frac{3 \cos \phi}{K_v K_c} \right] \quad A10.2$$

It was found by the author that the value of the term in the bracket $\left[\frac{3 \cos \phi}{K_v K_c} \right]$ was equal to unity when the values of $\cos \phi$, K_v , K_c were substituted, for different modes of operation of the rectifier. This implies that the d.c. power supplied to the generator field winding by the exciter is fully accounted for by the a.c. power supplied to the effective load impedance ($R + jx$ per phase), calculated on the basis of fundamental frequency component of the exciter phase current. Therefore

$$P_{ac(f)} = P_{dc} \quad A10.3$$

APPENDIX A11A11.1 Induction Motor Design Data

Input	:	200V, 3 phase, 400 Hz
Output	:	12 H.P. (nominal)
Stator	:	6 pole, lap wound star connected
Rotor	:	Squirrel cage (aluminium die cast)

A11.2 Calculation of Induction Motor Phase Model Parameters

The parameters of the equivalent circuit of the induction motor given in Figure A11.1 were calculated from the locked rotor test and the no load test to be

$$X_1, X_2 = 0.487 \quad \Omega$$

$$X_m = 14.843 \quad \Omega$$

$$R_{11} = 0.1138 \quad \Omega \quad \text{at } 20^\circ\text{C ambient}$$

$$R_{22} = 0.113 \quad \Omega \quad \text{at } 20^\circ\text{C ambient}$$

The corresponding phase model parameters as defined in Chapter 7 are:

- a) Stator phase winding resistance (R_S)

$$R_S = 0.1138 \quad \Omega \quad \text{at } 20^\circ \text{ ambient}$$

- b) Stator phase winding self inductance (L_S)

$$L_S = (X_1 + \frac{2}{3} X_m) \cdot \frac{1}{2\pi f} = 4.131 \times 10^{-3} \text{ H}$$

- c) Rotor phase winding self inductance (L_R)

$$L_R = (X_2 + \frac{2}{3} X_m) \cdot \frac{1}{2\pi f} = 4.131 \times 10^{-3} \text{ H}$$

- d) Stator winding phase to phase mutual inductance (M_S)

$$M_S = -\frac{1}{2} \left(\frac{2}{3} X_m \right) \cdot \frac{1}{2\pi f} = -1.9686 \times 10^{-3} \text{ H}$$

- e) Rotor winding phase to phase mutual inductance (M_R)

$$M_R = -\frac{1}{2} \left(\frac{2}{3} X_m \right) \cdot \frac{1}{2\pi f} = -1.9686 \times 10^{-3} \text{ H}$$

- f) The inductance coefficient of the stator phase winding to the rotor phase winding mutual inductance

$$M = \frac{2}{3} X_m \cdot \frac{1}{2\pi f} = 3.9372 \times 10^{-3} \text{ H}$$

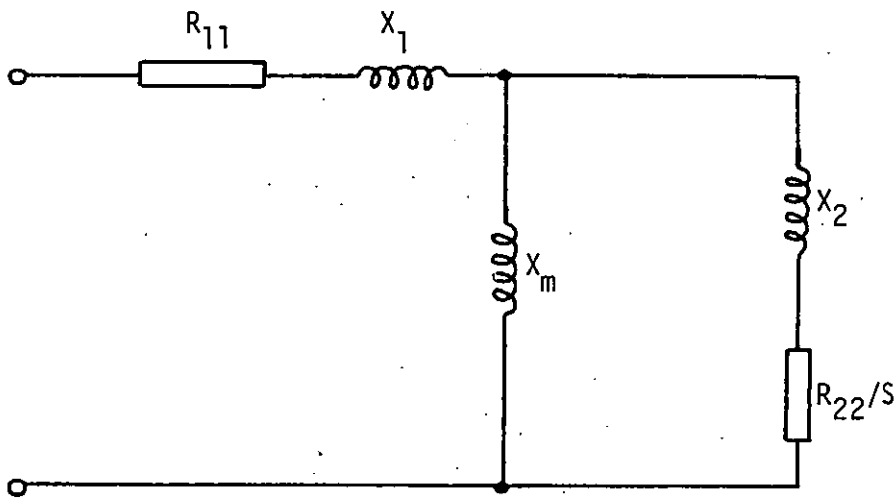


FIGURE A11.1 Induction motor equivalent circuit

APPENDIX A12

A12.1 Electromagnetic Torque Equation of Induction Motor

The electromagnetic torque T_e of the induction motor is given by⁵⁷

$$T_e = (\text{pole pairs}) \cdot [I]_t [G] [I] \quad \text{A12.1}$$

For the phase model of the induction motor discussed in Chapter 7, $[I]$ in equation A12.1 is equal to $[I_{pm}]$ given by equation 7.2 and $[G]$ is equal to $[G_{pm}]/(\frac{d\theta}{dt})$ from equation 7.5.

Therefore

$$T_e = (\text{pole pairs}) \{ [I_{pm}]_t \} \{ [G_{pm}]/(\frac{d\theta}{dt}) \} [I_{pm}] \quad \text{A12.2}$$

A12.2 The Mechanical Load Torque Equation

Assuming the load torque of the fan on the induction motor shaft is proportional to the square of the rotational speed, the mechanical load torque T_L is given by

$$T_L = T_F + K_S \omega^2 \quad \text{A12.3}$$

where T_F is a constant load torque due to friction etc. and K_S is a constant.

Equations A12.2 and A12.3 can be combined to give the differential equations A12.4 suitable for numerical integration on the digital computer

$$\begin{bmatrix} p\theta \\ p\omega \end{bmatrix} = \begin{bmatrix} 0 & 1 \\ 0 & 0 \end{bmatrix} \begin{bmatrix} \theta \\ \omega \end{bmatrix} + \begin{bmatrix} 0 & 0 \\ \frac{1}{J} & -\frac{1}{J} \end{bmatrix} \begin{bmatrix} T_e \\ T_L \end{bmatrix} \quad \text{A12.4}$$

where J is the moment of inertia.

APPENDIX A13

TRANSFORMATION OF $[L_{ryb}]$ TO $[L_{dgo}]$

The inductance tensor $[L_{dgo}]$ is obtained from $[L_{ryb}]$ by using the transformation $[C]$ given in equation 9.3, Chapter 9.

$$[L_{dgo}] = [C][L_{ryb}][C]_t \quad A13.1$$

Consider the general form of inductance tensor $[L_{ryb}]$ given by equation A13.2. It can be shown that $[L_{dgo}]$ obtained from equation A13.1 using the general form of inductance tensor $[L_{ryb}]$ is

$$[L_{dgo}] = \begin{array}{|c|c|c|} \hline L_1 + \frac{L_2}{2} + L_3 + L_4 & 0 & \frac{1}{\sqrt{2}} (L_2 - L_4) \cos 3\theta_r \\ \hline 0 & L_1 - \frac{L_2}{2} + L_3 - L_4 & \frac{1}{\sqrt{2}} (L_2 - L_4) \sin 3\theta_r \\ \hline \frac{1}{\sqrt{2}} (L_2 - L_4) \cos 3\theta_r & \frac{1}{\sqrt{2}} (L_2 - L_4) \sin 3\theta_r & L_1 - 2L_3 \\ \hline \end{array}$$

A13.3

Equation A13.3 shows that L_{dgo} is not time invariant as θ_r is time dependent, if the assumptions made in the dgo model are invalid (i.e. if $L_2 \neq L_4$).

Comparing equations 9.15, Chapter 9 and A13.2,

$$L_1 = L_{a1} + L_{g0} \quad A13.4$$

$$L_2 = L_{g2} \quad A13.5$$

$[L_{ryb}] =$

$L_1 + L_2 \cos 2\theta_r$	$-L_3 + L_4 \cos 2(\theta_r - 60^\circ)$	$-L_3 + L_4 \cos 2(\theta_r + 60^\circ)$
$-L_3 + L_4 \cos 2(\theta_r - 60^\circ)$	$L_1 + L_2 \cos 2(\theta_r - 120^\circ)$	$-L_3 + L_4 \cos 2\theta_r$
$-L_3 + L_4 \cos 2(\theta_r + 60^\circ)$	$-L_3 + L_4 \cos 2\theta_r$	$L_1 + L_2 \cos 2(\theta_r + 120^\circ)$

A13.2

$$L_3 = \frac{1}{2} L_{go} \quad \text{A13.6}$$

$$L_4 = L_{g2} \quad \text{A13.7}$$

Substituting for L_1 , L_2 , L_3 and L_4 from equations A13.4 to A13.7 into equation A13.3 gives

$$[L_{dqo}] = \begin{array}{|c|c|c|} \hline L_{a1} + \frac{3}{2} (L_{go} + L_{g2}) & 0 & 0 \\ \hline 0 & L_{a1} + \frac{3}{2} (L_{go} - L_{g2}) & 0 \\ \hline 0 & 0 & L_{a1} \\ \hline \end{array}$$

A13.8

